NATIONAL CONFERENCE ON NANO/BIO-TECHNOLOGY 2019, INDIA

EDITED BY: Pratima R. Solanki, Ajeet Kaushik and Anil Kumar

frontiers Research Topics

About Frontiers

Frontiers is more than just an open-access publisher of scholarly articles: it is a pioneering approach to the world of academia, radically improving the way scholarly research is managed. The grand vision of Frontiers is a world where all people have an equal opportunity to seek, share and generate knowledge. Frontiers provides immediate and permanent online open access to all its publications, but this alone is not enough to realize our grand goals.

Frontiers Journal Series

The Frontiers Journal Series is a multi-tier and interdisciplinary set of open-access, online journals, promising a paradigm shift from the current review, selection and dissemination processes in academic publishing. All Frontiers journals are driven by researchers for researchers; therefore, they constitute a service to the scholarly community. At the same time, the Frontiers Journal Series operates on a revolutionary invention, the tiered publishing system, initially addressing specific communities of scholars, and gradually climbing up to broader public understanding, thus serving the interests of the lay society, too.

Dedication to Quality

Each Frontiers article is a landmark of the highest quality, thanks to genuinely collaborative interactions between authors and review editors, who include some of the world's best academicians. Research must be certified by peers before entering a stream of knowledge that may eventually reach the public - and shape society; therefore, Frontiers only applies the most rigorous and unbiased reviews.

Frontiers revolutionizes research publishing by freely delivering the most outstanding research, evaluated with no bias from both the academic and social point of view. By applying the most advanced information technologies, Frontiers is catapulting scholarly publishing into a new generation.

What are Frontiers Research Topics?

Frontiers Research Topics are very popular trademarks of the Frontiers Journals Series: they are collections of at least ten articles, all centered on a particular subject. With their unique mix of varied contributions from Original Research to Review Articles, Frontiers Research Topics unify the most influential researchers, the latest key findings and historical advances in a hot research area! Find out more on how to host your own Frontiers Research Topic or contribute to one as an author by contacting the Frontiers Editorial Office: frontiersin.org/about/contact

NATIONAL CONFERENCE ON NANO/BIO-TECHNOLOGY 2019, INDIA

Topic Editors:
Pratima R. Solanki, Jawaharlal Nehru University, India
Ajeet Kaushik, Florida Polytechnic University, United States
Anil Kumar, National Institute of Immunology (NII), India

Table of Contents

Editorial: National Conference on Nano/Bio-Technology 2019, India

G. B. V. S. Lakshmi[1], Ajeet Kaushik[2], Anil Kumar[3] and Pratima R. Solanki[1]*

[1]Special Centre for Nanoscience, Jawaharlal Nehru University, New Delhi, India, [2]NanoBioTech Laboratory, Department of Natural Sciences, Division of Sciences, Art, and Mathematics, Florida Polytechnic University, Lakeland, FL, United States, [3]Gene Regulation Laboratory, National Institute of Immunology, New Delhi, India

Editorial on the Research Topic

National Conference on Nano/Bio-Technology 2019, India

The National Conference on Nano/Bio-Technology 2019 organized jointly by the Jawaharlal Nehru University and the National Institute of Immunology, New Delhi, India during December 19 to 21, 2019. This multidisciplinary conference focused on state-of-art synergies between nanoscience and biotechnology, and their significant technological aspects. As a result, the attending scholars gained cutting edge knowledge of nano-supported technological advancements for developing nanomedicine, nano-biosensors, point of care devices, and other biomedical devices relating to health care. The key scientific findings presented in this conference were published as a special issue in Frontiers in Nanotechnology under the title "National Conference on Nano/Bio-Technology 2019, India" (https://www.frontiersin.org/research-topics/15270/national-conference-on-nanobio-technology-2019-india). In this special issue, the editors selected nanomaterials-based articles that deal with applications in biosensors, drug delivery, nanotoxicity, etc. These articles were contributed a variety of reputed Indian universities, national laboratories, and research institutions with the aim to bring together scholars of various disciplines, including nanomaterials, enabled biotechnology, nano-biosensors, bio-imaging, drug delivery, diagnostic devices, nano-toxicity, and microbiology.

Wide varieties of nano/bio-technology related topics were covered in this special issue. The electrochemical sensors based on different nanomaterials for various analytes were reported. A new electrochemical sensor was reported, based on β-tricalcium phosphate $(Ca_3(PO_4)_2)$ nanoparticles modified by a glassy carbon electrode for the selective non-enzymatic determination of methyl parathion and mercury (II) ions independently. This sensor has high selectivity towards MP and Hg in the presence of major interfering compounds such as 3-nitrophenol, 4-nitrophenol, 4-aminophenol, catechol, hydroquinone and heavy metals such as lead, cadmium and arsenic. Applicability of the fabricated sensor for detection of MP and Hg (II) ions has been tested in tap water by the standard addition method. An electrochemical sensor for the detection of cholesterol based on thin films of nafion (polymer) and hematite or α-Fe_2O_3 (nanoparticles) nanocomposite was fabricated on indium tin oxide (ITO) coated glass substrates.

The synergy between the antifungal drugs and the ZnO quantum dots was studied, and it was found that the incorporation of quantum dots can decrease dose size in the treatment of fungal infections leading to reduces toxicity, and their multitargeted action could limit evolution of fungal drug resistance. Gelatin nanoparticles were used for therapeutic applications: the Etoposide loaded gelatin nanoparticles (EGNPs) were tested for *in-vivo* therapeutic potential by studying pharmacokinetics, biodistribution and tumor regression in Ehrlich Ascites Carcinoma (EAC),

using a mice model. High biocompatibility and bio-efficacy of EGNPs proved their therapeutic potential in cancer treatment.

Two different nanomaterials based optical sensors were reported for the detection of toxins and antibiotics. Manganese oxide nanoparticles (MnO_2 nps) were explored to study the interaction with aflatoxin (AFB1) and ochratoxin (OchA) using UV-visible spectroscopy. This bio-active free direct sensing approach of AFB1 and OchA sensing was reported as a potential analytical tool to estimate food quality rapidly and in an affordable manner at the point of use. The L-Cysteine capped magnesium sulfide quantum dots (L-Cyst-MgS QDs) were used to detect Levofloxacin antibiotic *via* the photoinduced electron transfer mechanism. The fluorescence of the QDs was used as the sensing platform for the selective detection of Levofloxacin antibiotic.

The oxidative stress and immunotoxicity imposed by Zinc selenium/Zinc sulphide quantum dots (ZnSe/ZnS QDs) was studied and reported. The higher concentrations of the ZnSe/ZnS QDs causes cell death due to reactive oxygen species production. The study evidenced that ZnSe/ZnS QDs is not capable of eliciting any serious damages to liver and brain tissues, which in turn substantiates its applicability in biomedical applications. The cerium doped tin oxide nanoparticles (Ce doped SnO_2 nps) were studied for their antimicrobial activity and photocatalytic activity. The Ce doped SnO_2 nps prevented the *E.coli* bacterial growth, and were successfully used for the photocatalytic degradation of Malachite Green dye under UV light irradiation.

A mathematical modelling of blood flow with the suspension of nanoparticles through a tapered artery with a blood clot was reported. Also, a small review was given on the applications of 3D-printed microfluidics in biomedical applications. The paper reviewed the emerging diagnostic technologies using 3D printing as a method for integrating living cells or biomaterials into 3D printing. It is important to have standards and regulations in the device development used in health care sector. The National Physical Laboratory (NPL), India, is playing a significant role in this aspect. A brief the summary on the significant achievements and role of NPL in supporting the Indian medical device regulations was presented.

Overall, the articles published in this special issue projected high-performance smart nano-systems for various biomedical applications focused on the detection, treatment, and monitoring of a targeted marker. At the same time, scholars also raised the concern of limited resources and lacking translational and sustainable efforts to introduce nanoscience for industrial and clinical application. The editor also supports this view, and believes that in future more efforts will be made to divert fundamental research of nano-biotechnology towards translational efforts. In this process, the Frontiers in Nanotechnology journal will always be one of the best platforms to publish such top ranked research to fill the gap between education and applied technology.

AUTHOR CONTRIBUTIONS

All the authors have contributed to prepare the special issue of the conference and gave significant inputs for writing the editorial card.

ACKNOWLEDGMENTS

Synthesis, Antimicrobial Activity, and Photocatalytic Performance of Ce Doped SnO$_2$ Nanoparticles

Bhawna[1,2], Ashish Kumar Choudhary[3], Akanksha Gupta[4]*, Sanjeev Kumar[1,2], Pramod Kumar[5], R. P. Singh[4], Prashant Singh[6] and Vinod Kumar[1,7]*

[1] Department of Chemistry, Kirori Mal College, University of Delhi, New Delhi, India, [2] Department of Chemistry, University of Delhi, New Delhi, India, [3] Department of Botany, University of Delhi, New Delhi, India, [4] Department of Chemistry, Sri Venkateswara College, University of Delhi, New Delhi, India, [5] Department of Chemistry, Sri Aurobindo College, Delhi University, New Delhi, India, [6] Department of Chemistry, Atma Ram Sanatan Dharma College, Delhi University, New Delhi, India, [7] Special Centre for Nano Sciences, Jawaharlal Nehru University, New Delhi, India

This work represented the synthesis of Ce doped SnO$_2$ nanoparticles by a wet chemical method and was characterized by various characterization techniques. PXRD confirmed the presence of the rutile phase for Ce doped SnO$_2$ nanoparticles. SEM image and elemental mapping showed agglomerated irregular shaped particles and uniform distribution of 5% Ce ions within the SnO$_2$ lattice, respectively. Ce doped SnO$_2$ nanoparticles showed antimicrobial activity against *E. coli* and prevented the growth of bacteria. The nanoparticles were found photocatalytic active and photocatalytic behavior was elucidated by the degradation of Malachite Green dye under UV light irradiation.

Keywords: cerium, *E. coli*, malachite green, photocatalyst, doping

INTRODUCTION

There has been a continuous threat to health, food packaging, cosmetics, and many more industries due to microbes and these industries highly depend on various antimicrobial agents (Ananpattarachai et al., 2009). Contaminated surfaces, colonization, subsequent biofilm formation, improper cleaning of equipments are found to be the primary carriers of microorganisms leading to several foodborne and other outbreaks (Swaminathan and Smidt, 2007; Yemmireddy and Hung, 2017). Nanotechnology has its impacts on all fields of science related to nanomedicine, biomedical, biosensor, development of smart cities, energy, environment, etc. (Kumar et al., 2019a; Bhawna et al., 2020; Gupta et al., 2020a,b).

Nanoparticles have been long known for their antimicrobial behavior against gram-positive and gram-negative bacteria, pathogens, and other microbes (Azam et al., 2012; Vargas-Reus et al., 2012). Metal oxide nanoparticles serve as antimicrobial agents owing to their large surface area (Raghunath and Perumal, 2017). Out of several metal oxide nanomaterials, scientists have more interest in SnO$_2$ nanoparticles because of their novel properties such as high chemical stability, high transparency, and low electrical sheet resistance, etc. (Jarzebski and Marton, 1976a,b; Jarzebski and Morton, 1976). The modified SnO$_2$ also has great technical and scientific interests because of its diverse applications, e.g., transparent conducting electrodes, gas sensors, as electrodes in lithium-ion batteries, electronic devices, dye-based solar cells, H$_2$ generation, etc. (Jiang et al., 2017, 2018; Park et al., 2017; Xie et al., 2017; Wang et al., 2018; Bhawna et al., 2020). Other than these applications, SnO$_2$ has been seeking attention as an antimicrobial agent and has played an essential role against the growth of various bacterial strains like *Staphylococcus aureus*, *E. coli*

(Kumari and Philip, 2015; Vidhu and Philip, 2015; Phukan et al., 2017). Green synthesis of SnO_2 nanoparticles using *Aloe barbadensis miller* showed antibacterial and antifungal activities (Ayeshamariam et al., 2013). Apart from antimicrobial activities, other important biological properties like anticancer, antitumor, and antioxidant activities have also been reported using green synthesized SnO_2 nanoparticles (Kamaraj et al., 2014; Khan et al., 2018). However, when doped with transition metal ions, SnO_2 disinfects microbes with good efficiency, i.e., Co-doped SnO_2 and Ag-doped SnO_2 nanoparticles have shown potent antibacterial activities (Chandran et al., 2015; Nasir et al., 2017; Qamar et al., 2017; Ali et al., 2018). Only a few reports are available on antimicrobial activities of Ce doped metal oxide NPs. Ce-doped ZnO NPs showed antimicrobial activity against both gram-negative and gram-positive bacteria (Rooshde et al., 2020). Similarly, Ce doped CuO NPs completely eradicated the *E. coli* and *S. aureus* bacteria (Jan et al., 2014) and Ce-doped ZrO_2 NPs showed high antibacterial property against gram-positive bacteria than gram-negative bacteria (Mekala et al., 2018).

Water is a crucial factor for the existence of life on earth and clean water is the necessity of the hour. Consumption of water by a rapid increasing population is leading to the depletion of major aquifers. On the other hand, organic manufacturing industries have been the target for disposing of their chemical wastes into water bodies. According to research, the world's dye production of about 0.7 million tons (>11%) is annually released as industrial wastewater (Samadi et al., 2019). Among various known dyes, Malachite green dye has its extensive uses worldwide. Besides its use as a dye in silk, jute, leather, wool and paper industries; it is also used as a food additive, coloring agent and as a disinfectant. However, due to its carcinogenic effects on human health and aquatic life, it has now become a controversial compound and has been banned in many countries. Continuous efforts are being made to recycle contaminated water containing bacteria, toxic chemicals, dyes, heavy metals, etc. to make it safe for drinking and other purposes. Some conventional methods are- photocatalysis, ozonation, Fenton's reagent, electrochemical routes, membrane filtration, coagulation, adsorption, ion-exchange, irradiation, anaerobic and aerobic degradation, etc. (Gusain et al., 2019). Though, metal oxides such as TiO_2, SnO_2, ZnO have been found as better photocatalysts for the degradation of organic dyes in aquoues solution. SnO_2 as an n-type semiconductor has also been reported for the degradation of various azo dyes. Besides antimicrobial activities, doped SnO_2 finds improved results in photocatalytic activities. Ce doping has been known for bandgap tailoring as well as lattice distortion in SnO_2. There are various methods reported in literature for the synthesis of Ce doped SnO_2 such as- sol-gel (Shide et al., 2010; Ahmed et al., 2019), hydrothermal (Lian et al., 2017), co-precipitation (Bharathi et al., 2017; Kumar et al., 2018), wet-chemical (Kumar et al., 2019b), flame spray method (Kotchasak et al., 2018), etc. Kumar et al. showed degradation of dyes such as methylene blue and methyl orange using Ce doped SnO_2 nanoparticles (Kumar et al., 2019b) whereas Wu et al. degraded methyl orange dye using Ce doped SnO_2 (Shide et al., 2010).

To the best of our knowledge, until now, no work has been reported on antimicrobial behavior using Ce doped SnO_2.

This work involves the facile synthesis of Ce doped SnO_2 nanoparticles and reports its antimicrobial behavior against microbes. It also represents photocatalytic degradation of malachite green dye using Ce doped SnO_2.

EXPERIMENTAL SECTION

Ce doped SnO_2 nanoparticles were synthesized by a wet-chemical method using hydrogen peroxide, as mentioned in our previous report (Kumar et al., 2019b). Solutions of $SnCl_2.2H_2O$ (Merck, 18 ml of 0.5 M) and $CeCl_3$ (Merck, 6 mL of 40 mM) were mixed and 30 mL hydrogen peroxide was added into the mixture. Then, the mixture was refluxed at 100°C for 14 h. The white suspension was cooled to room temperature, centrifuged, and was dried after washing several times to remove dissolved impurities.

Characterization Details

The powder X-ray diffraction (PXRD) pattern was recorded using Rigaku, Miniflex 600 X-ray diffractometer employing monochromatized Cu K_α radiation. The Field Emission Scanning Electron Microscope (FESEM) image of the SnO_2 NPs was recorded on a ZEISS Gemini SEM 500.

EVALUATION OF ANTIMICROBIAL ACTIVITY

The Antimicrobial activity of Ce doped SnO_2 nanoparticles was carried out using Diffusion Susceptibility Test method (Bauer et al., 1966). The bacterial strain, *E. coli* was inoculated in 5 ml LB Media (Luria-Bertani; HiMedia Laboratories) and was kept at 37°C and 180 rpm for overnight incubation. The overnight incubated bacterial culture was diluted in 1:100 ratios with fresh LB media. A zone of inhibition experiment was analyzed using an LB Agar plate well-diffusion method. Then, the sterilized
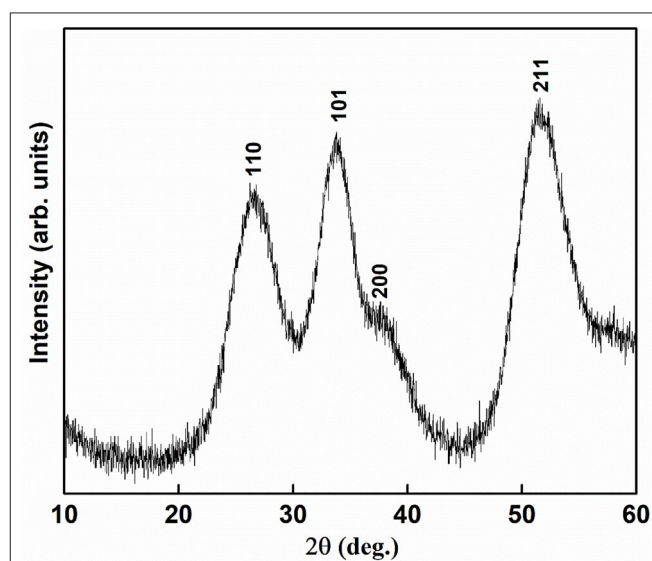
FIGURE 1 | PXRD pattern of Ce doped SnO_2.
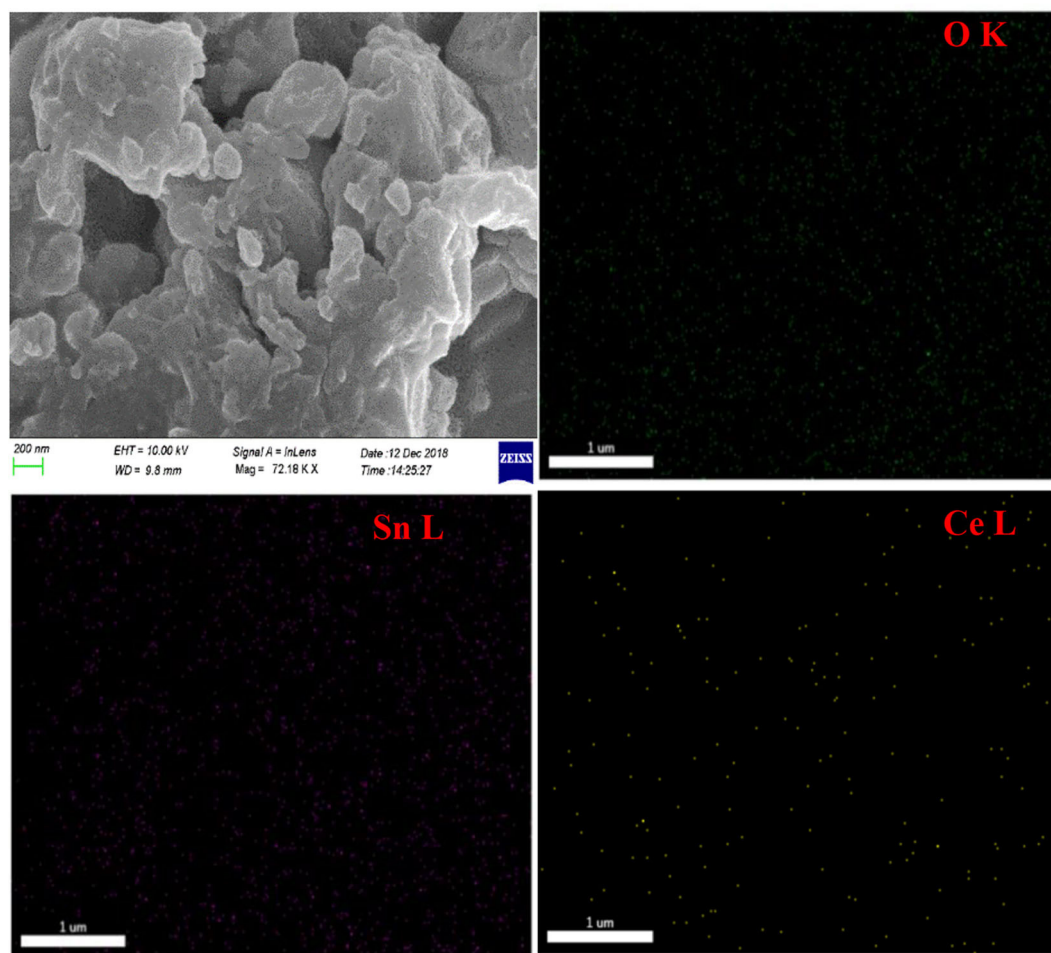
FIGURE 2 | SEM image and Elemental mapping of Ce doped SnO_2.

well cutter was used for boring the LB Agar plate. The diluted overnight bacterial culture of *E. coli* was spread on LB agar plate. Thereafter, seven concentrations of Ce: SnO_2 NPs, namely, 0.25, 0.50, 1, 2, 3, 4, and 5 mg were poured into LB Agar wells. The well in the center of LB agar plate did not contain Ce doped SnO_2 NPs and was used as a control. Thereafter, the LB agar plate with Ce doped SnO_2 NP was incubated at 37°C for 16 h.

Photocatalytic Degradation of Pollutants

Photocatalytic degradation of dye was performed in an in-house fabricated solar reactor under UV (λ < 400 nm) light by high vapor pressure mercury lamp 125 W (Osram, India) (Kumar et al., 2011). In the photocatalytic activity, 0.1 g of Ce: SnO_2 NPs were suspended into an aqueous solution of 100 mL of 15 μM MG dye, which was taken in the photoreactor. The dye solution suspended with the catalyst was stirred for 30 min in the dark to attain the equilibrium and then the light was irradiated over the solution. Each time, five mL volume were pipetted out timely, centrifuged and the absorbance was noted using the UV-visible spectrometer.

RESULT AND DISCUSSION

The Powder X-ray diffraction pattern of the synthesized Ce doped SnO_2 nanoparticles has been shown in the **Figure 1**. It shows a rutile structure with tetragonal symmetry space group $P4_2/mnm$ [a = 4.680 (4) Å and c = 3.167 (4) Å] and shows clear reflection at (110), (101), (200), and (211) crystallographic planes corresponding to JCPDS file no. 41-1445 (Kumar et al., 2019b). The absence of any other characteristic peaks rule out possibilities of impurities or other species within the lattice represents high phase purity. The broadness of the diffracted peaks depicts a small size of crystals and the average crystallite size determined using the Scherrer formula was found to be ∼6 nm (Scherrer, 1912).

The morphology and elemental mapping of Ce doped SnO_2 nanoparticles was investigated through FESEM (**Figure 2**). Irregularly shaped particles distributed unevenly over the lattice surface has been shown through SEM imaging. Elemental mapping shows the spatial distribution of elements within the lattice and provides the evidence that Ce (yellow), Sn (purple), and O (green) were homogeneously distributed within the crystal lattice.

After elucidation of the phase formation and morphology of the formed nanoparticles, the concentration of Ce ions was found to be 5% as determined through X-ray photoelectron spectroscopy in our previous report (Kumar et al., 2019b). Also, the presence of Ce^{3+} and Ce^{4+} ions was confirmed into SnO_2 lattice, which caused charge imbalance and hence disorderness in the lattice (Kumar et al., 2019b).

Analysis of Antimicrobial Activity

Antibacterial activity of Ce doped SnO_2 NPs was observed on LB Agar well-diffusion method (Dil and Sadeghi, 2018). Antibacterial activity of the NPs was compared with the control well (without NPs). The antibacterial activity of Ce doped SnO_2 NPs was not observed at concentration 0.25–3 mg (**Figure 3**). **Figure 3** suggested that the zones of inhibition were prominent at two concentrations namely, 4 and 5 mg, respectively and was highest at 5 mg concentration. The antibacterial activities have been assessed through the diameter of the zone of inhibition. At a concentration of 4 mg or above, Ce doped SnO_2 NPs showed potent antibacterial activities (**Table 1**). Previously, other metal ions doped with SnO_2 like Co-doped SnO_2, Cu-doped SnO_2, Fe-doped SnO_2, and Ag-doped SnO_2 nanoparticles have also been reported for their antibacterial activities (Chandran et al., 2015; Nasir et al., 2017; Ali et al., 2018; Baig et al., 2020; Sathishkumar and Geethalakshmi, 2020). Generally, nanoparticles kill the bacteria through cell membrane

disruption, free radical formation causing reactive oxygen species responsible for antibacterial action (Sirelkhatim et al., 2015).

Photocatalytic Dye Degradation

The degradation of malachite green was performed photocatalytically using Ce: SnO_2 nanoparticles (**Figure 4**) under UV light irradiation. It degrades malachite green dye ~50% in 120 min of light irradiation. When compared with other metal oxides, it is found that undoped TiO_2 NPs and F doped TiO_2 NPs photocatalytically degraded 99.9 and 54.26% MG dye in 240 min and 120 min, respectively (Chen et al., 2007; Panahian and Arsalani, 2017). Sn doped TiO_2 has been reported degrading 85% MG in 340 min under light irradiation (Sayilkan et al., 2007), while SnO_2 NPs degraded 27% MG in 180 min under UV light irradiation (Kumar et al., 2016).

The probable mechanism for the degradation of malachite green dye using Ce doped SnO_2 NPs has been revealed in **Figure 5**. Electrons were excited into the conduction band of Ce doped SnO_2 nanoparticles from its valence band on light irradiation [bandgap = 3.80 eV (Kumar et al., 2019b)]. Electrons were also injected into the conduction band of photocatalyst after transfer from HOMO to LUMO of malachite green dye (Helaïli et al., 2017). These electrons from two different sites then move to the surface for surface reactions. The electrons at the surface react with adsorbed/dissolved oxygen to produce $\dot{O}_2^-$ radical. The concentration of the O_2 molecule is responsible for the efficiency

FIGURE 3 | Antibacterial activity of Ce-doped-SnO_2 NPs.
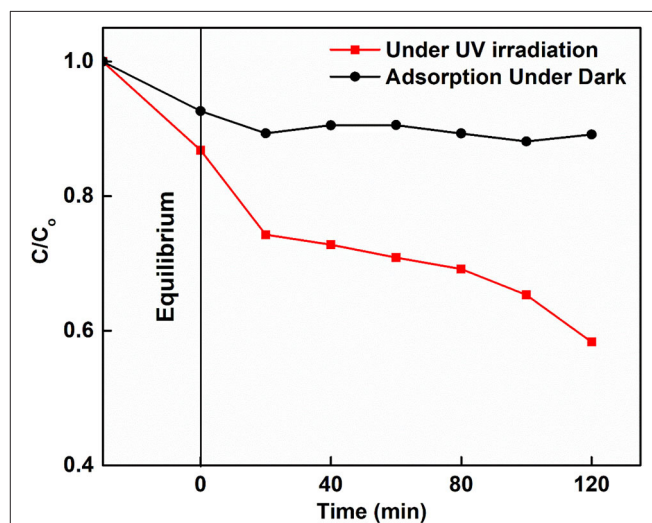
FIGURE 4 | Adsorption of MG in dark and photocatalytic degradation of MG in the presence of Ce doped SnO_2 under UV irradiation.

TABLE 1 | Concentration and observation of zone of inhibition of Ce doped SnO_2.

Concentration of Ce doped SnO_2 (mg)	0.25	0.50	1	2	3	4	5
Zone of inhibition	No	No	No	No	Least	Moderate	Strong activity

FIGURE 5 | Proposed malachite green degradation mechanism using Ce doped SnO_2 nanoparticles.
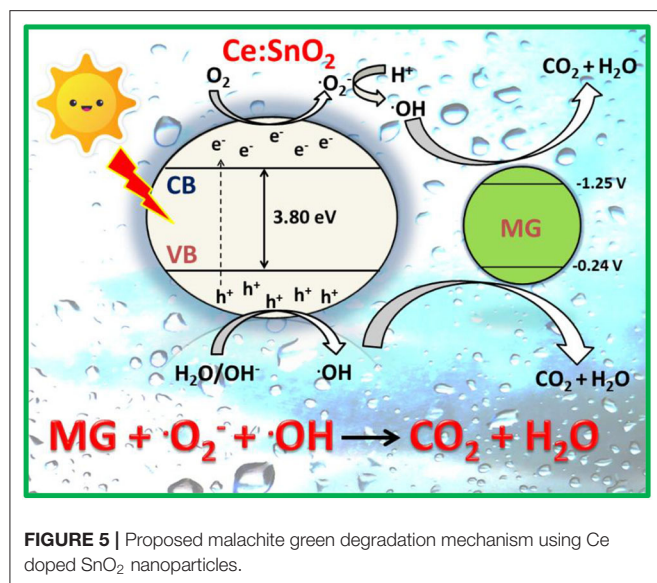
of degradation as these molecules scavenge the electrons in the conduction band, preventing electron-hole recombination. Moreover, holes in the valence band react with water molecules or hydroxide ions to produce hydroxyl radicals (OH·) (Kumar et al., 2016; Ma et al., 2018). The generated oxidizing agents (superoxide radical anions and hydroxyl radicals) contributed to the oxidative degradation of malachite green, which was then converted into simple and less harmful products. The high stability of Ce doped SnO_2 NPs mentioned in the previous report

and hence, these nanoparticles can be reused without undergoing any change in structure (Kumar et al., 2019b).

CONCLUSION

Facile and economical synthesis of Ce doped SnO_2 NPs showed potent antimicrobial properties so far. Also, nanomaterials were able to degrade toxic organic pollutants like malachite green. These nanomaterials could be used against bacterial infection as well as for multidrug-resistant bacteria along with wastewater treatment purposes.

DATA AVAILABILITY STATEMENT

The raw data supporting the conclusions of this article will be made available by the authors, without undue reservation.

AUTHOR CONTRIBUTIONS

All authors listed have made a substantial, direct and intellectual contribution to the work, and approved it for publication.

ACKNOWLEDGMENTS

REFERENCES

Ahmed, A., Siddique, M. N., Ali, T., and Tripathi, P. (2019). Defect assisted improved room temperature ferromagnetism in Ce doped SnO_2 nanoparticles. *Appl. Surf. Sci.* 483: p. 463–471. doi: 10.1016/j.apsusc.2019. 03.209

Ali, T., Ahmed, A., Alam, U., Uddin, I., Tripathi, P., and Muneer, M. (2018). Enhanced photocatalytic and antibacterial activities of Ag-doped TiO2 nanoparticles under visible light. *Mater. Chem. Phys.* 212, 325–335. doi: 10.1016/j.matchemphys.2018.03.052

Ananpattarachai, J., Kajitvichyanukul, P., and Seraphin, S. (2009). Visible light absorption ability and photocatalytic oxidation activity of various interstitial N-doped TiO2 prepared from different nitrogen dopants. *J. Hazard. Mater.* 168, 253–261. doi: 10.1016/j.jhazmat.2009.02.036

Ayeshamariam, A., Meera, T., Jayachandran, M., Kumar, P., and Bououdina, M. (2013). Green synthesis of nanostructured materials for antibacterial and antifungal activities. *Int. J. Bioassays* 2, 304–311.

Azam, A., Ahmed, A. S., Oves, M., Khan, M. S., Habib, S. S., and Memic, A. (2012). Antimicrobial activity of metal oxide nanoparticles against Gram-positive and Gram-negative bacteria: a comparative study. *Int. J. Nanomed.* 7:6003. doi: 10.2147/IJN.S35347

Baig, A. B. A., Rathinam, V., and Ramya, V. (2020). Synthesis and investigation of Fe doped SnO2 nanoparticles for improved photocatalytic activity under visible light and antibacterial performances. *Mater. Technol.* 2020, 1–13. doi: 10.1080/10667857.2020.1786781

Bauer, A., Kirby, W. M., Sherris, J. C., and Turck, M. (1966). Antibiotic susceptibility testing by a standardized single disk method. *Am. J. Clin. Pathol.* 45, 493–496. doi: 10.1093/ajcp/45.4_ts.493

Bharathi, P. M. R. M., Amutha, T., Rameshbabu, M., and Prabha, K. (2017). Synthesis and Investigation of Ce doped Tinoxide (SnO_2) nanoparticles. *Int. Res. J. Eng. Technol.* 4:334–337.

Bhawna, Gupta, A., Kumar, P., Tyagi, A., Kumar, R., Kumar, A., Singh, P., et al. (2020). Facile synthesis of N-Doped SnO_2 nanoparticles: a cocatalyst-free promising photocatalyst for hydrogen generation. *ChemistrySelect* 5, 7775–7782. doi: 10.1002/slct.202001301

Chandran, D., Nair, L. S., Balachandran, S., Babu, K. R., and Deepa, M. (2015). Structural, optical, photocatalytic, and antimicrobial activities of cobalt-doped tin oxide nanoparticles. *J. Sol Gel Sci. Technol.* 76, 582–591. doi: 10.1007/s10971-015-3808-z

Chen, C., Lu, C. S., Chung, Y. C., and Jan, J. L. (2007). UV light induced photodegradation of malachite green on TiO2 nanoparticles. *J. Hazard. Mater.* 141, 520–528. doi: 10.1016/j.jhazmat.2006. 07.011

Dil, N. N., and Sadeghi, M. (2018). Free radical synthesis of nanosilver/gelatin-poly (acrylic acid) nanocomposite hydrogels employed for antibacterial activity and removal of Cu (II) metal ions. *J. Hazard. Mater.* 351, 38–53. doi: 10.1016/j.jhazmat.2018.02.017

Gupta, A., Kumar, S., Kumar, R., Choudhary, A. K., Kumari, K., Singh, P., et al. (2020a). COVID-19: emergence of infectious diseases, nanotechnology aspects, challenges, and future perspectives. *ChemistrySelect* 5:7521. doi: 10.1002/slct.202001709

Gupta, A., Kumar, V., Ahmed, S., and Gautam, S. (2020b). "Impact of nanotechnology in the development of smart cities," in *Smart Cities-Opportunities and Challenges, Smart Cities-Opportunities and Challenges. Lecture Notes in Civil Engineering*, eds S. Ahmed, S. Abbas, and H. Zia (Singapore: Springer), 845–857. doi: 10.1007/978-981-15-2545-2_68

Gusain, R., Gupta, K., Joshi, P., and Khatri, O. P. (2019). Adsorptive removal and photocatalytic degradation of organic pollutants using metal oxides and their composites: a comprehensive review. *Adv. Colloid Interface Sci.* 272:102009. doi: 10.1016/j.cis.2019.102009

Helaïli, N., Boudjamaa, A., Kebir, M., and Bachari, K. (2017). Efficient photo–catalytic degradation of malachite green using nickel tungstate material as photo–catalyst. *Environ. Sci. Pollut. Res.* 24, 6481–6491. doi: 10.1007/s11356-016-8296-3

Jan, T., Iqbql, J., Mansoor, Q., Ismail, M., Naqvi, M. S. H., Gul, A., et al. (2014). Synthesis, physical properties and antibacterial activity of Ce doped CuO: a novel nanomaterial. *J. Phys. D Appl. Phys.* 47:355301. doi: 10.1088/0022-3727/47/35/355301

Jarzebski, Z., and Marton, J. (1976a). Physical properties of SnO_2 materials: I. preparation and defect structure. *J. Electrochem. Soc.* 123:199C. doi: 10.1149/1.2133010

Jarzebski, Z., and Marton, J. (1976b). Physical properties of SnO2 materials: II. Electrical properties. *J. Electrochem. Soc.* 123:299C. doi: 10.1149/1.2133090

Jarzebski, Z., and Morton, J. (1976). Physical properties of SnO2 materials: III. Optical properties. *J. Electrochem. Soc.*, 123, 333C. doi: 10.1149/1.2132647

Jiang, B., He, Y., Li, B., Zhao, S., Wang, S., He, Y. B., et al. (2017). Polymer-templated formation of polydopamine-coated SnO_2 nanocrystals: anodes for cyclable lithium-ion batteries. *Angew. Chem. Int. Ed.* 56, 1869–1872. doi: 10.1002/anie.201611160

Jiang, Q., Zhang, X., and You, J. (2018). SnO2: a wonderful electron transport layer for perovskite solar cells. *Small* 14:1801154. doi: 10.1002/smll.201801154

Kamaraj, P., Vennila, R., Arthanareeswari, M., and Devikala, S. (2014). Biological activities of tin oxide nanoparticles synthesized using plant extract. *World J. Pharm Pharm Sci.* 3, 382–388.

Khan, S. A., Kanwal, S., Rizwan, K., and Shahid, S. (2018). Enhanced antimicrobial, antioxidant, *in vivo* antitumor and *in vitro* anticancer effects against breast cancer cell line by green synthesized un-doped SnO_2 and Co-doped SnO_2 nanoparticles from clerodendrum inerme. *Microb. Pathog.* 125: p. 366–384. doi: 10.1016/j.micpath.2018.09.041

Kotchasak, N., Wisitsoraat, A., Tuantranont, A., Phanichphant, S., Yordsri, V., and Liewhiran, C. (2018). Highly sensitive and selective detection of ethanol vapor using flame-spray-made CeOx-doped SnO_2 nanoparticulate thick films. *Sens. Actuators B Chem.* 255, 8–21. doi: 10.1016/j.snb.2017.08.027

Kumar, A., Rout, L., Achary, L. S. K., Mohanty, A., Marpally, J., Chand, P. K., et al. (2016). "Design of binary SnO2-CuO nanocomposite for efficient photocatalytic degradation of malachite green dye," in *AIP Conference Proceeding AIP Publishing LLC* (Rajasthan). doi: 10.1063/1.4945147

Kumar, M., Bhatt, V., Abhyankar, A. C., Kim, J., Kumar, A., Patil, S. H., et al. (2018). New insights towards strikingly improved room temperature ethanol sensing properties of p-type Ce-doped SnO_2 sensors. *Sci. Rep.* 8, 1–12. doi: 10.1038/s41598-018-26504-3

Kumar, V., Bhawna, Y.adav, S. K., Gupta, A., Dwivedi, B., Kumar, A., Singh, P., et al. (2019a). Facile synthesis of Ce–doped SnO_2 nanoparticles: a promising Photocatalyst for hydrogen evolution and dyes degradation. *ChemistrySelect* 4, 3722–3729. doi: 10.1002/slct.201900032

Kumar, V., Choudhary, A. K., Kumar, P., and Sharma, S. (2019b). Nanotechnology: nanomedicine, nanotoxicity and future challenges. *Nanosci. Nanotechnol. Asia* 9, 64–78. doi: 10.2174/2210681208666180125143953

Kumar, V., Govind, A., and Nagarajan, R., Optical and photocatalytic properties of heavily F—doped SnO2 nanocrystals by a novel single-source precursor approach. *Inorg. Chem.* (2011). 50, 5637–5645. doi: 10.1021/ic2003436

Kumari, M. M., and Philip, D. (2015). Synthesis of biogenic SnO_2 nanoparticles and evaluation of thermal, rheological, antibacterial and antioxidant activities. *Powder Technol.* 270, 312–319. doi: 10.1016/j.powtec.2014.10.034

Lian, X., Li, Y., Tong, X., Zou, Y., Liu, X., An, D., et al. (2017). Synthesis of Ce-doped SnO2 nanoparticles and their acetone gas sensing properties. *Appl. Surf. Sci.* 407:447–455. doi: 10.1016/j.apsusc.2017.02.228

Ma, Y., Ni, M., and Li, S. (2018). Optimization of malachite green removal from water by TiO2 nanoparticles under UV irradiation. *Nanomaterials* 8:428. doi: 10.3390/nano8060428

Mekala, R., Rajendran, V., and Deepa, B. (2018). Effect of cerium doped Baddeleyite on their antibacterial activity by co-precipitation method. *Mater. Sci. Eng.*, 360:012014. doi: 10.1088/1757-899X/360/1/012014

Nasir, Z., Shakir, M., Wahab, R., Shoeb, M., Alam, P., Khan R. H., et al. (2017). Co-precipitation synthesis and characterization of Co doped SnO_2 NPs, HSA interaction via various spectroscopic techniques and their antimicrobial and photocatalytic activities. *Int. J. Biol. Macromol.* 94, 554–565. doi: 10.1016/j.ijbiomac.2016.10.057

Panahian, Y., and Arsalani, N. (2017). Synthesis of hedgehoglike F-TiO2 (B)/CNT nanocomposites for sonophotocatalytic and photocatalytic degradation of malachite green (MG) under visible light: kinetic study. *J. Phys. Chem. A* 121, 5614–5624. doi: 10.1021/acs.jpca.7b02580

Park, G. D., Lee, J. K., and Kang, Y. C. (2017). Synthesis of uniquely structured SnO_2 hollow nanoplates and their electrochemical properties for Li-ion storage. *Adv. Funct. Mater.* 27:1603399. doi: 10.1002/adfm.201603399

Phukan, A., Bhattacharjee, R. P., and Dutta, D. K. (2017). Stabilization of SnO_2 nanoparticles into the nanopores of modified montmorillonite and their antibacterial activity. *Adv. Powder Technol.* 28, 139–145. doi: 10.1016/j.apt.2016.09.005

Qamar, M., Shahid, S., Khan, S. A., Zaman, S., and Sarwar, M. N. (2017). Synthesis characterization, optical and antibacterial studies of Co-doped SnO2 nanoparticles. *Dig. J. Nanomater. Biostruct.* 12, 1127–1135. doi: 10.13140/RG.2.2.29282.22720

Raghunath, A., and Perumal, E. (2017). Metal oxide nanoparticles as antimicrobial agents: a promise for the future. *Int. J. Antimicrob. Agents* 49, 137–152. doi: 10.1016/j.ijantimicag.2016.11.011

Rooshde, M. S., Abdullah, W. R. W., Amran, A. Z., Ibrahim, N. F., Ariffin, F., Sabri, M., et al. (2020). Antimicrobial Activity of Photoactive Cerium Doped Zinc Oxide. in Solid State Phenomena. *Trans. Tech. Publ.* 307, 217–222. doi: 10.4028/www.scientific.net/SSP.307.217

Samadi, M., Zirak, M., Naseri, A., Kheirabadi, M., Ebrahimi, M., and Moshfegh, A. Z. (2019). Design and tailoring of one-dimensional ZnO nanomaterials for photocatalytic degradation of organic dyes: a review. *Res. Chem. Intermed.* 45, 2197–2254. doi: 10.1007/s11164-018-03729-5

Sathishkumar, M., and Geethalakshmi, S. (2020). Enhanced photocatalytic and antibacterial activity of Cu: SnO2 nanoparticles synthesized by microwave assisted method. *Mater. Today* 20, 54–63. doi: 10.1016/j.matpr.2019.08.246

Sayilkan, F., Asiltürk, M., Tatar, P., Kiraz, N., Arpa,ç, E., and Sayilkan, H. (2007). Photocatalytic performance of Sn-doped TiO2 nanostructured mono and double layer thin films for malachite green dye degradation under UV and vis-lights. *J. Hazard. Mater.* 144, 140–146. doi: 10.1016/j.jhazmat.2006.10.011

Scherrer, P. (1912). "Bestimmung der inneren struktur und der Größe von kolloidteilchen mittels röntgenstrahlen," in *kolloidchemie Ein Lehrbuch.* (Berlin; Heidelberg: Springer), 387–409. doi: 10.1007/978-3-662-33915-2_7

Shide, W., Chao, L., Wei, W., Huanxin, W., and Youqi, Z. (2010). Synthesis and photocatalytic property of Ce-doped SnO_2. *J. Rare Earths* 28:168–170. doi: 10.1016/S1002-0721(10)60312-2

Sirelkhatim, A., Mahmud, S., Seeni, A., Kaus, N. H. M., Ann, L. C., Bakhori, S. K. M., et al. (2015). Review on zinc oxide nanoparticles: antibacterial activity and toxicity mechanism. *Nanomicro Lett.*, 7, 219–242. doi: 10.1007/s40820-015-0040-x

Swaminathan, B., and Smidt, P. G. (2007). The epidemiology of human listeriosis. *Microb Infect.* 9, 1236–1243. doi: 10.1016/j.micinf.2007.05.011

Vargas-Reus, M. A., Memarzadeh, K., Huang, J., Ren, G. G., and Allaker, R. P. (2012). Antimicrobial activity of nanoparticulate metal oxides against peri-implantitis pathogens. *Int. J. Antimicrob. Agents* 40, 135–139. doi: 10.1016/j.ijantimicag.2012.04.012

Vidhu, V., and Philip, D. (2015). Phytosynthesis and applications of bioactive SnO_2 nanoparticles. *Mater. Charact.* 101, 97–105. doi: 10.1016/j.matchar.2014.12.027

Wang, Z., Han, T., Fei, T., Liu, S., and Zhang, T. (2018). Investigation of microstructure effect on NO_2 sensors based on SnO_2 nanoparticles/reduced graphene oxide hybrids. *ACS Appl. Mater. Interf.* 10, 41773–41783. doi: 10.1021/acsami.8b15284

Xie, J., Huang, Y., Yu, X., Yang, Z., Xiao, K., Qiang, Y., et al. (2017). Enhanced electronic properties of SnO_2 via electron transfer from graphene quantum dots for efficient perovskite solar cells. *Acs Nano* 11, 9176–9182. doi: 10.1021/acsnano.7b04070

Yemmireddy, V. K., and Hung, Y. C. (2017). Using photocatalyst metal oxides as antimicrobial surface coatings to ensure food safety—Opportunities and challenges. *Compr. Rev. Food Sci. Food Saf.* 16, 617–631. doi: 10.1111/1541-4337.12267

Conflict of Interest: The authors declare that the research was conducted in the absence of any commercial or financial relationships that could be construed as a potential conflict of interest.

Investigating the Nanocomposite Thin Films of Hematite α-Fe₂O₃ and Nafion for Cholesterol Biosensing Applications

Indra Sulania[1], R. Blessy Pricilla[2] and G. B. V. S. Lakshmi[1,3]*

[1] Materials Science Group, Inter University Accelerator Centre, New Delhi, India, [2] Karunya University, Coimbatore, India,
[3] Special Center for Nanoscience, Jawaharlal Nehru University, New Delhi, India

Nanocomposite materials are multi-phase materials, usually solids, which have two or more component materials having different chemical and physical properties. When blended together, a newer material is formed with distinctive properties which make them an eligible candidate for many important applications. In the present study, thin films of nafion (polymer) and hematite or α-Fe₂O₃ (nanoparticles) nanocomposite is fabricated on indium tin oxide (ITO) coated glass substrates, due to its enhanced ionic conductivity, for cholesterol biosensor applications. Scanning electron microscopy and Atomic force microscopy revealed the formation of nanorod structured α-Fe₂O₃ in the films. The cyclic voltammetry (CV) studies of nafion-α-Fe₂O₃/ITO revealed the redox properties of the nanocomposites. The sensing studies were performed on nafion-α-Fe₂O₃/CHOx/ITO bioelectrode using differential pulse voltammetry (DPV) at various concentrations of cholesterol. The enzyme immobilization leaded to the selective detection of cholesterol with a sensitivity of 64.93×10^{-2} μA (mg/dl)$^{-1}$ cm^{-2}. The enzyme substrate interaction (Michaelis–Menten) constant K_m, was obtained to be 19 mg/dl.

Keywords: cholesterol, iron oxide nanoparticles, electrochemical detection, DPV, biosensor

INTRODUCTION

Nanocomposite (NC) materials are multiphase solid materials which have one of the blended materials in nano dimensions (Ajayan et al., 2006). The structure of nanocomposites mostly consists of the matrix material which may contain the nano-sized reinforcement components in the form of particles, fibers, nanotubes, etc. Nanocomposites are also found in nature in abalone shell and bone in living beings (Din, 2019). NC are different from the standard composite due to the atypically higher surface to volume percentage of the reinforcing agent and/or higher aspect ratio. Generally, composites are materials made from two or more different materials each having dissimilar physical and chemical properties. The composite materials often exhibit unique characteristics compared to their individual components. Such materials are stronger, lighter, less expensive to prepare (Ajayan et al., 2006; Din, 2019).

Metal oxide nanoparticles have several applications in various fields as electronic, optical, biosensing, catalytic, cosmetic, telecommunication, pharmaceutical areas etc. (Demir et al., 2015). Fe₂O₃ NPs were used as a chemisorptive to remove the metals from aqueous solutions (Grover et al., 2012). Heavy metal ions such as Cd^{2+}, Zn^{2+}, Pb^{2+}, and Cu^{2+} have been successfully

removed from the aqueous solution by the use composite of polymer and magnetic NPs as reported by Ge et al. (2012). Sorption kinetic study was done in the different phases of selenite and selenate by the application of pressurized aged iron oxide nanomaterials (Gonzalez et al., 2012). The catalytic activity of Fe_2O_3 NPs in wastewater treatment is extensively used in lab tests too (Perez, 2007). The tendency of Fe_3O_4 NPs in oxidation and agglomeration, restricts its usage, therefore, many researchers have encased them in a shell of different material to avoid them from oxidation and agglomeration (Sharma et al., 2013). Specifically, the encasing of oxide nanoparticles with electroactive polymers is useful for application in biosensors as they improve the biocompatibility with the improvement in the ligand exchange between the metal-oxide nanoparticles and biomolecules which is the crucial property for biosensor application (Jun et al., 2008). Nafion is the well-known electroactive polymer, that was used in electrochemical platforms. It was found that, in aqueous solutions, Nafion is used as a proton conductor and it does not mitigate the electrochemical response of the inserted electroactive species therefore used as a binder in the electrocatalytic devices and the phase separation takes place in the ionomer allows the formation of a continuous network of ion conducting channels (Chen et al., 2018). The Nafion/MNPs nanocomposite shows high ionic conductivity (Raymond et al., 1996).

Iron oxide nanoparticles composited with Nafion were used as very good sensors toward glucose and cholesterol (Woo et al., 2003; Umar et al., 2014). It was reported that, the presence of sulphonated groups led to an increase in the absorbed moisture in nafion and α-Fe_2O_3 composite. The α-Fe_2O_3 nanostructures shows very high density and they have a very good crystallinity due to its rhombohedral structures. The sensors produced can have very good reproducibility with a good detection limit of $0.018 \mu m$ (Hasanabadi et al., 2013). Further, an immobilized enzyme on α-Fe_2O_3 may ensure prolonged activity and hence enhanced stability of the biosensors. It has been reported that the activated GOx displayed good catalytic activity toward glucose, and Fe_3O_4 nanoparticles provide suitable domain to immobilize GOx and helps in electron transfer among the analyte (glucose) and electrode surface (CH–Fe_3O_4/ITO) in the biosensing applications (Kaushik et al., 2008a).

Biosensors have vast applications in various fields such as food and environmental industry, fermentation industry, medical sciences, and plant biology sector along with marine and defense fields (Mehrotra, 2016). Extensive research is going on all around the world to improve the performance, in terms of sensitivity and selectivity, user friendly and to reduce the cost of the biosensors so that it can be available at lower prices to the people. Few of the biosensors work based on iron oxide nanoparticles has been highlighted here. Kaushik et al. (2009) have studied the nano-bio-composite of CH and Fe_3O_4 in super-paramagnetic form to detect the urea via immobilization of Urs and GLDH. The biosensor exhibits linearity in the range ~5–100 mg/dL with a weak detection ~2 mg/dL. The sensor had a response time of 10 s with sensitivity of $12.5 \mu A/mM \, cm^{-2}$. In another work,

surface charged Fe_3O_4 NPs comes together and agglomerate in the CH matrix to form bio-composite to detect antigens Ochratoxin A, via immobilizing the IgGs and bovine serum albumin in rabbit. It showed good sensitivity in the order of $\sim 3.6 \times 10^{-5}$ A dL^{-1}, and has a reproducibility and long-term stability in comparison to CH/ITO based immunosensors (Kaushik et al., 2008b). They have also studied the composite for glucose sensing. The nanocrystals of Fe_3O_4 with an average size of 10 nm were synthesized on silica by Sharma et al. (2013). Due to non-conducting nature of $Fe_3O_4@SiO_2$ NPs, they showed bad response toward electrochemical activities. Further, synthesis of $Fe_3O_4@C$, in non-crystalline film, resulted in a good cholesterol biosensor. The Nps showed sensitivity in the order of ~193 and 218 nA $mg^{-1}dl \, cm^{-2}$, as observed from cyclic voltammetry studies. It was concluded that the encasing Fe_2O_3 NPs with conducting polymers like polypyrrole and polyaniline etc., may enhance the sensitivity of biosensor.

The literature survey revealed that, cholesterol sensing can be done using various metal oxide-chitosan composites and some work was performed in the field of nanocomposite bio-sensors using iron oxide nanoparticles synthesized by various other methods for the detection of few analytes. Whereas, iron oxide nanoparticles for biosensing of cholesterol was not reported. This has motivated us to carry-out this study and synthesize a nanocomposite material to sense cholesterol in a user-friendly way. In the present study, we have synthesized nafion-iron oxide nanocomposites and tested for cholesterol sensing applications with and without cholesterol oxidase enzyme (CHOx) enzyme. The composites show good sensitivity with and without the help of CHOx enzyme, whereas the selectivity was obtained only after the immobilization of enzyme. The enzyme CHOx was immobilized on the electrodes without the help of any cross-linking agent. The electrodes showed a very good sensitivity of $64.93 \times 10^{-2} \mu A \, (mg/dl)^{-1} \, cm^{-2}$ for with enzyme and $0.012 mA \, (mg/dl)^{-1} \, cm^{-2}$ for without enzyme in the detection range of 0–390 mg/dl. The enzyme—substrate kinetic parameter was obtained to be 19 mg/dl which is very less indicating the indicates increased affinity of nafion-α-Fe_2O_3/CHOx/ITO bioelectrode that is attributed to favorable conformation of ChOx and higher loading onto the electrode. The composite prepared by very simple method in the present work which showed higher sensitivity and better selectivity.

EXPERIMENTAL

Reagents

Nafion (Sigma), α-Fe_2O_3 (Merck), Cholesterol (Sigma), Phosphate buffer solution (prepared using monosodium and disodium phosphate salts, in the lab), ferri and ferrocyanide (Sigma-Aldrich), Indium Tin Oxide (ITO) coated glass substrates, Cholesterol oxidase (Sigma), Alcohol, acetone and de-ionized water.

Instruments

A composite film of Nafion/aα-Fe_2O_3 films deposited on ITO glass substrates were characterized by D8 X-ray diffractometer

(with x-ray source of CuKα at 1.54 Å wavelength) from Bruker. The functional group study was carried out using Fourier transform infrared spectroscopy (FTIR) on Bruker model Tensor 37 FTIR spectrometer. The morphology of the composite films was observed using 25 keV electron beam in field emission scanning electron microscope (FESEM) from MIRA II LMH (TESCAN). The films were further characterized with Nanoscope IIIa Atomic Force Microscope (AFM) for the topological studies (Sulania et al., 2018). The contact angle measurements with water drop were performed using DSA3 contact angle measurement set-up from KRUSS. In bulk materials and polymers, the dynamics of the water droplet mostly hinge on the liquid-surface interaction. The curvature of the droplet varies when the water droplet falls on the surface of the thin film showing the interaction between them (Bico et al., 2002). A 3-electrode electro-chemical cell assembly was used for the Electrochemical studies with Pt wire as the counter electrode (CE), nafion-α-Fe$_2$O$_3$/ITO as the working electrode (WE) and Ag/AgCl as the reference electrode (RE) dipped into the solution of PBS (0.1M PBS, pH 7.4) comprising 5 mM [Fe(CN)$_6$]$^{3-/4-}$ and the redox probe allied to CHI-600D electrochemical analyzer. Further, the Cyclic Voltammetry studies were performed to observe the redox behavior of the nafion-α-Fe$_2$O$_3$/ITO electrodes. The sensing measurements were performed on nafion-α-Fe$_2$O$_3$/ITO and nafion-α-Fe$_2$O$_3$-CHOx/ITO electrodes with change in concentration of the cholesterol using electrochemical differential pulse voltammetry method.

Electrode Preparation

In the present work, thin films of nanocomposite of α-Fe$_2$O$_3$ nanoparticles with nafion polymer have been fabricated after forming a uniform solution (as shown in **Figure 1**) by solution mixing method and then drop casting the films of this composite onto the ITO substrates. Nafion is a synthetic polymer. It is a tetrafluoroethylene-based fluoropolymer—copolymer. It has excellent thermal and mechanical stability. Its unique ionic properties arise due to the presence of sulfonate groups. The chemical formula of nafion is C$_7$HF$_{13}$O$_5$S.C$_2$F$_4$. Nafion functions as an ion exchange resin and acid catalyst because of the strong acidic properties of the sulfonic acid group.

Iron oxide (Fe$_2$O$_3$) or Ferric oxide is the main source of iron in the steel industry. It is ferromagnetic in nature, commonly known as rust and in chemical terms it is known as hydrated ferric oxide. It exists in three phases; Alpha phase, Gamma phase and Beta phase. The most stable one is the alpha phase (Sulania et al., 2016). The nanoparticles of α-Fe$_2$O$_3$ exhibit super para magnetism and show low toxicity. They are biocompatible and may be used as a distinction agent in magnetic resonance imaging and as guided carriers in drug discovery. They exhibit long term chemical stability in neutral solution. They are also used as catalyst and photocatalyst. α-Fe$_2$O$_3$ nanostructures have good stability under physiological conditions. Therefore, we intended to form the composite of the nafion and iron oxide as iron oxide nanoparticles to improve the ionic exchange interaction

FIGURE 1 | Nano-composite solution of nafion-α-Fe$_2$O$_3$.

when composited with the polymeric chains of nafion during the sensing of cholesterol.

RESULTS AND DISCUSSIONS

Morphology Studies (SEM and AFM)

The surface morphology of α-Fe$_2$O$_3$-nafion nanocomposite films formed on ITO was observed using FESEM and AFM. SEM analysis confirms the rod type structure of the α-Fe$_2$O$_3$ nanoparticles and the images are shown in **Figures 2a,b**. A thin layer covering the rod type structures is observed at higher magnification image in **Figure 2b** showing nafion was surrounding the nanoparticles in the composite. The diameter of the rods is <50 nm including the nafion coating. The EDX analysis carried out on α-Fe$_2$O$_3$-nafion nanocomposite films during FESEM study showed the presence of the elements Fe, O, S, F, and C as shown in the **Figure 2c**, which is clearly indicating the formation of the nanocomposite.

Figure 3 shows the 2D, 3D AFM images of α-Fe$_2$O$_3$-nafion nanocomposite film and the sectional analysis of the single rod. These AFM images clearly indicate the rod like structures that were observed in SEM images also. The breadth of a rod has been calculated using section analysis. The horizontal diameter of the rods is found to be 33 nm which is in agreement with the diameter of the rods <50 nm that was observed in SEM images.

XRD and FTIR Studies

The composite films deposited on glass substrates were used for XRD measurements. XRD spectrum was carried out in the
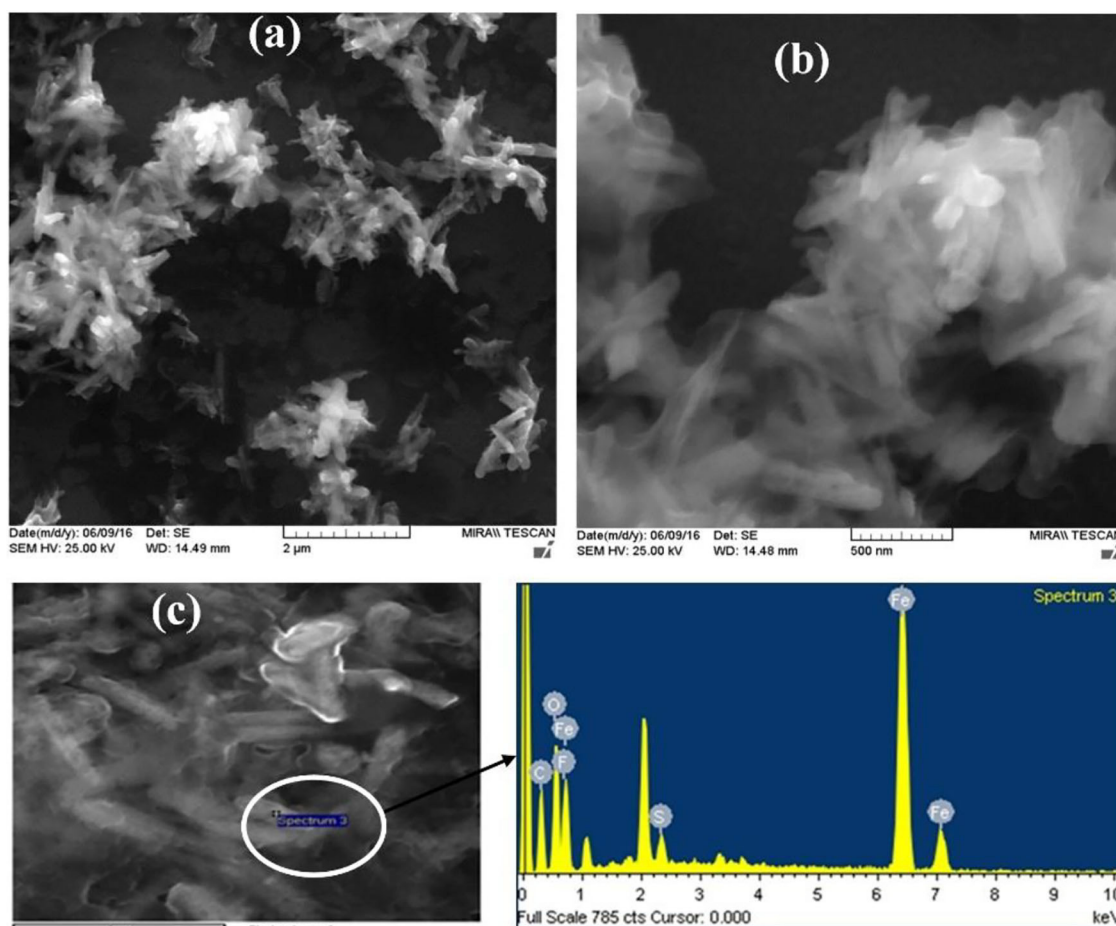
FIGURE 2 | (a,b) SEM images and **(c)** EDX spectrum of α-Fe$_2$O$_3$-nafion nanocomposite films.

range of 2θ from 10° to 50° using Cu-Kα source with wavelength 1.54Å with scan rate 1° *per sec* and the spectrum was shown in **Figure 4A**. The peaks visible at 2θ ≈ 21.8°(111), 27.5°(012), 30.1°(220), 35°(104), 43°(113), confirms the formation of α-Fe$_2$O$_3$ phase in the composite film (Banerjee et al., 2011; Mallick and Dash, 2013).

From the Scherrer's formula the crystallite size can be estimated as:

$$\beta \text{Cos} (\theta) = \frac{K\lambda}{D}$$

where $K = 0.98$, D is the crystallite size, b is the FWHM of the highest intense peak and l is the incident x-ray wavelength. The crystallite size was obtained as 33.8 nm for the highest intense peak corresponding to (220).

Figure 4B shows the FTIR spectra of nafion-α-Fe$_2$O$_3$/ITO (a) and nafion-α-Fe$_2$O$_3$/CHOx/ ITO (b) electrodes. The peaks at 440 and 520 cm^{-1} were attributed to Fe-O bond vibrations. The peaks at 985, 1,065, 1,155, 1,227, 1,285 cm^{-1} correspond to S-O, C-O-C, C-F, and SO$_3$H in sulfonic acids, C-F stretch bands

respectively of nafion. The peak at 1,650 cm^{-1} corresponding to C=O was observed in the enzyme electrode spectrum (b). The major changes observed in the peaks at 1,065 cm^{-1} after the enzyme incorporation and appearance of peak at 1,650 cm^{-1} confirming the successful immobilization (Chen et al., 2013; Singh et al., 2016). The functional groups on nafion helped in the immobilization of CHOx on the electrode.

Water Wettability Studies

It is well-known that nafion is a super hydrophobic polymer and therefore not useful for sensing. Whereas, when nafion is used in composite form, the properties such as hydrophobicity, photon conductivity, water swelling properties etc. of the composite films found much more different than their individual components (Paul and Karan, 2014; Paul et al., 2016; Kurihara et al., 2017; Singh et al., 2019). The composite films were formed on the ITO coated glass plates and CHOx enzyme was immobilized on one electrode. The contact angle of the composite films before (a) and
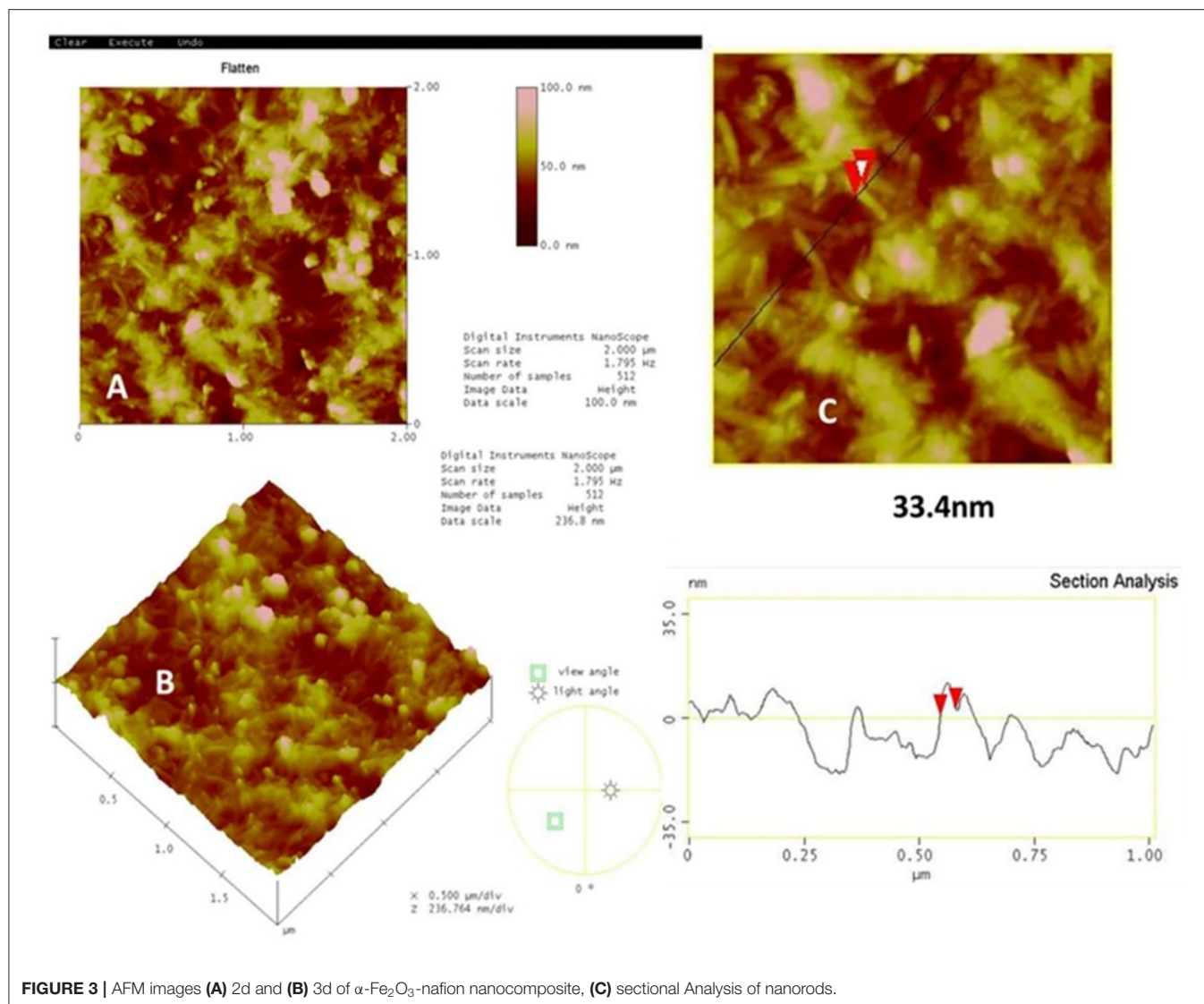
FIGURE 3 | AFM images **(A)** 2d and **(B)** 3d of α-Fe$_2$O$_3$-nafion nanocomposite, **(C)** sectional Analysis of nanorods.

after enzyme immobilization (b) of CHOx on the nanocomposite films are shown in **Figure 5**.

It was found that the contact angle was 98.64° ± 2.7° of the α-Fe$_2$O$_3$-nafion-nanocomposite films showing slightly hydrophobic nature due to the presence of nafion. Upon the immobilization of the enzyme CHOx, the contact angle was drastically reduced to 8.05° ± 1.46°. So, the films have become completely hydrophilic in nature, which is the foremost requirement for the biosensing applications. The contact angle changed due to the incorporation of nanoparticles that were present in the nanocomposite that modified the surface as of only nafion. Further, enzyme immobilization leaded to increase in water surface interaction which contributed to the decrease in CA (Singh et al., 2019).

Electrochemical Studies

The electrochemical properties of nafion-α-Fe$_2$O$_3$/ITO and nafion-α-Fe$_2$O$_3$/CHOx/ITO electrodes were studied by CV technique in a three-electrode cell of 7.4 pH PBS buffer solution comprising 5 mM [Fe(CN)$_6$]$^{3-/4-}$ used as the redox species. The CV curves of nafion-α-Fe$_2$O$_3$/ITO and nafion-α-Fe$_2$O$_3$/CHOx/ITO obtained at various scan rates shown in **Figures 6A,B**, respectively.

Figure 6 shows the good oxidation and reduction peaks for both the nanocomposite films. The increase in current with the increase in the scan rate shows the favorable redox nature of the electrodes for electrochemical sensing applications. The anodic and cathodic peaks currents and the area of the CV curve were found to increase with scan rate. This increase implies the homogeneous electron transfer of the electrodes. The plot between scan rate$^{1/2}$ and oxidation and reduction peak currents and voltages were showed in the inset and the linearity was observed. The linearity of these curves indicates the facile charge transfer kinetics and the charge transfer process was diffusion controlled (Xiong et al., 2012) and these electrodes provide
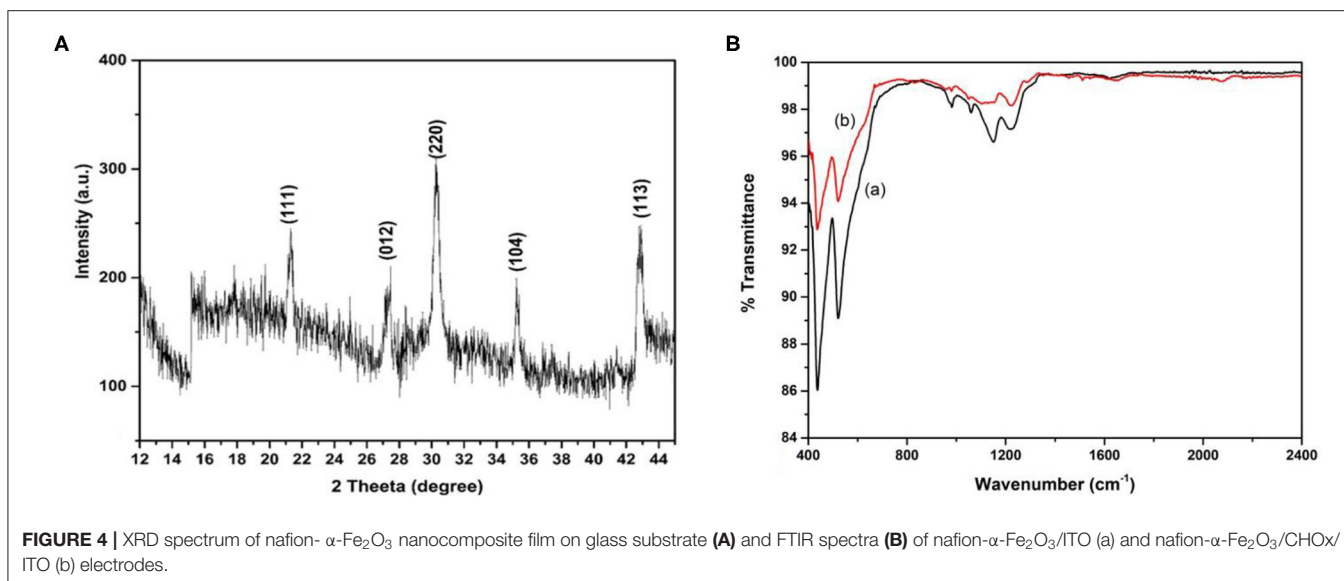
FIGURE 4 | XRD spectrum of nafion- α-Fe$_2$O$_3$ nanocomposite film on glass substrate **(A)** and FTIR spectra **(B)** of nafion-α-Fe$_2$O$_3$/ITO (a) and nafion-α-Fe$_2$O$_3$/CHOx/ITO (b) electrodes.
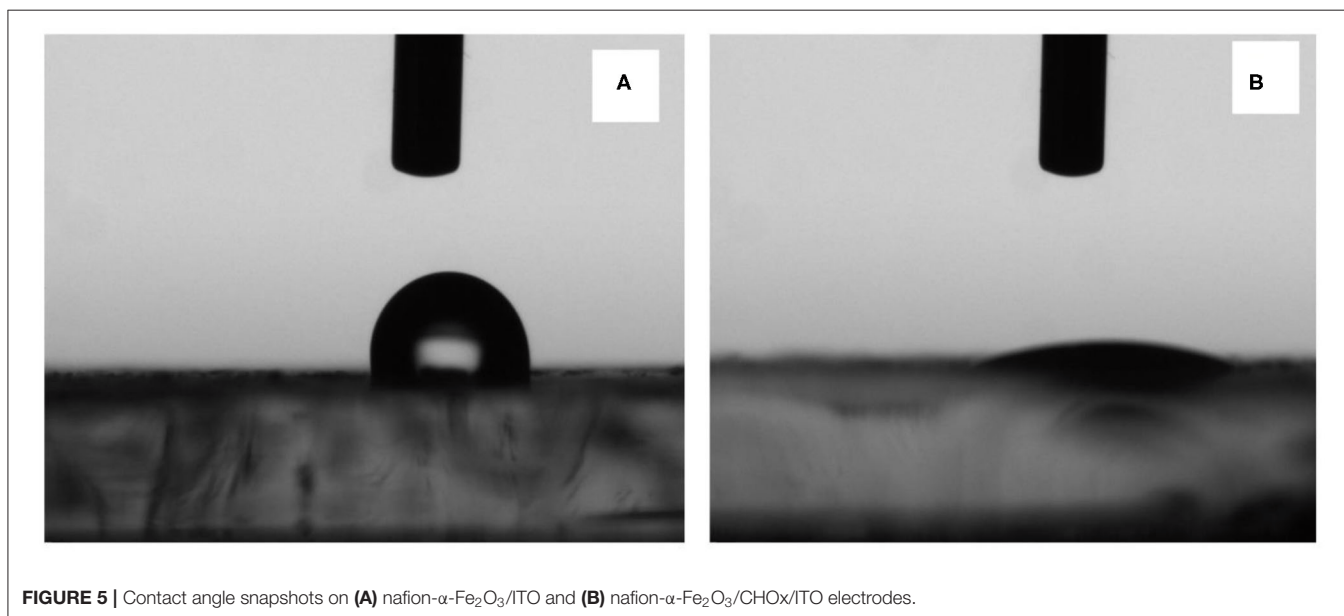
FIGURE 5 | Contact angle snapshots on **(A)** nafion-α-Fe$_2$O$_3$/ITO and **(B)** nafion-α-Fe$_2$O$_3$/CHOx/ITO electrodes.

adequate conductivity for charge flow among electrode and electrolyte.

The different electrochemical parameters as Ea, Ia, Ec, Ic, and the diffusion co-efficient (D) of the Nafion-α-Fe$_2$O$_3$/ITO and Nafion-α-Fe$_2$O$_3$/CHOx/ITO electrodes found at the scan rate, 50 mV/s. The D value was assessed from the equation,

$$D = \frac{I_a^2}{\left(2.69 X 10^5\right)^2 A^2 n^3 C^2 v} \qquad (1)$$

where C; the concentration of mediator buffer, A; the area of the working electrode, n; the number of electrons participated in redox process and v; the scan rate.

The surface concentration (γ^*) of the ionic species of the Nafion-α-Fe$_2$O$_3$/ITO and Nafion-α-Fe$_2$O$_3$/CHOx/ ITO electrodes were assessed by Brown-Anson model (Bard and Faulkner, 2001) using the equation given by

$$\gamma^* = \frac{4RTI_a}{n^2 F^2 Av} \qquad (2)$$

The values of the heterogeneous electron transfer rate constant (k$_s$) was found for bioelectrodes using Laviron's equation (Singh et al., 2013).

$$k_s = \frac{mnFv}{RT} \qquad (3)$$
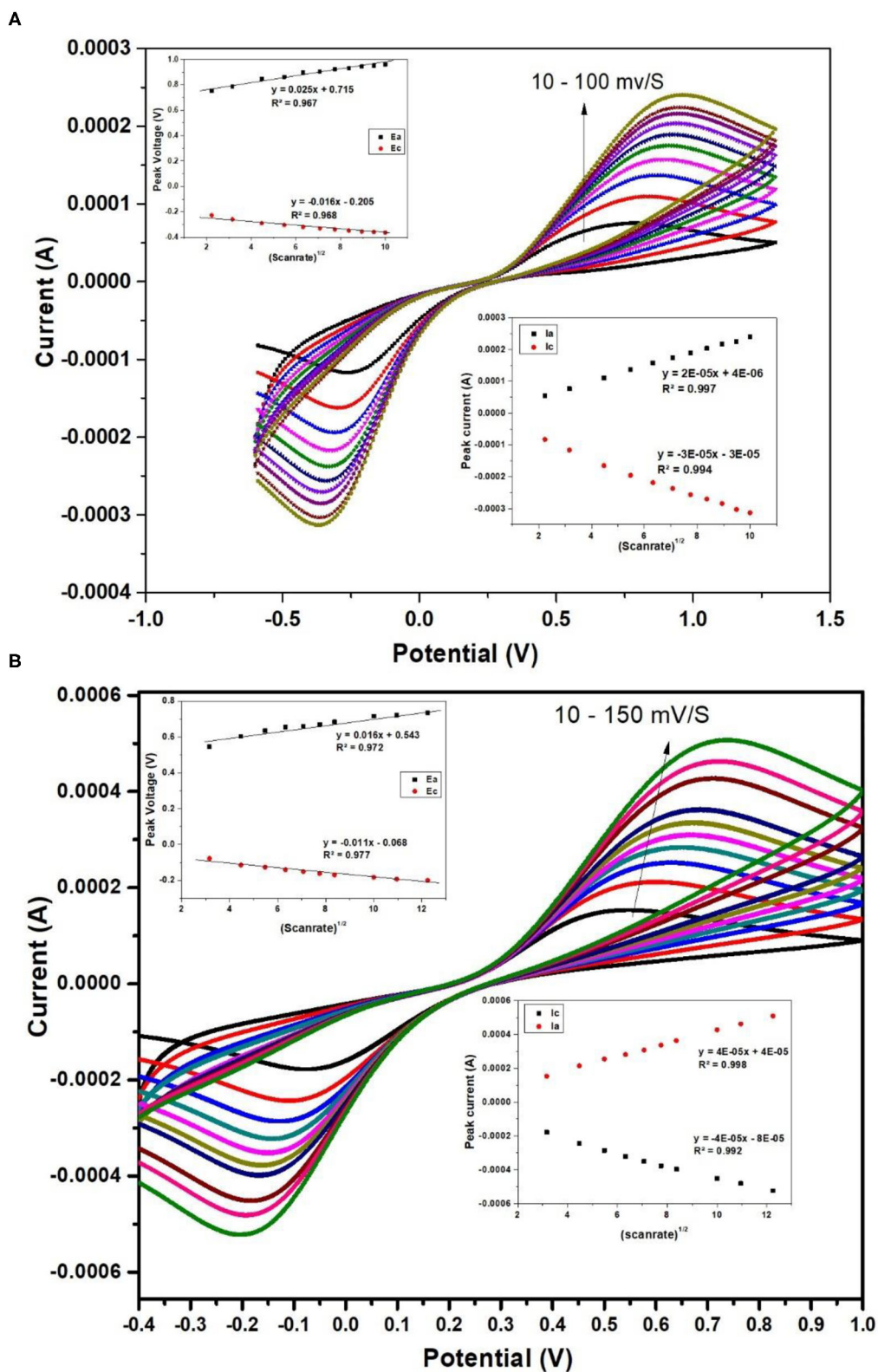
FIGURE 6 | CV curves of nafion-α-Fe$_2$O$_3$/ITO **(A)** and nafion-α-Fe$_2$O$_3$/CHOx/ ITO **(B)** electrodes at different scan rates.

Electrode	A (cm^2)	k$_s$ (s^{-1})	γ*(mol/cm^2)	D (cm^2 s^{-1})
Fe2O3-naf/ITO	1.54 ($r = 0.7$)	1568.63	4.288E-6	8.954E-7
Fe2O3-naf-Chox/ITO	1.54 ($r = 0.7$)	421.55	9.165E-6	4.09E-6

Where m is $\Delta E = E_{pa} - E_{pc}$, n is the electrons participated in charge transfer, F; the Faraday constant, v; scan rate, R; the gas constant and T; room temperature.

The surface concentration of the redox species of electrodes was calculated using Brown–Anson model (Bard and Faulkner, 2001).

$$I_p = \frac{n^2 F^2 I^* A V}{4RT} \tag{4}$$

Where the slope of the scan rate vs. I_{pc} is I_p/V and the surface concentration of the electrode is I^*. All the electrochemical parameters are tabulated in **Table 1**.

Electrochemical Response Studies

For cholesterol response measurements, nafion-α-Fe$_2$O$_3$/ITO and nafion-α-Fe$_2$O$_3$/CHOx/ ITO electrodes were positioned in the buffer and various concentrations of cholesterol solutions from 4 to 770 mg dl^{-1} were added and DPV for each concentration was recorded. There is an increase in the peak current of Nafion-Fe$_2$O$_3$/ITO electrodes with increased concentrations was observed as shown in **Figure 7A**. The linear calibration plot of peak current with concentration was plotted and shown in inset of the **Figure 7A**.

The electrodes are suitable for sensing of cholesterol without any enzyme immobilization with sensitivity of 0.012 μA (mg/dl)$^{-1}$ cm^{-2}. But, the crucial limitation of the enzyme less biosensor is the selectivity or specificity. The electrode was verified for selectivity with common interfering agents such as Ascorbic Acid (AA), Urea (U), 4-Acetymanophenol (4-AP), Citric Acid (CA), and glucose (Glu) at 4 mM concentrations and the results are shown in **Figure 8A**. Unfortunately, the Naf-Fe$_2$O$_3$/ITO electrode did not show much change in the peak currents as compared to cholesterol at 4 mM concentration implies the enzyme less sensing is not possible with real samples. Therefore, the enzyme cholesterol oxidase was immobilized on the electrode's surface by casting method through adsorption, dried, washed and dried again. The enzyme was immobilized without any cross-linking agent. The DPV response of different cholesterol concentrations on enzyme electrodes was tested. The DPV curves with different concentrations from a very low concentration from about 4–770 mg dl^{-1} was carried out as given in **Figure 7B**. The peak currents vs. the concentration was plotted against and the obtained linearity plot was shown in the inset. The electrode sensitivity of was estimated as 64.93 $\times$ 10^{-2} μA (mg/dl)$^{-1}$ cm^{-2}. The enzyme-substrate interaction (Michaelis–Menten) constant K$_m$, was obtained to

be 19 mg/dl. The lower detection limit (LOD) is obtained as 2 mg dl^{-1}. The specificity or the selectivity was verified with the general interfering agents such as U, CA, 4-AP, AA, and glu at 4 mM concentrations, and the DPV peak currents of each of these analytes were less than the peak current of 4 mM cholesterol (**Figure 8B**) which confirmed the specificity of the developed electrode.

The synthesized nanocomposite was found suitable for the cholesterol sensing without the help of enzyme but without selectivity. Therefore, the enzymatic electrode was fabricated. The current values were found to increase after the enzyme immobilization with cholesterol concentration by showing the increase in the DPV peak current. The immobilization of CHOx on magnetic nanoparticles showed the improved biochemical activity and the immobilized CHOx proved to be the effective biocatalyst to catabolize cholesterol (Ghosh et al., 2018). The increased stability and activity of CHOx leading to the suitable application in biosensors (Ghosh et al., 2018). The enzyme mediated electrochemical reaction took place at the electrode surface (Nakaminami et al., 1997) causes the change in the current with the addition of cholesterol. The catabolic reaction of CHOx combined with the electrochemical oxidation of mediator at the surface of the electrode produces reduced CHOx [CHOx (red)] and cholestenon when cholesterol was added in the first step. When CHOx (red) was combined with the mediator (M) (ferri/ferro) at oxidation potential it produces CHOx (ox) and M$_{red}$ in the second step. In the third step, M$_{red}$ becomes again M$_{ox}$ by releasing electrons. The first and second steps utilize O$_2$/H$_2$O$_2$ which is available in the buffer solution and forms an intermediate in the reaction. The H$_2$O$_2$ produced during second step gets electrochemically oxidize by giving the anodic current, which is the final measure of the cholesterol concentration. The schematic representation of the developed biosensing platform is given in **Figure 9**. The enzyme electrodes were found stable for almost 8 weeks when stored in the refrigerator, and after that the peak current started decreasing as shown in **Figure 10**.

CONCLUSIONS

The present study represents the development of a selective enzymatic sensing platform for the detection of cholesterol. The sensing platform was based on the nanocomposite of iron oxide nanoparticles and the ionic conducting polymer nafion coated on the ITO coated glass substrate. The detection of cholesterol was carried out using electrochemical DPV method. The enzymatic sensor showed the better detection capability by showing higher sensitivity [64.93 $\times$ 10^{-2} μA (mg/dl)$^{-1}$ cm^{-2}] with better selectivity. The interaction of CHOx with cholesterol produced charge carriers which led to the increase in the DPV peak current with increased concentration. The semiconducting iron oxide nanoparticles helped in the transfer of electrons.
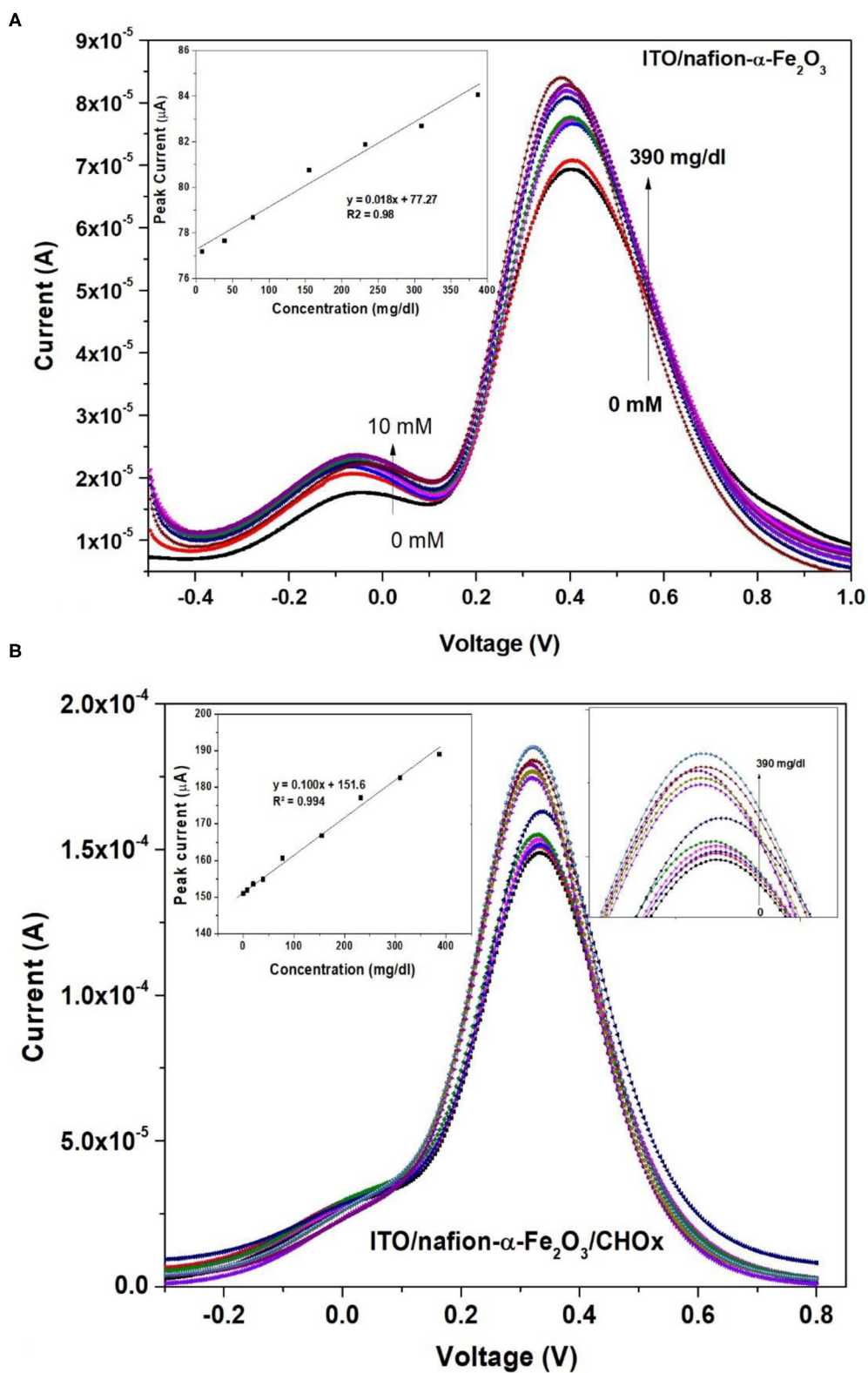
FIGURE 7 | DPV of **(A)** nafion-α-Fe$_2$O$_3$/ITO (inset shows the calibration curve) and **(B)** nafion-α-Fe$_2$O$_3$/CHOx/ITO electrodes at different concentrations (insets show the calibration curve and enlarged peaks).
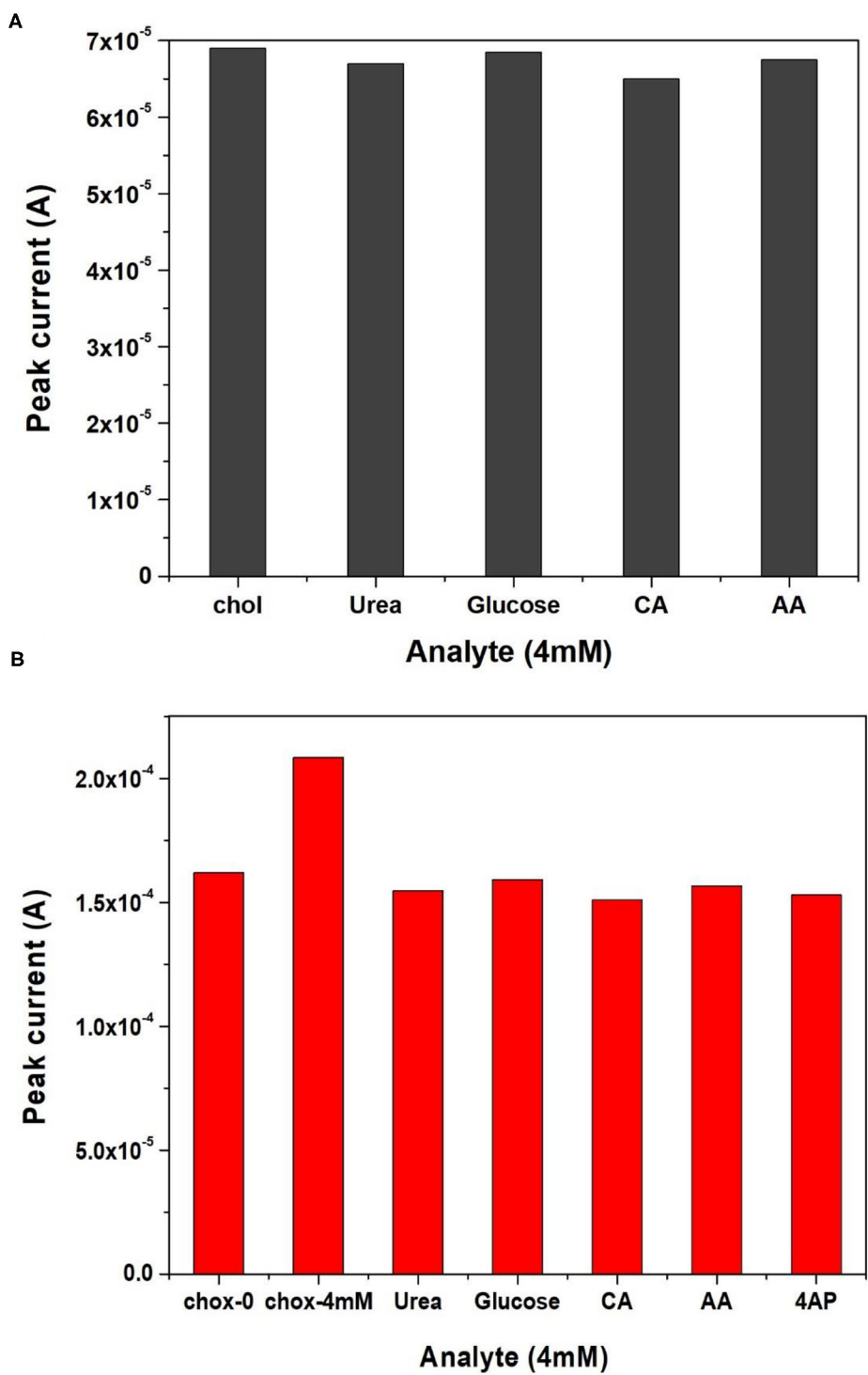
FIGURE 8 | Selectivity studies of **(A)** nafion-Fe_2O_3/ITO and **(B)** nafion-Fe_2O_3/CHOx/ITO electrodes with different analytes.
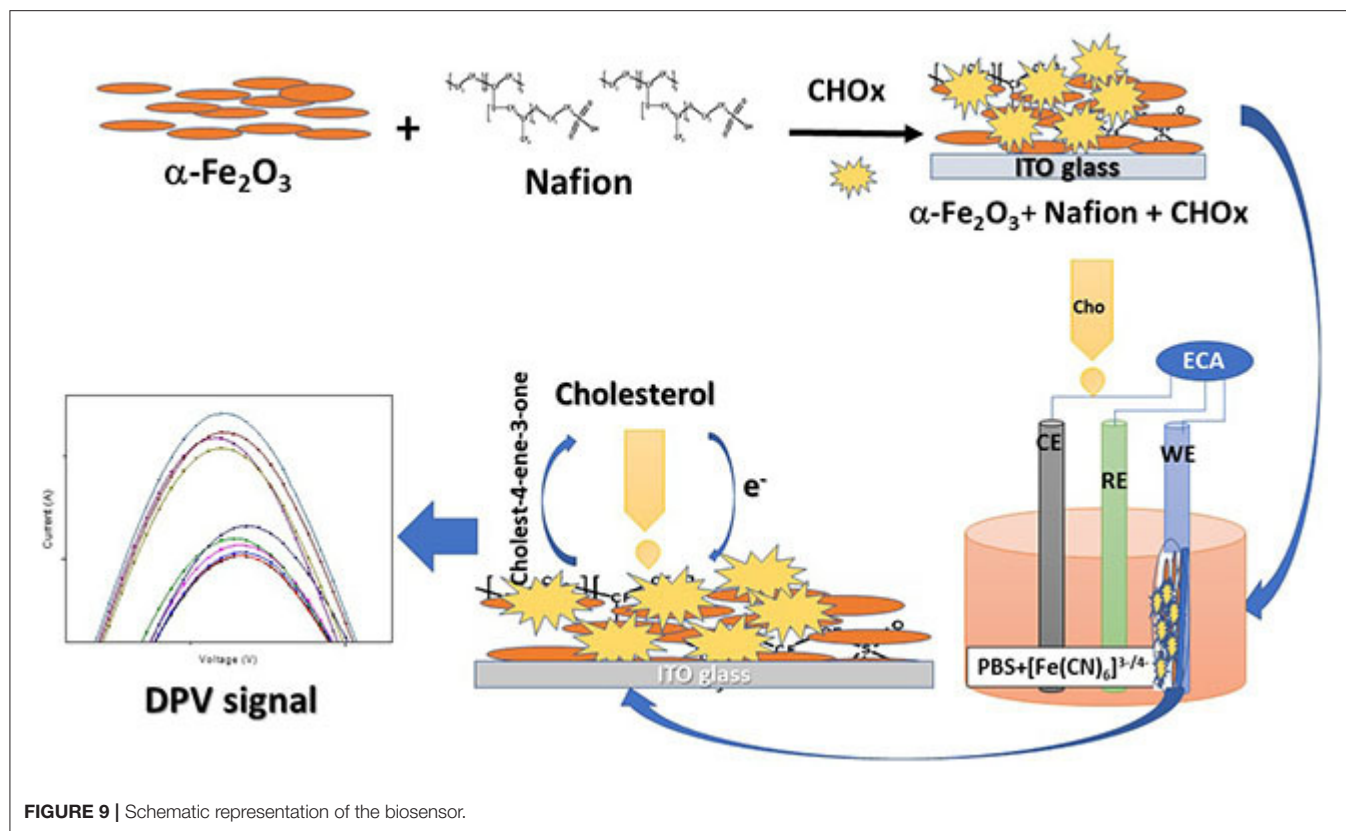
FIGURE 9 | Schematic representation of the biosensor.
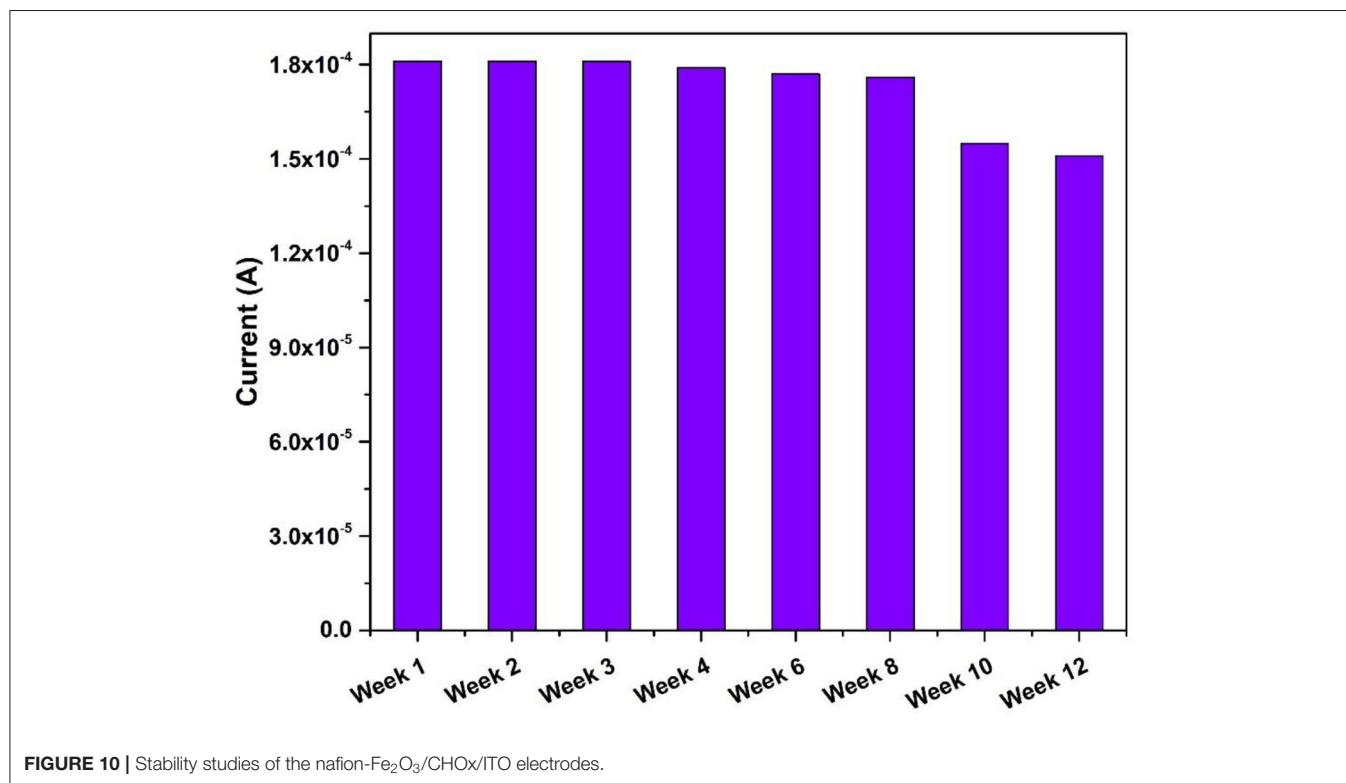
FIGURE 10 | Stability studies of the nafion-Fe_2O_3/CHOx/ITO electrodes.

DATA AVAILABILITY STATEMENT

The original contributions presented in the study are included in the article/supplementary material, further inquiries can be directed to the corresponding author/s.

AUTHOR CONTRIBUTIONS

GL has formulated the study. IS and RP have carried out sample preparation and characterization part. All authors participated in electrochemical characterization and sensing study.

ACKNOWLEDGMENTS

REFERENCES

Ajayan, P. M., Schadler, L. S., and Braun, P. V. (2006). *Nanocomposite Science and Technology*. New York, NY: John Wiley and Sons. doi: 10.1002/3527602127

Banerjee, A., Patra, S., Chakrabarti, M., Sanyal, D., Pal, M., and Pradhan, S. K. (2011). *Microstructure, Mössbauer, and Optical Characterizations of Nanocrystalline α-Fe₂O₃ Synthesized by Chemical Route*. Egypt: ISRN Ceramics.

Bard, A. J., and Faulkner, L. R. (2001). Fundamentals and applications. *Electrochem. Methods* 2, 580–632.

Bico, J., Thiele, U., and Quéré, D. (2002). Wetting of textured surfaces. *Colloids Surf. A Physicochem. Eng. Asp.* 206, 41–46. doi: 10.1016/S0927-7757(02)00061-4

Chen, Y., Xin, Y., Yang, H., Zhang, L., Zhang, Y., Xia, X., et al. (2013). Immobilization and stabilization of cholesterol oxidase on modified sepharose particles. *Int. J. Biol. Macromol.* 56, 6–13. doi: 10.1016/j.ijbiomac.2013.01.026

Chen, Y., Zhong, Q., Li, G., Tian, T., Tan, J., and Pan, M. (2018). Electrochemical study of temperature and Nafion effects on interface property for oxygen reduction reaction. *Ionics* 24, 3905–3914. doi: 10.1007/s11581-018-2533-3

Demir, V., Ates, M., Arslan, Z., Camas, M., Celik, F., Bogatu, C., et al. (2015). Influence of Alpha and gamma-iron oxide nanoparticles on marine microalgae species. *Bull. Environ. Contam. Toxicol.* 95, 752–757. doi: 10.1007/s00128-015-1633-2

Din, S. H. (2019). Nano-composites and their applications: a review. *Character. Appl. Nanomater.* 25, 407–415. doi: 10.24294/can.v2i1.875

Ge,. F., Li, M.-M., Ye, H., and Zhao, B.-X. (2012). Effective removal of heavy metal ions Cd²⁺, Zn²⁺, Pb²⁺, Cu²⁺ from aqueous solution by polymer-modified magnetic nanoparticles. *J. Hazard. Mater.* 211, 366–372. doi: 10.1016/j.jhazmat.2011.12.013

Ghosh, S., Ahmad, R., Gautam, V. K., and Khare, S. K. (2018). Cholesterol-oxidase-magnetic nanobioconjugates for the production of 4-cholesten-3-one and 4-cholesten-3, 7-dione. *Bioresour. Technol.* 254, 91–96. doi: 10.1016/j.biortech.2018.01.030

Gonzalez, C. M., Hernandez, J., Peralta-Videa, J. R., Botez, C. E., Parsons, J. G., and Gardea-Torresdey, J. L. (2012). Sorption kinetic study of selenite and selenate onto a high- and low-pressure aged iron oxide nanomaterial. *J. Hazard. Mater.* 211, 138–145. doi: 10.1016/j.jhazmat.2011.08.023

Grover, V. A., Hu, J., Engates, K. E., and Shipley, H. J. (2012). Adsorption and desorption of bivalent metals to hematite nanoparticles. *Environ. Toxicol. Chem.* 31, 86–92. doi: 10.1002/etc.712

Hasanabadi, N., Ghaffarian, S. R., and Hasani-Sadrabadi, M. M. (2013). Nafion-based magnetically aligned nanocomposite proton exchange membranes for direct methanol fuel cells. *Solid State Ion.* 232, 58–67. doi: 10.1016/j.ssi.2012.11.015

Jun, Y. W., Lee, J. H., and Cheon, J. (2008). Chemical design of nanoparticle probes for high-performance magnetic resonance imaging. *Angew. Chem. Int. Ed. Engl.* 47, 5122–5135. doi: 10.1002/anie.200701674

Kaushik, A., Khan, R., Solanki, P. R., Pandey, P., Alam, J., Ahmad, S., et al. (2008a). Iron oxide nanoparticles–chitosan composite based glucose biosensor. *Biosen. Bioelectron.* 24, 676–683. doi: 10.1016/j.bios.2008.06.032

Kaushik, A., Solanki, P. R., Ansari, A. A., Ahmad, S., and Malhotra, B. D. (2008b). Chitosan–iron oxide nanobiocomposite based immunosensor for ochratoxin-A. *Electrochem. Commun.* 10, 1364–1368. doi: 10.1016/j.elecom.2008.07.007

Kaushik, A., Solanki, P. R., Ansari, A. A., Sumana, G., Ahmad, S., and Malhotra, B. D. (2009). Iron oxide-chitosan nanobiocomposite for urea sensor. *Sens. Actuators B Chem.* 138, 572–580. doi: 10.1016/j.snb.2009.02.005

Kurihara, Y., Mabuchi, T., and Tokumasu, T. (2017). Molecular analysis of structural effect of ionomer on oxygen permeation properties in PEFC. *J. Electrochem. Soc.* 164:F628. doi: 10.1149/2.1301706jes

Mallick, P., and Dash, B. N. (2013). X-ray diffraction and UV-visible characterizations of α-Fe₂O₃ nanoparticles annealed at different temperature. *J. Nanosci. Nanotechnol.* 3, 130–134. doi: 10.5923/j.nn.20130305.04

Mehrotra, P. (2016). Biosensors and their applications–a review. *J. Oral Biol. Craniof. Res.* 6, 153–159. doi: 10.1016/j.jobcr.2015.12.002

Nakaminami, T., Kuwabata, S., and Yoneyama, H. (1997). Electrochemical oxidation of cholesterol catalyzed by cholesterol oxidase with use of an artificial electron mediator. *Anal. Chem.* 69, 2367–2372. doi: 10.1021/ac960996p

Paul, D. K., and Karan, K. (2014). Conductivity and wettability changes of ultrathin Nafion films subjected to thermal annealing and liquid water exposure. *J. Phys. Chem. C* 118, 1828–1835. doi: 10.1021/jp410510x

Paul, D. K., Shim, H. K., Giorgi, J. B., and Karan, K. (2016). Thickness dependence of thermally induced changes in surface and bulk properties of Nafion nanofilms. *J. Polym. Sci. Part B Polymer Phys.* 54, 1267–1277. doi: 10.1002/polb.24034

Perez, J. (2007). Iron oxide nanoparticles-Hidden talent. *Nat. Nanotech.* 2, 535–536. doi: 10.1038/nnano.2007.282

Raymond, L., Revol, J. F., Ryan, D. H., and Marchessault, R. H. (1996). Precipitation of ferrites in Nafion membranes. *J. App. Poly. Sci.* 59, 1073–1086. doi: 10.1002/(SICI)1097-4628(19960214)59:7<1073::AID-APP4>3.0.CO;2-B

Sharma, R., Agrawal, V. V., Srivastava, A. K., Nain, L., Imran, M., Kabi, S. R., et al. (2013). Phase control of nanostructured iron oxide for application to biosensor. *J. Mater. Chem. B* 1, 464–474. doi: 10.1039/C2TB00192F

Singh, B., Ali, N., Chakravorty, A., Sulania, I., Ghosh, S., and Kabiraj, D. (2019). Wetting behavior of MoS₂ thin films. *Mater. Res. Express* 6:096424. doi: 10.1088/2053-1591/ab2e5a

Singh, J., Roychoudhury, A., Srivastava, M., Solanki, P. R., Lee, D. W., Lee, S. H., et al. (2013). A highly efficient rare earth metal oxide nanorods based platform for aflatoxin detection. *J. Mater. Chem. B* 1, 4493–4503. doi: 10.1039/C3TB20690D

Singh, U. B., Yadav, R. P., Pandey, R. K., Agarwal, D. C., Pannu, C., and Mittal, A. K. (2016). Insight mechanisms of surface structuring and wettability of ion-treated Ag thin films. *J. Phys. Chem. C* 120, 5755–5763. doi: 10.1021/acs.jpcc.5b11944

Sulania, I., Kaswan, J., Attatappa, V., Karn, R. K., Agarwal, D. C., and Kanjilal, D. (2016). "Investigations of electrical and optical properties of low energy ion irradiated α-Fe₂O₃ (hematite) thin films," in *AIP Conference Proceedings, Vol. 1731* (Indonesia: AIP Publishing LLC), 120021. doi: 10.1063/1.4948093

Sulania, I., Yadav, R. P., and Karn, R. K. (2018). "Atomic and magnetic force studies of co thin films and nanoparticles: understanding the surface correlation using fractal studies," in *Handbook of Materials Characterization*, ed S. Sharma (Cham: Springer), 263–291. doi: 10.1007/978-3-319-92955-2_7

Umar, A., Ahmad, R., Hwang, S. W., Kim, S. H., Al-Hajry, A., and Hahn, Y. B. (2014). Development of highly sensitive and selective cholesterol biosensor based on cholesterol oxidase co-immobilized with α-Fe$_2$O$_3$ micro-pine shaped hierarchical structures. *Electrochim. Acta* 135, 396–403. doi: 10.1016/j.electacta.2014.04.173

Woo, K., Lee, H. J., Ahn, J. P., and Park, Y. S. (2003). Sol–gel mediated synthesis of Fe$_2$O$_3$ nanorods. *Adv. Mater.* 15, 1761–1764. doi: 10.1002/adma.200305561

Xiong, S., Yang, F., Jiang, H., Ma, J., and Lu, X. (2012). Covalently bonded polyaniline/fullerene hybrids with coral-like morphology for high-performance supercapacitor. *Electrochim. Acta* 85, 235–242. doi: 10.1016/j.electacta.2012.08.056

frontiers
in Nanotechnology

Check for
updates

Mathematical Modeling of Blood Flow With the Suspension of Nanoparticles Through a Tapered Artery With a Blood Clot

Sapna Ratan Shah* and Rohit Kumar

Bio-Mathematical Lab-34, School of Computational and Integrative Sciences, Jawaharlal Nehru University, New Delhi, India

In this study, some key new developments in nanoscience which highlight the problem of nanoparticles in blood flow through mild stenosis in the presence of a blood clot have been presented. The blood flow behavior through the stenosed artery is considered using the Prandlt fluid model and the flow of blood is considered as suspension of nanoparticles. An appropriate non-linear system of equations governing blood flow is represented in a cylindrical coordinate system and solved exactly under mild stenotic conditions using the geometry of the stenotic artery in the presence of a clot. Heat transfer phenomena have been examined for the physical features of the flow of blood through a stenosed artery, which is tapered in shape and with the presence of a clot. The temperature profile has been discussed with graphs for several different parameters of clot size, stenosis height, heat source, and sink parameter. Tapering phenomena has been analyzed for temperature profile. It is examined that in converging tapering the temperature provides greater values as estimated together with the non-tapered arteries and diverging tapering arteries. In this work, it is also analyzed that with a rise in the clot size (σ) the temperature (θ) increases, whereas the radius of the artery with stenosis h(z) decreases and heat source and sink parameter (D) increases.

Keywords: Prandlt fluid model, blood flow, stenotic artery with clot, tapering parameter, converging tapering

INTRODUCTION

Heart disease is sometimes called coronary heart disease. It is the leading cause of death among adults all over the world. Learning about the causes and risk factors of this disease may help to avoid heart problems (Akbar and Butt, 2016). According to the WHO's 2016 report, ~17.7 million people died from heart diseases, which makes up 31% of all deaths in that year, with ~7.5 million dying because of Coronary Heart Disease (CHD) and 6.67 million by heart stroke. Coronary heart disease, stroke, and other cardiovascular diseases are the main cause of a lack of oxygen to organs (Ellahi et al., 2013). This occurs when blood is passing through the blood vessels and blood flow passage is reduced, by reducing radius (stenosis), because of the deposition of fatty acids or plaque inside the inner wall of the blood vessels (Young, 1968). Stenosis is an anomalous and an unnatural expansion of cholesterol that grows at several inner layer locations of the cardiovascular system and is responsible for cardiovascular diseases (Fry, 1968). Arterial thrombosis is another form of heart disease, which usually occurs after the erosion or rupture of an atherosclerotic plaque and may hinder blood flow to many of the most important organs. If blood flow in the heart is unexpectedly

blocked, then a heart attack occurs in the circulatory system (Dintenfass, 1971). Hemodynamic activities of the blood flow is changed by the existence of arterial stenosis. Many scientists Young and Tsai (1973) and Young (1979) have investigated and created a better interpretation of flow fluid, dynamic of fluid, and rheological blood flow characteristics through arteries in the presence of stenosis, which is essential in the study of cardiovascular diseases. In 2009, Siddiqui et al. (2009) represented the flow of blood by Casson's fluid model in a stenosed artery. Mekheimer and El Kot (2008) studied the axis-symmetric flow of blood in a radially symmetric but axially non-symmetric mild stenosed artery, which is a tapered artery, using blood as a Micropolar fluid model. Mandal (2005) obtained an unsteady flow of blood by remembering that the behavior of blood is like a non-Newtonian fluid, along with an artery that is tapered with mild stenosis. He obtained the numerical solution, expression, and graphical results for the blood flow.

In 2010, Varshney et al. (2010) presented a comprehensive model known as the Power-law fluid model for the flow of blood in blood vessels like arteries and treated blood flow using multiple stenoses. Nadeem et al. (2011) has discussed a model for blood, Power-law fluid, wherein the flow is through a tapered artery with mild stenosis. In 2011, Nadeem and Akbar (2011) again discussed the flow of blood and its analysis in Nadeem et al. (2011) for different fluid models, like Jeffrey fluid model. Mustafa et al. (2011) have investigated and concluded the study for the modified Newtonian fluid blood flow through a pair of arterial mild stenosis which is irregular. Abdullah et al. (2011) have studied the effect of a magnetic field on the flow of blood with an irregular mild stenosis. An annular region has been found in the vessel of blood, between the wall of the stenosis and blood clot. Mekheimer and Elmaboud (2008) studied the Micropolar fluid model in a region which is annular and under a long wavelength. The Reynolds number approximation for peristaltic transport has also been taken into consideration and they assumed the artery as a very small tube with a very small clot and a sinusoidal wave moving down to its wall. Ellahi et al. (2013) calculated mass and heat transfer on blood flow through a mild stenosed artery by using the Homotopy Perturbation method for the Jeffery fluid model with the suspension of nanoparticles. Ajdari et al. (2017) and Akbar and Butt (2016) discussed at which point the stenosis, which starts at a young age with increasing plaque build-up in the major or minor arteries of the human body, such a build-up becomes large enough in the coronary artery. Rahbari et al. (2017) investigated the fluid flow of blood and the effects of the magnetic field and heat transfer with nanoparticles through porous blood vessels.

We have done this work because in several investigations the velocity profile has been discussed but the temperature profile has never been discussed for tapered stenosed artery. So in this work we have aimed to understand the effects of heat transfer phenomenon on the Prandalt fluid model through a tapered stenosed atherosclerotic artery. The non-linear equations governing blood flow are modeled in a cylindrical coordinate system. The convection of heat transfer with a catheterized mild stenotic artery with a clot has been taken into consideration. And the non-linear coupled equations are solved exactly under mild

stenotic conditions using the geometry for a mild stenotic artery in the presence of a clot. The heat and mass transfer phenomenon was discussed with distinct values of the temperature profile for some distinct values of flow parameters using graphs. As of now, this model has not been discussed for this kind of blood flow problem.

MATHEMATICAL FORMULATION

This present study aims to examine an nanoparticles in blood flow with a constant viscosity μ and density ρ in two coaxial tubes with length L; the inner tube contains a clot on its wall and the outer tube contains an axially symmetric mild stenosis. The cylindrical coordinate system (r, θ, and z) is chosen such that u and w are the velocity components in the r and z directions, respectively. Mixed convection is used to calculate the heat transfer by assigning the temperature $T0$ to the wall of the tube. The consideration of the stenosis in the outer tube and clot in the inner tube is defined by the h (z) and ε (z), respectively, and can be delineated as Rahbari et al. (2017):

$$h(z) = \mathrm{d}\,(\mathrm{z})\left[1 - k\left(b^{n-1}(z-a) - (z-a)^n\right)\right]; \ a < z \le a + b$$
$$= d\,(z); \ otherwise \tag{1}$$

$$\varepsilon(\mathrm{z}) = \mathrm{d}\,(\mathrm{z})\left[c + \sigma\,e^{-\Pi^2(z-z_d-0.5)^2}\right]; \ a < z \le a + b$$
$$= cd\,(z); \ otherwise \tag{2}$$

$$with \quad d(z) = R_0 + \xi_z \tag{3}$$

In the above equations, $d(z)$ is the radius of the tapered arterial segment in the stenotic region, while R_0 is the radius of the artery in the non-stenotic region, ξ is the tapering parameter, b is the length of the stenosis, $n \ge 2$ is the parameter determining the shape of the constriction profile and referred to as the shape parameter, a is the stenosis location, and k is given by:

$$k = \frac{\delta^*}{R_0 b^n} \frac{n^{\left(\frac{n}{n-1}\right)}}{(n-1)} \tag{4}$$

where δ^* is the maximum height of the stenosis located at, $z = a + \frac{b}{n^{\frac{1}{n-1}}}$, σ is the maximum height attained by the clot at $z = z_d + 0.5$, $c\,d(z)$ is the radius of the inner tube, and $c << 1$ and z_d is the axial displacement of the clot as shown in **Figure 1**.

The constitutive equations for the Prandalt fluid model are given by Akbar et al. (2011)

$$\overline{S} = \frac{A\sin^{-1}\left\{\frac{1}{c_1}\left[\left(\frac{\partial u}{\partial z}\right)^2 + \left(\frac{\partial w}{\partial z}\right)^2\right]^{\frac{1}{2}}\right\}}{\left[\left(\frac{\partial u}{\partial z}\right)^2 + \left(\frac{\partial w}{\partial z}\right)^2\right]^{\frac{1}{2}}}\frac{\partial w}{\partial r} \tag{5}$$
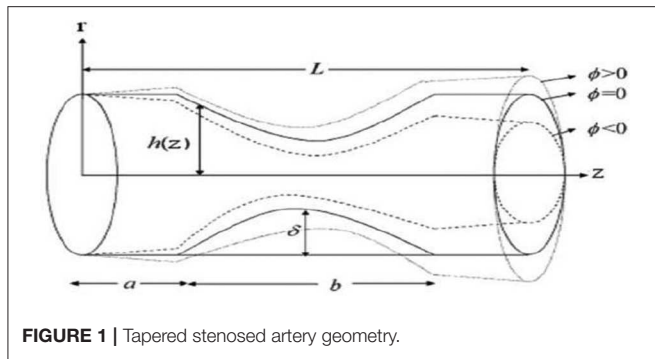
FIGURE 1 | Tapered stenosed artery geometry.

FIGURE 2 | Temperature (θ) for distinct values of clot size (σ) = 0.2, 0.3, 0.4.

The equations for incompressible nanoparticles in blood flow in the presence of body forces are given by

$$\frac{1}{r}\frac{\partial (ru)}{\partial r} + \frac{\partial w}{\partial z} = 0 \tag{6}$$

$$\rho\left(u\frac{\partial u}{\partial r} + w\frac{\partial u}{\partial z}\right) = -\frac{\partial p}{\partial r} + \frac{1}{r}\frac{\partial}{\partial r}(rS_{rr}) + \frac{\partial}{\partial z}(S_{rz}) - \frac{S_{\theta\theta}}{r} \tag{7}$$

$$\rho\left(u\frac{\partial w}{\partial r} + w\frac{\partial w}{\partial z}\right) = -\frac{\partial p}{\partial z} + \frac{1}{r}\frac{\partial}{\partial r}(rS_{rz}) + \frac{\partial}{\partial z}(rS_{zz}) - \rho g\alpha(T - T_0) \tag{8}$$

$$u\frac{\partial T}{\partial r} + w\frac{\partial T}{\partial z} = \frac{k}{(\rho c)_f}\left(\frac{\partial^2 T}{\partial r^2} + \frac{1}{r}\frac{\partial T}{\partial r} + \frac{\partial^2 T}{\partial z^2}\right) + \frac{Q_0}{(\rho c)_f} \tag{9}$$

In the presented equations, p is the fluid pressure, μ is the viscosity of the base fluid, g is gravity, and Q_0 is the constant heat absorption or heat generation. To solve the governing equations, we introduce the following dimensionless parameters:-

$$p' = R_0^2\frac{p}{u_0 b\mu}, R_e = \frac{\rho b u_0}{\mu}, S'_{rr} = \frac{bS_{rr}}{u_0\mu}, \theta = \frac{T - T_0}{T_0}$$

$$\alpha = \frac{A}{\mu c_1}, \beta = \frac{Au_0^2}{6R_0^2\mu c_1^3}, D = \frac{Q_0 R_0^2}{T_0 k} \tag{10}$$

where u_0 is the average velocity over the section of the channel, A and c_1 are material constants for Prandalt fluid model, D is the dimensionless heat source or sinks parameter with the fluid, and G_r is the Grashof number. Using the above non-dimensional parameters along with the additional conditions:-

$$\frac{\partial p}{\partial z} = \frac{1}{r}\frac{\partial}{\partial r}\left[r\left(\alpha\left(\frac{\partial w}{\partial r}\right) + \beta\left(\frac{\partial w}{\partial r}\right)^3\right)\right] + G_r\theta \tag{11}$$
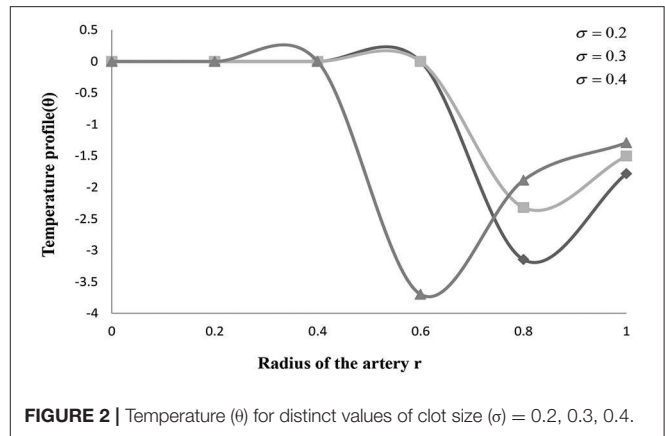
$$\frac{\partial^2\theta}{\partial r^2} + \frac{1}{r}\frac{\partial\theta}{\partial r} + D = 0 \tag{12}$$

Further, we consider three types of arteries, converging tapering ($\phi < 0$), non-tapering ($\phi = 0$), and diverging tapering arteries ($\phi > 0$). To calculate the heat transfer, the general solution for the temperature profile using the boundary conditions is found exactly, which is given by.

$$\theta = -\frac{D}{4}\left(r^2 - h^2\right) + \ln(rh - h + \varepsilon)\left(1 - \frac{D}{4}\left(h^2 - \varepsilon^2\right)\right) \tag{13}$$

RESULTS AND GRAPHICAL DISCUSSIONS

The system of equations has been solved and the expression (Mustafa et al., 2011) has been plotted to study the outcome of the work. The main aim of this mathematical study is to explore the heat transfer phenomena of blood flow through a tapered stenosed artery along with the clot with the flow of blood using the Prandalt fluid model. The effects of Prandalt fluid parameters tapering angle (ϕ), heat source and sink (D), the stenosis shape parameter (n), and a maximum height of the stenosis (δ) are analyzed for (1) converging tapering, (2) diverging tapering, and (3) non-tapered arteries.

Figures 2–4 explains the heat transfer phenomenon by depicting the changes in temperature profile (θ) for distinct flow parameters graphically. It is obtained here that, due to a rise in the value of the maximum height of the clot (σ), the temperature profile (θ) increases. The temperature profile (θ) shows the identical variation for the maximum height of the stenosis (δ) and the maximum height extended by the clot (σ). The temperature profile (θ) shows quite interesting results for some values of tapering angle (ϕ) and heat source and sink (D).

The effect of the radius of the artery with a stenosis is understood, and further results are explored in the case of converging tapered artery for distinct values of clot size in the present study. **Figure 2** depicts the variation for temperature profile (θ) with the radius of an artery with stenosis h(z) for distinct values of σ, i.e., the maximum height attained by the
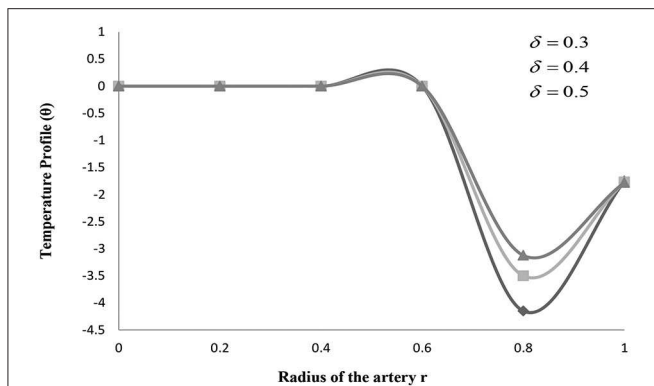
FIGURE 3 | Temperature (θ) for distinct values of stenisis height (δ) = 0.3, 0.4, 0.5.
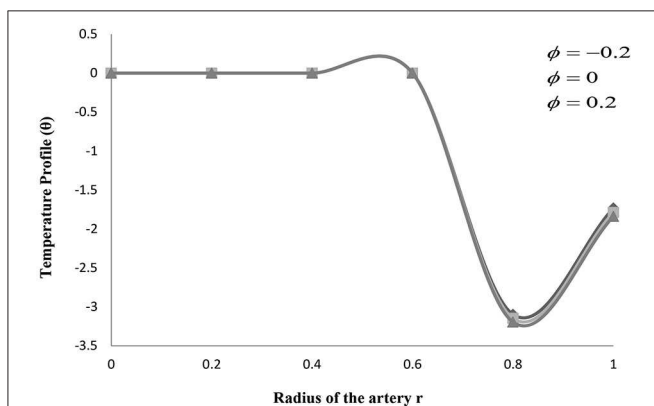
FIGURE 4 | Temperature (θ) for distinct values of tapering angle (ϕ) = (−0.2, 0, 0.2).

clot. It is seen in this figure that, due to a rise in the height of the clot, the temperature profile (θ) increases. However, it is also observed in the figure that at σ = 0.4, the temperature attains a minimum value at stenosis size h(z) = 0.6, and then it starts increasing again after attaining certain values of h(z). **Figure 3** depicts the variation for temperature profile (θ) with the radius of an artery with stenosis h(z) for distinct values of δ, i.e., the maximum height of the stenosis. It is seen in this figure that, due to an increase in the height of the stenosis, the temperature profile decreases primarily. Whereas, it is also observed in the figure that after attaining minimum value h(z) = 0.8, it is continuously increasing. These figures also show that an increase in the value of the maximum height attained by the clot (σ) and the maximum height attained by the stenosis (δ) will result in an increase in the amount of heat generated. An increase in the amount of heat generated will raise the blood pressure inside the artery. Higher blood pressure has a strong possibility of creating extra pressure that could make the artery burst. Also in a narrow artery, the risk of being blocked is greater.

In both cases, the body part that received its blood from that affected artery will not be able to get the energy and oxygen which

is essential for that area of the body and then, because of the lack, the cells in the affected area will die in that body part. If the ruptured blood vessels deliver blood to any part of the heart, then that area of heart muscle, due to lack of blood supply, will die, causing the heart attack.

Figure 4 also depicts how the non-tapered, diverging tapering, and converging tapering arteries affect the temperature profile (θ) with a radius of artery and stenosis h(z) for distinct values of tapering angles (ϕ). It is seen here in the figure that for a decrease in the tapering angle the temperature profile decreases up to h(z) = 0.8, and then increases for the greater values of h(z). However, it is also observed in the figure that the temperature attains a minimum value at stenosis size (r) = 0.8, and then it starts increasing after attaining convinced values of (r). It is shown that, for the case of converging tapering, the temperature gives greater values as compared to the case of diverging tapering. And it is observed that the temperature rises in the case of non-tapered arteries as well.

CONCLUSION

This study focus on the heat transfer phenomena of blood flow that happens in the human cardiovascular system and the study aims to contribute to a better understanding of the circulatory system in the presence of minor growth of the stenosis in the artery, where the clot is present inside it. So the objective of the study was to explore the influence of Prandalt fluid parameters like tapering angle (ϕ), heat source and sink (D), the stenosis shape parameter (n), and the maximum height of the stenosis (δ) on temperature profile (θ). In this study, the tapering phenomena have been analyzed for temperature profiles especially. It is found that, for converging tapering, the temperature gives greater results as compared to the case of diverging tapering arteries. It is also observed that the temperature gives superior values in the case of non-tapered arteries as well. It has also been examined that, due to a rise in the clot size (σ), the temperature profile (θ) increases while the radius of the artery with stenosis h(z) decreases and the heat source and sink parameter (D) increases.

DATA AVAILABILITY STATEMENT

The raw data supporting the conclusions of this article will be made available by the authors, without undue reservation.

AUTHOR CONTRIBUTIONS

SS: formulation of the problem and mathematical modeling. RK: calculation and the graphical part of the paper. All authors contributed to the article and approved the submitted version.

ACKNOWLEDGMENTS

REFERENCES

Abdullah, I., Amin, N. S., and Hayat, T. (2011). Magnetohydrodynamic effects on blood flow through irregular stenosis. *Int. J. Number. Method Fluids* 67, 1624–1636. doi: 10.1002/fld.2436

Ajdari, N., Vyas, C., Bogan, S. L., Lwaleed, B. A., and Cousins, B. G. (2017). Gold nanoparticle interactions in human blood: a model evaluation. *Nanomed. Nanotechnol. Biol. Med.* 13, 1531–1542. doi: 10.1016/j.nano.2017.01.019

Akbar, N. S., and Butt, A. W. (2016). Bio-mathematical venture for the metallic nanoparticles due to ciliary motion, Comput. *Methods Prog. Biol.* 134, 43–51. doi: 10.1016/j.cmpb.2016.06.002

Akbar, N. S., Nadeem, S., and Lee, C. (2011). Peristaltic flow of a Prandtl fluid model in an asymmetric channel. *Int. J. Phy. Sci.* 7, 687–695. doi: 10.5897/IJPS11.1375

Dintenfass, L. (1971). Viscosity factors in hypertensive and cardiovascular diseases. *Cardiovasc. Med.* 2, 337–349.

Ellahi, R., Rahman, S. U., and Nadeem, S. (2013). Theoretical study of unsteady blood flow of Jeffery fluid through stenosed arteries with permeable walls. *Zeitschr Naturforschung A* 68, 489–498. doi: 10.5560/zna.2013-0032

Fry, D. L. (1968). Acute vascular endothelial changes associated with increased blood velocity gradients. *Circ. Res.* 22, 165–197. doi: 10.1161/01.RES.22.2.165

Mandal, P. K. (2005). An unsteady analysis of non-Newtonian blood flow through tapered arteries with stenosis. *Int. J. Non Linear Mech.* 40, 151–164. doi: 10.1016/j.ijnonlinmec.2004.07.007

Mekheimer, K. H. S., and El Kot, M. A. (2008). The micropolar fluid model for blood flow through a tapered artery with stenosis. *Acta Mech. Sin.* 24, 637–644. doi: 10.1007/s10409-008-0185-7

Mekheimer, K. S., and Elmaboud, Y. A. (2008). The influence of a micropolar fluid on peristaltic transport in an annulus: application of the clot model. *Appl. Bionics Biomech.* 5:302195. doi: 10.1155/2008/302195

Mustafa, N., Mandal, P. K., Abdullah, I., Amin, N. S., and Hayat, T. (2011). Numerical simulation of generalized Newtonian blood flow past a couple of irregular arterial stenosis. *Numer. Meth. Partial Diff. Eqs.* 27, 960–981. doi: 10.1002/num.20563

Nadeem, S., and Akbar, N. S. (2011). Jeffrey fluid model for blood flow through a tapered artery with stenosis. *J. Mech. Med. Biol.* 11, 529–545 doi: 10.1142/S0219519411003879

Nadeem, S., Akbar, N. S., Hayat, T., and Hendi, A. A. (2011). Power-law fluid model for blood flow through a tapered artery with stenosis. *Appl. Math. Comput.* 217, 7108–7116. doi: 10.1016/j.amc.2011.01.026

Rahbari, A., Fakour, M., Hamzehnezhad, A., Vakilabadi, M. A., and Ganji, D. D. (2017). Heat transfer and fluid flow of blood with nanoparticles through porous vessels in a magnetic field: a quasi-one-dimensional analytical approach. *Math. Biosci.* 283, 38–47. doi: 10.1016/j.mbs.2016.11.009

Siddiqui, S. U., Verma, N. K., Mishra, S., and Gupta, R. S. (2009). Mathematical modeling of the pulsatile flow of Casson's fluid in arterial stenosis. *Appl. Math. Comput.* 210, 1–10. doi: 10.1016/j.amc.2007.05.070

Varshney, G., Katiyar, V. K., and Kumar, S. (2010). Effect of magnetic field on the blood flow in an artery having multiple stenoses: a numerical study. *Int. J. Eng. Sci. Tech.* 2, 67–82. doi: 10.4314/ijest.v2i2.59142

Young, D. F. (1968). Effects of a time-dependent stenosis on flow through a tube. *J. Eng. Ind. Trans. ASME* 90, 248–254. doi: 10.1115/1.3604621

Young, D. F. (1979). Fluid mechanics of arterial stenosis. *J. Biomech. Eng. Trans. ASME* 10, 157–175. doi: 10.1115/1.3426241

Young, D. F., and Tsai, F. Y. (1973). Flow characteristic in models of arterial stenosis-I, steady flow. *J. Biomech.* 6, 395–410. doi: 10.1016/0021-9290(73)90099-7

Levofloxacin Detection Using L-Cysteine Capped MgS Quantum Dots *via* the Photoinduced Electron Transfer Process

S. Z. H. Hashmi[1†], Tarun Kumar Dhiman[1†], Navneet Chaudhary[1,2], Avinash Kumar Singh[1,3], Rahul Kumar[1,3], Jai Gopal Sharma[2], Anil Kumar[4] and Pratima R. Solanki[1]*

[1]Special Centre for Nanoscience, Jawaharlal Nehru University, New Delhi, India, [2]Department of Biotechnology, Delhi Technological University, New Delhi, India, [3]School of Physical Sciences, Jawaharlal Nehru University, New Delhi, India, [4]National Institute of Immunology, New Delhi, India

Antibiotics resistance is becoming one of the biggest problems of the 21st century. The prior detection of antibiotics resistance can help human beings in better treatment of diseases. Here, we have used L-Cysteine capped magnesium sulfide quantum dots (L-Cyst-MgS QDs) to detect Levofloxacin antibiotic. L-Cyst-MgS QDs were synthesized using the hydrothermal method. Transmission electron microscopy study showed monodispersed L-Cyst-MgS QDs of 2–4 nm in size. Energy dispersive x-ray photoemission spectroscopy study confirmed the elemental composition of the L-Cyst-MgS QDs without any impurity. UV-vis absorption study showed a peak centered around 340 nm. The photoluminescence study exhibited the maximum peak at 410 nm for 340 nm of excitation wavelength. L-Cyst-MgS QDs were studied with thirteen antibiotics, namely Thiamphenicol, Gentamicin, Erythromycin, Ofloxacin, Ampicillin, Ciprofloxacin, Tetracycline, Chloramphenicol, Florfenicol, Amoxicillin, Moxifloxacin, Norfloxacin, and Levofloxacin. Among these, Levofloxacin showed the most significant change in the peaks' intensity and was further used for the interaction study. In the interaction study, the peak corresponding to MgS showed a continuous decrease, while the peak corresponding to Levofloxacin showed an increase with the increased concentrations (0–100 μg/ml) of Levofloxacin. Linear behavior was obtained in the range of 1–90 μg/ml. FT-IR study confirmed the interaction of the Levofloxacin with L-Cyst-MgS QDs. The Time-resolved fluorescence spectroscopy showed identical lifetime for both the samples and no spectral overlap confirm the FRET free system. The underlying mechanism is explained based on the electron transfer from the conduction band of the L-Cyst-MgS QDs to the HOMO of Levofloxacin. The limit of detection was found to be 0.21 μg/ml.

Keywords: hydrothermal synthesis, levofloxacin antibiotic, MgS quantum dots, L-cysteine, photo-induced electron transfer

INTRODUCTION

The population increase in the last two centuries has considerably increased pharmaceuticals use in society because of growing health problems. The discovery of the first antibiotic in 1928 has revolutionized the pharmaceutical industry as antibiotics can cure many diseases (Martinez et al., 2008; Adzitey, 2015). There is a considerable increase in antibiotics use since then in both human and

animal hosts because of two main reasons. Firstly, because of the specific nature against bacteria and fungi (Levy, 1978; Bungau et al., 2015; Ferrone et al., 2017) and secondly, because of their capability to increase the growth rate of animals and improve their feed efficiency (Aarestrup and Wegener., 1999; Cháfer-Pericás et al., 2010; Deng et al., 2014). However, their presence in the environment is equally dangerous and alarming. If a large quantity of antibiotics is introduced in the environment, then it will give rise to bacterial resistance to antibiotics making an adverse effect on the use of antibiotics for treatment of both humans and animals (Martínez, 2008; Bungau et al., 2015; Mahmood et al., 2019). These effects necessitate the need to detect antibiotics in the environment as it is a matter of great concern in modern times. Conventionally, the methods available for detecting antibiotics are chromatography, which requires extensive equipment and preparation. The chromatography process is quite complicated since it requires accurate quantification, simultaneous detection, and high specificity based on the structural information of the analytes (Deng et al., 2014; Dai et al., 2017; Pérez et al., 2017). Other methods for antibiotic determination include electrophoresis (Dai et al., 2017; Jang et al., 2017; Ji et al., 2017), diode array (Bitas and Samanidou, 2016), or enzyme immunosorbent assay (ELISA) (Kong et al., 2017; Váradi et al., 2017), polymerase chain reaction (PCR), or immunologic reactions have been developed. While such well-established techniques are present for the detection of antibiotics, there are also some disadvantages of these techniques like costly equipment, tiring and laborious work for the preparation of samples, and a constant requirement for well-trained human resources (Chauhan et al., 2016; Yadav et al., 2020). These disadvantages give rise to the necessity of economically feasible techniques. Optical sensing of antibiotics is a solution for this significant problem since it requires fewer human resources and instruments and involves less time than other methods.

Fluorescent materials are mostly used for optical sensing applications (Sarkar et al., 2020). Among various fluorescent materials, quantum dots (QDs) have the highest fluorescence. Also, their size can be easily controlled using different capping agents and synthesis parameters. Such tunability of size allows the fluorescence emission between UV and visible range (Garimella et al., 2020; Kujur and Singh., 2020). Quantum dots as QDs only show unique optical properties, such as the dramatic enhancement of photoluminescence (PL) compared with the bulk counterpart of the same material. This happens due to the quantum confinement effect. Size is one of the significant parameters which affect the PL of a material. Several authors have shown that with the decrease in the size of the material, PL properties increases. Also, PL emission can be obtained in either the UV region or visible region. The UV region's PL spectra arise due to the direct transfer of e-from the conduction band to the valence band. The PL spectra in the visible light can be due to the material's surface defect, giving non-radiative recombination. QDs have symmetrical fluorescence emission spectra and broad absorption spectra, having only 25–40 nm of half-width.

They can also emit multicolor fluorescence when excited at the same wavelength, making them ideal optical detection materials (Alivisatos et al., 2005). The capping agent also allows for making them specific toward the detection of a particular biomolecule. Magnesium sulfide (MgS) QDs have been synthesized earlier using the hydrothermal method for using as a potential replacement of electrode material in lithium-ion batteries, but this material's optical properties remain unexplored (Zhang et al., 2018). MgS is a well-known material for a potential replacement of electrode material in lithium-ion batteries, but this material's optical properties remain unexplored. Here, we have tried to explore the optical properties of MgS QDs. We have studied the absorption and emission characteristics of extremely small size of L-Cyst-MgS. This also helps us in understanding the effect of reduction in size on optical properties of MgS QDs. In this work, optical sensing of Levofloxacin was carried out by analyzing its interaction with L-Cyst-MgS QDs. In this context, a novel and fully optimized method for the synthesis of L-Cyst capped MgS QDs, and their specific nature antibiotic for the detection of Levofloxacin has been proposed. L-Cyst-MgS QDs were synthesized using the hydrothermal method and characterized using transmission electron microscopy (TEM), energy dispersive x-ray emission (EDX), UV-visible, and fluorescence spectroscopy. L-Cyst-MgS QDs were studied with thirteen antibiotics. Among these, Levofloxacin antibiotics showed the most significant change. Linear detection of Levofloxacin antibiotic was obtained in the 1–90 µg/ml range.

EXPERIMENTAL

Reagents

Magnesium nitrate $[Mg(NO_3)2.H_2O]$ (98.99%) and L-cysteine (99.99%) were purchased from Sigma Aldrich, and sodium sulfide pellets $[Na_2S]$ (99.99%) was purchased from SDL. All the antibiotics i.e., Thiamphenicol, Gentamicin, Erythromycin, Ofloxacin, Ampicillin, Ciprofloxacin, Tetracycline, Chloramphenicol, Florfenicol, Amoxicillin, Moxifloxacin, Norfloxacin, Levofloxacin, were purchased from SRL, Hi-media, and Sigma Aldrich. 10 ml of 0.1 millimolar concentration was prepared for each antibiotic.

Characterizations Techniques

The obtained L-Cyst-MgS-QDs were further characterized using high-resolution transmission electron microscopy (HR-TEM; JEOL-TEM-2100F), energy dispersive x-ray spectroscopy (EDX) (Bruker), UV-vis absorption spectroscopy (T-90+UV-vis spectrometer, P. G. Instruments), and fluorescence spectroscopy (Carry Eclipse Spectrophotometer, Agilent Technologies). The interaction of L-Cyst-MgS-QDs with thirteen antibiotics was studied using fluorescence spectroscopy. The interaction study of Levofloxacin with L-Cyst-MgS-QDs was studied at various concentrations in the range of 0–100 µg/ml. These results were further confirmed with Fourier transform infrared (FT-IR-Spectrum 2-Perkin Elmer),
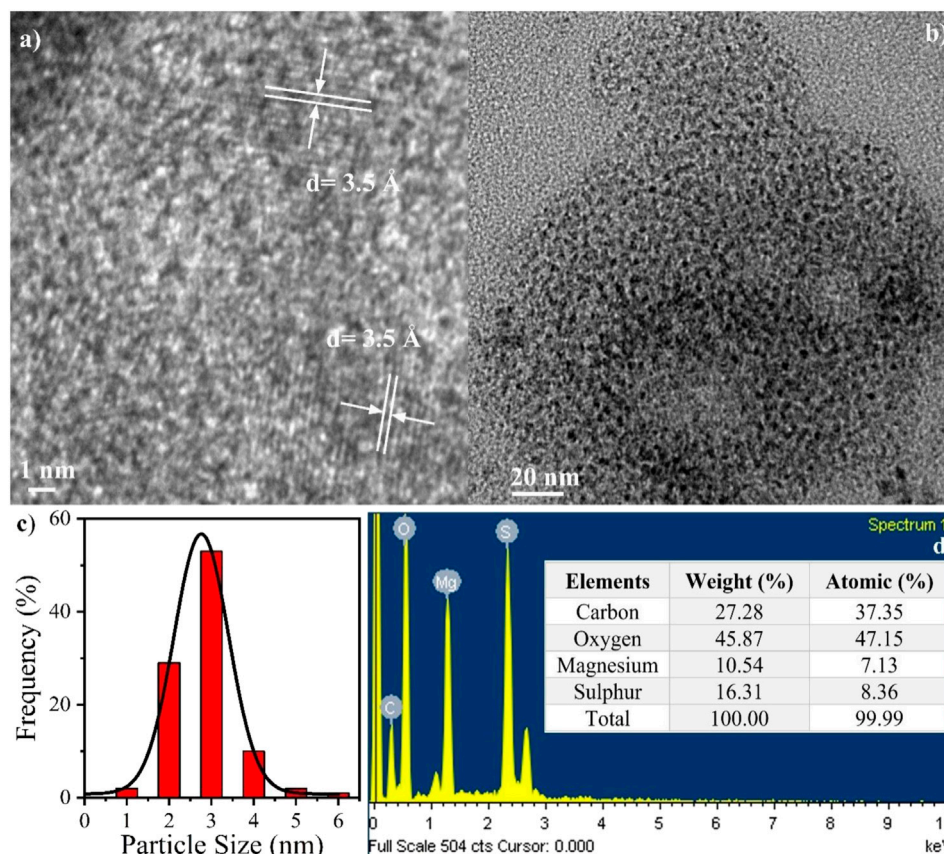
FIGURE 1 | (A) HR-TEM image, **(B)** TEM image, **(C)** size distribution bar plot fitted with Gaussian function, and **(D)** EDX results showing the constituent elements, and the inset Table shows the corresponding weight and atomic distribution.

and Fluorescence life-time decay was recorded in a commercial TCSPC setup FL-920 (Edinburgh Instruments) by exciting the samples at 375 nm using a picosecond diode laser (pulse width ~60 ps).

Synthesis of L-Cyst Capped MgS QDs

Magnesium nitrate [$Mg(NO_3)_2.H_2O$] (98.99%) powder and sodium sulfide pellets [Na_2S] (99.99) were mixed with L-Cysteine in various concentrations till the solution becomes transparent. This solution was placed in a hydrothermal teflon vessel and kept in a steel chamber for hydrothermal synthesis at 200°C for 4 h. The obtained solution was the first centrifuge for 30 min and then dialyzed overnight to remove the impurities.

RESULTS AND DISCUSSIONS

Transmission Electron Microscopy (TEM) Analysis

TEM study was carried out to observe the structure and the particle size of the synthesized QDs. **Figure 1A** shows the HR-TEM image of L-cyst-MgS-QDs. The d spacing calculated from the lattice fringes was found to be 3.5 Å. **Figure 1B** shows images of TEM of L-cyst-MgS-QDs showing uniformly distributed L-Cyst-MgS-QDs. It can be seen from the image that the L-cyst-MgS-QDs size is very small and monodispersed. The size of the QDs was calculated using a histogram and fitted with the gaussian function [**Figure 1C**] and obtained the average size ranging from 2 to 4 nm. TEM study shows that we have synthesized small size quantum dots with high surface area to volume ratio capped with L-Cysteine.
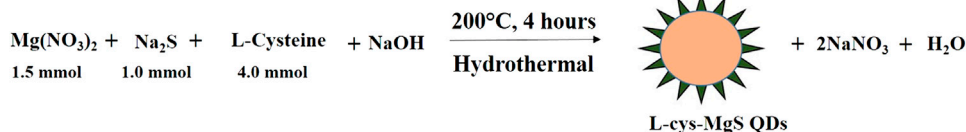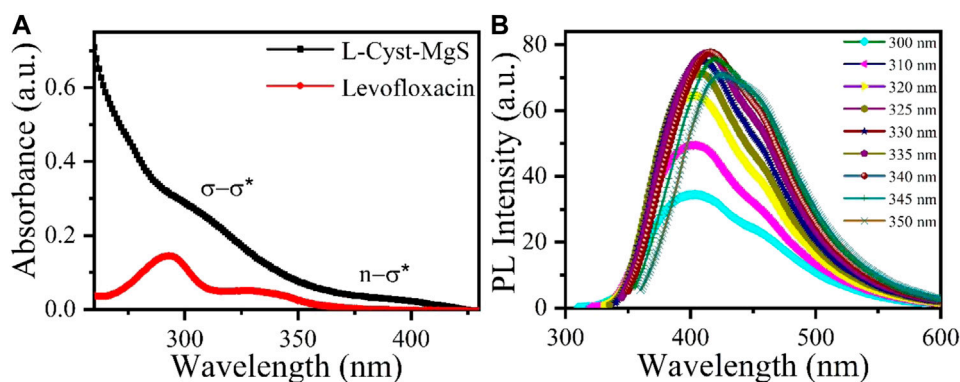
FIGURE 2 | (A) UV-Vis absorption spectra of L-Cyst-MgS-QDs and Levofloxacin and **(B)** shows the fluorescence spectra of L-Cyst-MgS-QDs for varying wavelengths.

Figure 1D shows EDX measurement to find the elemental composition. It can be seen from **Figure 1D** that the elemental composition of L-cyst-MgS-QDs consists of carbon, oxygen, magnesium, and sulfur (Sankararamakrishnan et al., 2019). Carbon and oxygen confirm the L-cysteine presence, while Mg and S confirm the presence of MgS. The inset of **Figure 1D** shows the Table for the elemental composition and their percentage by weight and atomic weight. It can be seen from the Table, the total weight and atomic of all the elements compose of L-cyst-MgS-QDs is 100 and 99.99%, respectively. This shows that the reaction was completed, and no residual precursor was left over after completing the reaction. Also, the atomic ratio of Mg and sulfur is nearly equal in the 1:1 ratio; results confirm the formation of L-cyst-MgS-QDs (Hu et al., 2010). TEM and EDX studies confirm the formation of pure and small size L-cyst-MgS-QDs without any impurity. These L-cyst-MgS-QDs were further studied using a UV-vis spectrometer and fluorescence spectrophotometer to study their optical properties.

UV-Vis Absorption Spectra and Fluorescence Study of L-Cyst-MgS-QDs

UV-VIS absorption spectrum and fluorescence emission spectra of L-Cyst-MgS QDs are shown in **Figure 2**. UV- vis absorption spectrum was recorded in the wavelength range of 270–430 nm. A small hump was obtained in L-Cyst-MgS QDs at a wavelength of 310 nm as shown in **Figure 2A**. The first peak hump around 320 nm is due to the σ - σ transition of an electron from sigma bond between Mg and S. The second hump at around 400 nm is due to the n-σ* transition due to lone pair electron of sulfur and sigma bond of Mg. The UV- vis absorption spectrum of Levofloxacin shows two peaks at 292 nm and 330 nm. Out of which broad peak at 292 nm indicate the n → π* transition while other peak at 330 nm shows the π → π* transition (Mat Amin et al., 2012). **Figure 2B** shows the fluorescence spectra obtained at different excitation wavelengths in the range of 260–360 nm. The fluorescence spectra were recorded for the varying excitation wavelengths of 300–350 nm. The highest emission was obtained at a wavelength of 410 nm for an excitation wavelength of 340 nm. These results indicate that L-Cyst-

MgS QDs is an excellent candidate to study antibiotics' interaction using fluorescence spectroscopy. The quantum yield of L-Cyst-MgS QDs was calculated against the reference (quinine sulfate) that's already known. The absorbance and photoluminescence (PL) spectrum of quinine sulfate were obtained using photometry at 340 nm. The quantum yield was found to be 2%.

Response Study of L-Cyst-MgS-QDs With Levofloxacin

L-Cyst-MgS-QDs were studied with thirteen antibiotics using fluorescence spectroscopy as shown in **Figure 3A**. The thirteen antibiotics are Thiamphenicol, Gentamicin, Erythromycin, Ofloxacin, Ampicillin, Ciprofloxacin, Tetracycline, Chloramphenicol, Florfenicol, Amoxicillin, Moxifloxacin, Norfloxacin and Levofloxacin. The experiment was performed by adding 200 μL of L-Cyst-MgS-QDs into a solution of 200 μL of each antibiotic (1 mg/ml) and 2.6 ml of DI and the responses were recorded. The area was calculated for each study and a bar graph was plotted to see the specific detection of the L-Cyst-MgS-QDs toward Levofloxacin. **Figure 3A** shows the area under the curve for the response of the fluorescence signal. The area under the curve for Levofloxacin is considerably higher than that of the other antibiotics. **Figures 3B,C** show the image of all the antibiotics under visible light and UV light, respectively. The most significant change in the intensity can be observed for Levofloxacin. These results demonstrate the high selectivity of L-Cyst-MgS-QDs toward Levofloxacin. **Figure 3B** shows the response study of the L-Cyst-MgS-QDs with varying Levofloxacin concentrations in the physiological range of 0–100 μg/ml. It can be seen from **Figure 3B** that with the increase in the Levofloxacin concentration, the peak corresponding to L-Cyst-MgS-QDs (410 nm) is decreasing; however, the peak corresponding to the Levofloxacin is increasing (480 nm). The inset of **Figure 3B** shows the calibration curve obtained using the area under the curve for each concentration and plotted against the Levofloxacin concentration. Good linearity of 0.95 was obtained from the linear fit of the experimental data. Also, from this curve, it can see that the linear range was obtained from 1 to 90 μg/ml. Using this linearity plot, the limit of detection (LOD) was found to be 0.21 μg/
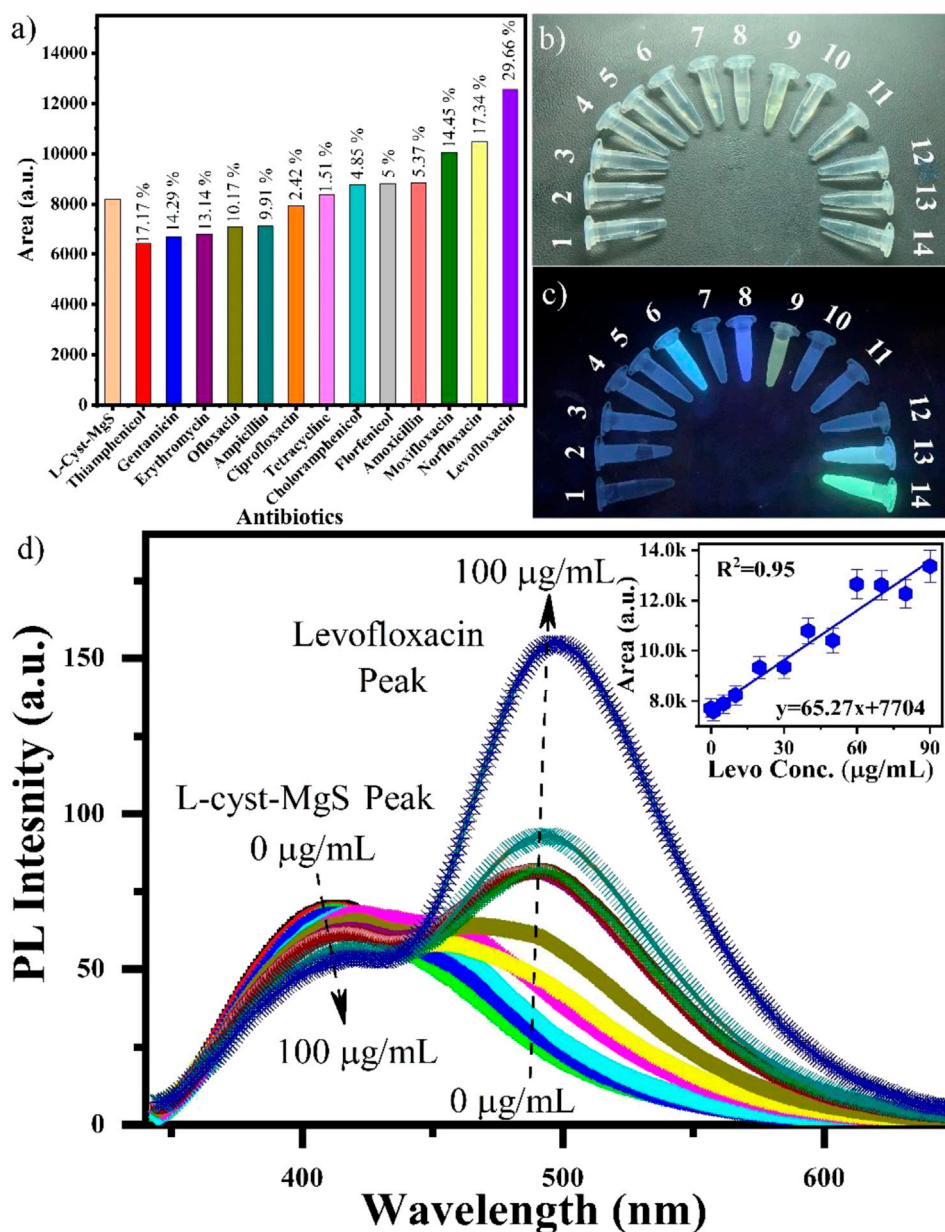
FIGURE 3 | (A) Selectivity study for L-cyst-MgS with thirteen antibiotics, photographic image of all the thirteen antibiotics 1: L-Cyst-MgS, 2: Thiamphenicol, 3: Gentamicin, 4: Erythromycin, 5: Ofloxacin, 6: Ampicillin, 7: Ciprofloxacin, 8: Tetracycline, 9: Chloramphenicol, 10: Florfenicol, 11: Amoxicillin, 12: Moxifloxacin, 13: Norfloxacin, and 14: Levofloxacin under **(B)** visible light, **(C)** UV light and **(D)** response study of L-cyst-MgS with Levofloxacin in the range of 0–100 g/ml concentrtion range. The inset shows the corresponding calibration curve.

ml. These studies suggest that L-Cyst-MgS-QDs is a suitable material for the detection of Levofloxacin.

FT-IR and TCSPC Studies of L-Cyst-MgS-QDs Interaction With Levofloxacin

Figure 4A shows the FT-IR study of L-Cyst-MgS-QDs and Levofloxacin. FTIR measurement was carried out in the wavenumber range between 400 and 4,000 cm^{-1}. **Figure 4A** represents the L-Cysteine capped MgS and having a well-resolved peak at 1,556 and 2,920 cm^{-1} are ascribed the asymmetric stretching vibration of COO- and anti-symmetric stretching of -CH$_2$. Considering the FTIR spectrum of pure L-Cysteine, the respective peak at 2,548 cm^{-1} corresponding to the stretching vibrations of S-H disappeared, resulting in the cleavage of the S-H bond formation of MgS bonds (Li et al., 2017). In **Figure 4B**, the symmetric stretching carboxylate (-COO-) peak of Levofloxacin was observed at 1,394 cm^{-1}, while in the case of L-Cys-MgS-Levo, this peak was shifted to 1,385 cm^{-1}, which suggests the binding of MgS with Levofloxacin (Qassim., 2015).

FIGURE 4 | (A) FT-IR spectra of (i) L-cysteine, (ii) L-cyst-MgS, (iii) Levofloxacin and (iv) L-cyst-MgS-levofloxacin; and **(B)** TCSPC plot for L-cyst-MgS and L-cyst-MgS-Levofloxacin.
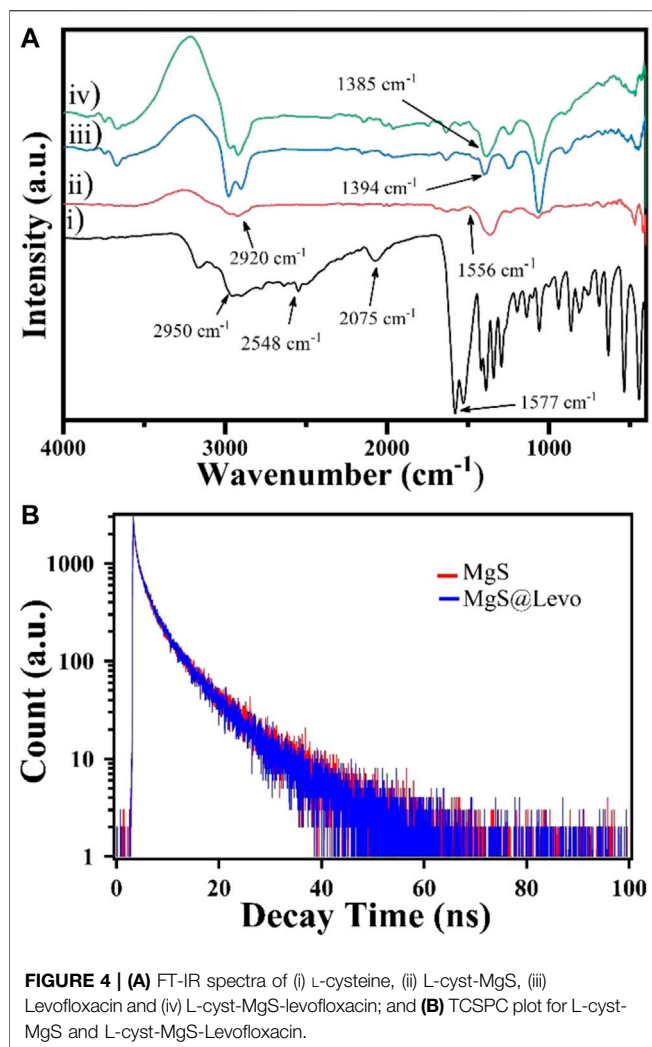
Figure 4B shows the time-resolved fluorescence plot of L-Cyst-MgS-QDs in the presence and absence of Levofloxacin and fitted with three exponential decay function, which is given below;

$$I(t) = a_1^* \exp\left(-\frac{t}{\tau_1}\right) + a_2^* \exp\left(-\frac{t}{\tau_2}\right) + a_3^* \exp\left(-\frac{t}{\tau_3}\right)$$

The calculated lifetime was obtained nearly 8.43 ns and 7.78 ns for MgS-QDs and Levofloxacin's presence, respectively, by three exponential decay functions. There is a little difference of lifetime among these two systems that showed no spectral overlap. So, there is no fluorescence resonance energy transfer process took place (Yan et al., 2015). From the plotted and calculated life-time data, it is clear that Levofloxacin is not quenching the fluorescence of MgS and this interaction between MgS and Levofloxacin takes place through the electron transfer process.

L-Cyst-MgS Levofloxacin Interaction Mechanism

While studying the UV-absorbance curve of Levofloxacin and L-Cyst-MgS-QDs, Levofloxacin's absorption band is much closer to the UV absorbance curve of L-Cyst-MgS-QDs, allowing the transfer of electron in the L-Cyst-MgS QDs to Levofloxacin. Moreover, time-resolved fluorescence measurement also showed no significant change in the fluorescence life-time of L-Cyst-MgS-QDs-LEVO and L-Cyst-MgS QDs, as shown in **Figure 4B**. This excludes the fluorescence resonance energy transfer mechanism (Yan et al., 2015). **Figures 5A,B** shows the deconvoluted PL spectra of L-cyst-MgS and L-cyst-MgS with 100 μg/ml Levofloxacin. The spectrum was deconvoluted using the Gaussian function, and in both the spectrum, two distinct peaks were obtained. These two peaks PL 1 and PL 2 in **Figure 5A** have been explained according to the band diagram of L-Cyst-MgS explained in **Figure 5C**. The PL 1 peak in L-cyst-MgS arises due to band edge transition of excited e-from conductance band to the valence band. The PL 2 peak in L-cyst-MgS appears due to the surface defect i.e., broadband transition (Pearson., 1963; Garimella et al., 2020). In the mixture of L-Cyst-MgS QDs and Levofloxacin solution, the Levofloxacin molecules tend to come close to the surface L-Cyst-MgS QDs with the help of hydrogen bonds. This bond forms among–NH_2 group of L-Cyst with the carbonyl group of Levofloxacin and similarly carboxylic group L-Cyst with a carboxylic group Levofloxacin as shown in **Figure 5E**. On the exposure of light at a fixed wavelength of 340 nm, the photoluminescence intensity successively decreased at 410 nm (band edge) and increased at 458 nm with the increasing concentration of Levofloxacin as shown in **Figure 3D**. It is because of the absorption of light at 340 nm by L-Cyst-MgS QDs, which create the electron and hole in the valence band and conduction band, respectively. The hole of MgS QDs has more tendency to trap Levofloxacin (electron-rich) because of the vicinity between MgS and Levofloxacin molecules *via* hydrogen bonding as shown in **Figures 5F,G**. Thus electron-hole recombination does not take place between them. As a result, the emission spectra of MgS become quenched as it was coming from 410 nm (PL1) and surface defect (PL2) (**Figure 5D**). At the same time, Levofloxacin molecules were also excited at 340 nm, which generated electron and hole in the valence band (VB) and conduction band (CB), respectively. And therefore, the electron in surface defect of MgS has an alternative route of recombination of electron-hole with HOMO (hole) of Levofloxacin. Thus, emission spectra were observed with enhanced PL intensity at 458 nm (PL3) (**Figure 5D**). The shifting in the PL spectra in **Figure 3D** is due to Levofloxacin's interaction with the MgS molecule as shown in **Figure 5G**. The above results indicate that electron transfer from the MgS-QDs to Levofloxacin is responsible for the increase in Levofloxacin and a slight decrease in the intensity of L-Cyst-MgS-QDs.

CONCLUSION

L-Cyst capped MgS QDS were synthesized using the hydrothermal method. TEM study showed that L-Cyst-MgS
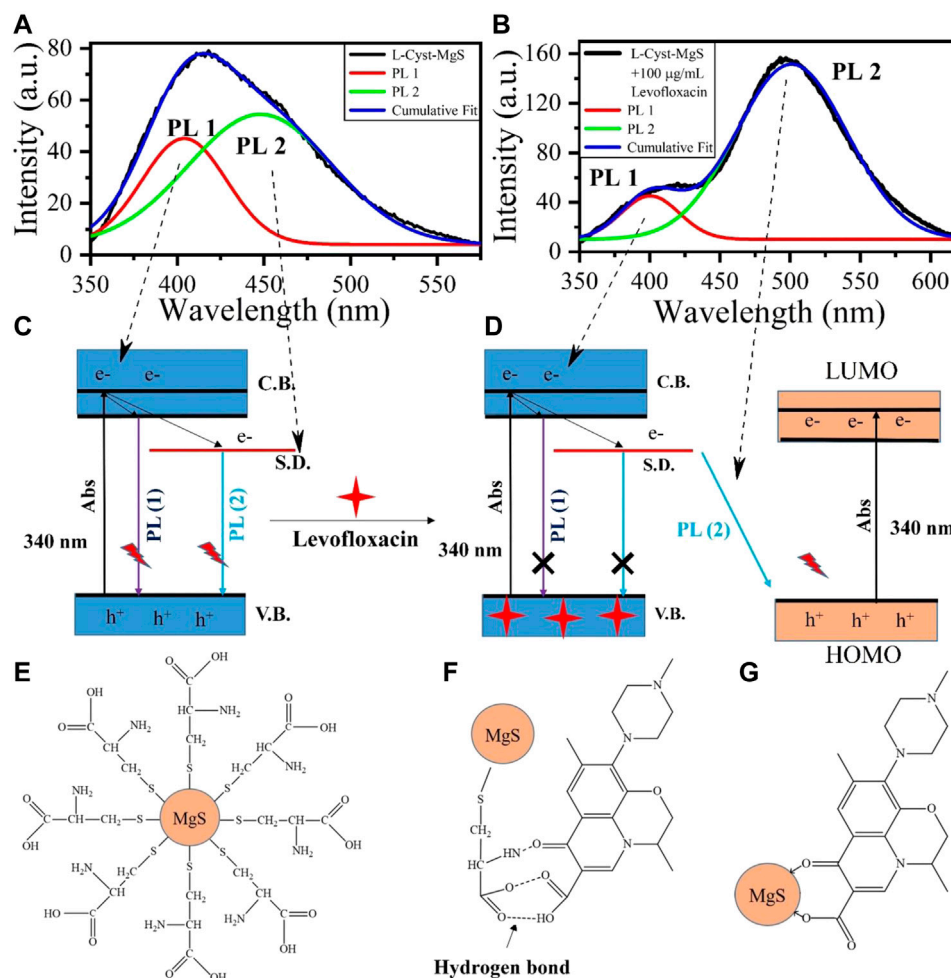
FIGURE 5 | L-Cyst-MgS interaction with Levofloxacin.

QDs have a size distribution from 2 to 4 nm and are very well dispersed. EDX study confirmed the completion of the reaction and formation of L-Cyst-MgS QDs without any impurity. UV absorbance study revealed maximum absorption in the range of 300–350 nm for L-Cyst-MgS. In the photoluminescence (PL) study, maximum emission was obtained at 410 nm for 340 nm of excitation for L-Cyst-MgS. Among Thiamphenicol, Gentamicin, Erythromycin, Ofloxacin, Ampicillin, Ciprofloxacin, Tetracycline, Chloramphenicol, Florfenicol, Amoxicillin, Moxifloxacin, Norfloxacin, Levofloxacin antibiotics, Levofloxacin showed the most significant change in PL spectra. Linear detection of Levofloxacin was obtained in the `range of 1–90 g/ml. The Time-resolved fluorescence spectroscopy showed identical lifetime for both the samples and no spectral overlap confirm the FRET free system. This was further confirmed using Fourier Transform infrared spectroscopy. The underlying mechanism can be explained based on the electron transfer from the conduction band of the L-Cyst-MgS QDs to the HOMO of Levofloxacin. The limit of detection (LOD) was found to be 0.21 μg/ml.

DATA AVAILABILITY STATEMENT

The raw data supporting the conclusions of this article will be provided after corresponding authors consent.

AUTHOR CONTRIBUTIONS

AK and PS have formulated the concept. ZH and TD have carried out the synthesis and characterization experiments. RK has helped in formulating the mechanism. JS helped in drafting the revised manuscript. AS and NC helped during measurements.

ACKNOWLEDGMENTS

India (34/13/2019-TF Nano/BMS), Government of India, for financial support. The authors also acknowledge the Advanced Instrument Research Facility (AIRF), JNU, New Delhi.

REFERENCES

Aarestrup, F. M., and Wegener, H. C. (1999). The effects of antibiotic usage in food animals on the development of antimicrobial resistance of importance for humans in Campylobacter and Escherichia coli. *Microb. Infect.* 1, 639–644. doi:10.1016/s1286-4579(99)80064-1

Adzitey, F. (2015). *Antibiotic classes and antibiotic susceptibility of bacterial isolates from selected poultry; a mini review*.

Alivisatos, A. P., Gu, W., and Larabell, C. (2005). Quantum dots as cellular probes. *Annu. Rev. Biomed. Eng.* 7, 55–76. doi:10.1146/annurev.bioeng.7.060804.100432

Bitas, D., and Samanidou, V. F. (2016). Effective cleanup for the determination of six quinolone residues in shrimp before HPLC with diode array detection in compliance with the European Union Decision 2002/657/EC. *J. Separ. Sci.* 39, 4805–4811. doi:10.1002/jssc.201600945

Bungau, S., Suciu, R., Bumbu, A., Cioca, G., and Tit, D. (2015). Study on hospital waste management in medical rehabilitation clinical hospital. *J. Environ. Prot. Ecol. Baile Felix.* 16, 980–987.

Cháfer-Pericás, C., Maquieira, Á., and Puchades, R. (2010). Fast screening methods to detect antibiotic residues in food samples. *Trac. Trends Anal. Chem.* 29, 1038–1049. doi:10.1016/j.trac.2010.06.004

Chauhan, R., Singh, J., Sachdev, T., Basu, T., and Malhotra, B. (2016). Recent advances in mycotoxins detection. *Biosens. Bioelectron.* 81, 532–545. doi:10.1016/j.bios.2016.03.004

Dai, T., Duan, J., Li, X., Xu, X., Shi, H., and Kang, W. (2017). Determination of sulfonamide residues in food by capillary zone electrophoresis with on-line chemiluminescence detection based on an Ag(III) complex. *Int. J. Mol. Sci.* 18, 1286. doi:10.3390/ijms18061286

Deng, F. Y., Huang, C. X., and Liu, Y. (2014). Determination of Levofloxacin in chicken tissue, manure and serum by self-ordered ring fluorescent microscopic imaging. *J. Anal. Chem.* 69, 283–289. doi:10.1134/s1061934814030046

Ferrone, V., Cotellese, R., Di Marco, L., Bacchi, S., Carlucci, M., Cichella, A., et al. (2017). Meropenem, Levofloxacin and linezolid in human plasma of critical care patients: a fast semi-automated micro-extraction by packed sorbent UHPLC-PDA method for their simultaneous determination. *J. Pharmaceut. Biomed. Anal.* 140, 266–273. doi:10.1016/j.jpba.2017.03.035

Garimella, L. B. V. S., Dhiman, T. K., Kumar, R., Singh, A. K., and Solanki, P. R. (2020). One-step synthesized ZnO np-based optical sensors for detection of aldicarb via a photoinduced electron transfer route. *ACS Omega* 5 (6), 2552–2560. doi:10.1021/acsomega.9b01987

Hu, J., Chen, Z., Chen, H., Chen, H., Song, Y., Sun, Y., et al. 2010). Single-crystal MgS nanotubes: synthesis and properties. *CrystEngComm* 12, 1286–1289. doi:10.1039/b919643a

Jang, M. G., Jang, M. D., and Park, J. (2017). Doxycycline as a new chiral selector in capillary electrophoresis. *J. Chromatogr. A* 1508, 176–181. doi:10.1016/j.chroma.2017.06.019

Ji, H., Wu, Y., Duan, Z., Yang, F., Yuan, H., and Xiao, D. (2017). Sensitive determination of sulfonamides in environmental water by capillary electrophoresis coupled with both silvering detection window and in-capillary optical fiber light-emitting diode-induced fluorescence detector. *Electrophoresis* 38, 452–459. doi:10.1002/elps.201600364

Kong, D., Xie, Z., Liu, L., Song, S., Kuang, H., and Xu, C. (2017). Development of ic-ELISA and lateral-flow immunochromatographic assay strip for the detection of vancomycin in raw milk and animal feed. *Food Agric. Immunol.* 28, 414–426. doi:10.1080/09540105.2017.1293014

Kujur, V. S., and Singh, S. (2020). Structural, magnetic, optical and photocatalytic properties of GaFeO3 nanoparticles synthesized via non-aqueous solvent-based sol–gel route. *J. Mater. Sci. Mater. Electron.* 31, 17633–17646. doi:10.1007/s10854-020-04318-2

Levy, S. B. (1978). Emergence of antibiotic-resistant bacteria in the intestinal flora of farm inhabitants. *J. Infect. Dis.* 137, 689–690. doi:10.1093/infdis/137.5.688

Li, L., Liao, L., Ding, Y., and Zeng, H. (2017). Dithizone-etched CdTe nanoparticles-based fluorescence sensor for the off-on detection of cadmium ion in aqueous media. *RSC Adv.* 7 (17), 10361–10368. doi:10.1039/c6ra24971j

Mahmood, A. R., Al-Haideri, H. H., and Hassan, F. M. (2019). *Detection of antibiotics in drinking water treatment plants in Baghdad City, Iraq.* Health: Advance Pub.

Martinez, J. L., Fajardo, A., Garmendia, L., Hernandez, A., Linares, J. F., Martínez-Solano, L., et al. (2008). A global view of antibiotic resistance. *FEMS Microbiol. Rev.* 33, 44–65. doi:10.1111/j.1574-6976.2008.00142.x

Martínez, J. L. (2008). Antibiotics and antibiotic resistance genes in natural environments. *Science* 321, 365–367. doi:10.1126/science.1159483

Mat Amin, K. A., Gilmore, K. J., Matic, J., Poon, S., Walker, M. J., Wilson, M. R., et al. (2012). Polyelectrolyte complex materials consisting of antibacterial and cell-supporting layers. *Macromol. Biosci.* 12 (3), 374–382. doi:10.1002/mabi.201100317

Pearson, R. G. (1963). Hard and soft acids and bases. *J. Am. Chem. Soc.* 85 (22), 3533–3539. doi:10.1021/ja00905a001

Pérez, R. A., Albero, B., Férriz, M., and Tadeo, J. L. (2017). Analysis of macrolide antibiotics in water by magnetic solid-phase extraction and liquid chromatography-tandem mass spectrometry. *J. Pharmaceut. Biomed. Anal.* 146, 79–85. doi:10.1016/j.jpba.2017.08.013

Qassim, A. W. (2015). Determination of Levofloxacin in pharmaceutical formulation tavanic by Visible spectrophotometry of its chelating complex with aluminum ion (iii). *Int. J. Dev. Res.* 5 (6), 4702–4706.

Sankararamakrishnan, N., Singh, R., and Srivastava, I. (2019). Performance of novel MgS doped cellulose nanofibres for Cd(II) removal from industrial effluent – mechanism and optimization. *Sci. Rep.* 9, 12639–12648. doi:10.1038/s41598-019-49076-2

Sarkar, T., Dhiman, T., Sajwan, R., Sri, S., and Solanki, P. R. (2020). Studies on carbon-quantum-dot-embedded iron oxide nanoparticles and their electrochemical response. *Nanotechnology* 31 (35), 355502. doi:10.1088/1361-6528/ab925e

Váradi, L., Luo, J. L., Hibbs, D. E., Perry, J. D., Anderson, R. J., Orenga, S., et al. (2017). Methods for the detection and identification of pathogenic bacteria: past, present, and future. *Chem. Soc. Rev.* 46, 4818–4832. doi:10.1039/c6cs00693k

Yadav, A. K., Dhiman, T. K., Lakshmi, G. B. V. S., Berlina, A. N., and Solanki, P. R. (2020). A highly sensitive label-free amperometric biosensor for norfloxacin detection based on chitosan-yttria nanocomposite. *Int. J. Biol. Macromol.* 151, 566–575. doi:10.1016/j.ijbiomac.2020.02.089

Yan, X., Li, H., Han, X., and Su, X. (2015). A ratiometric fluorescent quantum dots based biosensor for organophosphorus pesticides detection by inner-filter effect. *Biosens. Bioelectron.* 74, 277–283. doi:10.1016/j.bios.2015.06.020

Zhang, B., Xia, G., Chen, W., Gu, Q., Sun, D., and Yu, X. (2018). Controlled-size hollow magnesium sulfide nanocrystals anchored on graphene for advanced lithium storage. *ACS Nano* 12, 12741–12750. doi:10.1021/acsnano.8b07770

Assessment of Immunotoxicity and Oxidative Stress Induced by Zinc Selenium/Zinc Sulphide Quantum Dots

V. G. Reshma and P. V. Mohanan*

Biomedical Technology Wing, Sree Chitra Tirunal Institute for Medical Sciences and Technology, Trivandrum, Kerala, India

Although ZnSe/ZnS quantum dots (QDs) have emerged as apparently less hazardous substitute to cadmium-based QDs, their toxicity has not been fully understood. Huge levels of ROS production and associated difficulties comprise the underlying reason for nanomaterial toxicity in cells. This will cause both immunotoxicity and genotoxicity. In the current work, Zinc Selenium/Zinc Sulphide (ZnSe/ZnS) QDs was synthesized, characterized and analyzed for its role in oxidative stress induction in two cell lines (HepG2 and HEK) and Swiss Albino mice. ROS production and influence of catalase activity in ROS production measured by DCFHDA assay in both HepG2 and HEK cells after exposure to ZnSe/ZnS QDs. Assessment of nitrile radical formation carried out by griess reagent. Level of GSH is assessed as a marker for oxidative stress induced by QDs. Cell death induced after exposure to ZnSe/ZnS QDs investigated by Calcein AM-PI live dead assay. Apoptotic DNA ladder assay carried out for studying the potential of ZnSe/ZnS QDs to induce DNA fragmentation. *In vivo* bio-nano interaction was studied by exposing Swiss Albino mice to ZnSe/ZnS QDs via i.v. and i.p. injection. Antioxidant assays were carried out in brain and liver homogenates to study the oxidative stress. LPO, GSH, GPx, GR and SOD are considered as biomarkers for the stress analysis. Blood brain barrier (BBB) integrity also studied. Spleenocytes proliferation assay was carried out to study the immunotoxicity response. ZnSe/ZnS QDs do not induce visible oxidative stress upto a concentration of 50 μg/ml. Cell death occurs at higher concentration (100 μg/ml) caused by ROS production. Overall study apparently provide attentive information that ZnSe/ZnS QDs is not capable of eliciting any serious damages to liver and brain tissues which in turn substantiates its applicability in biomedical applications.

Keywords: oxidative stress, ROS production, genotoxicity, immunological responses, cadmium free QDs
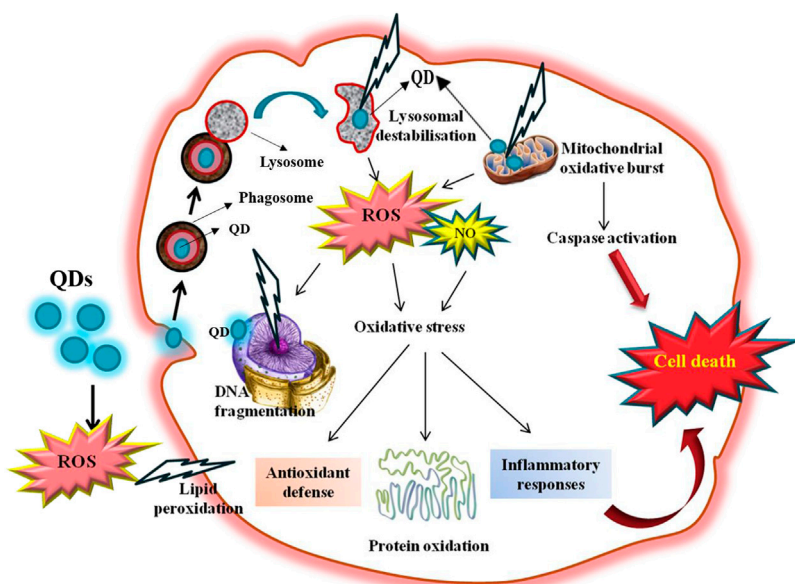
GRAPHICAL ABSTRACT |

INTRODUCTION

Quantum Dots (QDs) have attracted enough attention among researchers because of their wide ranging biomedical application potentials. This wide range application is due to the size-tunable, discrete fluorescence emission, tunable surfaceproperties, efficient luminescence along with their unique photostability behavior (Medintz et al., 2005; Michalet et al., 2005; Xing and Rao, 2008). They are used in the development of solar cells (Milliron et al., 2004; Pal et al., 2012) and light-emitting diodes (Mocatta et al., 2011) in the electrical field as well as in therapeutic delivery (Diagaradjane et al., 2008; Hu et al., 2010; Walker et al., 2012) and cellular imaging (Bagalkot et al., 2007; Hu et al., 2010.; Muthu et al., 2012). However, controversy on their safety concern exists. The mechanism behind the cytotoxicity induced by heavy metals containing QDs is well studied. The primary mechanism of cellular toxicity is widely been accepted as ionization of QDs and subsequent discharge of free Cd ions (Cd^{2+}) (Kirchner et al., 2005a; Kirchner et al., 2005b; Su et al., 2010). These ions will induce ROS formation (Zhao et al., 2010; Tang et al., 2013; Katsumiti et al., 2014) and following oxidative stress (Lovri et al., 2005; Lee et al., 2009; Li et al., 2009).

ROS is generally produced as a byproduct of cellular metabolic reactions. Upto a moderate level, they perform several obligatory roles in physiological processes. However, higher level exposure of ROS leads to oxidative stress, which further results in irreparable harm in cells and tissues. The imbalance in oxidative and antioxidative pool of molecules in body is termed as oxidative stress. The most sensitive biological targets for ROS are proteins, membrane lipids and DNA. ROS possess an inclination to give off or accept electrons as an attempt to reach stability; which generally exhibits shorter half-life than other reactive molecules. Two major categories of ROS are: free radicals and nonradicals. Free radicals contain one or more unpaired electrons which make the molecule reactive. When two free radicals share their unpaired electrons, it is termed as non-radicals. Physiologically significant three major ROS are superoxide anion ($\cdot O_2-$), hydroxyl radical ($\cdot OH$) and hydrogen peroxide (H_2O_2). An endogenous antioxidant system is present inside the body to neutralize the upshot of oxidative molecules in ROS induced oxidative stress. There are two categories of scavengers of antioxidant defense system, enzymatic and nonenzymatic. Superoxide dismutase (SOD), Catalase (CAT), Glutathione peroxidase (GPx) etc., are the enzymatic and Vitamin A, C, E, β-Carotene, Glutathione are the nonenzymatic antioxidants. Such antioxidants selectively combine with free radicals and cease their reactivity prior to the destruction of essential biomolecules. Oxidative stress-mediated by ROS formation is one of the dominant mechanisms of QDs induced cytotoxicity. Elucidation of the free radical mechanism is very difficult because of the direct detection is impossible as a result of their high reactivity and short-life period. The antioxidant-ROS equilibrium gets perturbed during oxidative stress due to either diminishing of antioxidants or buildup of ROS. Elevated levels of ROS leads to structural instability to DNA strand and further results in modification of biomolecules including proteins and lipids, onset of stress induced transcriptional pathways, immunomodulation as well as apoptosis (Birben et al., 2012). There are many reports on the impact of heavy metals containing QDs on ROS production and oxidative stress analyzed *in vitro* as well as *in vivo* senario. As many of the literature explains the impact of heavy metals containing QDs on ROS production and oxidative stress analyzed *in vitro* as well as *in vivo*. However, very fewer studies were carried out on the effect of

heavy metal-free ZnSe/ZnS QDs on ROS production and oxidative stress induction. In the present study, oxidative stress induced by ZnSe/ZnS QDs studied in HepG2 and HEK cell lines and also the effect in apoptosis by DNA laddering. In view of higher levels of antioxidative substances in liver and brain, present study addresses an investigation of oxidative stress markers in liver and brain of mice. QDs are widely exploited as theranostics of the brain because of their ability to cross the BBB. Here, the impact of ZnSe/ZnS QDs on BBB integrity is also studied. Effect of ZnSe/ZnS QDs on immunomodulation by splenocyte proliferation also carried out.

MATERIALS AND METHODS

Chemicals

High glucose (HG)-Dulbecco's Modified Eagles Medium (DMEM), fetal bovine serum (FBS), phosphate buffered saline (Ca^{2+}, Mg^{2+}free PBS), trypsin EDTA, antibiotic and antimycotic solution were purchased from Gibco, Grand Island, NY, United States. Histopaque, griess reagent, sodium hydroxide, L-glutathione (GSH) sodium dodecyl sulphate (SDS), thiobarbituric acid and tris base were obtained from Sigma Chemicals Co. Ltd. (St. Louis, MO, United States). 2,7-dichlorofluoresceindiacetate (DCFH-DA) was purchased from Molecular probes, Invitrogen, Carlsbad, CA, United States. Diluent for DNA extractionwas purchased from Hi-media Pvt. Ltd. India. Calcien AMand apoptotic DNA ladder kit was purchased from Thermo Fisher Scientific, United States. Folin's reagent was obtained from Merck, India. 3H-tritiated thymidine was obtained from American Radiolabelled Chemicals Inc, United States.

Assessment of Reactive Oxygen Species Formation by DCFHDA

Intracellular ROS can be detected using DCFH-DA (Dichloro dihydro fluorescein diacetate); the fluorimetric probe that enters the cell submissively. When this DCFH-DA reacts with ROS inside cells, it forms dichlorofluorescein (DCF); a highly fluorescent compound. 1×10^4 cells were seeded into each well of a 96 well plate and allowed to grow for 24 h. Various concentrations of ZnSe/ZnS QDs (12.5, 25, 50, and 100 μg/ml) were prepared in DMEM and exposed to incubated cells for 6 and 24 h. 0.09% hydrogen peroxide (H_2O_2) was used as a positive control. After media removal and PBS wash, cells were incubated with 100 μl of DCFH-DA (1 μM) for 45 min in the dark. 200 μl PBS was added to all wells followed by removal of DCFH-DA. Fluorescence was measured using a microplate reader (Plate Chameleon TMV, Hidex, Finland) using 450/535 nm excitation/emission respectively.

Influence of Catalase Activity on ROS Production

Impact of ZnSe/ZnS QDs on catalase activity of HepG2 cells on ZnSe/ZnS QDs induced ROS was assessed using a catalase inhibitor sodium azide (NaN_3). 1×10^4 cells/well were seeded into a 96 well plate and allowed to attach overnight. The cells were pre-incubated with 0.1 μM NaN_3 for 1 h. Cells were exposed with 12.5, 25, 50 and 100 μg/ml ZnSe/ZnS QDs. ROS production was estimated in the presence of DCFH-DA as described in section 3.13.15.1. The results were compared with that of cells exposed to QDs in the absence of catalase inhibitor.

Assessment of Nitrile Radical Formation by Griess Reagent

Griess reagent is used for the analysis of nitric oxide production in HepG2 cells. In brief, 1×10^4 cells were seeded per well of a 96 well plate and incubated overnight. Cells were then exposed to 12.5, 25, 50, and 100 μg/ml of ZnSe/ZnS QDs for 6 and 24 h. Half the volume of supernatant (50 μl/well) was taken out and allowed to react with 50 μl of Griess reagent for 10 min in dark at room temperature. The absorbance was read at 540 nm using a multiwell plate reader (Bio-Tek, Winooski, United States). A standard graph was prepared using sodium nitrate (0.5, 2.5, 5 and 7.5 μg/ml) and concentration of nitric oxide was calculated.

Assessment of Oxidative Stress Induced by QDs

Various concentrations of ZnSe/ZnS QDs were exposed to cells (6×10^6) in a 25 cm^2 culture flask for 24 h. After QD treatment, the cells were scraped off and washed with pre-cooled 1X phosphate buffered solution (1X PBS). Cell pellet thus obtained was lyzed using lysis buffer (20 mM Tris-HCl with pH 7.5, 150 mM NaCl and 1 mM Na_2EDTA, 1% Triton, 2.5 mM sodium pyrophosphate). The cells were centrifuged at 15,000 g for 10 min at 4°C. The cell extract (supernatant) was preserved on ice until the evaluation of oxidative stress biomarkers. Protein content was measured using Lowry's method (Lowry et al., 1951) with bovine serum albumin (BSA) as standard.

Protein Estimation

Cell lysis was carried out as mentioned in section 3.13.16.1. The total protein in the lysate was assessed by Lowry's method. This method has a sensitivity between 0.01–1 mg/ml and it relies on the reaction between Cu^{2+} ions generated from oxidative cleavage of peptide bonds and the Folin-Ciocalteu reagent. The experimental procedure is carried out as described in **Table 1** (a). Reading was taken at 660 nm using Lambda 25, UV/Vis spectrophotometer, Perkin Elmer, United States. The protein concentration is calculated from the standard graph (BSA as standard).

Glutathione Levels

Quantification of glutathione levels was done by the method proposed by Moron et al., 1979 using Ellman's reagent. The assay mixture contained 4 ml of 0.2 M phosphate buffer and 0.5 ml of cell extract (**Table 1** (c)) and 0.5 ml of 2 mM DTNB (5,5-dithio-bis-(2-nitrobenzoic acid). Measurement was obtained using Lambda 25, UV/Vis spectrophotometer, Perkin Elmer, United States at 412 nm. The amount of glutathione was expressed in terms of nmol glutathione/mg protein.

TABLE 1 | (a) Protein estimation by Lowry's method; Reaction mixture for (b) LPO assay (c) GSH level (d) GPx (e) GR (f) SOD activity estimation.

Reagent	Blank	Standard	Test
(a)			
Reagents	Blank		Test
Distilled water	1 ml		0.9 ml
Tissue homogenate	—		0.1 ml
Solution C	5 ml		5 ml
Incubate at room temperature for 10 min.			
Folin-Ciocalteu reagent	0.5 ml		0.5 ml
Incubate at dark for 30 min			
(b)			
0.2 M phosphate buffer (pH-8)	4 ml		4 ml
Tissue homogenate	—		0.5 ml
2 mM DTNB	0.5 ml		0.5 ml
Distilled water	0.5 ml		—
(c)			
0.8% TBA	1.5 ml		1.5 ml
8.1% SDS	0.2 ml		0.2 ml
20% acetic acid	1.5 ml		1.5 ml
Tissue homogenate	—		0.2 ml
Distilled water	1.0 ml		0.8 ml
Incubate in water bath at 90 °C for 1 h			
Distilled water	1 ml		1 ml
Centrifuge at 3,500 rpm for 10 min			
(d)			
0.1 M phosphate buffer (pH-7)			0.4 ml
Sodium azide			0.1 ml
EDTA			0.1 ml
Tissue homogenate			0.1 ml
Hydrogen peroxide			0.1 ml
Distilled water	1 ml		1 ml
4 mM GSH			0.2 ml
Incubate at 37°C for 0, 90 and 180 s for each group of test			
10% TCA			0.5 ml
Centrifuge at 3500 rpm for 5 min at 4°C. Collect the supernatant			
Supernatant			1 ml
0.3 M phosphate solution	4 ml		4 ml
0.6 mM DTNB	0.5 ml		0.5 ml
(e)			
0.1 M phosphate buffer (pH-7.6)	2.1 ml		2 ml
0.5 mM EDTA	0.5 ml		0.5 ml
20 mM oxidized glutathione	0.15 ml		0.15 ml
Incubate at 37°C for 10 min			
2 mM NADPH	0.15 ml		0.15 ml
Tissue homogenate	—		0.1 ml
(f)			
Reagent	Blank	Standard	Test
0.1 M Tris buffer (pH-8.2)	3.1 ml	2.6 ml	2.5 ml
1 mM EDTA	0.1 ml	0.1 ml	0.1 ml
1 mM DTPA	0.5 ml	0.5 ml	0.5 ml
Tissue homogenate	—	—	0.1 ml
Pyrogallol	—	0.5 ml	0.5 ml

DNA Ladder Assay

Inter-nucleosomal DNA fragmentation is one of the characteristics of apoptosis and was carried out by activated nuclease. 3×10^6 cells were cultured in T25 flasks at 37°C for overnight. The cells were subsequently treated with 12.5, 25, 50 and 100 µg/ml of ZnSe/ZnS QDs for 24 h. DNA ladder assay was performed as per the manufacturer's instructions using Quick Apoptotic DNA ladder detection kit. After exposure, cell pellets were obtained and washed well with PBS. 35 µl of TE lysis buffer and 5 µl Enzyme A were used to lyse cells and incubated for 10 min in water bath at 37°C. Enzyme B solution was added and incubated for 30 min at 50°C. DNA was then precipitated using Ammonium acetate solution and absolute ethanol at −20°C. This mixture was centrifuged at 12,000 rpm for 10 min and the cell pellet was obtained. The pellet was air dried for 10 min and resuspended in 30 µl DNA suspension buffer. DNA was loaded on to 1.2% agarose gel provided with 0.5 µg/ml ethidium bromide in 1X TBE (Tris/Borate/EDTA) running buffer and run at 5 V/cm for 1–2 h. DNA bands were visualized using a transilluminator (Bio Imaging system, Syngene, United Kingdom).

Live Dead Assay by Calcien AM-PI

1×10^6 cells were seeded into each well of a 96 well plate and allowed to attach overnight.

Different concentrations of ZnSe/ZnS QDs (12.5, 25, 50 and 100 µg/ml) were added to cells and incubated for 6 and 24 h. Harvested cells were then washed with PBS and treated with calcein AM (1 µg/ml) for 45 min in dark. After centrifugation, these cells were resuspended in 500 µl PBS containing 0.25 µl of PI and kept for 5 min in dark. These cells were subjected to flow cytometric analysis a using flow cytometer (DAKO GALAXY, Germany) with 630 nm long pass filter.

Effects of ZnSe/ZnS QDs on Antioxidant Capacities of the Liver and Brain

A portion of liver and brain collected from the treated and untreated mice after euthanization and were subjected to estimate the antioxidant levels as mentioned below.

Sample Preparation

Liver and brain were collected at the end of 3, 7 and 14 days after exposure of ZnSe/ZnS QDs in mice. The isolated organs were washed in saline and transferred to a container kept on ice. Tissue homogenate (10%) was prepared in 0.1 M phosphate buffer (pH 7.4) by keeping the samples on ice. The tissue was homogenized at 1,000 rpm using tissue homogeniser, Polytron P 3100 (Switzerland). The supernatant of the homogenate was collected after centrifugation at 3,500 rpm for 10 min at 4°C. The supernatant was maintained on ice for further use.

Total Protein Estimation

Amount of total protein in tissue homogenate was assessed by Lowry's method. This method based on the reaction between Folin-Ciocalteu reagent and copper ions released from protein linkages. This method is sensitive down to a range of 10 µg/ml. Incubation time and pH is very crucial for getting the reproducible data. The experimental procedure is as described in **Table 1** (a). Solution C described in the table was prepared by mixing 50 ml solution of sodium carbonate (1 g in 50 ml distilled water) and 1 ml solution of sodium potassium tartarate (10 mg) and 5 mg copper sulphate. Reading was taken at 660 nm using Lambda 25, UV/Vis spectrophotometer, Perkin Elmer, United States. The protein

concentration is calculated from the bovine serum albumin (BSA) standard graph.

Lipid Peroxidation

Oxidative damage occurring in lipids was assessed based on malonedialdehyde (MDA) level; released as a byproduct of lipid peroxidation (LPO). The method was adopted from the protocol proposed by Ohkawa et al., 1979. Detailed experimental procedure given in the **Table 1** (b). Final pink colored solution formed from the reaction between thiobarbituric acid and MDA was subjected to spectrophotometer analysis (Lambda 25, UV/Vis spectrophotometer, Perkin Elmer, United States) at 532 nm.

Reduced Glutathione (GSH)

Moron et al., 1979 developed a method for detecting the GSH level in the cells. Yellow colored product formed from reaction between GSH and DTNB [5, 5′-dithiobis-(2-nitrobenzoic acid)) was detected spectrophotometrically at 412 nm using Lambda 25, UV/Vis spectrophotometer, Perkin Elmer, United States. Detailed experimental procedure given in the **Table 1** (c).

Glutathione Peroxidase

Rotruck et al., 1973 developed a method for the detection of GPx. GPx is an enzyme family that induces the oxidation of GSH to form GSSG in the presence of H_2O_2 with water as the by-product i.e. $2GSH + H_2O_2 \rightarrow GS\text{-}SG + 2H_2O$. Spectrophotometer (Lambda 25, UV/Vis spectrophotometer, Perkin Elmer, United States) was used to obtain reading at 412 nm. Each step of the procedure is given in **Table 1** (d).

Glutathione Reductase

GR converts GSSH back to GSH in the presence of NADPH. The method was developed by Mize and Langdon., 1962. The reaction contents are given in **Table 1** (e). The reading was taken at 0, 1, 2 and 3 min at a wavelength of 340 nm (Lambda 25, UV/Vis spectrophotometer, Perkin Elmer, United States).

Superoxide Dismutase

SOD assay was carried out in liver and brain homogenate using modified pyrogallol auto oxidation method developed by Marklund and Marklund., 1974. Reading was taken at 420 nm (Lambda 25, UV/Vis spectrophotometer, Perkin Elmer, United States) immediately after the addition of pyrogallol at 0, 1, 2 and 3 min. Detailed procedure is given in **Table 1** (f).

Blood Brain Barrier Integrity

Break down of blood brain barrier leads to water influx and concomitant increase in water content. The protocol was proposed by Yang et al., 2015 was followed to estimate the brain water content. Mice were exposed to ZnSe/ZnS QDs at a dosage of 10 mg/kg body weight. At the end of 3, 7 and 14 days, brain was collected carefully and wet weight was noted. Brain samples were dried at 110°C for 24 h prior to take dry weight. The brain water content was calculated as: Percentage water content = (wet weight-dry weight)/wet weight × 100%.

Immunotoxicity by Splenocyte Proliferation Assay

Immunotoxicity of ZnSe/ZnS QDs assessed by the splenocyte proliferation assay. The splenocytes of animals isolated after each observation period. Spleen was transferred to cold PBS containing antibiotic/antimicotics and was placed on a metallic cell strainer kept over 10 mm petridish under sterile condition. Spleen was mashed by softly teasing it over the metallic cell strainer. The single cell suspension was kept carefully over histopaque and centrifuged at 1,500 rpm for a time period of 40 min. The cells present in the resulting buffy coat were isolated and washed three times with PBS. 2×10^5 cells/well in DMEM medium supplemented with 10% FBS were cultured for the experiment. After 48 h, 0.5 μCi of tritiated thymidine was added to each well and incubated for 24 h. Later, Trichloroacetic acid (5% solution) was used for cell fixation and SDS/NaOH lysis buffer was used to cell lysis. Then, scintillation fluid was added and Scintillation counter (Hidex, Finland) was used to find the radioactivity. The values were expressed as mean ± SD of counts per minute (CPM).

RESULTS

Assessment of ROS Formation by DCFHDA

Intracellular ROS production is one among the very primary responses happening in account of nanoparticle toxicity and DCFHDA was used for its measurement. The results are expressed in relative fluorescence intensity (RFU) (**Figure 1A**). None of the ZnSe/ZnS QDs treated group exhibited statistically significant increase in ROS formation in HepG2 cells (12.5 μg/ml: 102.15 ± 28.01, 25 μg/ml: 102.54 ± 16.7, 50 μg/ml: 105.44 ± 23, 100 μg/ml: 106.81 ± 30.2) at 6 h. The ROS formation after 24 h exposure was (12.5 μg/ml: 99.32 ± 24.24, 25 μg/ml: 106.15 ± 28.2, 50 μg/ml: 118.23 ± 13.19, 100 μg/ml: 129.09 ± 42.93). In case of HEK cells, significant increase (25%) in DCF fluorescence can be seen only at 100 μg/ml concentrations at 6 h. ROS production was comparable with the control cells in all other groups (**Figure 1B**). Cells exposed to H_2O_2 were kept as positive control. The values are stated in fluorescence (%) in comparison with control. The data denote mean ± SD from three independent tests.

Influence of Catalase Activity on ROS Production

Catalase enzyme is an important enzyme in protecting the cells from oxidative damage by ROS. It is present inside the cells which convert hydrogen peroxides into water and oxygen. The activity of catalase neutralize H_2O_2 generated in hepatocytes. **Figure 1C** shows effect of catalase activity on ROS production in HepG2 cells exposed to ZnSe/ZnS QDs at 6 h and **Figure 2D** shows the effect of 24 h exposure. HepG2 cells exhibited high ROS production compared to control cells only at two concentrations (50 μg/ml and 100 μg/ml for 24 h exposure) (**Figure 1D**) when pre-treated with catalase inhibitor (NaN_3). In all other case, ROS production is almost same in both
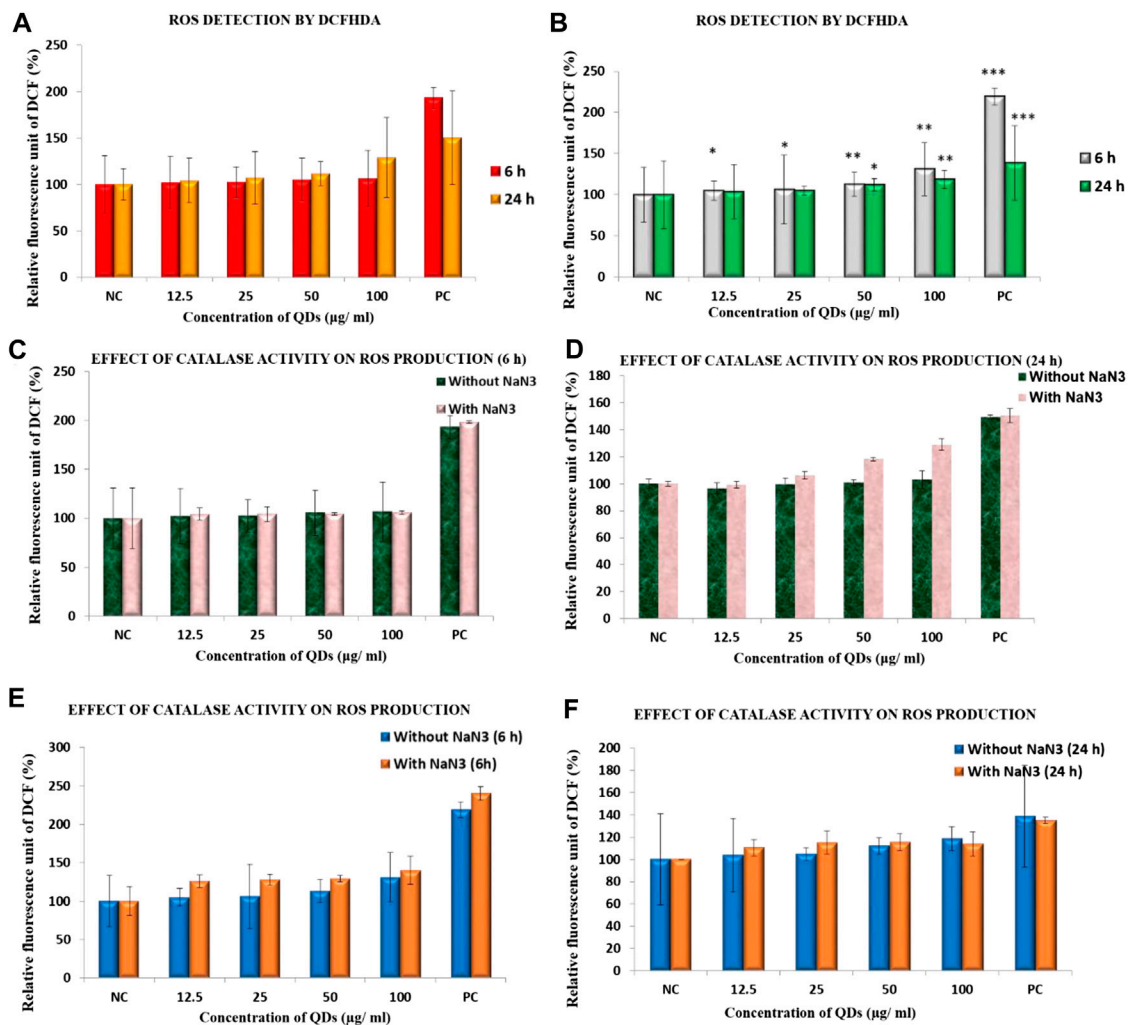
FIGURE 1 | ROS production in **(A)** HepG2 cells **(B)** HEK cells exposed to ZnSe/ZnS QDs at6 and 24 h using DCFH-DA. Effect of catalase activity on ROS production in HepG2 cells at **(C)** 6 h **(D)** 24 h and in HEK cells at **(E)** 6 h **(F)** 24 h exposure to ZnSe/ZnS QDs(*$p < 0.05$, **$p < 0.01$).

conditions (with and without NaN_3). HEK cells exhibited more or less same level of ROS production compared to control cellswhen pre-treated with catalase inhibitor (NaN_3) at 6 (**Figure 1E**) and 24 h (**Figure 1F**).

Assessment of Nitrile Radical Formation by Griess Reagent

RNS production in HepG2 and HEK cells onexposure to ZnSe/ZnS QDs was estimated with the help of Griess reagent assay. Only positive control cells which were treated with LPS showed a statistically significant rise in amount of RNS generated. The comparison was done with the negative control (cells alone). However, ZnSe/ZnS QDs did not induce RNS production in both the cells. The values obtained were almost comparable in case of negative and treated groups (**Figures 2B,D** represents nitrite production standard graph).

Assessment of Oxidative Stress Induced by QDs
Protein Estimation

Protein in HepG2 cells estimated by Lowry's method. Control cells containing 0.951 ± 0.001 mg protein. Compared to control cells, ZnSe/ZnS QDs treated HepG2 cells contains 0.896 ± 0.002 (12.5 μg/ml), 0.871 ± 0.01 (25 μg/ml), 0.823 ± 0.02 (50 μg/ml) and 0.710 ± 0.001 (100 μg/ml). Protein concentration in HEK cells upon treatment with QDs of various concentrations was estimated and found to be 0.586 ± 0.015, 0.551 ± 0.008, 0.535 ± 0.006, 0.523 ± 0.011 respectively when compared to control (0.620 ± 0.002) (**Figures 3A,B**).

Glutathione Levels

GSH level in HepG2 cells significantly increased with increased concentration of QDs when compared to control at 24 h. **Figure 3C** showed that GSH level in cells with QDs
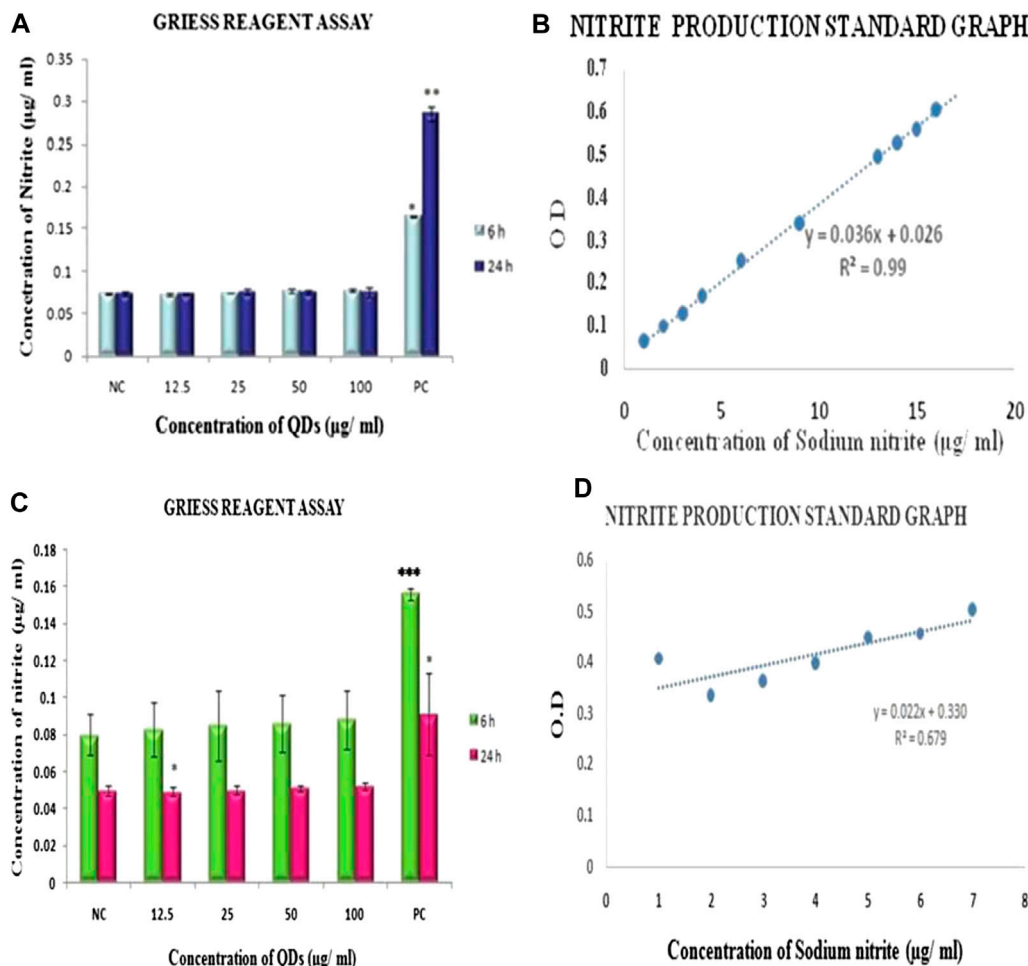
FIGURE 2 | Evaluation of RNS generation by Griess reagent assay showing nitrite production in **(A)**. HepG2 cells **(C)** HEK exposed to ZnSe/ZnS QDs for 6 and 24 h. Samples exposed with LPS served as positive control. Nitrite production standard graph **(B)** HepG2 **(D)** HEK. Reading of three independent experiments are represented as mean ± SD. Asterisk indicates statistically significant difference (*$p < 0.05$, **$p < 001$).

concentrations of 12.5, 25, 50 and 100 µg/ml were 1.826 ± 0.017, 1.722 ± 0.183, 1.844 ± 0.147, 1.403 ± 0.123 respectively. In HEK cells also GSH level was significantly increased as concentration of QDs increased upto 50 µg/ml. Upon 100 µg/ml of QDs concentration, GSH level decreased compared to that of control. The level of GSH was 1.847 ± 0.20, 2.09 ± 0.21, 2.113 ± 0.218, 1.014 ± 0.225 at 12.5, 25, 50, 100 µg/ml correspondingly (**Figure 3D**).

DNA Ladder Assay
DNA ladder or smear patterns formation was not evident in any of the treated groups of both HepG2 and HEK cells. Both control and treatment samples exhibited a thick band of unfragmented DNA of more than 10,000 bp size with no laddering (**Figures 4A,B**).

Live Dead Assay by Calcien AM-PI
Live dead assay of HepG2 cells upon QDs treatment was carried out by flow cytometry study using Calcein AM-PI staining.

However, the cells treated with 12.5, 25, 50 and 100 µg/ml of ZnSe/ZnS QDs at 24 h showed 91.21, 88.96, 84.30 and 50.80% viable cells (**Figures 5A–D**). **Figure 5E** shows graphical representation of flow cytometric analysis. Results of the HEK cells live dead assay were shown in **Figure 6**. The results suggest that 0.28, 3.27, 3.90, 13.66% live cells and 9.08, 24.93, 28.57, 41.32% dead cells were found after treatment at various concentrations (12.5, 25, 50 and 100 µg/ml) of ZnSe/ZnS QDs on HEK cells. **Figure 6F** shows graphical representation of flow cytometric analysis data.

Effects of ZnSe/ZnS QDs on the Antioxidant Capacities of the Liver and Brain
Liver and brain tissues were collected from mice injected (both i.v and i.p) with ZnSe/ZnS QDs. All the assays were carried out in 10% liver and brain homogenate. The lipid peroxidation, GSH, GR, GPx and SODs were analyzed for antioxidant assays.
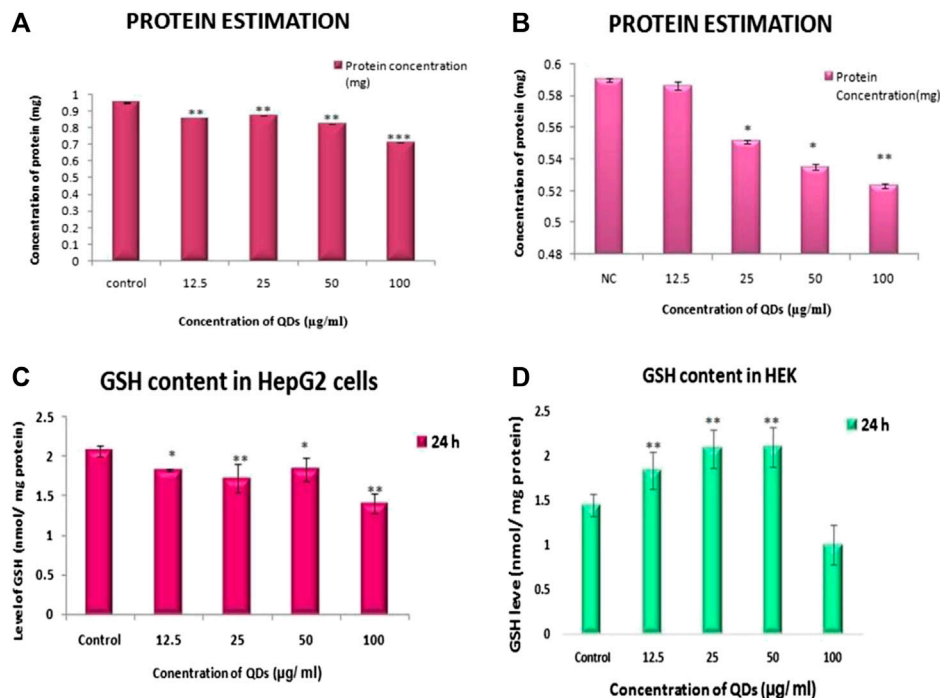
FIGURE 3 | Protein level in **(A)** HepG2 **(B)** HEK cells and GSH level in **(C)** HepG2 cells **(D)** HEK cells after ZnSe/ZnS QDs exposure at 24 h.

Lipid Peroxidation

Lipid peroxidation is predicted by the amount of malondialdehyde formed. Statistically significant increase in malondialdehyde (MDA) was found in the liver of ZnSe/ZnS QDs exposed mice. The results are demonstrated in **Figure 7A**. Similarly MDA production in brain was increased significantly on 3rd and 7th day of treatment and normalized on 14th day. The results are demonstrated in **Figure 7B**.

Reduced Glutathione

The amount of GSH was altered in QD exposed animals when related to control animals. A statistically significant reduction in GSH levels of liver was observed at 3rd, 7th and 14th day of observation period (**Figure 7C**). In brain the GSH level was found to decrease on 3rd, 7th and 14th day when compared to control in both i.v and i.p treated mice (**Figure 7D**).
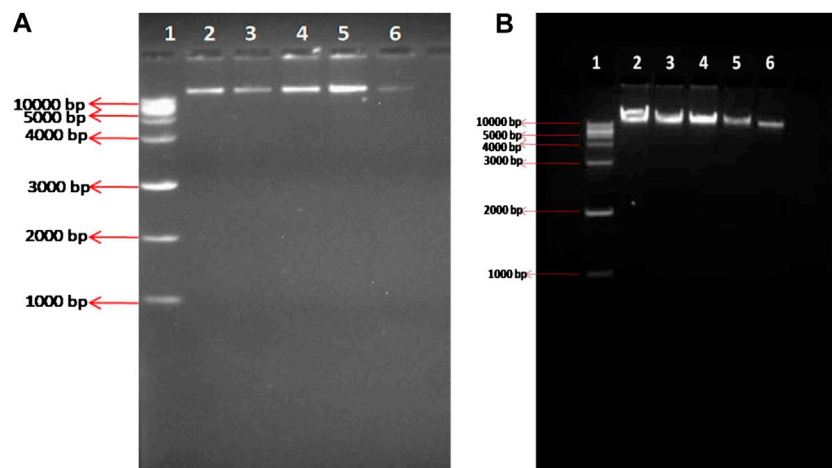
FIGURE 4 | DNA ladder assay of **(A)** HepG2 cells **(B)** HEK cells- Lane 1: Marker DNA, lane 2: Control, Lane 3: 12.5 μg/ml ZnSe/ZnS QDs, Lane 4: 25 μg/ml ZnSe/ZnS QDs, Lane 5: 50 μg/ml ZnSe/ZnS QDs, Lane 6: 100 μg/ml ZnSe/ZnS QDs. Markings shown in left side of the figure represent corresponding base pairs (bp) of DNA markers.
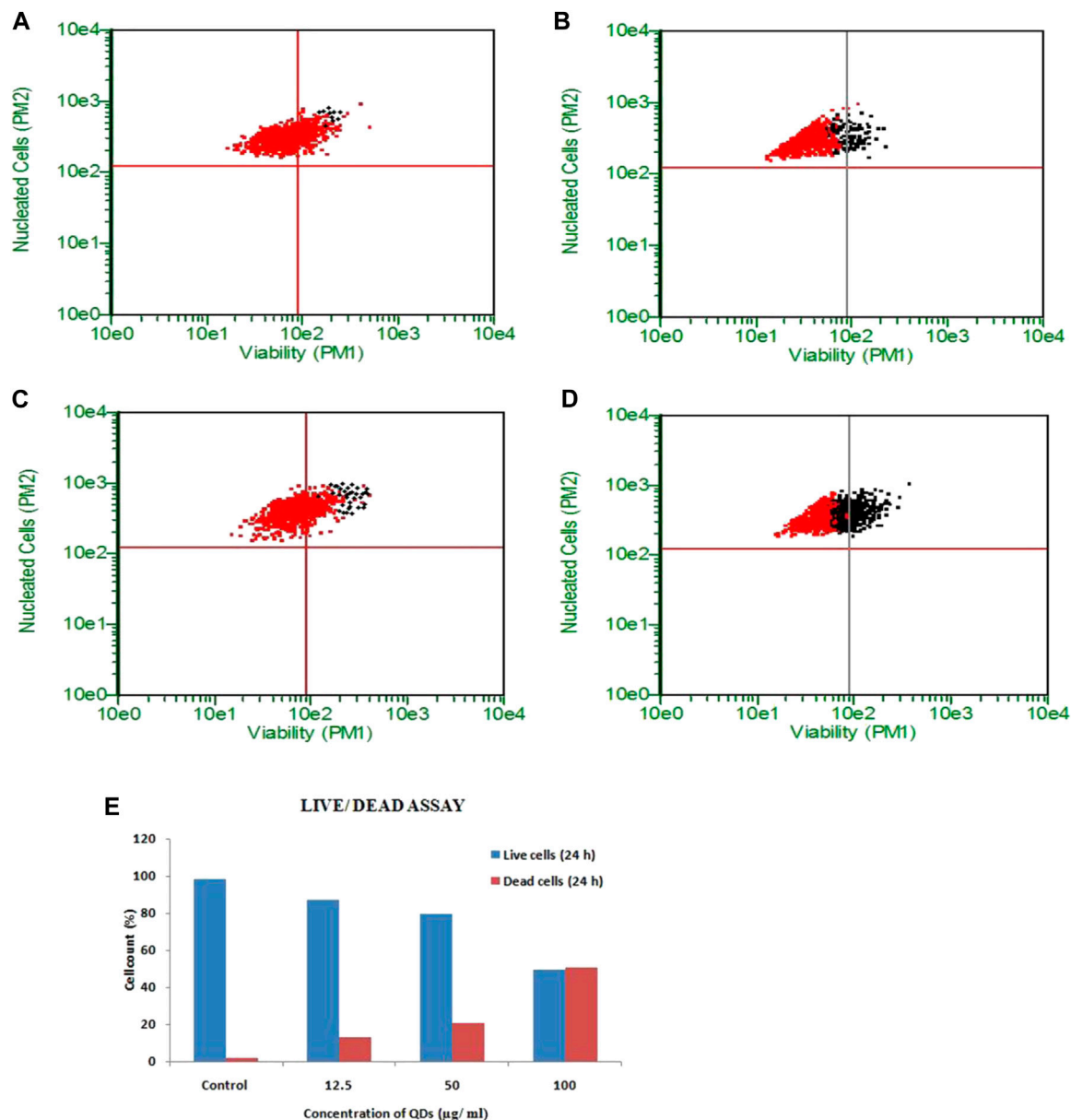
FIGURE 5 | ZnSe/ZnS QDs induced death in HepG2 cells: a-c Flow cytometric evaluation of Calcein AM stained cells. Black dots represent cells undergoing apoptosis and red dots represent live cells. **(A)** untreated cells, **(B)** 12.5 µg/ml, **(C)** 50 µg/ml, **(D)** 100 µg/ml ZnSe/ZnS QDs treated cells after 24 h. **(E)** Graph showing percentage of viable and dead cells at different concentrations of ZnSe/ZnS QDs (12.5, 50 and 100 µg/ml) after 24 h.

Glutathione Peroxidase

Figure 7E shows a statistically significant increase in GPx activity in liver on 7th day post exposure. This increase in activity was normalized on 14th day of observation period. It was observed that an increase in GPx level in brain was found at the end of 3rd day (i.v:0.052 ± 0.006, i.p: 0.106 ± 0.009) and 7th Day (i.v: 0.014 ± 0.004, i.p: 0.106 ± 0.04). The increased level of GPx was found to be normal at the end of 14 days (i.v: 0.053 ± 0.01, i.p: 0.08 ± 0.059). The increase was not statistically significant (**Figure 7F**).

Glutathione Reductase

GR activity in the liver (i.v) was lowered when correlated to the QD unexposed animals. A statistically significant increase in GR activity was found in the liver of treated animals on 3rd day and gradually decreased on the 7th and 14th days of observation of i.p treated mice (**Figure 7G**). A statistically significant rise in the GR activity was observed in the brain of ZnSe/ZnS QDs exposed mice on 3rd (i.v: 1.263 ± 0.522, i.p: 0.941 ± 0.0821), 7th (i.v: 0.971 ± 0.103, i.p: 0.89 ± 0.016) and 14th day (i.v: 1.062 ± 0.061, i.p: 0.857 ± 0.015) of observation (**Figure 7H**).
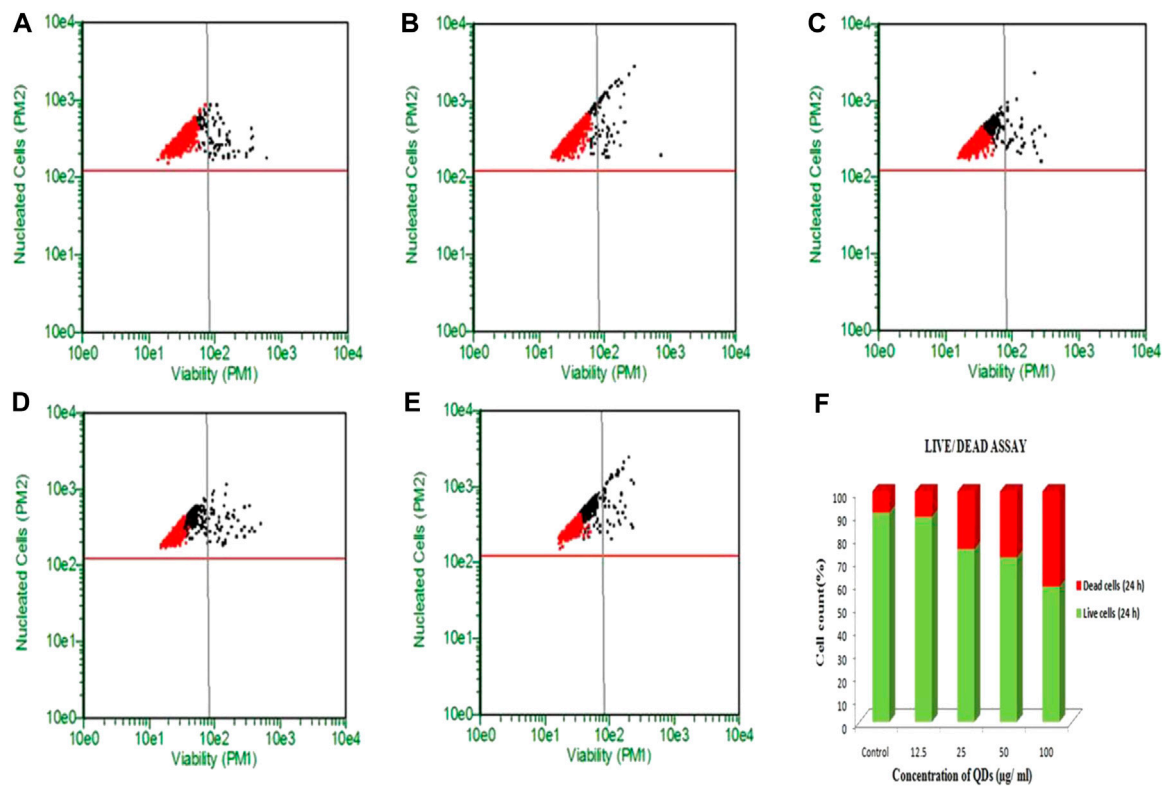
FIGURE 6 | ZnSe/ZnS QDs induced death in HEK cells: A-C Flow cytometric analysis of Calcein AM stained cells. Black dots represent apoptotic cells and red dots represent viable cells. **(A)** untreated cells, **(B)** 12.5 μg/ml **(C)** 25 μg/ml **(D)** 50 μg/ml **(E)** 100 μg/ml ZnSe/ZnS QDs treated cells. **(F)** Graph representing percentage of viable and dead cells at different concentrations of ZnSe/ZnS QDs (5, 25, 50 and 100 μg/ml) after 6 h **(I)** and 24 h (II).

Superoxide Dismutase

A statistically significant drop in SOD activity was observed in liver of both i.v and i.p treated animals when compared to control (**Figure 7I**). An increased SOD activity was observed in the brain of ZnSe/ZnS QDs exposed mice on 3rd day (i.v: 0.181 ± 0.002, i.p: 0.259 ± 0.001) and 7th day (i.v: 0.224 ± 0.002, i.p: 0.228 ± 0.003). SOD level decreasedon 14th day (i.v: 0.053 ± 0.01, i.p: 0.358 ± 0.136) when compared with control mice (0.0172 ± 0.007). The decrease in SOD level was not statistically significant (**Figure 7J**).

Blood-Brain BarrierIntegrity

Figure 8 displays the change in brain volume of mice injected with ZnSe/ZnS QDs in i.v. and i.p. administration. There was no evidence of brain volume change in i.v or i.p injected animals.

Immunotoxicity by Splenocyte Proliferation Assay

Splenocytes proliferation assay was carried out in spleen isolated from the treated mice using tritiated thymidine. It measures lymphocyte activation and cell-mediated immune responses. The result of the study suggests that splenocytes proliferation rate is increased on 3rd day and decreased on subsequent days and become normal at the end of 14 days (**Figure 8**).

DISCUSSION

Activation of immune cells like macrophages and neutrophils occurs as a result of cellular internalization of NPs, and oxidative stress persists over longer time periods contributing to ROS/RNS production (Risom et al., 2005; Huang et al., 2010). Macrophages plays responsible role in providing innate and adaptive immunity. M1 macrophages metabolize arginine to produce a "killer" molecule, nitric oxide (NO). This requires the activation of NADPH oxidase enzymes. Reactive oxygen species (ROS) such as superoxide, hydroxyl radical, hydrogen peroxide and reactive nitrogen species (RNS) like nitric oxide and peroxynitrite can result in cell death (Soenen et al., 2014). *In vivo* silica exposures activate inflammatory phagocytes in the lung resulting in oxidative outbreak (Coccini et al., 2013). The ability of ZnSe/ZnS QDs to induce ROS and RNS in HepG2 cells was investigated since oxidative stress is a prominent cause of nanomaterial toxicity. They can react with macromolecules such as lipids, proteins, DNA, etc., which affects the structure and function of macromolecules, and then causes oxidative cellular damage (Cho et al., 2007; Juzenas et al., 2008; Lu et al., 2019). The result of the current study showed an increase in ROS production as evident from DCFHDA assay only at 24 h exposure of QDs. A clear generation of reactive oxygen species (ROS) is established by the Soenen et al., 2014 and reaching significant levels at 30 nM for ZnSe
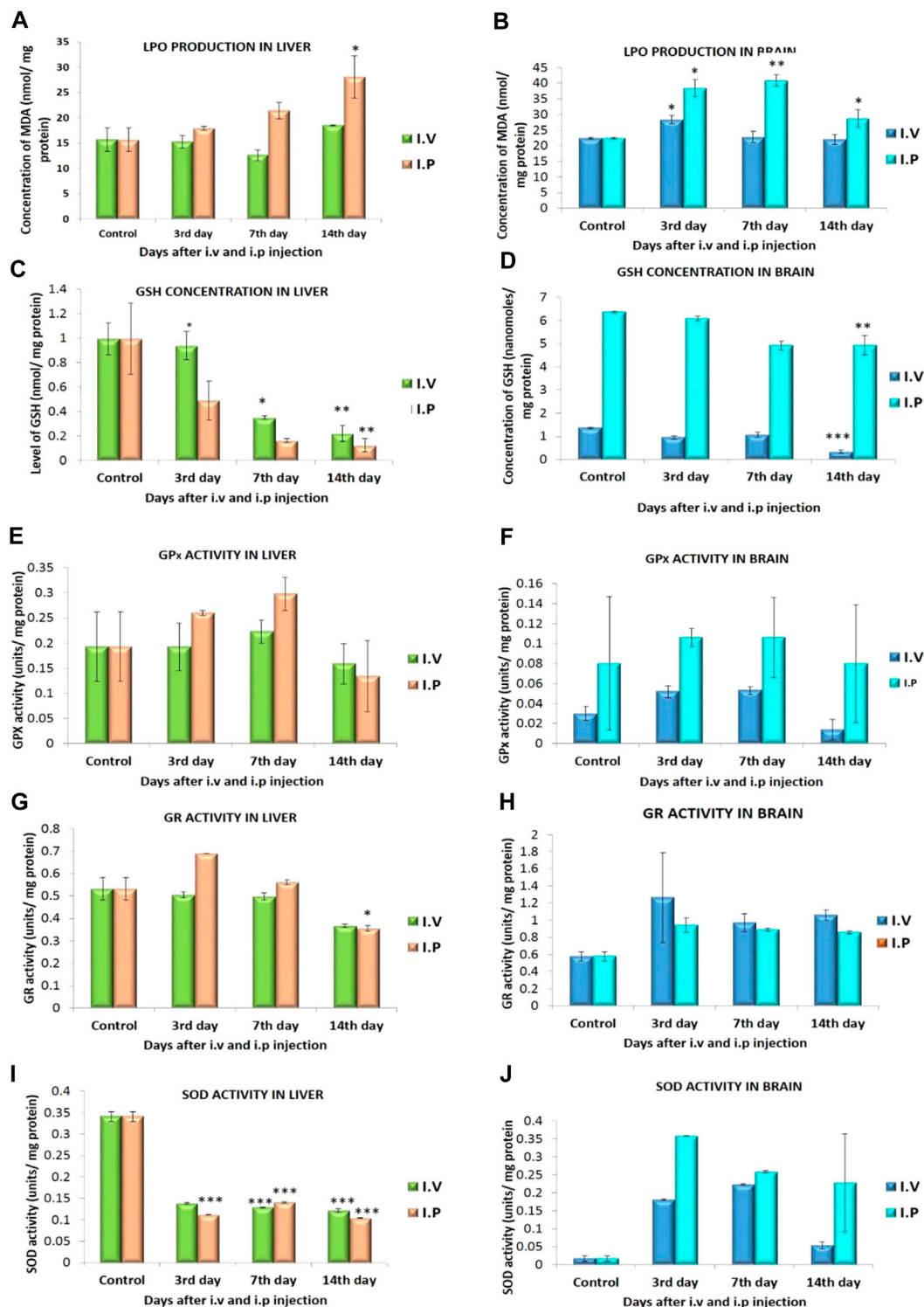
FIGURE 7 | LPO production in **(A)** liver **(B)** brain; GSH level in **(C)** liver, **(D)** brain; GPx activity in **(E)** liver, **(F)** brain; GR activity in **(G)** liver, **(H)** brain; SOD activity in **(I)** liver, **(J)** brain of mice exposed to ZnSe/ZnS QDs. n = 3. The data represent mean ± SD. Asterisk denotes statistically significant difference (*$p < 0.05$, **$p < 0.01$).

QDs. The higher level of oxidative stress for the ZnSe QDs suggests the critical role of ROS in QD cytotoxicity. ZnSe/ZnS QDs were incubated with HEK for 6 h and 24 h. As observed in HepG2 cells,

QDs were unable to evoke ROS generation at 24 h. This effect may be either because of aggregation of QDs or because of ROS scavenging property of glutathione. The quantitative estimation

FIGURE 8 | Brain volume change and Splenocytes proliferation in mice exposed to ZnSe/ZnS QDs. n = 3. Data represents mean ± SD. Asterisk denotes statistically significant difference (*$p < 0.05$).
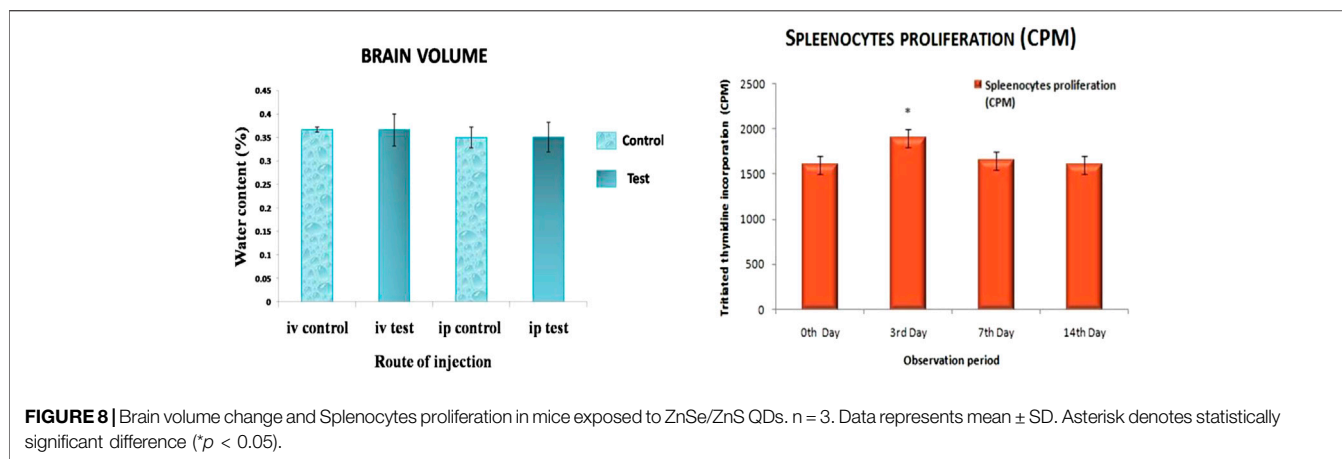
of ROS can be identified by the presence of elevated amount of thiol or sulfhydryl radicals formed by glutathione along with other agents that can cause of ROS scavenging (Cossarizza et al., 2009). However, 6 h exposure to a high concentration of ZnSe/ZnS QDs led to an increased ROS generation in HEK.

Catalase plays a central role in ROS detoxification and known as scavengers of ROS. It is an antioxidant enzyme that converts hydrogen peroxide into water and oxygen. Cytosolic-enzyme catalase (CAT) protects the cells from the destructive effects of reactive oxygen species (ROS). Catalase activity is very high in liver cells (Sani et al., 2006). Catalase inhibitor sodium azide (0.2 μM) was used to study the influence of catalase on the production of ROS in both HepG2 and HEK cells. Sodium azide treated samples showed high ROS production in both the cells. It was noted that catalase activity in the cells could resist the ROS production induced by ZnSe/ZnS QDs in a time and dose-dependent manner.

Nitric oxide (NO) is a gaseous free radical that has been recognized as an essential signaling molecule in virtually every tissue in the body. As in the case of other organs, NO has many actions and cellular sources in both the liver (Clemens, 1999) and kidney (Mount and Power, 2006). Under inflammatory and stress conditions, hepatocytes are able to convey repeated inducible NO synthase (iNOS) expression. This iNOS expression controls cell viability as well as cellular functions. Hepatocytes contain mainly two pools of iNOS: a soluble pool composed of both active dimer/ monomer and a peroxisomal pool of monomeric iNOS. In cells such as hepatocytes, iNOS is localized in peroxisomes as a defensive means to eliminate incompetent enzymes. Nitric oxide (NO) has significant signaling role in cells but can also cause cell dysfunction or toxicity (Loughran et al., 2005). In the present study, cellular levels of NO produced in HepG2 cells triggered by ZnSe/ ZnS QDs or lipopolysaccharide (LPS) (i.e., a pro-inflammatory marker) was examined. It was found that a significantly higher amount of NO was generated when cells were exposed to LPS. However, the treatment of ZnSe/ZnS QDs at the concentrations up to 100 μg/ml did not cause any difference in NO production. Endothelium-derived NO is produced in the kidney and it does decisive role in the regulation of renal hemodynamics and excretory function (Bachmann and Mundel, 1994). In the

present study, a negligible increase in NOS generation was seen in HEK cells when compared to control.

Proteins are vital biochemical constituents that is present in all biological systems. It is essential for the synthesis of various enzymes crucial for maintaining stable metabolic pathways. No significant changes were observed in protein concentrations of the ZnSe/ZnS QDs treated HepG2 cells except 100 μg/ml when compared with control. Protein estimation in HEK cells treated with ZnSe/ZnS QDs confirmed that a substantial decline of protein concentration was observed in a dose-dependent manner. Protein synthesis is one of the fundamental functions of cells that control all the metabolic activities that take place inside the cells. Variation in protein synthesis is not ideally related to a single biochemical system. Changes can also occur due to interactions of QDs with subcellular organelles such as the nucleus, ribosomes, endoplasmic reticulum, cytoplasm and cytoskeleton.

GSH is an abundant non-enzymatic antioxidant tripeptide and is sensitive to NP treatment (Akhtar et al., 2012). The liver is the organ that contains the highest levels of GSH because it involves in GSH synthesis and metabolism. GSH helps in metabolism of fat, sugar and protein, and keep natural cell metabolism and cell membrane integrity. It can bind toxic substances, such as electrophilic radicals and oxygen free radicals, and has broad antioxidative effects (Chen et al., 2008). Under physiological conditions, oxidative stress in the liver can resist through GSH synthesis in hepatocytes. GSH can avoid oxidative stress by serving as a substrate for antioxidative enzymes including GSH-Px which converts hydroperoxide into less damaging fatty acids, GSH disulfide and water (Day, 2009). Therefore, GSH can resist ZnSe/ZnS QDs induced oxidative stress. Glutathione plays a significant role at cellular level. In mitochondria, it is involved in regulating apoptosis vs. necrosis. GSH is used as a indicator of oxidative stress as it is one of the major scavengers of ROS. Results obtained for the particular study points out that, GSH level declined at higher concentrations of NPs. This finding could be a sign of oxidative stress as the primary toxicity mechanism. It is known that GSH is an essential component for the protection of thiolgroups which guards mitochondria against permeability transition or opening of MPT pores and oxidative stress. The inverse linear relationship between the ROS level and the GSH level indicated that free radical species were generated by

exposure to the ZnSe/ZnS QDs with decreased mitochondrial and cellular antioxidant levels.

DNA ladder assay is very useful for quick screening of apoptotic changes in cell populations. The DNA laddering technique is used to visualize the endonuclease cleavage products of apoptosis. One of the most peculiar features exhibited by cells go through apoptosis is the fragmentation of DNA into oligonucleosomal fragments. It can be observed as DNA laddering when genomic DNA is subjected to agarose gel electrophoresis (Barry et al., 2000). DNA ladder assay makes the apparent hallmark of apoptosis–mono and oligonucleosomal DNA fragments (Saadat et al., 2015). In the present work, the ladder pattern of DNA cleavage was not exhibited in any of the treated DNA samples. This may be due to the size that prevents them from entering the nucleus or because of the surface charge carried by QDs. The negative charge of the QDs repelled with negatively charged DNA. Negatively charged NPs have no effect on the cell cycle (Liu et al., 2015). An intact plasma membrane and ubiquitous intracellular esterase activity are distinguishing characteristics of live cells. Calcein AM is capable of penetrating live cell membranes, making an strong uniform green fluorescence in viable cells. PI is only capable of entering damaged membranes and gives red fluorescence upon binding to nucleic acids, thereby producing a bright red fluorescence in dead cells. Flow cytometric data showed a dose and time-dependent effect on cell viability.

Induction of oxidative stress is one of the main mechanisms involved in QD toxicity. Oxidative stress status of the liver and brain of mice treated with QDs was analyzed by stress markers like LPO, GSH, GR, GPx and GR activity. In living organisms, lipid peroxidation is one of the vital reasons of cellular injury causing the formation of lipid peroxides and this pheneomenon is used as an evidence of oxidative stress. These unstable lipid peroxides decomposes to form a complex series of compounds including reactive carbonyl compounds. MDA is one of the by-products of LPO. Quantitative assessment of MDA has been used as an indicator of lipid peroxidation. The present study demonstrated a significant dose-dependent hike in MDA level in the liver. This indicates the lowest values of the free radical clearance rate of the liver. Also, the time-course study showed that the levels of MDA reached their highest values at 7 days (i.p.) in the case of brain tissue. These results are in accordance with the report by Wang et al. (2006) that ·OH generation reached a peak value on the 7th day (Wang et al., 2006). GSH plays an important role in the endogenous antioxidant system. A high concentration of GSH is found in the liver and brain; hence it is known to have a crucial function in the protection process. ZnSe/ZnS QDs decreased the hepatic and brain GSH contents. It implies that the reduction in ZnSe/ZnS QD-induced antioxidant capacity of the liver and brain are associated with GSH depletion. It was believed that the activity of GR might be the major determinant that regulates GSH/GSSG (Hazelton and Lang, 1985). Glutathione peroxidase and SOD are the major antioxidative enzymes that can protect polyunsaturated fatty acid (PUFA) from lipid peroxidation by reducing H_2O_2 and superoxide radical (Wang et al., 2017). Dismutation of ROS is by SOD is of prime importance in cells since superoxide is the primary ROS formed. SOD quenches the free radical superoxide

by converting it to peroxide, which can then be inactivated by reactions catalyzed by GPx. It is the most critical H_2O_2 scavenging enzyme, closely associated with the maintenance of reduced glutathione (Brunetti et al., 2013).

Diverse engineered nanoparticles have many positive aspects over conventional contrast agents like the ability to overcome the blood-brain barrier (BBB) for drug delivery. Fundamental, as well as clinical research, explored QD applications in the brain (Thorne and Nicholson, 2006; Minami et al., 2012; Marshall and Schnitzer, 2013; Xu and Mahajan, 2013; Zhang, 2013; Walters et al., 2015; Dawson, 2016; Dante et al., 2017). Reports promote scope of functionalized QDs as drug-delivery vehicles or targeted-imaging biomarkers for central nervous system (CNS) diseases. Effect of ZnSe/ZnS QDs in mice brain is studied on the basis of their volume change. The volume of brain changes in response to injuries, inflammation and disruption of BBB. However, in the present study, there were no ZnSe/ZnS QDs mediated volume changes in treated mice demonstrating that ZnSe/ZnS QDs exposure at the given concentration does not cause mechanical damage and oedema. Ou et al. reported that positively charged nanoparticles alter the BBB integrity and permeability when compared to negatively charged or neutral nanoparticles (2018) (Ou et al., 2018). ZnSe/ZnS QDs and external membrane of the endothelial cell have negative charge repel with each other.

Immunotoxicity of ZnSe/ZnS QDs was studied by splenocyte proliferation assay. Splenocytes are one kind of white blood cells positioned in the spleen or purified from splenic tissue (Mebius and Kraal, 2005). Splenocytes compromises of cells such as T and B lymphocytes, macrophages and dendritic cells, which have different immune functions. The function of T and B cells is to recognize non self-antigen. T cells undergo proliferation as a result of activation by antigen-presentingcells and cytokines. Proliferations of both the cells result in clonal expansion and initiate specific immune response (Bao-An et al., 2010). In proliferating cells, rate of DNA and protein synthesis trend to increase. Radioisotope labeled nucleotides liketritiated thymidine ([3H] thymidine) can be used to estimate the increase in DNA synthesis. The rate of proliferation is considered propotional to total tritium taken up by the dividing cells (Ghoneum, 1998). This technique is used widely for evaluating the immuno-toxicological response of nanoparticles by [3H] thymidine incorporation (Seur and Doucras, 1997; Guity et al., 2001; Li et al., 2012). The systemic immuneresponse induced upon exposure to ZnSe/ZnS QDs was analyzedon the basis of the proliferation rate of splenocytes. In the current study slight change in splenocytes proliferationwas observed only on 3rd day, whereas no changes were seen on subsequent days. These results suggest that single exposure of ZnSe/ZnS QDs at a concentration (10 mg/kg) induce inflammatory responses in mice only on 3rd day and eliminate by means of phagocytosis, without such effects in subsequent days.

CONCLUSION

In summary, Oxidative stress exerted by the ZnSe/ZnS QDs in both HepG2 and HEK cells studied, and the results clearly demonstrate that

100 µg/ml concentration caused ROS production. Catalase has an active part in the regulation of ROS production in both the cell lines. Significant amount of RNS production is not found in any of the treatment groups. GSH content also analyzed for the oxidative stress analysis. QDs do not cause DNA fragmentation. The degree of cell death was found to be raised with an increase in the concentration of QDs and a significant concentration resulted in cellular death in both cell lines. The results of our study demonstrate that ZnSe/ZnS QDs induce oxidative stress and cell death in HepG2 and HEK cells, and this effect is likely mediated through ROS generation. ZnSe/ZnS QDs do not cause nuclear damage. ZnSe/ZnS QDs caused fluctuations of oxidative stress markers in mice but not severe. Immunotoxicity evaluation showed slight alteration and the same was recovered to the normal range. Declaration about safety of ZnSe/ZnS QDs in clinical application scenarios requires long term toxicity studies.

DATA AVAILABILITY STATEMENT

The original contributions presented in the study are included in the article/Supplementary Material, further inquiries can be directed to the corresponding author.

REFERENCES

Akhtar, M. J., Ahamed, M., Kumar, S., Khan, M. M., Ahmad, J., and Alrokayan, S. A. (2012). Zinc oxide nanoparticles selectively induce apoptosis in human cancer cells through reactive oxygen species. *Int. J. Nanomed.* 7, 845. doi:10.2147/IJN. S29129

Bachmann, S., and Mundel, P. (1994). Nitric oxide in the kidney: synthesis, localization, and function. *Am. J. Kidney Dis.* 24 (1), 112–129. doi:10.1016/ s0272-6386(12)80170-3

Bagalkot, V., Zhang, L., Levy-Nissenbaum, E., Jon, S., Kantoff, P. W., Langer, R., et al. (2007). Quantum dot-aptamer conjugates for synchronous cancer imaging, therapy, and sensing of drug delivery based on bi-fluorescence resonance energy transfer. *Nano Lett.* 7, 3065–3070. doi:10.1021/ nl071546n

Bao-An, C., Nan, J., Jun, W., Jiahua, D., Chong, G., Jian, C., et al. (2010). The effect of magnetic nanoparticles of Fe3O4 on immunefunction in normal ICR mice. *Int. J. Nanomed.* 5, 593–599. doi:10.2147/ijn.s12162

Barry, M., Heibein, J., Pinkoski, M., and Bleackley, R. C. (2000). Quantitative measurement of apoptosis induced by cytotoxic T lymphocytes. *Methods Enzymol.* 322, 40–46. doi:10.1016/s0076-6879(00)22006-5

Birben, E., Sahiner, U. M., Sackesen, C., Erzurum, S., and Kalayci, O. (2012). Oxidative stress and antioxidant defense. *World Allergy Organ J.* 5 (1), 9–19. doi:10.1097/WOX.0b013e3182439613

Brunetti, V., Chibli, H., Fiammengo, R., Galeone, A., Malvindi, M. A., Vecchio, G., et al. (2013). InP/ZnS as a safer alternative to CdSe/ZnS core/shell quantum dots: *in vitro* and *in vivo* toxicity assessment. *Nanoscale* 5 (1), 307–317. doi:10. 1039/c2nr33024e

Chen, Z., Li, G., Zhang, L., Jiang, J., Li, Z., Peng, Z., et al. (2008). A new method for the detection of ATP using a quantum-dot-tagged aptamer. *Anal. Bioanal. Chem.* 392 (6), 1185–1188. doi:10.1007/s00216-008-2342-z

Cho, S. J., Maysinger, D., Jain, M., Roder, B., Hackbarth, S., and Winnik, F. M. (2007). Long-term exposure to CdTe quantum dots causes functional impairments in live cells. *Langmuir* 23, 1974–1980. doi:10.1021/la060093j

Clemens, M. G. (1999). Nitric oxide in liver injury. *Hepatology* 30 (1), 1–5. doi:10. 1002/hep.510300148

Coccini, T., Barni, S., Vaccarone, R., Mustarelli, P., Manzo, L., and Roda, E. (2013). Pulmonary toxicity of instilled cadmium-doped silica nanoparticles during acute and subacute stages in rats. *Histol. Histopathol.* 28 (2), 195–209. doi:10. 14670/HH-28.195

ETHICS STATEMENT

AUTHOR CONTRIBUTIONS

PM: Design, literature survey, drafting, discussion, submission VR: analysis, data collection, literature survey, drafting, discussion.

ACKNOWLEDGMENTS

Cossarizza, A., Ferraresi, R., Troiano, L., Roat, E., Gibellini, L., Bertoncelli, L., et al. (2009). Simultaneous analysis of reactive oxygen species and reduced glutathione content in living cells by polychromatic flow cytometry. *Nat. Protoc.* 4 (12), 1790. doi:10.1038/nprot.2009.189

Dante, S., Petrelli, A., Petrini, E. M., Marotta, R., Maccione, A., Alabastri, A., et al. (2017). Selective targeting of neurons with inorganic nanoparticles: revealing the crucial role of nanoparticle surface charge. *ACS Nano* 11 (7), 6630–6640. doi:10.1021/acsnano.7b00397

Dawson, G. (2016). Quantum dots and potential therapy for Krabbe's disease. *J. Neurosci. Res.* 94 (11), 1293–1303. doi:10.1002/jnr.23805

Day, B. J. (2009). Catalase and glutathione peroxidase mimics. *Biochem. Pharmacol.* 77 (3), 285–296. doi:10.1016/j.bcp.2008.09.029

Diagaradjane, P., Orenstein-Cardona, J. M., Colón-Casasnovas, N. E., Deorukhkar, A., Shentu, S., Kuno, N., et al. (2008). Imaging epidermal growth factor receptor expression *in vivo*: pharmacokinetic and biodistribution characterization of a bioconjugated quantum dot nanoprobe. *Clin. Canc. Res.* 14, 731–741. doi:10. 1158/1078-0432.CCR-07-1958

Ghoneum, M. (1998). Anti-HIV activity *in vitro* of MGN-3, an activated arabinoxylane from rice bran. *Biochem. Biophys. Res. Commun.* 243, 25–29. doi:10.1006/bbrc.1997.8047

Guity, G., Dominick, J., Bradley, S. B., Debora, J. B., Maureen, M. G., and John, W. S. (2001). Human lymphocyte proliferation responsesfollowing primary immunization with rabies vaccine as neoantigen. *Clin. Diagn. Lab. Immunol.* 8, 880–883. doi:10.1128/CDLI.8.5.880-883.2001

Hazelton, G. A., and Lang, C. A. (1985). Glutathione peroxidase and reductase activities in the aging mouse. *Mech. Ageing Dev.* 29 (1), 71–81. doi:10.1016/ 0047-6374(85)90048-x

Hu, M., Yan, J., He, Y., Lu, H., Weng, L., Song, S., et al. (2010). Ultrasensitive, multiplexed detection of cancer biomarkers directly in serum by using a quantum dot-based microfluidic protein chip. *ACS Nano* 4, 488–494. doi:10. 1021/nn901404h

Huang, C. C., Aronstam, R. S., Chen, D. R., and Huang, Y. W. (2010). Oxidative stress, calcium homeostasis, and altered gene expression in human lung epithelial cells exposed to ZnO nanoparticles. *Toxicol. Vitro* 24 (1), 45–55. doi:10.1016/j.tiv.2009.09.007

Juzenas, P., Generalov, R., Juzeniene, A., and Moan, J. (2008). Generation of nitrogen oxide and oxygen radicals by quantum dots. *J. Biomed. Nanotechnol.* 4, 450–456. doi:10.1166/jbn.2008.008

Katsumiti, A., Gilliland, D., Arostegui, I., and Cajaraville, M. P. (2014). Cytotoxicity and cellular mechanisms involved in the toxicity of CdS quantum dots in

hemocytes and gill cells of the mussel *Mytilus galloprovincialis*. *Aquat. Toxicol.* 153, 39–52. doi:10.1016/j.aquatox.2014.02.003

Kirchner, C., Javier, A. M., Susha, A. S., Rogach, A. L., Kreft, O., Sukhorukov, G. B., et al. (2005a). Cytotoxicity of nanoparticle-loaded polymer capsules. *Talanta* 67 (3), 486–491. doi:10.1016/j.talanta.2005.06.042

Kirchner, C., Liedl, T., Kudera, S., Pellegrino, T., Muñoz Javier, A., Gaub, H. E., et al. (2005b). Cytotoxicity of colloidal CdSe and CdSe/ZnS nanoparticles. *Nano Lett.* 5 (2), 331–338. doi:10.1021/nl047996m

Lee, H. M., Shin, D. M., Song, H. M., Yuk, J. M., Lee, Z. W., Lee, S. H., et al. (2009). Nanoparticles up-regulate tumor necrosis factor-alpha and CXCL8 via reactive oxygen species and mitogen-activated protein kinase activation. *Toxicol. Appl. Pharmacol.* 238, 160. doi:10.1016/j.taap.2009.05.010

Li, K. G., Chen, J. T., Bai, S. S., Wen, X., Song, S. Y., Yu, Q., et al. (2009). Intracellular oxidative stress and cadmium ions release induce cytotoxicity of unmodified cadmium sulfide quantum dots. *Toxicol. Vitro* 23, 1007–1013. doi:10.1016/j.tiv.2009.06.020

Li, T., Jamil, A., Mincheol, K., Marwan, M., Rong, T., Qian, Y., et al. (2012). Immunosuppressive activity of size-controlled PEG-PLGA nanoparticles containing encapsulated cyclosporine. *Am. J. Transplant.* 2012, 1–9. doi:10.1155/2012/896141

Liu, L., Tao, R., Huang, J., He, X., Qu, L., Jin, Y., et al. (2015). Hepatic oxidative stress and inflammatory responses with cadmium exposure in male mice. *Environ. Toxicol. Pharmacol.* 39 (1), 229–236. doi:10.1016/j.etap.2014.11.029

Loughran, P. A., Stolz, D. B., Vodovotz, Y., Watkins, S. C., Simmons, R. L., and Billiar, T. R. (2005). Monomeric inducible nitric oxide synthase localizes to peroxisomes in hepatocytes. *Proc. Natl. Acad. Sci. U.S.A.* 102 (39), 13837–13842. doi:10.1073/pnas.0503926102

Lovrić, J., Cho, S. J., Winnik, F. M., and Maysinger, D. (2005). Unmodified cadmium telluride quantum dots induce reactive oxygen species formation leading to multiple organelle damage and cell death. *Chem. Biol.* 12, 1227. doi:10.1016/j.chembiol.2005.09.008

Lowry, O. H., Rosebrough, N. J., Farr, A. L., and Randall, R. J. (1951). Protein measurement with the Folin phenol reagent. *J. Biol. Chem.* 193, 265–275. doi:10.1016/s0021-9258(19)52451-6

Lu, J., Tang, M., and Zhang, T. (2019). Review of toxicological effect of quantum dots on the liver. *J. Appl. Toxicol.* 39 (1), 72–86. doi:10.1002/jat.3660

Marklund, S., and Marklund, G. (1974). Involvement of the superoxide anion radical in the autoxidation of pyrogallol and a convenient assay for superoxide dismutase. *Eur. J. Biochem.* 47, 469–474. doi:10.1111/j.1432-1033.1974.tb03714.x

Marshall, J. D., and Schnitzer, M. J. (2013). Optical strategies for sensing neuronal voltage using quantum dots and other semiconductor nanocrystals. *ACS Nano* 7 (5), 4601–4609. doi:10.1021/nn401410k

Mebius, R. E., and Kraal, G. (2005). Structure and function of the spleen. *Nat. Rev. Immunol.* 5, 606–616. doi:10.1038/nri1669

Medintz, I. L., Uyeda, H. T., Goldman, E. R., and Mattoussi, H. (2005). Quantum dot bioconjugates for imaging, labelling and sensing. *Nat. Mater.* 4 (6), 435–446. doi:10.1038/nmat1390

Michalet, X., Pinaud, F. F., Bentolila, L. A., Tsay, J. M., Doose, S., Li, J. J., et al. (2005). Quantum dots for live cells, *in vivo* imaging, and diagnostics. *Science* 307, 538–544. doi:10.1126/science.1104274

Milliron, D. J., Hughes, S. M., Cui, Y., Manna, L., Li, J., Wang, L. W., et al. (2004). Colloidal nanocrystal heterostructures with linear and branched topology. *Nature* 430, 190–195. doi:10.1038/nature02695

Minami, S. S., Sun, B., Popat, K., Kauppinen, T., Pleiss, M., Zhou, Y., et al. (2012). Selective targeting of microglia by quantum dots. *J. Neuroinflammation* 9, 22. doi:10.1186/1742-2094-9-22

Mize, C. E., and Langdon, R. G. (1962). Hepatic glutathione reductase. I. Purification and general kinetic properties. *J. Biol. Chem.* 237, 1589–1595. doi:10.1016/s0021-9258(19)83745-6

Mocatta, D., Cohen, G., Schattner, J., Millo, O., Rabani, E., and Banin, U. (2011). Heavily doped semiconductor nanocrystal quantum dots. *Science* 332, 77–81. doi:10.1126/science.1196321

Moron, M. S., Depierre, J. W., and Mannervik, B. (1979). Levels of glutathione, glutathione reductase and glutathione S-transferase activities in rat lung and liver. *Biochim. Biophys. Acta* 582, 67–78. doi:10.1016/0304-4165(79)90289-7

Mount, P. F., and Power, D. A. (2006). Nitric oxide in the kidney: functions and regulation of synthesis. *Acta Physiol.* 187 (4), 433–446. doi:10.1111/j.1748-1716.2006.01582.x

Muthu, M. S., Kulkarni, S. A., Raju, A., and Feng, S. S. (2012). Theranostic liposomes of TPGS coating for targeted co-delivery of docetaxel and quantum dots. *Biomaterials* 33, 3494–3501. doi:10.1016/j.biomaterials.2012.01.036

Ohkawa, H., Ohishi, N., and Yagi, K. (1979). Assay for lipid peroxides in animal tissues by thiobarbituric acid reaction. *Anal. Biochem.* 95, 351–358. doi:10.1016/0003-2697(79)90738-3

Ou, H., Cheng, T., Zhang, Y., Liu, J., Ding, Y., Zhen, J., et al. (2018). Surface-adaptive zwitterionic nanoparticles for prolonged blood circulation time and enhanced cellular uptake in tumor cells. *Acta Biomater.* 65, 339–348. doi:10.1016/j.actbio.2017.10.034

Pal, B. N., Ghosh, Y., Brovelli, S., Laocharoensuk, R., Klimov, V. I., Hollingsworth, J. A., et al. (2012). "Giant" CdSe/CdS core/shell nanocrystal quantum dots as efficient electroluminescent materials: strong influence of shell thickness on light-emitting diode performance. *Nano Lett.* 12, 331–336. doi:10.1021/nl203620f

Risom, L., Moller, P., and Loft, S. (2005). Oxidative stress-induced DNA damage by particulate air pollution. *Mutat. Res.* 592, 119–137. doi:10.1016/j.mrfmmm.2005.06.012

Rotruck, J. T., Pope, A. L., Ganther, H. E., Swanson, A. B., Hafeman, D. G., and Hoekstra, W. G. (1973). Selenium: biochemical role as a component of glutathione peroxidase. *Science* 179, 588–590. doi:10.1126/science.179.4073.588

Saadat, Y. R., Saeidi, N., Vahed, S. Z., Barzegari, A., and Barar, J. (2015). An update to DNA ladder assay for apoptosis detection. *BI* 5 (1), 25. doi:10.15171/bi.2015.01

Sani, M., Sebaï, H., Gadacha, W., Boughattas, N. A., Reinberg, A., and Mossadok, B. A. (2006). Catalase activity and rhythmic patterns in mouse brain, kidney and liver. *Comp. Biochem. Physiol. B Biochem. Mol. Biol.* 145 (3-4), 331–337. doi:10.1016/j.cbpb.2006.08.005

Seur, J. S., and Doucras, M. (1997). TritiatedThymidine incorporation and cell-mediated lympholysis as correlates of acute graft-versus-host reaction. *Exp. Hematol.* 5, 443–455.

Soenen, S. J., Manshian, B. B., Aubert, T., Himmelreich, U., Demeester, J., De Smedt, S. C., et al. (2014). Cytotoxicity of cadmium-free quantum dots and their use in cell bioimaging. *Chem. Res. Toxicol.* 27 (6), 1050–1059. doi:10.1021/tx5000975

Su, Y., Hu, M., Fan, C., He, Y., Li, Q., Li, W., et al. (2010). The cytotoxicity of CdTe quantum dots and the relative contributions from released cadmium ions and nanoparticle properties. *Biomaterials* 31 (18), 4829–4834. doi:10.1016/j.biomaterials.2010.02.074

Tang, S., Cai, Q., Chibli, H., Allagadda, V., Nadeau, J. L., and Mayer, G. D. (2013). Cadmium sulfate and CdTe-quantum dots alter DNA repair in zebrafish (*Danio rerio*) liver cells. *Toxicol. Appl. Pharmacol.* 272 (2), 443–452. doi:10.1016/j.taap.2013.06.004

Thorne, R. G., and Nicholson, C. (2006). *In vivo* diffusion analysis with quantum dots and dextrans predicts the width of brain extracellular space. *Proc. Natl. Acad. Sci. U.S.A.* 103 (14), 5567–5572. doi:10.1073/pnas.0509425103

Walker, K. A., Morgan, C., Doak, S. H., and Dunstan, P. R. (2012). Quantum dots for multiplexed detection and characterisation of prostate cancer cells using a scanning near-field optical microscope. *PloS One* 7, e31592. doi:10.1371/journal.pone.0031592

Walters, R., Medintz, I. L., Delehanty, J. B., Stewart, M. H., Susumu, K., Huston, A. L., et al. (2015). The role of negative charge in the delivery of quantum dots to neurons. *ASN Neuro* 7 (4), 1759091415592389. doi:10.1177/1759091415592389.10.1177/1759091415592389

Wang, J., Chen, C., Li, B., Yu, H., Zhao, Y., Sun, J., et al. (2006). Antioxidative function and biodistribution of [Gd@C82(OH)22]n nanoparticles in tumor-bearing mice. *Biochem. Pharmacol.* 71 (6), 872–881. doi:10.1016/j.bcp.2005.12.001

Wang, J., Sun, H., Meng, P., Wang, M., Tian, M., Xiong, Y., et al. (2017). Dose and time effect of CdTe quantum dots on antioxidant capacities of the liver and kidneys in mice. *Int. J. Nanomed.* 12, 6425. doi:10.2147/IJN.S142008

Xing, Y., and Rao, J. (2008). Quantum dot bioconjugates for *in vitro* diagnostics and *in vivo* imaging. *Canc. Biomarkers* 4 (6), 307–319. doi:10.3233/cbm-2008-4603

Xu, G., and Mahajan, S. I. (2013). Theranostic quantum dots for crossing blood-brain barrier *in vitro* and providing therapy of HIV-associated encephalopathy. *Front. Pharmacol.* 4, 140. doi:10.3389/fphar.2013.00140

Yang, L., Wang, F., Han, H., Yang, L., Zhang, G., and Fan, Z. (2015). Functionalized graphene oxide as a drug carrier for loading pirfenidone in treatment of subarachnoid hemorrhage. *Colloids Surf. B Biointerfaces* 129, 21–29. doi:10.1016/j.colsurfb.2015.03.022

Zhang, Q. (2013). Imaging single synaptic vesicles in mammalian central synapses with quantum dots. *Methods Mol. Biol.* 1026, 57–69. doi:10.1007/978-1-62703-468-5_5

Zhao, Y., Lin, K., Zhang, W., and Liu, L. (2010). Quantum dots enhance Cu2+ -induced hepatic L02 cells toxicity. *J. Environ. Sci. (China)* 22 (12), 1987–1992. doi:10.1016/s1001-0742(09)60350-8

Bio-Active Free Direct Optical Sensing of Aflatoxin B1 and Ochratoxin A Using a Manganese Oxide Nano-System

Avinash Kumar Singh[1,2], G. B. V. S. Lakshmi[1], Tarun Kumar Dhiman[1], Ajeet Kaushik[3]* and Pratima R. Solanki[1]*

[1]Special Centre for Nanoscience, JNU, New Delhi, India, [2]School of Physical Sciences, JNU, New Delhi, India, [3]NanoBioTech Laboratory, Department of Natural Sciences, Division of Scientist, Art, and Sciences, Florida Polytechnic University, Lakeland, FL, United States

Aflatoxins-B1 (AFB1) and Ochratoxin-A (OchA) are the two types of major mycotoxin produced by *Aspergillus flavus*, *Aspergillus parasiticus* fungi, *Aspergillus carbonarius, Aspergillus niger, and Penicillium verrocusumv*. These toxins are mainly found in metabolite cereals, corn, coffee beans, and other oil-containing food items. Excessive consumption of these toxins can be carcinogenic and lead to cancer. Thus, their rapid testing became essential for food quality control. Herein, manganese oxide nanoparticles (MnO_2 nps) have been proposed to explore the interaction with AFB1 and OchA using UV-visible spectroscopy. MnO_2 nps were synthesized using the co-precipitation method. They were pure and crystalline with an average crystallite size of 5–6 nm. In the UV-vis study, the maximum absorbance for MnO_2 nps was observed around 260 nm. The maximum absorbance for AFB1 and OchA was observed at 365 and 380 nm, respectively, and its intensity enhanced with the addition of MnO_2 nps. Sequential changes were observed with varying the concentration of AFB1 and OchA with a fixed concentration of MnO_2 nps, resulting in proper interaction. The binding constant (k_b) and Gibbs free energy for MnO_2 nps-AFB1 and OchA were observed as $1.62 \times 10^4 \, L \, g^{-1}$ and $2.67 \times 10^4 \, L \, g^{-1}$, and −24.002 and −25.256 kJ/mol, respectively. The limit of detection for AFB1 and OchA was measured as 4.08 and 10.84 ng/ml, respectively. This bio-active free direct sensing approach of AFB1 and OchA sensing can be promoted as a potential analytical tool to estimate food quality rapidly and affordable manner at the point of use.

Keywords: direct sensing, nano-system, manganese oxide, UV-visible spectroscopy, aflatoxin-B1, Ochratoxin-A

1 INTRODUCTION

Aflatoxins-B1 (AFB1) has been identified as a significant contaminant in food materials like maize, corn, cottonseed, peanuts, cereals, etc. Fungal infection is a primary source of toxin production, mainly originated from *Aspergillus flavus* and parasiticus fungi. (Battacone et al., 2005) (Borneman and Becker, 2007) (Payne and Brown, 1998) (Ronchi et al., 2005) (Sarma et al., 2017) (Zheng et al., 2017) This toxin had an adverse effect on human health and animals, causing acute diseases like jaundice, lethargy, nausea, etc. According to the international agency for cancer research, AFB1 is the most toxic among other mycotoxins and is classified as a group 1 carcinogen. (Cancer, 1982) (Roberts et al., 2014) The United States department of agriculture (USDA) and food and drug

administration (FDA) have set a scale of 20ppb AFB1 consumption in food as a tolerable limit. (Altug, 2002) (van Egmond and Dekker, 1996) (van Egmond and Jonker, 2004). According to the WHO report, large doses of AFB1 are carcinogenic and cause liver cancer. Similarly, for animals like chickens, AFB1 is unfriendly, and its effect reduces egg production, impairs reproductive efficiency, and damages the liver. (Administration (FAD), 1988) (Henry et al., 1999) (Smith et al., 1995). It has been categorized into more than 10 different isomers, including B1, B2, G1, G2, M1, M2, etc. (Crook, 2003) Among these, AFB1 is more precarious and can be lethal. (Jaimez et al., 2000).

Ochratoxin-A (OchA) is also a developed class of mycotoxin, a secondary metabolite of *Aspergillus ochraceous, Aspergillus carbonarius, Aspergillus niger,* and *Penicillium verrocusumv.* (Abarca et al., 1994) (Van der Merwe et al., 1965) (Heenan et al., 1998) The primary sources of these toxins are food commodities such as cereal grains like corn, coffee beans, dairy products, wine, raisins, vegetables (yam, garlic, onions, potatoes, and tomatoes), fruits, and spices. (Duarte et al., 2010) (Lim et al., 2015) (Kaushik et al., 2009b) (Kaushik et al., 2009a) (Solanki et al., 2010) (Marin and Taranu, 2015) (Pfohl-Leszkowicz and Manderville, 2007) OchA is more potent and toxic compared to ochratoxin B and C. (Kőszegi and Poór, 2016) (Gallo et al., 2017) The OchA is cancerous in humans; the International Agency for Research on Cancer has therefore categorized this toxin as belonging to the 2B group. (Pflaum et al., 2016) The World Health Organization (WHO) set the tolerable parameter for ochratoxin A as 5 ng/kg body weight per day. (Pitt, 2000).

Detection of these toxins has always remained challenging due to the lack of complete information. For quantitative detection, an electrochemical-biosensor has been used to check the sensitivity of toxins. Also, analytical techniques like enzyme-linked immunosorbent assays (ELISA) are used for the determination of AFB1. (Azri et al., 2018) These toxins' optical properties open up a new detection approach because they consist of spectral shift, change in fluorescence intensity, lifetime and quantum yield, etc. Few toxins like ochratoxin and citrinin have been employed to detect absorption and fluorescence through a shift in intensity and environmental change. (Keller et al., 2018).

The conventional techniques to detect the toxins mentioned above, including HPLC-tandem mass spectrometry (HPLC-MS/MS) (Abramson et al., 1995), are costly, elaborate, and require a trained candidate for the operation. (Sarkar et al., 2020) These techniques are also limited to analytes' mass scale determination, which is one of the major drawbacks. Considering comparison to these techniques, UV-visible spectroscopy is a well-known and absorbance-based technique that is relatively cost effective, easy to handle, and requires a tiny sample from an experimental point of view. (Dhiman et al., 2019) One such approach is exploring nano-systems for direct and label-free detection of foodborne toxins. There is an urgent need to design and develop an electro-optical metal oxide-based nano-system for sensing applications to achieve this task. Among many, manganese oxide nanoparticles (MnO_2 nps) are emerging as promising sensing nano-systems. The MnO_2 nps are semiconducting in nature owing to multiple

properties like smaller in size, a large surface-to-volume ratio, and having magnetic, electrochemical, and optical properties. (Wei et al., 2011) MnO_2 nps have applied in various fields, including sensors, biosensors, biomedical devices, catalysis, drug delivery, rechargeable batteries, and other commercial purposes. (Ragupathy et al., 2007) (Ganeshan et al., 2017) (Liu et al., 2013) Despite having a tremendous application of MnO_2 nps, it is optically less explored, and it is expected that, similar to other properties, its optical nature can provide a new approach in the detection of analytes. Several nanoparticle systems have been reported regarding the adsorption of mycotoxins. Few graphene-based adsorptive techniques have been studied for bacteria detection in food samples. (Bajpai et al., 2019) (Shukla et al., 2019) Jouni et al. have reported the complex of aptamer-based Fe_2O_3 nps detoxification of aflatoxin M1 in the milk sample. (Jouni et al., 2018) Puzyr et al. have demonstrated sorption properties of nanodiamonds (NDs) to study the adsorption of AFB1. (Purtov et al., 2007) Liu at el. have reported the adsorption of OchA on the surface of gold nanoparticles (Au nps) and have located the effects of Au nps using localized surface plasmon resonance. (Liu et al., 2018) Velu at el. has reported the adsorption–desorption approach for OchA based on lateral flow assays using gold (Au) or silver (Ag) nanoparticles. (Velu and DeRosa, 2018).

Here, we have used the UV-visible absorption technique for the detection of AFB1 and OchA using MnO_2 nps, synthesized using the co-precipitation method. Many papers exist on the sensing of AFB1 and OchA in literature. However, the present study involves the interaction through UV-titration of AFB1 and OchA with MnO_2 nps based on the UV-visible absorbance change. MnO_2 nps are directly interacting with AFB1 and OchA, resulting in enhanced absorption and variation of absorption observed in the presence of a different concentration of AFB1 and OchA. It has been found that a strong interaction occurred between AFB1 and OchA with MnO_2 nps, and this can be used in the development of a detection platform for AFB1 and OchA. The UV-visible absorption intensity of AFB1 and OchA is enhanced with MnO_2 nps, indicating the interaction between themselves, which suggests the effect of MnO_2 nps on AFB1 and OchA. Following this methodology, an experiment was performed, which produced a significant result for developing an optical sensing platform. This optical method is cost-effective and easy to perform without any complications. This can be further treated as the primary platform for the development of optical sensors in the future.

2 MATERIALS AND METHODS

2.1 Reagents

Manganese acetate tetrahydrate (99.99%) and sodium hydroxide (98%) were purchased from Sigma-Aldrich and Fisher Scientific, respectively. Aflatoxin B1 was purchased from LKT laboratories inc and Ochratoxin A and Fumonisin B1 were bought from Cayman chemical company. Cellulose and starch were procured from Sigma-Aldrich, and d-fructose from CDH Chemicals Ltd.

FIGURE 1 | (A) XRD pattern of MnO$_2$ nps calcined at 350°C; **(B)** Scanning electron microscopic image of MnO$_2$ nps recorded (a) lower magnification and (b) at higher magnification showing spherically shaped MnO$_2$ nps calcined at 350 °C.
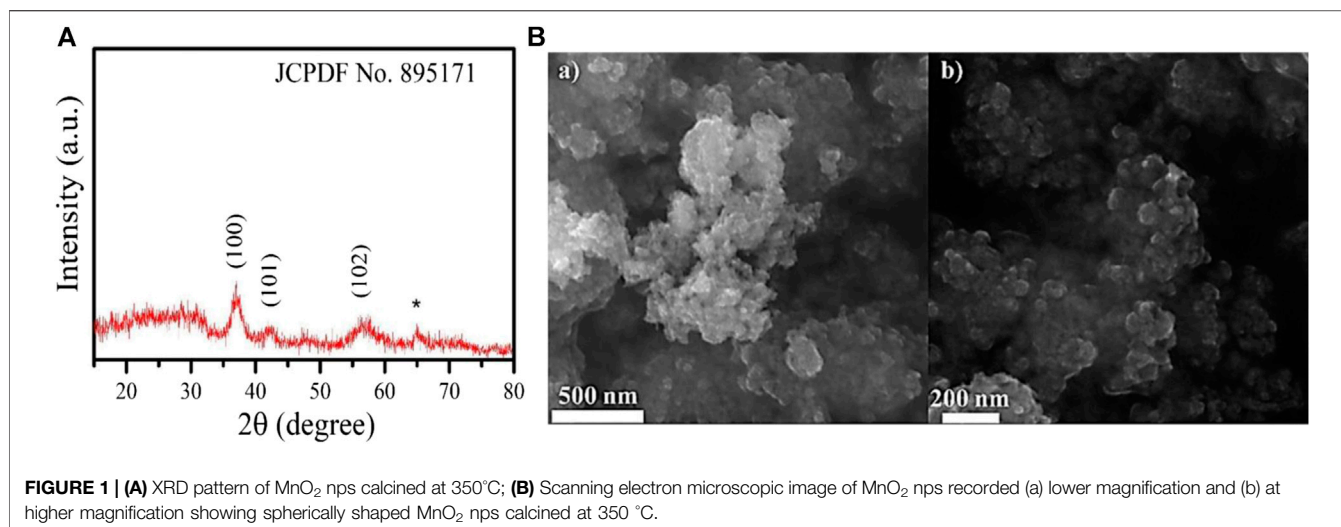
Phosphate buffer saline was prepared in the laboratory at different pH.

2.2 Synthesis of MnO$_2$ nps

MnO$_2$ nps were synthesized by the co-precipitation method described in our previous paper with a different calcination temperature (Singh et al., 2020) (Dhiman et al., 2020). After completing the synthesis process, the obtained dried powder was first ground to a fine powder and calcined at 350°C to get the MnO$_2$ phase.

2.3 Characterization Techniques

The phase and structure of synthesized nanomaterials were examined by the X-ray diffraction (XRD) method using XRD, Rigaku MiniFlex 600 X-Ray Diffractometer with CuKα radiation at λ = 1.54Å; operating at 40 kV and 15 mA of the samples from 20 to 80° at a scan rate of 3° per min with a step size of 0.02°. Raman spectra were recorded using Enspectr R 532 in the range of 250–1,250 cm^{-1} with a 532 nm excitation wavelength. The morphology, shape, and structure of the materials were explored by the MIRA II KMH-TESCAN field emission scanning electron microscope (FE-SEM) operated at 25 keV. For this study, MnO$_2$ nps were ultrasonically dispersed in deionized water. Interaction of MnO$_2$ nps with mycotoxins was determined using a Perkin-Elmer spectrum two Fourier transform infrared (FTIR) spectroscopy. The UV-visible absorption technique was used for the detection study through the titration process using T90 + UV/VIS Spectrometer PG Instruments Ltd.

2.4 Sensing Procedure

Absorption spectra of AFB1 and OchA were recorded in the wavelength range of 230–460 nm. The binding constant (k$_b$) between MnO$_2$ nps and AFB1/OchA was measured by UV-visible spectrophotometric titration method by changing the concentration of analytes (AFB1 and OchA). The sensing medium was phosphate buffer silane (PBS) maintained at pH 7. MnO$_2$ nps were dispersed in PBS, and the UV-Visible absorbance

was measured. Different concentrations (400 ng ml^{-1}–15 µg ml^{-1}) of the analyte solutions prepared in PBS were mixed with the MnO$_2$ nps dispersions, and the UV-Vis absorbance was carried out in the same wavelength range under similar conditions. The concentration of MnO$_2$ nps dispersion was fixed at 5 µg ml^{-1}.

3 RESULTS AND DISCUSSION

3.1 Structural and Morphological Studies

The XRD spectrum pattern of MnO$_2$ nps was recorded at room temperature to determine the phase-crystal structure and purity. **Figure 1A** shows the XRD spectrum of MnO$_2$ nps. MnO$_2$ nps were obtained by calcining the synthesized MnO$_2$ at 350°C. The diffraction peaks were observed at 2θ = 37.02°, 42.02°, and 56.81° and indexed as (100), (101), and (102). The observed peaks were matched with JCPDS file no. 895171 and ascribed to the hexagonal structure of Ɛ-MnO$_2$. The average crystallite size was calculated using Debye-Scherrer formulae as given below: (Kujur and Singh, 2020)

$$D = K\lambda / (\beta \cos(\theta))$$

where $K \sim 0.9$; wavelength (λ) = 1.5406 Å; full width at half maximum (FWHM) of the diffraction peaks is β, and the Bragg's diffraction angle is θ. The size calculated from Debye-Scherrer formulae was found to be 5.18 nm. Since the peaks are broad, having high FWHM indicates that the size of the MnO$_2$ is very small.

To further study morphology and nano crystallinity of the material, field-emission scanning electron microscopy (FE-SEM) was studied. **Figure 1B** shows the FE-SEM image of MnO$_2$ nps. The nanoparticles were found mostly in an aggregated form, which is due to the magnetic behavior. Even after the agglomeration, the structure of the MnO$_2$ nps was observed to be a spherical shape with a size ranging from 40 to 100 nm. These two studies confirm the hexagonal phase structure of MnO$_2$ with spherically shaped MnO$_2$ nps.
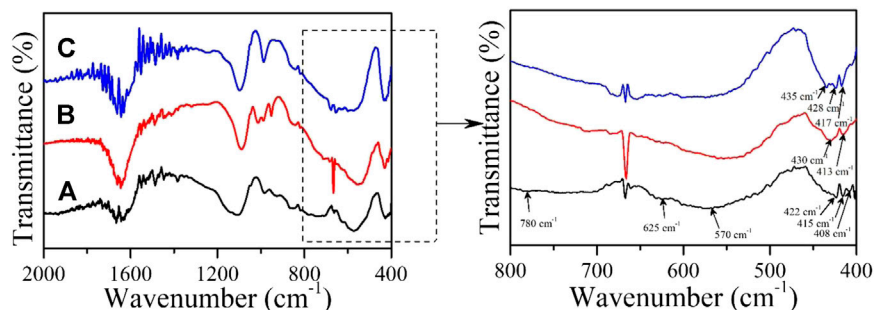
FIGURE 2 | Fourier transform infrared spectra of **(A)** MnO_2 nps, **(B)** AFB1-MnO_2, and **(C)** OchA-MnO_2 were recorded at room temperature.
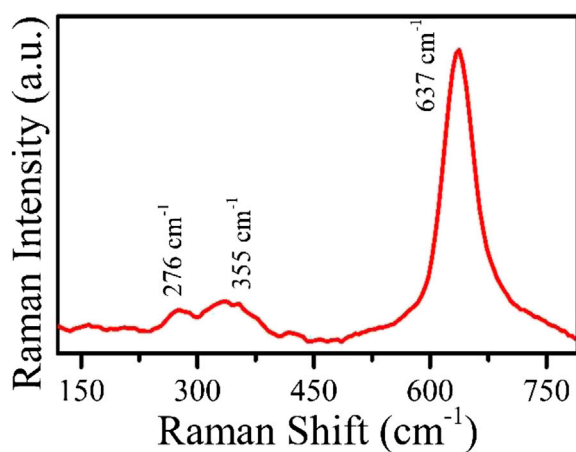
FIGURE 3 | Raman spectrum of MnO_2 nps recorded at room temperature (25°C).

The FTIR spectra of MnO_2 nps in the presence and absence of OchA and AFB1 is shown in **Figure 2**. The FTIR spectra were carried out to determine the interaction among MnO_2 nps with AFB1 and OchA and were recorded in the wavenumber range between 400 and 2000 cm^{-1}. The major peaks of Mn-O could be assigned in the range of 400–800 cm^{-1}. (Kang et al., 2007) (Feng et al., 1992). In the present study, several peaks for MnO_2 nps appeared at 408, 415, 422, 570, 625, and 780 cm^{-1}, representing the presence of Mn-O bond. During the interaction of AFB1 with the MnO_2 nps, the peaks of MnO_2 nps for Mn-O bond appeared slightly shifted or changed in their position between 400 and 440 cm^{-1}, indicating the interaction among these two molecules. Similar behavior obsereved for the OchA in presence of MnO_2 nps, and peak positions of Mn-O bond changed between 400 and 440 cm^{-1} as shown in **Figure 2**.

Raman spectroscopy was performed to see the crystal defects and phase composition of the material. The spectrum of MnO_2nps is shown in **Figure 3** recorded at 532 nm excitation source. The range shows three peaks at 276, 335, and 637 cm^{-1}. Theoretically, MnO_2 with a hexagonal structure has a significant peak centered at 637 cm^{-1}. Here the peaks at 276 and 335 cm^{-1}

are due to the bending vibration of Mn-O bond, and another peak at 637 cm^{-1} shows stretching vibration in MnO_2 bond. (Barai et al., 2016) (Gao et al., 2008). The indexing of the three peaks confirms the phase purity of MnO_2 without any defects.

3.2 UV-Visible Spectroscopic Studies of AFB1 and OchA With MnO_2 nps

UV-visible spectroscopy is a reliable and straightforward technique to study nanoparticles' optical activity, and it has also been used to monitor the interaction between nanomaterials and biomolecules. Increase or decrease of absorption and shifting of wavelength toward red/blue shift represents the interaction between the involved components. This technique has been proposed for the interaction study of the aromatic chromophore with nucleic acids like DNA, RNA, etc. In the study of interactions between nanoparticles and the analytes, the medium's pH plays an important role. Therefore, the pH-dependent study has been carried out at five different pHs. The pH-dependent analysis of AFB1 and OchA is shown in **Figure 4A** and **Figure 4B**. The absorption spectra were measured at different pH from five to nine between 230 and 460 nm of the wavelength range. In the case of AFB1, a significantly less pH effect was measured in the given range. While OchA shows increased absorption spectra with increasing the pH. However, the study was performed at neutral pH 7 for both the toxins as it is neutral.

3.3 UV-Visible Spectroscopic Studies to Explore Interactions of AFB1 and OchA With MnO_2 nps

The absorption spectrum of MnO_2 nps was recorded in the absence and presence of AFB1 and OchA mycotoxins in the range between 230 and 460 nm in PBS at pH 7. The MnO_2 nps absorption peak was obtained at 260 nm, as shown in the inset of **Figure 5** (a) and (b). Absorption spectra were recorded for both AFB1 and OchA under similar conditions in the presence of MnO_2nps. Two peaks were observed for AFB1 at 265 and 365 nm wavelength in which the broad peak at 365 nm of AFB1 shows a significant peak, as shown in **Figure 5A**. Similarly, two peaks were observed for OchA at 340 and 380 nm, where the 380 nm
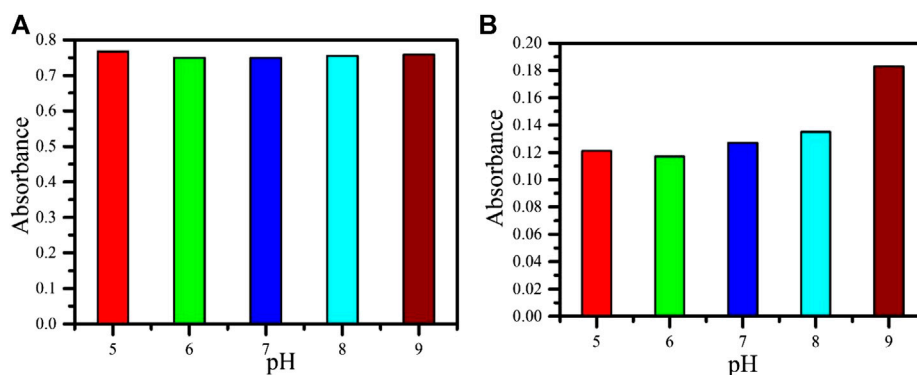
FIGURE 4 | (A) The effect of different pH for AFB1. **(B)** The effect of different pH for OchA.
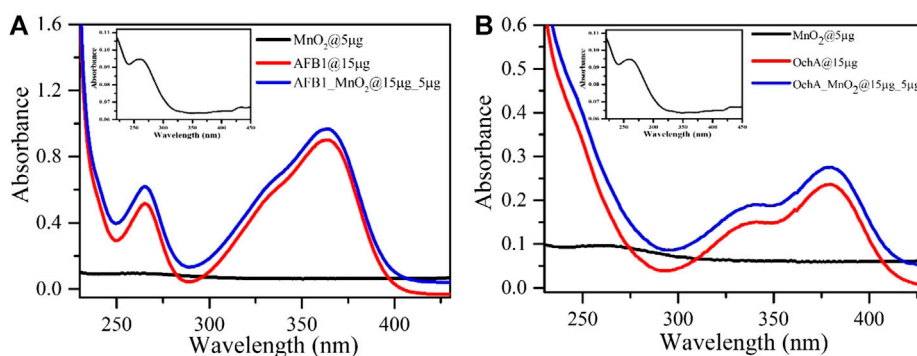
FIGURE 5 | (A) UV-visible absorption plot of MnO$_2$nps (zoomed image in both insets), AFB1, and AFB1 in the presence of MnO$_2$nps. **(B)** UV-visible absorption plot of OchA and OchA in the presence of MnO$_2$nps.
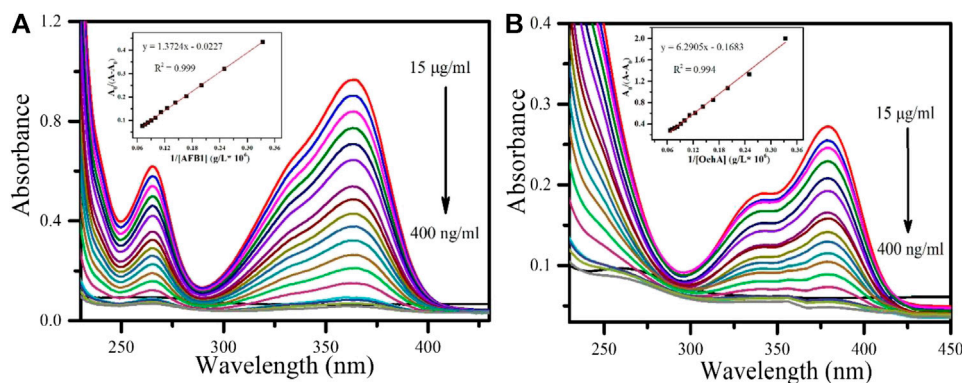
FIGURE 6 | UV-visible response study of **(A)** AFB1 at different concentrations (inset) calibration curve of AFB1 **(B)** OchA at different concentrations (inset) calibration curve of OchA.

wavelength broad peak shows the major one, as shown in **Figure 5B**. The absorption intensities of both AFB1 and OchA were increased, with the addition of MnO$_2$nps. This increase in the absorption peak of both toxins in the presence of MnO$_2$ nps indicates the interaction with MnO$_2$ nps.

The interaction study was performed using different concentrations of AFB1 and OchA (400 ng ml^{-1}–15 µg ml^{-1}) at fixed MnO$_2$ nps concentrations. The molecular interaction between the chromophore and nucleic acid was observed based on the absorption spectra changes and shifting of
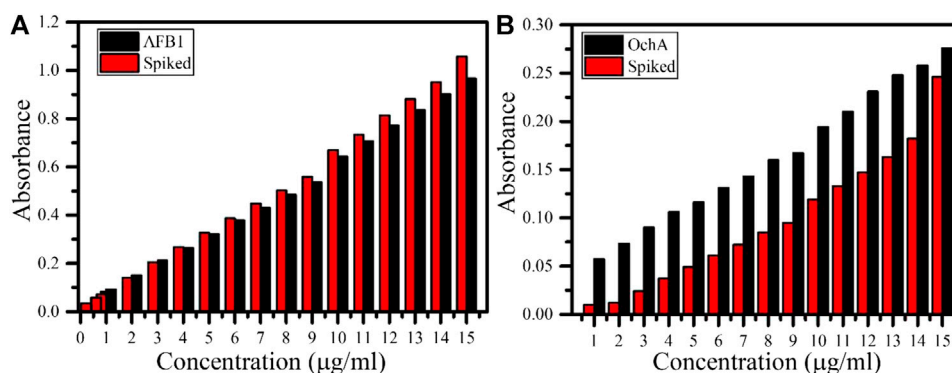
FIGURE 7 | Spiked corn sample study in comparison of **(A)** AFB1 and **(B)** OchA.

the wavelength toward the red/blue side (Hajian and Guan Huat, 2013).

The interaction between AFB1 (**Figure 6A**) and OchA (**Figure 6B**) with MnO_2 nps was measured using the principle of UV titration method. In this phenomenon, the absorption peak of AFB1 for the highest concentration $(15\,\mu g\,ml^{-1})$ at 365 nm wavelength was observed to be highest because of maximum interaction and energy exchange from MnO_2 nps to AFB1. With decreasing the concentration of AFB1, the sequential decreased in absorption peaks was observed due to fewer AFB1 molecules in the solution. On the other hand, OchA also performed similarly to that of AFB1. In the case of OchA, the absorption peak for the highest concentration $(15\,\mu g\,ml^{-1})$ was observed at 380 nm wavelength, and by decreasing the concentration, the absorption decreased. Thus, using the same MnO_2 nps, the two different mycotoxins AFB1 and OchA, were detected at the different absorption wavelengths.

The continuous decrease in the concentration from $15\,\mu g\,ml^{-1}$–$400\,ng\,ml^{-1}$ of AFB1 and OchA led to a change in absorption spectra intensity, which was slowly saturated. The peak intensity at 365 nm corresponding to AFB1 decreases with the decrease in the concentration of AFB1. Similarly, for OchA, the decreasing pattern corresponded to 380 nm and decreased the concentrations. This approach was followed by calculating the binding constant between MnO_2 nps and AFB1, determined using the Wolfe–Shimer equation. (Hajian et al., 2017) (Hajian and Guan Huat, 2013) The Wolfe–Shimer equation is given below:

$$\frac{A_0}{A - A_0} = \frac{\varepsilon_G}{\varepsilon_{H\text{-}G} - \varepsilon_G}\left[1 + \frac{1}{k_b\,[AFB1/OchA]}\right]$$

Here, A_0 and A represent the absorbance of MnO_2nps in the absence and presence of AFB1 and OchA, respectively, ε_G, $\varepsilon_{H\text{-}G}$ are their respective absorption coefficient, k_b represents the binding constant, and [AFB1] and [OchA] shows the concentration of [AFB1] and [OchA].

A linear plot was observed between $\frac{A_0}{A - A_0}$ vs. $\frac{1}{[AFB1]/[OchA]}$. The binding constant (k_b) was calculated as 1.62×10^4 and

$2.67\times10^4\,Lg^{-1}$ for AFB1 and OchA, respectively, from the linear equation, and the intercept ratio was the slope.

3.4 Spiked Sample Study

The response of AFB1 and OchA was also monitored in the spiked real corn sample with varying concentrations of $15\,\mu g\,ml^{-1}$ to $1\,\mu g\,ml^{-1}$ under similar conditions shown in **Figure 7 (A)** and **(B)**, respectively. During the measurement, the above-mentioned concentrations of each AFB1 and OchA were spiked in the corn sample. In the case of AFB1 **Figure 7A**, the magnitude of the spiked sample's absorbance was increased slightly compared to AFB1. The recovery percentage of the spiked sample was obtained between 78.26 and 109.42%. On the other hand, the spiked OchA sample's absorbance was much decreased compared to OchA (**Figure 7B**), and the recovery percentage was recorded between 17.5 and 89.13%.

3.5 Interferent Study

The interference study was carried out to prove the proposed system's applicability in real corn samples, as shown in **Figure 8** for AFB1(A) and OchA (B) separately. This study was carried out in the presence of fumonisin (FuB1) mycotoxin and naturally occurring chemicals in corn, such as D-fructose, cellulose, and starch. To test the selectivity, $10\,ug\,ml^{-1}$ of interferents (FuB1, D-fructose, cellulose, and starch) were introduced inside the solution MnO_2 nps, and absorption spectra were recorded. Results have shown the higher selectivities for AFB1 and OchA with MnO_2 nps compared to various interferents.

3.6 Thermodynamic Analysis

To understand the mechanism involved in the titration interactions, the thermodynamic parameters help. The Gibbs free energy of the system was therefore calculated. The Gibbs free energy is the thermodynamic system that measures the thermodynamic parameter at constant temperature and pressure. Study of Gibbs free energy for AFB1 led to the driving forces that govern the binding of AFB1 to MnO_2 nps. The driving forces dictate the association between AFB1 and MnO_2 nps, which results from interaction and energy exchange
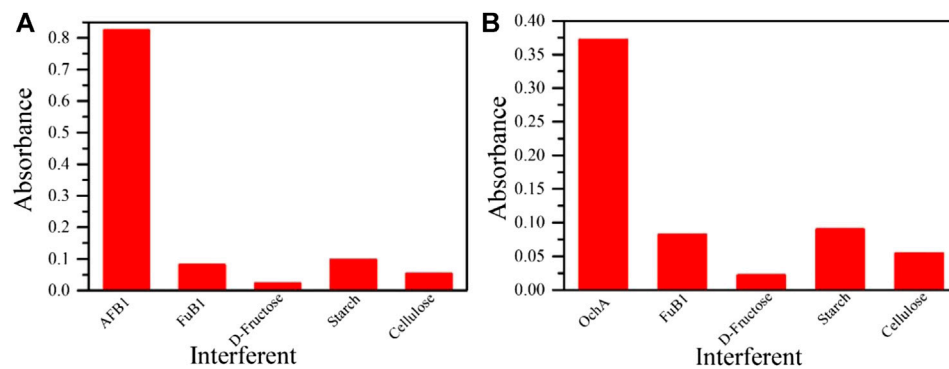
FIGURE 8 | Selectivity studies of **(A)** AFB1 and **(B)** OchA.
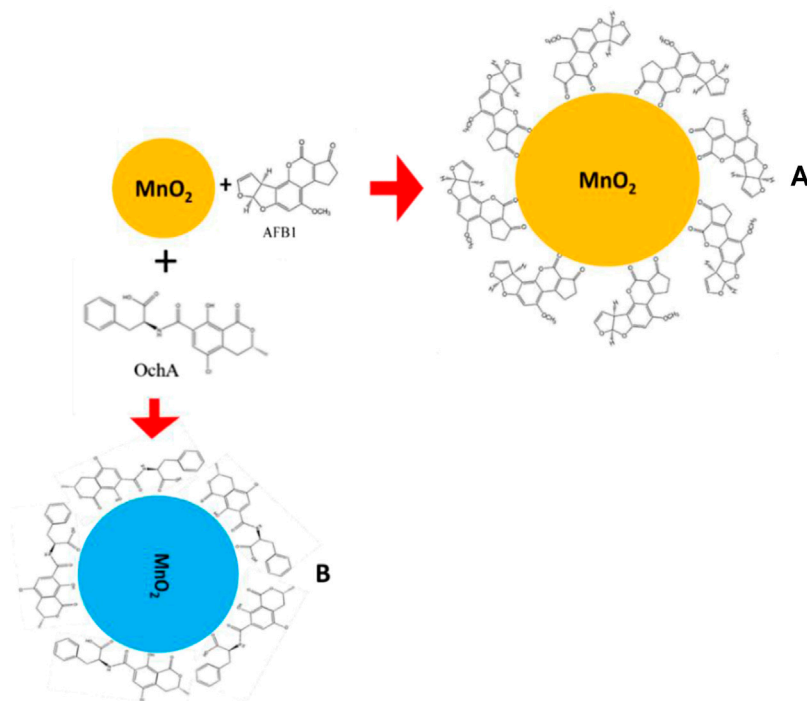
FIGURE 9 | Schematic of interaction between MnO$_2$ nps and AFB1 **(A)** and OchA **(B)** explaining a sequential decrease in the absorbance of OchA.

among them. In this respect, the thermodynamic analysis was carried out to investigate the standard Gibbs free energy (ΔG^0) change for the binding of AFB1 and OchA with MnO$_2$ nps. (Hajian and Guan Huat, 2013). The expression of a standard Gibbs relation is given below:

$$\Delta G = -RTlnk_b$$

where R is gas constant, and T is the temperature (25°C) in Kelvin.

The calculated Gibbs free energy for the interaction between AFB1 and OchA with MnO$_2$ nps are −24.002 and −25.256 kJ/mol, respectively. The interaction between the AFB1 and OchA with MnO$_2$ nps took place through electrostatic interaction because of

the positive nature of MnO$_2$ nps as it interacts with AFB1 and OchA. As is shown in **Figures 5A,B**, the UV-visible absorption spectra of AFB1 and OchA have maximum absorption peaks at 365 and 380 nm, respectively. The intensity enhancement of the absorption peaks of MnO$_2$ nps after toxins is the preliminary identification of interaction. The increase of the absorption spectra was associated with the AFB1, and OchA molecules adsorbed at the interface of the MnO$_2$ nps. The schematic illustration to propose electrostatic interaction between MnO$_2$ nps with AFB1 and OchA is shown in **Figure 9**. The outcomes of the sensing performance achieved in this research and comparison of reported systems are summarized in **Table 1**. In all the reported literature, the

TABLE 1 | Summary of sensing performance in comparison to reported sensors.

S.No	Material	Technique	LOD	Range	Refernces
1	PAN/ZnO nanofibers	Photoluminoscence	39 pg/ml	0.1–20 ng/ml	Myndrul et al. (2020)
2	Aptamer/Au nps	TIRE/LSPR	–	0.01–100 ng/ml	Ghanim Al-Rubaye et al. (2018)
3	GO-Cd/Se quantum dots	FRET	0.004 µg/ml	0.002–0.2 µg/ml	VV et al. (2018)
4	CdTe quantum dots	FRET	20 pm	0.1–0.6 µmol/ml	Zekavati et al. (2013)
5	MnO_2 nps	Absorbance	AFB1–4.08 ng/ml OchA–10.84 ng/ml	0.4–15 µg/ml	Present work

photoluminescence property of SPR was mainly used, whereas, in the present study, the sensing parameter was absorbance change through the UV-titration method. Also, in the present study, two toxins AFB1 and OchA were studied simultaneously with different absorbance wavelengths.

4 CONCLUSION

This research, for the first time, presented MnO_2 nps for bio-active, mediator, and labeled free detection of AFB1 and OchA rapidly and at a very low level. In this optical sensing approach, it is observed that the UV-visible spectroscopic technique exhibited a well-defined distinguished absorption peak for AFB 1 and OchA at wavelengths of 365 and 380 nm, respectively, binding with MnO_2 nps. Such a distinguished absorption band, specific to the targeted toxin, varied as a function of AFB 1 and OchA concentration. Such MnO_2 nps-toxin (AFB1/OchA) exhibited detection range as $15\,\mu g\,ml^{-1}$–$400\,ng\,ml^{-1}$ and LOD as 4.08 (AFB1)/10.84 (OchA) ng/ml. We believe that such of highly sensitive MnO_2 nps based AFB1 and OchA optical sensing can be developed as an analytical system of reduced form factor with potential application in food safety management.

DATA AVAILABILITY STATEMENT

The original contributions presented in the study are included in the article/Supplementary Material, further inquiries can be directed to the corresponding authors.

AUTHOR CONTRIBUTIONS

All the authors discussed and visualized scientific aspects of the research. AKS, TKD and GBVSL conducted experiments. AK and PRS guided well throughout the research.

REFERENCES

Abarca, M. L., Bragulat, M. R., Castella, G., and Cabanes, F. J. (1994). Ochratoxin A production by strains of Aspergillus niger var. niger. *Appl. Environ. Microbiol.* 60, 2650–2652. doi:10.1128/AEM.60.7.2650-2652.1994

Abramson, D., Usleber, E., and Märtlbauer, E. (1995). An indirect enzyme immunoassay for the mycotoxin citrinin. *Appl. Environ. Microbiol.* 61, 2007–2009. doi:10.1128/AEM.61.5.2007-2009.1995

Administration (FAD) (1988). Action levels for added poisonous or deleterious substances in food. *Not. Fed. Regist.* 53, 5043–5044.

Altug, T. (2002). *Introduction to toxicology and food.* Boca Raton, Florida: CRC Press, 168.

Azri, F. A., Sukor, R., Selamat, J., Abu Bakar, F., Yusof, N. A., and Hajian, R. (2018). Electrochemical immunosensor for detection of aflatoxin B1 based on indirect competitive ELISA. *Toxins* 10, 196. doi:10.3390/toxins10050196

Bajpai, V. K., Shukla, S., Khan, I., Kang, S.-M., Haldorai, Y., Tripathi, K. M., et al. (2019). A sustainable graphene aerogel capable of the adsorptive elimination of biogenic amines and bacteria from soy sauce and highly efficient cell proliferation. *ACS Appl. Mater. Interf.* 11, 43949–43963. doi:10.1021/acsami.9b16989

Barai, H. R., Banerjee, A. N., Hamnabard, N., and Joo, S. W. (2016). Synthesis of amorphous manganese oxide nanoparticles–to–crystalline nanorods through a simple wet-chemical technique using K+ ions as a 'growth director'and their morphology-controlled high performance supercapacitor applications. *RSC Adv.* 6, 78887–78908. doi:10.1039/c6ra18811g

Battacone, G., Nudda, A., Palomba, M., Pascale, M., Nicolussi, P., and Pulina, G. (2005). Transfer of aflatoxin B1 from feed to milk and from milk to curd and whey in dairy sheep fed artificially contaminated concentrates. *J. Dairy Sci.* 88, 3063–3069. doi:10.3168/jds.S0022-0302(05)72987-8

Borneman, J., and Becker, J. O. (2007). Identifying microorganisms involved in specific pathogen suppression in soil. *Annu. Rev. Phytopathol.* 45, 153. doi:10.1146/annurev.phyto.45.062806.094354

Cancer (1982). Chemicals, industrial processes and industries associated with cancer in humans. *IARC Monogr. Eval. Carcinog. Risk Chem. Hum. Suppl.* 1982, 7–24.

Crook, M. (2003). Handbook of toxicologic pathology. *J. Clin. Pathol.* 56, 160. doi:10.1136/jcp.56.2.160-b

Dhiman, T. K., Lakshmi, G., Kumar, R., Asokan, K., and Solanki, P. R. (2020). Non-enzymatic detection of Glucose using a capacitive nanobiosensor based on PVA capped CuO synthesized via co-precipitation route. *IEEE Sensor. J.* 20, 10415–10423. doi:10.1109/JSEN.2020.2994356

Dhiman, T. K., Lakshmi, G., Roychoudhury, A., Jha, S. K., and Solanki, P. R. (2019). Ceria-nanoparticles-based microfluidic nanobiochip electrochemical sensor for the detection of ochratoxin-A. *Chemistry* 4, 4867–4873. doi:10.1002/slct.201803752

Duarte, S. C., Pena, A., and Lino, C. M. (2010). A review on ochratoxin A occurrence and effects of processing of cereal and cereal derived food products. *Food Microbiol.* 27, 187–198. doi:10.1016/j.fm.2009.11.016

Feng, Q., Miyai, Y., Kanoh, H., and Ooi, K. (1992). Lithium (1+) extraction/insertion with spinel-type lithium manganese oxides. Characterization of redox-type and ion-exchange-type sites. *Langmuir* 8, 1861–1867. doi:10.1021/la00043a029

Gallo, A., Ferrara, M., and Perrone, G. (2017). Recent advances on the molecular aspects of ochratoxin A biosynthesis. *Curr. Opin. Food Sci.* 17, 49–56. doi:10.1016/j.cofs.2017.09.011

Ganeshan, S., Ramasundari, P., Elangovan, A., Arivazhagan, G., and Vijayalakshmi, R. (2017). Synthesis and characterization of MnO$_2$ nanoparticles: study of structural and optical properties. *Int. J. Sci. Res. Phys. Appl. Sci.* 5, 5–8. doi:10.26438/ijsrpas/v5i6.58

Gao, T., Glerup, M., Krumeich, F., Nesper, R., Fjellvåg, H., and Norby, P. (2008). Microstructures and spectroscopic properties of cryptomelane-type manganese dioxide nanofibers. *J. Phys. Chem. C* 112, 13134–13140. doi:10.1021/jp804924f

Ghanim Al-Rubaye, A., Nabok, A., Catanante, G., Marty, J.-L., Takács, E., and Székács, A. (2018). Label-free optical detection of mycotoxins using specific aptamers immobilized on gold nanostructures. *Toxins* 10, 291. doi:10.3390/toxins10070291

Hajian, R., and Guan Huat, T. (2013). Spectrophotometric studies on the thermodynamics of the ds-DNA interaction with irinotecan for a better understanding of anticancer drug-DNA interactions. *J. Spectrosc.* 2013, 1–8. doi:10.1155/2013/380352

Hajian, R., Hossaini, P., Mehrayin, Z., Woi, P. M., and Shams, N. (2017). DNA-binding studies of valrubicin as a chemotherapy drug using spectroscopy and electrochemical techniques. *J. Pharm. Anal.* 7, 176–180. doi:10.1016/j.jpha.2017.01.003

Heenan, C. N., Shaw, K. J., and Pitt, J. I. (1998). Ochratoxin A production by Aspergillus carbonarius and A. niger isolates and detection using coconut cream agar. *J. Food Mycol.* 1 (2), 67–72.

Henry, S. H., Bosch, F. X., Troxell, T. C., and Bolger, P. M. (1999). Reducing liver cancer–global control of aflatoxin. *Science* 286 (80), 2453–2454. doi:10.1126/science.286.5449.2453

Jaimez, J., Fente, C. A., Vazquez, B. I., Franco, C. M., Cepeda, A., Mahuzier, G., et al. (2000). Application of the assay of aflatoxins by liquid chromatography with fluorescence detection in food analysis. *J. Chromatogr. A* 882, 1–10. doi:10.1016/s0021-9673(00)00212-0

Jouni, F. J., Zafari, J., Abdolmaleki, P., Vazini, H., Ghandi, L., and Satari, M. (2018). Aflatoxin M$_1$ detoxification from infected milk using Fe$_3$O$_4$ nanoparticles attached to specific aptamer. *J. Nanostruct. Chem.* 8, 13–22. doi:10.1007/s40097-017-0250-5

Kang, L., Zhang, M., Liu, Z.-H., and Ooi, K. (2007). IR spectra of manganese oxides with either layered or tunnel structures. *Spectrochim. Acta Mol. Biomol. Spectrosc.* 67, 864–869. doi:10.1016/j.saa.2006.09.001

Kaushik, A., Solanki, P. R., Pandey, M. K., Ahmad, S., and Malhotra, B. D. (2009a). Cerium oxide-chitosan based nanobiocomposite for food borne mycotoxin detection. *Appl. Phys. Lett.* 95, 173703. doi:10.1063/1.3249586

Kaushik, A., Solanki, P. R., Sood, K. N., Ahmad, S., and Malhotra, B. D. (2009b). Fumed silica nanoparticles–chitosan nanobiocomposite for ochratoxin-A detection. *Electrochem. Commun.* 11, 1919–1923. doi:10.1016/j.elecom.2009.08.016

Keller, J., Moldenhauer, D., Byrne, L., Haase, H., Resch-Genger, U., and Koch, M. (2018). Complexes of the mycotoxins citrinin and ochratoxin A with aluminum ions and their spectroscopic properties. *Toxins* 10, 538. doi:10.3390/toxins10120538

Kujur, V. S., and Singh, S. (2020). Structural, magnetic, optical and photocatalytic properties of GaFeO$_3$ nanoparticles synthesized via non-aqueous solvent-based sol–gel route. *J. Mater. Sci. Mater. Electron.*, 1–14. doi:10.1007/s10854-020-04318-2

Kőszegi, T., and Poór, M. (2016). Ochratoxin A: molecular interactions, mechanisms of toxicity and prevention at the molecular level. *Toxins* 8, 111. doi:10.3390/toxins8040111

Lim, C. W., Yoshinari, T., Layne, J., and Chan, S. H. (2015). Multi-mycotoxin screening reveals separate occurrence of aflatoxins and ochratoxin a in Asian rice. *J. Agric. Food Chem.* 63, 3104–3113. doi:10.1021/acs.jafc.5b00471

Liu, B., Huang, R., Yu, Y., Su, R., Qi, W., and He, Z. (2018). Gold nanoparticle-aptamer-based lspr sensing of ochratoxin a at a widened detection range by double calibration curve method. *Front. Chem.* 6, 94. doi:10.3389/fchem.2018.00094

Liu, X., Chen, C., Zhao, Y., and Jia, B. (2013). A review on the synthesis of manganese oxide nanomaterials and their applications on lithium-ion batteries. *J. Nanomater.* 2013, 7. doi:10.1155/2013/736375

Marin, D. E., and Taranu, I. (2015). Ochratoxin A and its effects on immunity. *Toxin Rev.* 34, 11–20. doi:10.3109/15569543.2014.958757

Myndrul, V., Coy, E., Bechelany, M., and Iatsunskyi, I. (2020). Photoluminescence label-free immunosensor for the detection of Aflatoxin B1 using polyacrylonitrile/zinc oxide nanofibers. *Mater. Sci. Eng. C* 118, 111401. doi:10.1016/j.msec.2020.111401

Payne, G. A., and Brown, M. P. (1998). Genetics and physiology of aflatoxin biosynthesis. *Annu. Rev. Phytopathol.* 36, 329–362. doi:10.1146/annurev.phyto.36.1.329

Pflaum, T., Hausler, T., Baumung, C., Ackermann, S., Kuballa, T., Rehm, J., et al. (2016). Carcinogenic compounds in alcoholic beverages: an update. *Arch. Toxicol.* 90, 2349–2367. doi:10.1007/s00204-016-1770-3

Pfohl-Leszkowicz, A., and Manderville, R. A. (2007). Ochratoxin A: an overview on toxicity and carcinogenicity in animals and humans. *Mol. Nutr. Food Res.* 51, 61–99. doi:10.1002/mnfr.200600137

Pitt, J. I. (2000). Toxigenic fungi and mycotoxins. *Br. Med. Bull.* 56, 184–192. doi:10.1258/0007142001902888

Purtov, K. V., Shenderova, O. A., Luo, M., Brenner, D. W., and Bondar, V. S. (2007). The adsorption of aflatoxin B1 by detonation-synthesis nanodiamonds. *Dokl. Biochem. Biophys.* 417, 299–301. doi:10.1134/s1607672907060026

Ragupathy, P., Vasan, H. N., and Munichandraiah, N. (2007). Synthesis and characterization of nano-MnO$_2$ for electrochemical supercapacitor studies. *J. Electrochem. Soc.* 155, A34. doi:10.1149/1.2800163

Roberts, S. M., James, R. C., and Williams, P. L. (2014). *Principles of toxicology: environmental and industrial applications*. Gainesville, Florida: John Wiley and Sons, 496.

Ronchi, B., Danieli, P. P., Vitali, A., Sabatini, A., Bernabucci, U., and Nardone, A. (2005). "Evaluation of AFB1/AFM1 carry-over in lactating goats exposed to different levels of AFB1 contamination," in *Book of abstracts of the 56th annual meeting of the european association for animal production*. Uppsala, Sweden: EAAP, 1–10.

Sarkar, T., Dhiman, T., Sajwan, R., Sri, S., and Solanki, P. R. (2020). Studies on carbon quantum dots embedded iron oxide nanoparticles and their electrochemical response. *Nanotechnology* 31 (35), 355502. doi:10.1088/1361-6528/ab925e

Sarma, U. P., Bhetaria, P. J., Devi, P., and Varma, A. (2017). Aflatoxins: implications on health. *Indian J. Clin. Biochem.* 32, 124–133. doi:10.1007/s12291-017-0649-2

Shukla, S., Khan, I., Bajpai, V. K., Lee, H., Kim, T., Upadhyay, A., et al. (2019). Sustainable graphene aerogel as an ecofriendly cell growth promoter and highly efficient adsorbent for histamine from red wine. *ACS Appl. Mater. Interfaces.* 11, 18165–18177. doi:10.1021/acsami.9b02857

Singh, A. K., Dhiman, T. K., Lakshmi, G., and Solanki, P. R. (2020). Dimanganese trioxide (Mn$_2$O$_3$) based label-free electrochemical biosensor for detection of Aflatoxin-B1. *Bioelectrochemistry* 137, 107684. doi:10.1016/j.bioelechem.2020.107684

Smith, J. E., Solomons, G., Lewis, C., and Anderson, J. G. (1995). Role of mycotoxins in human and animal nutrition and health. *Nat. Toxins.* 3, 187–192. doi:10.1002/nt.2620030404

Solanki, P. R., Kaushik, A., Manaka, T., Pandey, M. K., Iwamoto, M., Agrawal, V. V., et al. (2010). Self-assembled monolayer based impedimetric platform for food borne mycotoxin detection. *Nanoscale* 2, 2811–2817. doi:10.1039/c0nr00289e

Van der Merwe, K. J., Steyn, P. S., Fourie, L., Scott, D. B., and Theron, J. J. (1965). Ochratoxin A, a toxic metabolite produced by Aspergillus ochraceus Wilh. *Nature* 205, 1112–1113. doi:10.1038/2051112a0

van Egmond, H. P., and Dekker, W. H. (1996). Worldwide regulations for mycotoxins—a compendium. *FAO Food Nutr. Pap.* 64, 1–43.

van Egmond, H. P., and Jonker, M. A. (2004). *Worldwide regulations for mycotoxins in food and feed in 2003*. Bilthoven, Netherlands: Food and Agriculture Organization of the United Nations, 188.

Velu, R., and DeRosa, M. C. (2018). Lateral flow assays for Ochratoxin A using metal nanoparticles: comparison of "adsorption–desorption" approach to linkage inversion assembled nano-aptasensors (LIANA). *Analyst* 143, 4566–4574. doi:10.1039/c8an00963e

VV, A. K. Y., Renuka, R. M., Achuth, J., Mudili, V., and Poda, S. (2018). Development of a FRET-based fluorescence aptasensor for the detection of aflatoxin B1 in contaminated food grain samples. *RSC Adv.* 8, 10465–10473. doi:10.1039/C8RA00317C

Wei, W., Cui, X., Chen, W., and Ivey, D. G. (2011). Manganese oxide-based materials as electrochemical supercapacitor electrodes. *Chem. Soc. Rev.* 40, 1697–1721. doi:10.1039/c0cs00127a

Zekavati, R., Safi, S., Hashemi, S. J., Rahmani-Cherati, T., Tabatabaei, M., Mohsenifar, A., et al. (2013). Highly sensitive FRET-based fluorescence immunoassay for aflatoxin B1 using cadmium telluride quantum dots. *Microchim. Acta.* 180, 1217–1223. doi:10.1007/s00604-013-1047-y

Zheng, N., Li, S. L., Zhang, H., Min, L., Gao, Y. N., and Wang, J. Q. (2017). A survey of aflatoxin M1 of raw cow milk in China during the four seasons from 2013 to 2015. *Food Contr.* 78, 176–182. doi:10.1016/j.foodcont.2017.02.055

3D-Printed Microfluidics and Potential Biomedical Applications

Priyanka Prabhakar[1,2], Raj Kumar Sen[1,2], Neeraj Dwivedi[1,2]*, Raju Khan[1,2], Pratima R. Solanki[3], Avanish Kumar Srivastava[1,2] and Chetna Dhand[1,2]*

[1]Industrial Waste Utilization, Nano and Biomaterials Division, CSIR-Advanced Materials and Processes Research Institute, Bhopal, India, [2]Academy of Scientific and Innovative Research (AcSIR), Ghaziabad, India, [3]Special Centre for Nanoscience, Jawaharlal Nehru University, New Delhi, India

3D printing is a smart additive manufacturing technique that allows the engineering of biomedical devices that are usually difficult to design using conventional methodologies such as machining or molding. Nowadays, 3D-printed microfluidics has gained enormous attention due to their various advantages including fast production, cost-effectiveness, and accurate designing of a range of products even geometrically complex devices. In this review, we focused on the recent significant findings in the field of 3D-printed microfluidic devices for biomedical applications. 3D printers are used as fabrication tools for a broad variety of systems for a range of applications like diagnostic microfluidic chips to detect different analytes, for example, glucose, lactate, and glutamate and the biomarkers related to different clinically relevant diseases, for example, malaria, prostate cancer, and breast cancer. 3D printers can print various materials (inorganic and polymers) with varying density, strength, and chemical properties that provide users with a broad variety of strategic options. In this article, we have discussed potential 3D printing techniques for the fabrication of microfluidic devices that are suitable for biomedical applications. Emerging diagnostic technologies using 3D printing as a method for integrating living cells or biomaterials into 3D printing are also reviewed.

Keywords: 3D printing, microfluidics, biosensor, disease diagnosis, biomedical applications

INTRODUCTION

Microfluidics is the science and technology used in channels with a range of 10–100 micrometers to control small amounts of fluid (10^{-9} to 10^{-18}). It offers new capabilities in space and time to control molecular concentrations (Tarn and Nicole, 2013; Bragheri et al., 2016). In terms of its bulk flow equivalent, microfluidic technology has several persuasive advantages, such as the need for fewer reagents and sample intake, favorable thermodynamics and chemical reaction kinetics, the profile of laminar flows, precise handling of single bioparticle, and strong parallels and multiplexing speeds (Knowlton et al., 2016; Kadimisetty et al., 2018a). Microfluidic chips allow accurate routing of fluid streams, but adequate sensing environments are needed for the external and internal stimuli (Han et al., 2019). Microfluidics is a lucrative sector that enables many biochemical and clinical applications such as cancer screening, engineering of microphysiological devices, medicinal research, and point-of-care diagnostics. Microfluidic systems are often complex, time-consuming, and costly with the requirement of sophisticated clean room setup (Weisgrab et al., 2019). 3D printing has changed the field of microfluidics significantly and also created innovative microfluidic devices that are usually impossible to design employing other approaches. Three-dimensional printing allows science and technology to be transformed by producing custom-made,

FIGURE 1 | (A) Timeline for producing 3D printing microfluidic devices in the last 10 years. Here, we emphasize on some examples of 3D printing microfluidic devices for biomedical applications. **(B)** The number of articles published on microfluidics and 3D printing annually. Data were obtained from "Web of Science" with "microfluidics and 3D printing" entered as "subject" in the search box (date: 07.09.2020). (Some portion of the figure is reproduced with permission of Lee et al., 2010; Gowers et al., 2015; Ruiz et al., 2020).

low-cost equipment requiring specialized equipment. An appealing but unexplored application is to use a 3D printer to initiate chemical reactions by printing the reagents directly into a 3D reaction ware matrix, putting reaction ware design, construction, and operation under digital control (Amin et al., 2016). 3D printing allows a microfluidic method but is currently limited to extraction-based printing and faces difficulties in applying it to other 3D printing modalities. 3D printing provides further potential for multi-material and multiphase printing (Symes et al., 2012). This article provides a detailed overview of 3D-printed microfluidics and their implication for different biomedical applications. One of the objectives of this review is to enrich the readers with knowledge about various potential 3D printing techniques explored for biomedical applications. Due to the main advantages of fast fabrication, simple accessibility, processing of different materials, and durability, 3D printing technology has flowered in sensing and for the development of 3D-printed microfluidic device for various applications in the biomedical sector (Zhang, 2019). **Figure 1A** shows the advancement in the development of 3D-printed microfluidic devices for various biomedical applications during the last 10 years. **Figure 1B** reveals the consistent enhancement in the total number of research publications in the field of 3D-printed microfluidics with progressing years.

3D PRINTING TECHNIQUES SUITABLE FOR BIOMEDICAL APPLICATION

A variety of 3D printing techniques are available which are suitable for a wide range of applications. In this review, we will be focusing on and presenting the 3D printing techniques which are relevant to the biomedical field. Some of the techniques are discussed in the following text.

Fused Deposition Modeling

Fused deposition modeling is the most popular additive manufacturing technique for making 3D-printed devices for biomedical applications because of its ease and cost-effectiveness. FDM is the extrusion-based 3D printing technique, in which thermoplastic polymeric materials are extruded to print objects layer by layer from a heated nozzle onto a surface or platform where it is cooled below its thermoplastic temperature, as shown in **Figure 2A**. This procedure is repeated until the 3D model is completed. FDM consists of the movable nozzle to print the materials in the x–y direction through which the model is built layer by layer. FDM was widely used to print scaffolds that can be seeded with living cells without loss of cell viability and to print biofriendly polymer materials. Polylactic acid (PLA), nylon, acrylonitrile butadiene
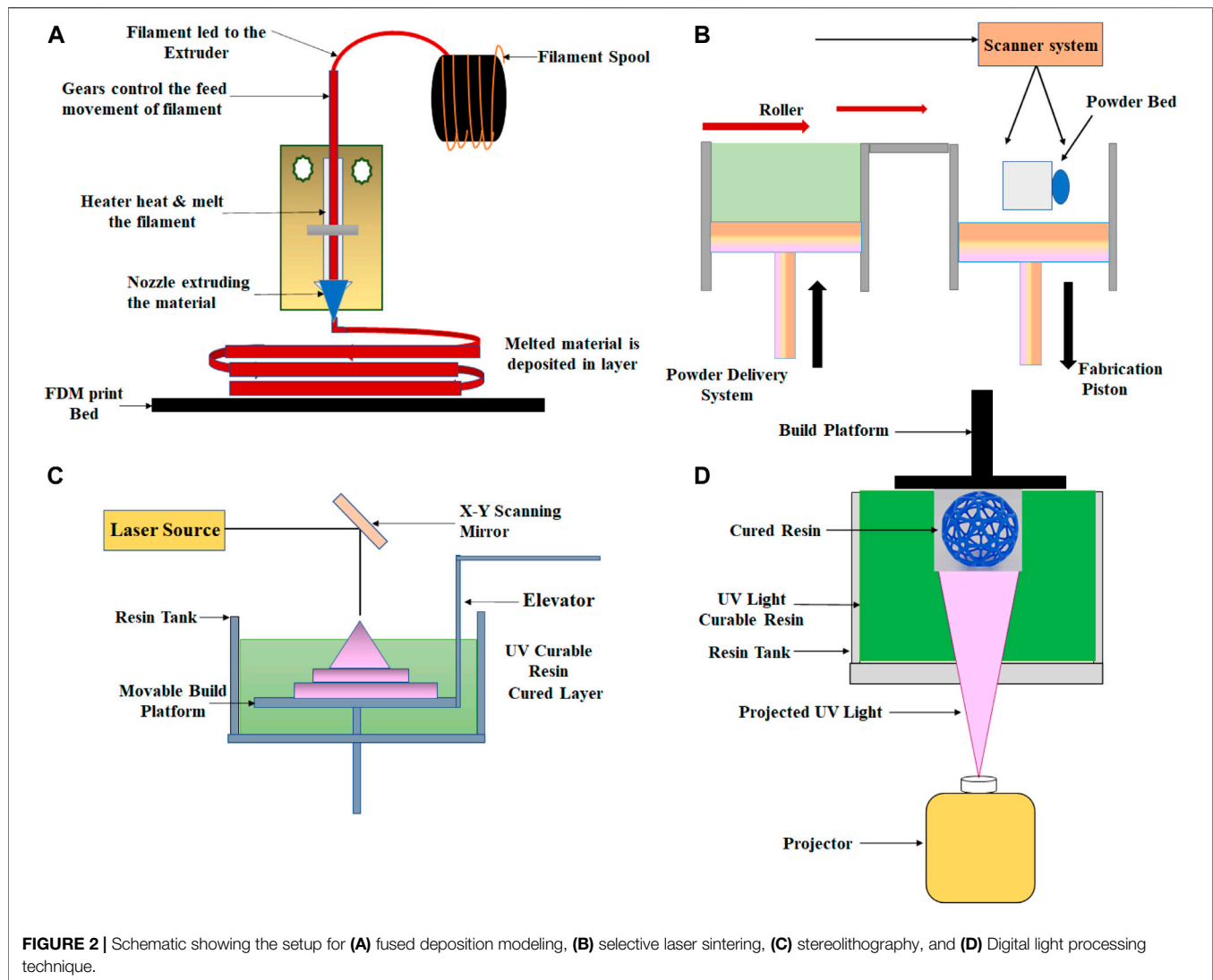
FIGURE 2 | Schematic showing the setup for **(A)** fused deposition modeling, **(B)** selective laser sintering, **(C)** stereolithography, and **(D)** Digital light processing technique.

styrene (ABS), wax blend, etc. are the commonly used thermoplastic materials in the FDM technique (Mohamed et al., 2015; Singh et al., 2016; Hagedorn 2017).

Selective Laser Sintering

SLS is a 3D printing technique which belongs to the family of powder bed fusion. In this technique, a laser beam is generally used to build layered objects by melting and fusing the powder, as shown in **Figure 2B**. In SLS, powder fusion is accomplished utilizing various particle-binding mechanisms, that is, by chemical reactions, by solid-state sintering, or by absolute or partial melting. The controlled laser beam scanning is used in this method to sinter the powder by heating. In this technique, the resolution parameter is dependent on the particle size of the powder, scanning speed and spacing, laser strength, and quality of the powder. To fabricate the final 3D object, the process is repeated several times. In the SLS process, polymers such as polystyrenes (PS), thermoplastic elastomers (TPE), polyamide (PA), polyaryletherketones (PAEK), and polycaprolactone (PCL)

are mainly used as laser sintering materials (Muzaffar et al., (2020); Munir et al., (2017); https://www.3dhubs.com/knowledge-base/indroduction-sls-3d-printing/).

Stereolithography

This additive manufacturing process is part of the Vat photopolymerization family. In this process, the ultraviolet (UV) laser beam is used to produce the object layer by layer, as shown in **Figure 2C**. In the stereolithography technique, the materials used are photosensitive thermoset polymers in the liquid form, and the procedure is repeated until the object is eventually created. By controlling the direction of the UV laser beam, the polymerization of the resin can be controlled to achieve the desired structure and design. The main advantages of the SL technique are high surface resolution and precision. Using this method, high-resolution products can be produced while keeping the minimum cost due to the relatively restricted use of the liquid medium (Melchels et al., 2010; Salonitis, 2014; Ko et al., 2017).
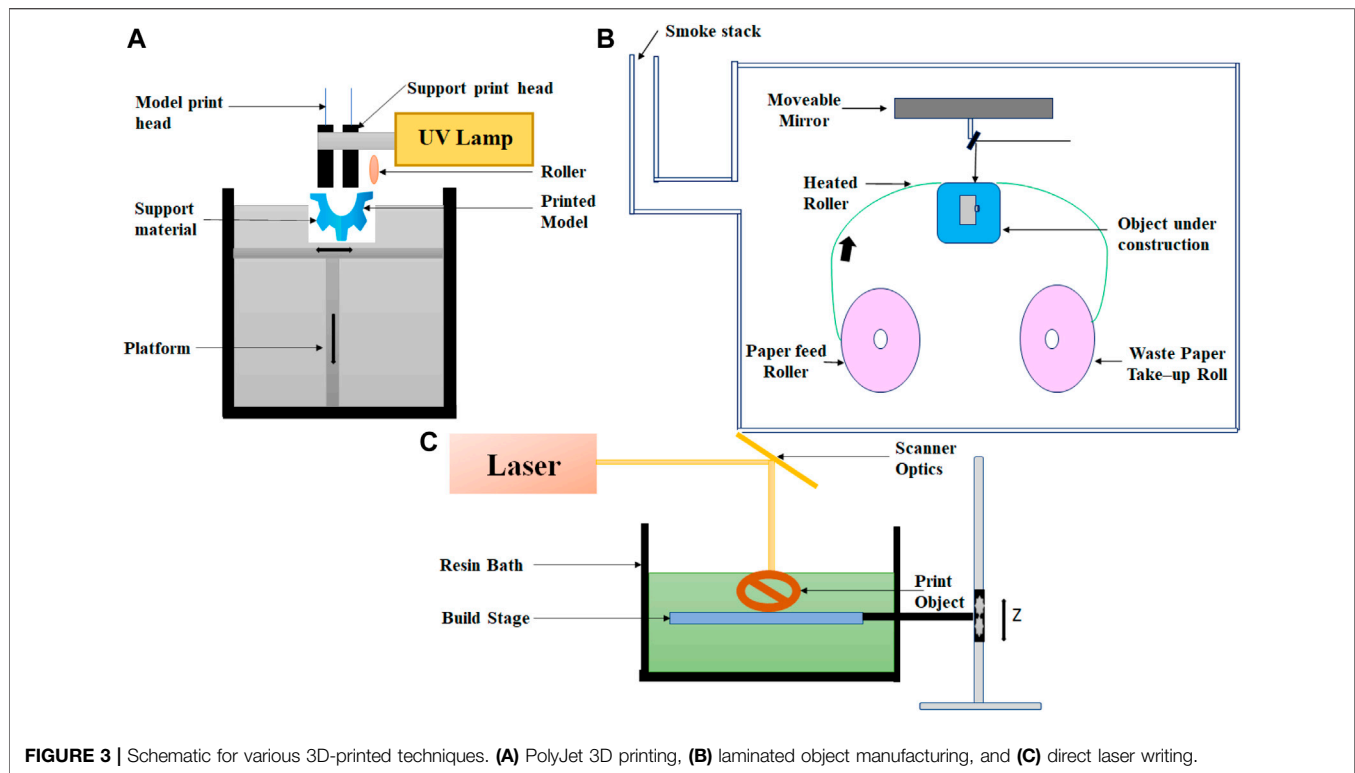
FIGURE 3 | Schematic for various 3D-printed techniques. **(A)** PolyJet 3D printing, **(B)** laminated object manufacturing, and **(C)** direct laser writing.

Digital Light Processing

DLP, an additive manufacturing technique, also belongs to the Vat photopolymerization family. DLP is quite similar to the SLA technique, except for the different photocuring process. In the DLP technique, the printer is used for the treatment of photopolymer resins, and UV light from the projector (light bulb) has been used to cure the photopolymer resin. In this process, each 2D layer is created after the liquid polymer is exposed to the light of the projector under the safest conditions, instead of having a layer with many laser scan paths, as shown in **Figure 2D**. DLP was used to build active component sensors that would alter their shape accordingly. In this technique, prototypes can be produced with good resolution, repeatability, and high accuracy (Schönberger and Hoffstetter, 2016; https://all3dp.com/2/what-is-a-dlp-3d-printer-3d-printing-simply-explain/).

PolyJet Process

The PolyJet process resembles inkjet printing. In this 3D printing technique, objects are built by jetting thousands of photopolymer droplets onto a built-in substrate and solidifying them with a UV light source, as shown in **Figure 3A**. The printer consists of many printing heads and movable platforms. Each printing head is filled with various types of liquid resins (different types of rubber or rigid, transparent, or opaque materials). In comparison to the inkjet process, a variety of materials may be sprayed and cured simultaneously. This technique has the potential to fabricate complex multi-material objects with smooth surface texture and with great accuracy. High-resolution objects of different modular strengths can be printed in three dimensions with high dimensional precision using this technology. Due to these capabilities, the PolyJet process is commonly used for different biomedical applications. (Tappa and Jammalamadaka, 2018; Matter-Parrat and Liverneaux, 2019; http://all3dp.com/2/polyjet-3d-printing-technologies-simply-explained; https://www.stratasys.co.in/polyjet-technology/).

Laminated Object Manufacturing

Laminated object manufacturing is one of the first commercially available 3D printing technique; it is based on layer-by-layer cutting and lamination of sheets or rolls of materials. A mechanical cutter or laser is used to cut the successive layer precisely, and then, it bonded together before it is laminated by the thermoplastic adhesive on top of the previous layer. Through a heated roller, the adhesive is activated, and the layer is laminated at a temperature between 60 and 80°C and a pressure of 10–30 MPa. Layers can be made out of metal sheets, plastic, or paper. The process may include postprocessing steps, including drilling and machining. The schematic diagram of LOM is shown in **Figure 3B**. This technique is very easy to use, cheap, and fast. Employing these techniques, relatively large-size objects can be fabricated but with a relatively lower resolution with the option of multicolor prototyping (Molitch-Hou, 2018; Ahangar et al., 2019; https://www.sculpteo.com/en/glossary/lom-definition).

Direct Laser Writing

It is the type of laser-based 3D printing where the focused laser light is used to illuminate at a single focal point, either on the surface or within a volume of photopolymerizable materials;

digitally controlled motorized stage and/or mirror galvanometers can then trace this illuminated focal point in a 3D space to produce a 3D structure (Hanada et al., 2011; Hwang et al., 2017). The block diagram of direct laser writing is shown in **Figure 3C**.

Inkjet Printing

In this 3D printing technique, powder particles are spread over the platform, and the hydrogel droplets or low-viscosity photocurable resin are used as printing materials. Liquid composition materials help to bind the powder particles to a solid of sufficient strength. Each layer can be constructed by ejecting the ink from the fine deposition nozzle, and the 3D model can be produced by a laser approach. Two types of inks are used in this technique for printing the object, one is wax-based and the other is liquid-based (Han et al., 2019).

Bioprinting

3D bioprinting is an additive manufacturing process in which organs and tissues are printed three dimensionally using a layer-by-layer method (Mukherjee et al., 2019). There are three stages in the 3D bioprinting process: pre-bioprinting, bioprinting, and postprinting. Bioprinting technologies, according to their working mechanism, can be divided into four main modalities: 1) inkjet-based bioprinting, 2) extrusion-based bioprinting, 3) stereolithography, and 4) laser-based bioprinting (Iordache, 2019). The ink used for bioprinting is commonly referred to as "bioink." In general, this bioink consists of living cells when printing tissues or organs, whereas in the case of printing scaffolds, it does not contain any living cells. Besides cells, the bioink consists of several polymer compositions in which the cells are suspended. Among the commonly used synthetic polymers in the bioprinting field are polycaprolactone (PCL), poly-l-lactic acid (PLLA), poly (lactic-co-glycolic acid) (PLGA), and poly (ethylene glycol) (PEG). The composite of synthetic and natural polymers offers tuneable viscosity, with high functionality (Papaioannou et al., 2019). Different 3D printing techniques were compared in **Table 1** on the basis of their working principle, material used, advantages, and disadvantages, for different biomedical application.

BIOMEDICAL APPLICATION FOR 3D PRINTING MICROFLUIDICS

In this section, we are discussing different 3D-printed microfluidic-based miniaturized devices and their implications toward different biomedical applications. A special focus has been emphasized on compiling the studies related to the designing of 3D-printed microfluidic-based sensors for various biomedical applications. On the road to this, Lee et al. have created hydrogel scaffolds containing fluidic channels to generate perfusable 3D artificial tissue composites by 3D bioprinting technique (Lee et al., 2010). The goal of this work is to simultaneously handle and print phase-transition materials, such as pH-sensitive, thermosensitive, photocurable, or chemically cross-linkable hydrogels, along with various cell types, which are essential for the creation of complex tissue-

like hydrogel scaffolds. The collagen hydrogel precursor is printed and cross-linked through a nebulized sodium bicarbonate solution. The heated gelatin solution that acts as a sacrificial factor for the fluidic channels was printed between the layers of collagen. To achieve 3D hydrogel block, the process was repeated layer by layer. This printed hydrogel block was then heated at 37°C, which allowed gelatin to liquefy selectively and drain, generating a hallow channel within the collagen scaffold. Interestingly, the human dermal fibroblast cells grown in the scaffolds with microfluidic channels showed better proliferation than the scaffold without the channels. Thus, integrating the on-demand capability of the 3D printing technique to print fluidic channel structures and cells in 3D scaffold architecture offers prospects to generate perfusable 3D artificial tissue composites. Yeong et al. fabricated porous PCL scaffolds for cardiac tissue engineering by selective laser sintering 3D printing technique (Yeong et al., 2010). In this method, a cardiac cell seeded construct is cultured *in vitro* before transplantation to the injured heart via minimally invasive surgery. C2C12 myoblasts have been cultivated on the scaffold to investigate the cellularity of the scaffold design for up to 21 days. The cell culture studies reveal that the scaffolds got densely populated with the growing cells even at 4 days postseeding (p.s.) and starts fusion and differentiation as early as 6 days p.s., which was confirmed using myosin heavy-chain immunostaining on 11th day p.s. Interesting, a steady number of cells were then maintained throughout 21 days of culturing.

Wu et al. fabricated 3D biomimetic microvascular networks embedded in the hydrogel matrix by omnidirectional printing (Wu et al., 2011). In this method, fugitive ink filaments are printed inside a photocurable gel reservoir that physically supports the patterned features, thereby enabling completely omnidirectional freeform fabrication. These hydrogel-based microvascular structures may have potential applications in 3D cell culture, tissue engineering, organ modeling, or autonomic healing. Wang et al. fabricated the 3D microfluidic origami device integrated with electrochemiluminescence (ECL) immunosensor for point-of-care detection of carcinoma antigen 125 (**Figure 4A**) (Wang et al., 2013). This ECL-based immunosensor device was manufactured by direct screen printing the carbon working counter electrodes and Ag/AgCl reference electrodes with their conductive pads on wax-patterned pure cellulose paper and was activated by folding to form a 3D electrochemical cell. To achieve high sensitivity, the working electrode was modified with gold nanoparticles (AuNPs) immobilized with first capture antibodies (**Figure 4B**). This microfluidic origami ECL immunodevice revealed a good linearity range from 0.01 to 100 U mL^{-1} and a detection limit of 0.0074 U mL^{-1} with good stability and sensitivity. The authors have proposed the possible application of this immunodevice in point-of-care testing of different tumor markers for remote regions and developing countries.

Toward the development of a rapid, sensitive, and specific detection system for influenza virus, Krejcova et al. have fabricated 3D-printed bead-based microfluidic chip (Krejcova et al., 2014). The working of the microfluidic device involves a
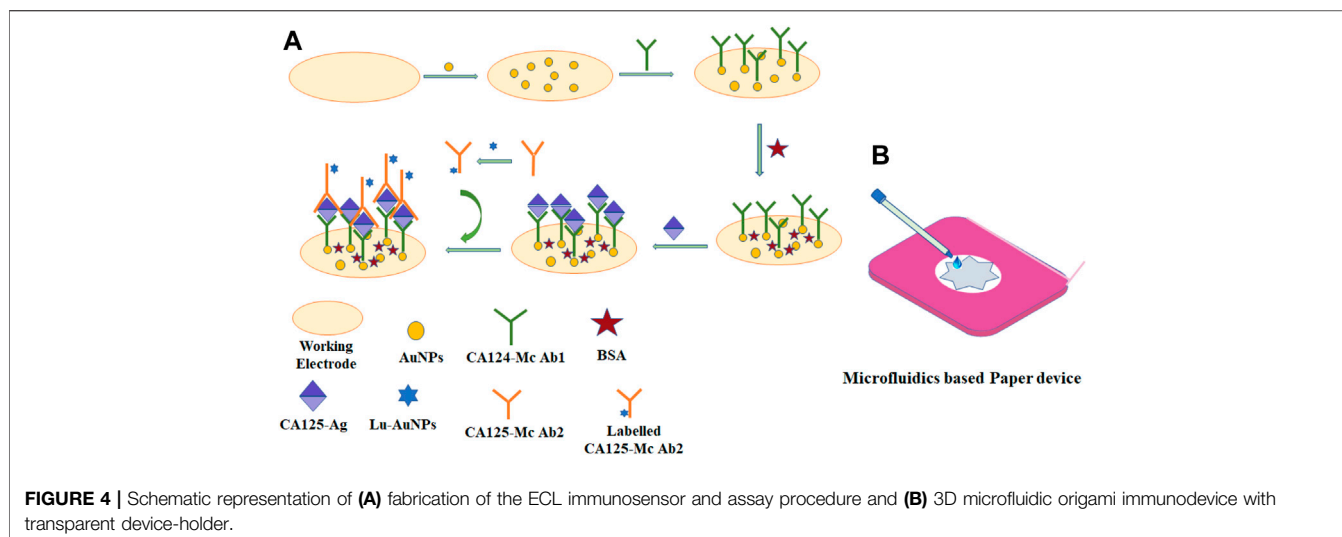
FIGURE 4 | Schematic representation of **(A)** fabrication of the ECL immunosensor and assay procedure and **(B)** 3D microfluidic origami immunodevice with transparent device-holder.

two-step procedure including the isolation involving the paramagnetic beads (MPs) and electrochemical detection. For the isolation process, the platform was created with streptavidin-modified MPs, which were conjugated via biotinylated glycan, followed by linkage of hemagglutinin to the glycan. Vaccine hemagglutinin (HAvaxi) was labeled with CdS quantum dots (HA-QDs) at first for detection purposes. Detection of the isolation product by voltammetry was the end point of the procedure. To design the 3D-printed chips, the FDM technique using polylactide material was used. This 3D-printed microfluidic system is emphasized to be a very promising and powerful tool for rapid influenza antigen diagnosis, and this approach can also be applied for the diagnosis of other pathogens. Lee et al. fabricated a novel method for the rapid detection of pathogenic bacteria using an immunomagnetic assay based on a 3D-printed microfluidic device and a luminescent ATP detection kit (Lee et al., 2014). In this work, binding between the antibody-functionalized magnetic nanoparticle clusters (AbMNCs) and the bacterium *Salmonella* was facilitated by magnetic immobilization of the AbMNCs on the surface of a three-dimensional microchannel in a hollow cylinder. This high capacity and sensitive diagnostic system showed a lower detection limit of 10 cfu/ml with a response time of 10 min. Erkal et al. fabricated two 3D-printed devices with acrylate-based polymer material using Objet Connex 350 multi-material printers for electrochemical detection of NO and dopamine (**Figure 5**) (Erkal et al., 2014). In both the printed devices, the electrode is housed in commercially available polymer-based fittings so that the various electrode materials (platinum, platinum black, carbon, gold, and silver) can be easily added to a threaded receiving port printed on the device. This will provide a module-like style to the experimental design, where the electrodes can be removed, repolished, and reused after biological sample treatment. The first printed device embodies a microfluidic stage with a 500 × 500-µm channel and a threaded receiving port to permit the integration of either polyetheretherketone

(PEEK) nut-encased platinum black or glassy carbon electrodes for nitric oxide (NO) and dopamine detection, respectively. The embedded Pt/Pt–black electrode was reported to have a limit of detection of 1 µM with a broad linearity range of 7.6–190 µM for NO gas, whereas with the glassy carbon electrode, the device showed the detection range of 25–500 µM with LOD of 500 nM for dopamine. The second 3D-printed fluidic device is reported to allow the assortment of biologically relevant analyte ATP and measures its release signal simultaneously.

Chen et al. have developed 3D-printed microfluidic device using Objet Connex 350 printers and successfully used it to facilitate the quantitative determination of ATP release from erythrocytes (ERYs) stored under different conditions by the use of a plate reader (Chen et al., 2014). They stored ERYs in AS-1 (a currently approved storage solution) and AS-1N (AS-1 with modified glucose concentrations) were circulated and checked on a single 3D printing unit, greatly improving the effectiveness of the experimental data by reducing the uncertainty of using different devices. Six channels incorporated into the system allow high-throughput flow analysis, and the static wells between channels facilitate simultaneous internal standards and/or calibrators. Roda et al. developed a smartphone-based chemiluminescence biosensor for noninvasive and easy monitoring of the endurance performance of athletes through lactate detection (Roda et al., 2014). Disposable mini cartridge fabricated by the FDM 3 D printing technology can easily be prototyped to turn any kind of smartphone or tablet into portable luminometer to detect chemiluminescence derived from enzyme-coupled reactions. As a proof of concept, lactate oxidase was combined with horseradish peroxidase for the determination of lactate in oral fluid and sweat. Lactate can be measured in less than 5 mins with detection limits of 0.5 and o.1 mmol/L in oral fluid and sweat. Chudobova et al. fabricated a 3D-printed chip, with gold nanoparticle (AuNP) probes as methicillin-resistant *Staphylococcus aureus* (MRSA) indicators, which are suitable for bacterial cultivation, DNA isolation, PCR, and detection of amplified genes (Chudobova et al., 2014). The detection of
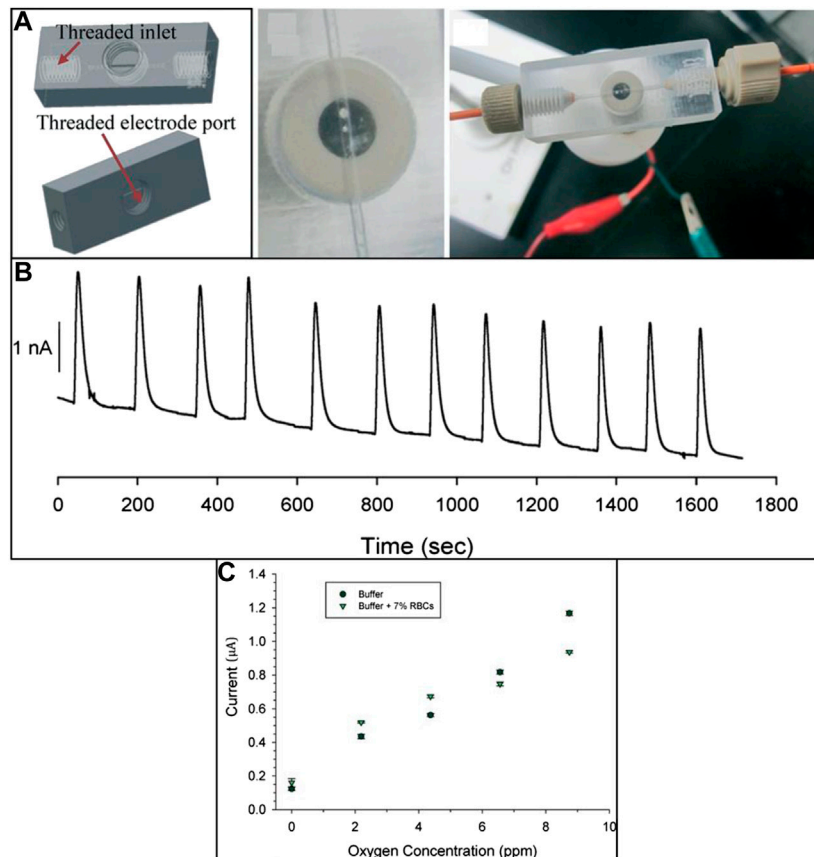
FIGURE 5 | (A) 3D-printed device with 0.5-mm wide microfluidic channels designed for the electrochemical detection of dopamine, nitrous oxide, and oxygen concentration. **(B)** Amperogram of reproducible 190 μM NO injections over the Pt/Pt–black electrode. **(C)** Calibration curve data for oxygen standards in the buffer and the presence of RBC (reproduced with permission from Erkal et al., 2014).

MRSA in the samples was based on the specific interactions between the mecA gene with AuNP probes and the colorimetric detection, which used the non–cross-linking aggregation phenomenon of DNA-functionalized AuNPs. This system was capable of colorimetric determination of the MRSA in a microfluidic reactor, allowing it to be used for *in vitro* diagnostics.

Wearable sensors connected to sensor networks of the body can deliver real-time information about the wearer's health and fitness, which are of great interest commercially. In this lane, Gowers et al. for the first time developed a 3D-printed wearable microfluidic device integrated with FDA-approved clinical microdialysis probes and needle-type biosensors for constant monitoring of the human tissue metabolite levels (Gowers et al., 2015) (**Figure 6**). The authors demonstrated the potential of this 3D-printed microfluidic system as a wearable device for subcutaneous monitoring of tissue glucose and lactate levels in cyclists during exercise. The clear changes recorded in the local glucose and lactate levels indicate that this device could have huge potential for real-time monitoring and assessing athlete training effectiveness.

Bishop et al. used the stereolithography technique for fabricating the 3D-printed microfluidic device which is integrated with a biosensor electrode for the measurement of

electrochemiluminescence signal (**Figure 7**) (Bishop et al., 2015). The ECL generated from [Ru(bpy)$_3$]$^{2+}$ in TPA buffer solution or DNA on a pencil graphite electrode was readily detected using a CCD bioimaging camera. The results derived from this study indicate that this 3D-printed platform can serve as an effective platform for designing more advanced and low-cost ECL-based sensing systems. Kadimisetty et al. have developed a novel, low-cost, gravity-flow microfluidic immunosensor with polylactide acid (PLA) using fused deposition modeling technique for detection of three cancer biomarker proteins (Kadimisetty et al., 2016). This supercapacitor-powered electrochemiluminescence (ECL) protein immune array detects simultaneously prostate-specific antigens (PSAs), prostate-specific membrane antigens (PSMAs), platelet factor-4 (PF-4), and prostate cancer biomarkers within 35 min. This technology will provide responsive on-site cancer diagnostic in resource-limited environments and require only minor training.

Ragone et al. fabricated a portable and disposable electrochemical sensor for the "downward" sensing of metabolites or excreted biologically active molecules (Ragones et al., 2015). The rapid detection capability of biomarker alkaline phosphatase (ALP) excreted from colon cancer cell lines was demonstrated. The microfluid chip
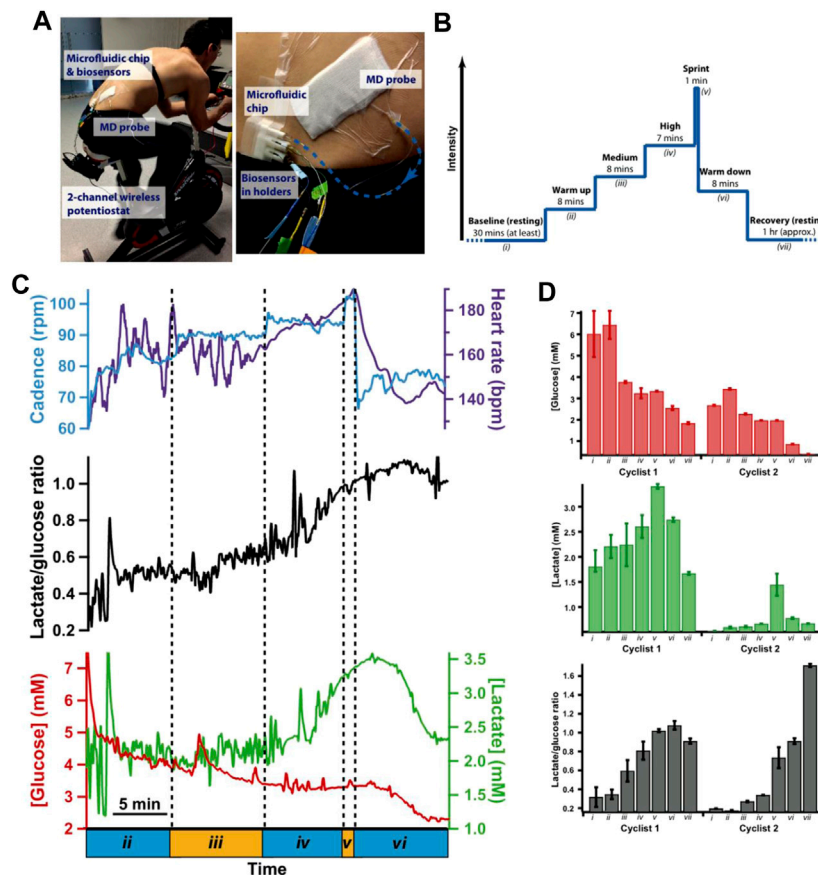
FIGURE 6 | (A) Photograph of a microfluidic device to measure tissue glucose and lactate levels in dialysate during the cycling protocol, (B) experimental protocol, (C) dialysate glucose, and lactate levels during the exercise phase of the cycling protocol system. (D) Histograms showing mean dialysate levels for two different cyclists during key points in the cycling protocol (reproduced with permission from Gowers et al., 2015).
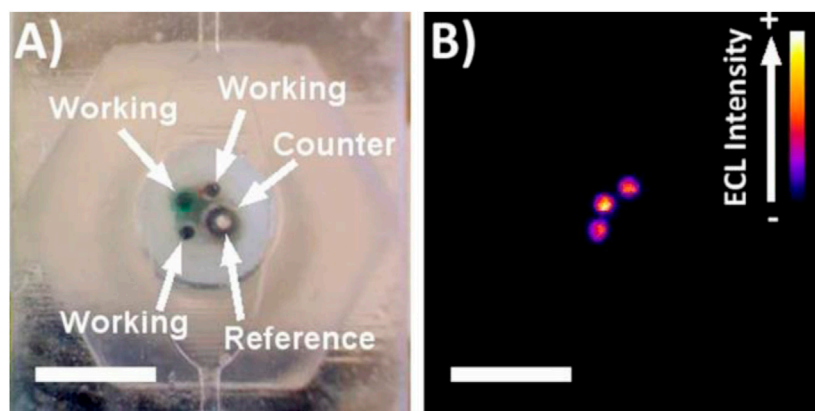
FIGURE 7 | (A) Picture of electrode arrays incorporated into 3D-printed channel. (B) ECL response from electrode array in 180 µM [Ru(bpy)$_3$]$^{2+}$ in 0.2 M phosphate buffer with 100 mM TPA (reproduced with permission from Bishop et al., 2015).

consists of a biocompatible substrate composed of an electrochemical cell with two gold electrodes as working and counter electrodes and an Ag/AgCl electrode as a quasi-reference electrode and it was fabricated by stereolithography 3D printing technique. The electroactivity of working electrodes was verified by cyclic voltammetry of a ferrocyanide/

FIGURE 8 | (A) 96-well malaria-based assay (APTEC) was modified to microbead based assay for improved functionality. The assay functions using aptamer-functionalized microbeads to collect PfLDH from patient blood samples. The production reagent is applied after washing, which creates a blue response for malaria-positive samples, using the enzymatic activity of PfLDH. **(B,C)** The response of prototypes of APTEC point-of-care devices using different PfLDH concentrations in serum samples (5% BSA) for the syringe test and well test which turns blue when positive. The response was quantified using absorbance (A570 nm) (reproduce with permission from Dirkzwager et al., 2016).

ferricyanide redox reaction. Amperometric *in vitro* detection of the biomarker alkaline phosphate was successfully demonstrated directly in a cell culture plate from three separate colon cancer lines while preserving their biological environment. Cevenini et al. have reported a compact stand-alone toxicity sensor that integrates bioluminescent cells into a smartphone-based system (Cevenini et al., 2016). They fabricated 3D-printed cartridges to incorporate a variety of bioluminescent cells into ready-to-use cartridges and demonstrated the feasibility of accurate detection and quantification of BL signals. Human embryonic kidney cells (Hek293T) have been constitutively used to express green-emitting luciferase as sentinel cells, and an Android app was created to provide a user-friendly environment. The smartphone adaptor and mini cartridges were fabricated by the 3D printing technique.

Dirkzwager et al. aimed to develop a point-of-care malaria diagnostic test using the adaption of an aptamer-tethered enzyme capture (APTEC) sensing system using 3D printing technology as a platform for rapid prototyping (Dirkzwager et al., 2016). The assay functions by capturing the malaria biomarker *Plasmodium falciparum* lactate dehydrogenase (PfLDH) from samples and using its intrinsic enzymatic activity to generate a visualizable

blue color in response to *Plasmodium*-positive samples (**Figure 8**). With the help of the stereolithography 3D printing technique, they developed two prototypes, magnetic bead-based well test and paper-based syringe test. Both were found to have been effective in detecting recombinant PfLDH at ngmL^{-1} concentration using low sample volumes (20 μL) and could work using distilled or spiked whole blood samples with easy sample preparation. The syringe test required additional preparation for measuring and found to be more analytically sensitive, while the magnetic bead-based well test required fewer steps and could therefore be ideally suitable for future clinical trials.

Su et al. fabricated flow bioreactors using a commercial 3D FDM-type printer and developed a simple procedure for the functionalization of printed ABS reactors to facilitate the determination of glucose and lactate in biological samples (Su et al., 2016). For monitoring the concentration of the rat brain extracellular glucose and lactate (**Figure 9**), this system involved microdialysis (MD) sampling and fluorescence determination in conjunction with a novel sample derivatization scheme in which glucose oxidase and lactate oxidase were immobilized in ABS flow bioreactors. To demonstrate the system's applicability, 1) spike analysis of
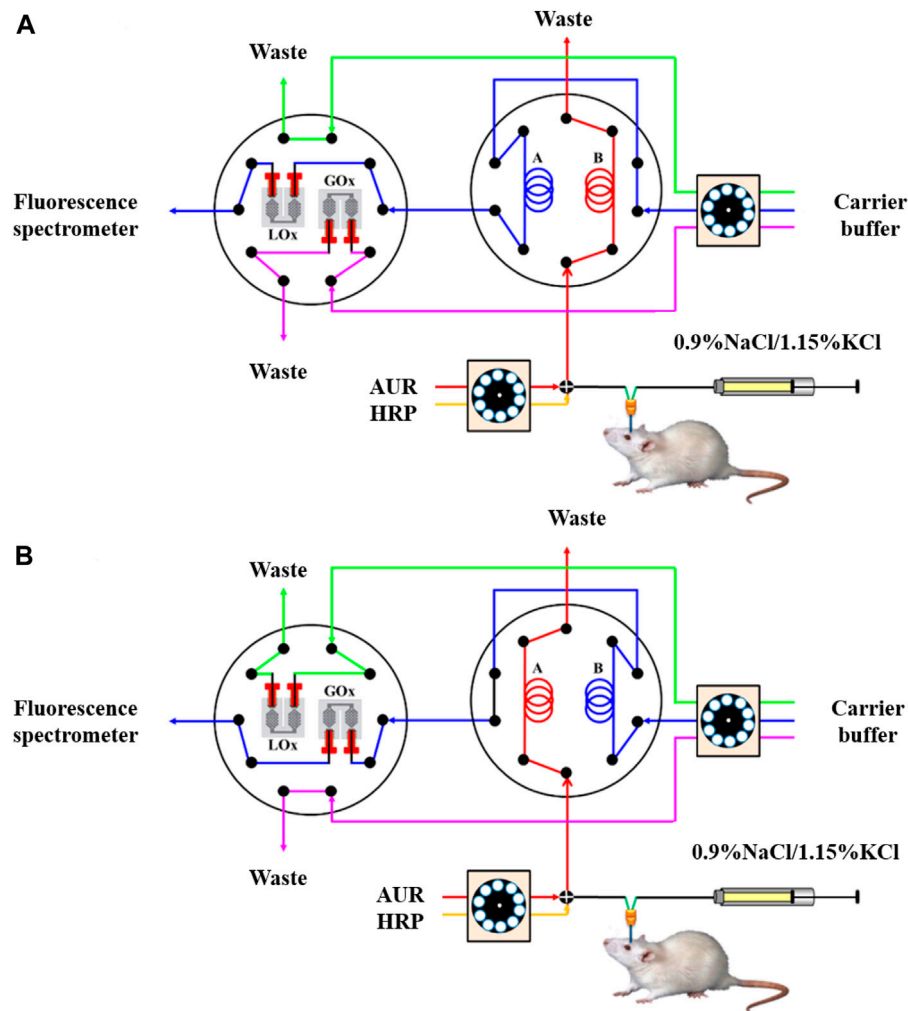
FIGURE 9 | Schematic representation of the proposed online glucose/lactate monitoring system. **(A)** Determination of lactate: The microdialysate was mixed online with two streams of AUR and HRP solutions and then loaded into sample loop A, while the conditioned microdialysate in sample loop B was transferred via the LOx-immobilized bioreactor to the fluorescence spectrometer. **(B)** Determination of glucose: The microdialysate was conditioned online and then loaded into sample loop B, while the conditioned microdialysate in sample loop A was transferred via the GOx-immobilized bioreactor to the fluorescence spectrometer (Reproduced with permission from Su et al., 2016).

offline-collected rat brain microdialysate and 2) *in vivo* dynamic monitoring of extracellular glucose and lactate in live rat brains, in addition to inducing neuronal depolarization by perfusing a high-K^+ medium from the implanted MD probe. Tang et al. developed the 3D-printed microfluidic system for automatic detection of cancer biomarker proteins using the stereolithography technique (Tang et al., 2017). This unibody consists of 1) three reagent reservoirs, 2) an effective 3D network for passive mixing, and 3) an optically transparent detection chamber housing in a glass slide decorated capture antibodies array for observing chemiluminescence output with CCD camera (**Figures 10A,B**). This low-cost automatic system was used for the diagnosis of cancer biomarker proteins such as platelet factor 4 (PF-4) and prostate-specific antigen (PSA). The detection limit of the sensor device is estimated to be 0.5 pg ml^{-1},

and good accuracy vs. ELISA was authenticated by analyzing human serum samples. This research system holds great promise for further advancement as a diagnostic device for early cancer treatment.

Sibbitt et al. fabricated the 3D microfluidic device by stereolithography technique (Sibbitt and He, 2017). The robustness and usability of these protocols allow the incorporation of modular 3D design and microfabrication of POC microfluidics integrated with smartphone-based interfaces as stand-alone disease diagnostic devices. It enables rapid exploration of biological phenomena at the microfluidic level by making microfluidic technology readily and easily accessible to researchers unfamiliar with microfabrication, expanding the reach of detection capabilities in POC microfluidic devices. Park et al.
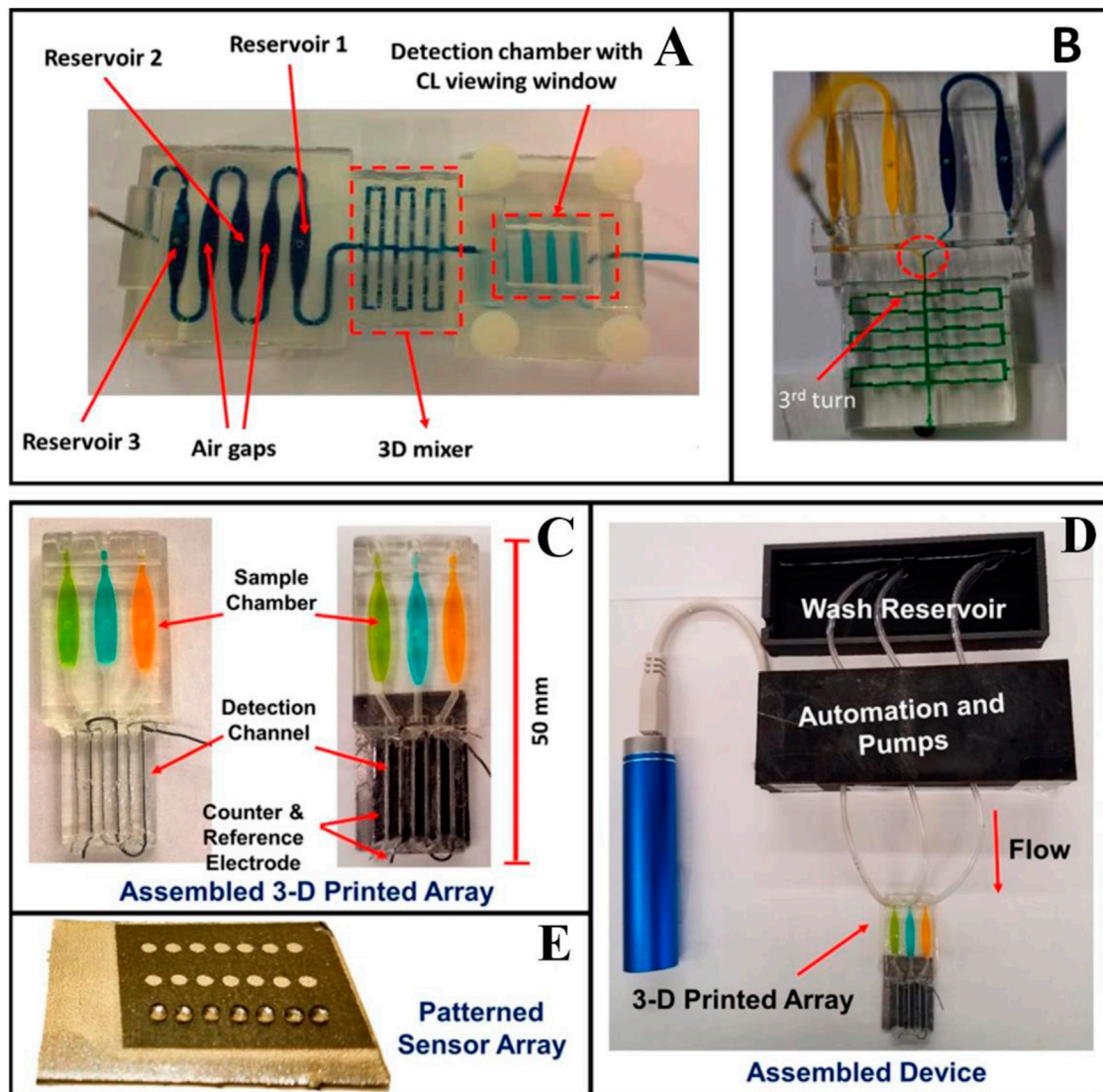
FIGURE 10 | (A) 3D-printed unibody CL immunoarray device. **(B)** A modified 3D-printed device to demonstrate the mixing ability of the passive 3D mixing network. **(C)** 3D-printed Automated genotoxicity screening device without or with microwell chip and counter electrode wires inserted showing the sample chamber dye solutions. **(D)** Microwell-patterned pyrolytic graphite detection array showing the first-row holding 1 μl water droplets retained by the hydrophobic microwell boundaries. Each row is fed by a separate sample line. The working array features films of DNA, metabolic enzymes, and RuPVP in each microwell. **(E)** Assembled array system showing box enclosing electronic microprocessors and micropumps driven by a rechargeable battery and connected to the 3-D printed array below with a wash reservoir with a containing pH 7.4 buffer. (Reproduced with permission from Tang et al., 2017 and Kadimisetty et al., 2017).

fabricated a 3D microfluidic magnetic preconcentrator (3DμFMP) which was used for the recognition of bacterial pathogen (*Escherichia coli* 0157:H7) (Park et al., 2017). *E. coli* 0157:H7 induces hemorrhagic colitis (HC) and hemorrhagic uremic syndrome (HUS) in a person who eats food infected with this microorganism. A 3D microfluidic magnetic preconcentrator is fabricated by a digital light processing 3D printer which is capable to selectively preconcentrate this bacterial pathogen in large-volume sample solutions into small volumes at the submillimeter scale by using specific antibody-conjugated magnetic nanoparticles for the pathogen. The optical determination was accomplished

through the use of a commercial ATP luminometer, where the ATP present on the preconcentrated bacterial cells was measured and quantified by the light emitted during each measurement, yielding a detection limit as low as 10 cfu/ml in blood. Kadimisetty et al. fabricated 3D-printed microfluidic array for the detection of the genotoxic potential of cigarettes, e-cigarette, and environmental samples (**Figures 10C–E**) (Kadimisetty et al., 2017). The microfluidic array is developed by using the stereolithography technique. Electronic cigarettes are battery-powered devices that vaporize nicotine and have been designed as an alternative to a tobacco cigarette; it is a very harmful substance for
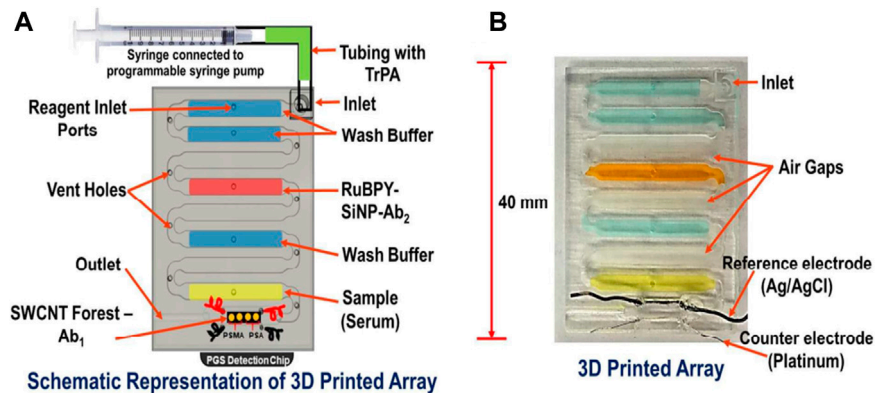
FIGURE 11 | (A) Model of an array with labelled reagent chambers connected to 4 microwells pyrolytic graphite (PGS) detection chip. **(B)** Picture of a 3D printed microfluidic array and fluidic chambers filled with colored dyes for identification. (Reproduced with permission from Kadimisetty et al., 2018b).

humans. The electrochemical luminescent (ECL) detection platform combines layer-by-layer film-assembled microsomal enzymes, DNA, and ECL-emitting ruthenium metallopolymers at a depth of 10 nm.

Santangelo et al. fabricated 3D printed microfluidic chip by using the stereolithography 3D printing technique which is coupled with the silicon photomultiplier (SiPM) (Santangelo et al., 2017). This 3D printed microfluidic chip is used for testing a miniaturized bioluminescence sensing system for highly sensitive real-time ATP detection. This interface allowed the sample solution to be delivered close to the SiPM to improve the detection efficiency of the bioluminescence light emitted from the sample solution. The use of SiPM as a detector greatly simplifies the analysis of signals compared to conventional systems, offering quantitative performance signals that do not require post-production of images and/or off-line analysis. Fraser et al. used stereolithography to fabricate the microfluidic device for malaria diagnosis (Fraser et al., 2018). They proposed a new design for malaria biosensors in which magnetic microbeads are coated with aptamers for magnet-guided capture, wash, and detection of the biomarker. A biosensor incorporating three separate microfluidic chambers was designed to enable such magnet guided equipment-free colorimetric detection of PfLDH. The biosensor showed high sensitivity and specificity when detecting PfLDH using both *in vitro* cultured parasite samples and using clinical samples from malaria patients. Kadimisetty et al. have demonstrated the use of stereolithography 3D printing technique to fabricate the microfluidic molecular diagnostic device involving nucleic acid amplification for preventing and treating infectious diseases (Kadimisetty et al., 2018a). They tested different surface coatings to enhance the biocompatibility of 3D printed microfluidic device, and showed that PEG coating provided the best results for nucleic acid-base molecular diagnostic. This device enables quick molecular diagnostic testing for infectious diseases at the point of diagnosis. They also demonstrated the suitability of the device for both real-time quantitative detection of fluorescence and end point colorimetric qualitative detection. This diagnostic device was

used to detect *Neisseria meningitides* in cerebrospinal fluid (CSF) samples and *Plasmodium falciparum* in plasma samples by loop-mediated, isothermal amplification (LAMP) in less time. This simple and affordable 3D printing tool has tremendous potential for POC molecular disease diagnosis in resource-constrained settings. In another report, Kadimisetty et al. demonstrated a 3D printed electrochemiluminescence (ECL) immunoarray for simultaneous detection of two proteins (Prostate-specific antigen and Prostate-specific membrane antigen) at the same time (**Figures 11A,B**) (Kadimisetty et al., 2018b). This 3D printed chip is combined with a nano pyrolytic graphite sheet microwell chip for detection of the same. Stereolithographic techniques are used to print this 3D device. With this program, a programmable syringe pump is used and allows the pump to halt and restore the reagent delivery as necessary for the completion of the sandwich immunoarrays. The designed device is reported to be very cost-effective with low detection time using a small sample size.

Diabetes has become a global public health epidemic. For testing the insulin level, Yao et al. have developed the pneumatic microfluidic device using a 3D-based extrusion printer for insulin detection using impedance spectroscopy measurement (Yao et al., 2018). The present research offers an important technological approach to the production of low-cost microfluidic tools for efficient reagent mixing in microscale biochemical detection systems. Oh et al. developed and fabricated a 3D-printed blood viscosity analysis (Oh and Choi, 2018). Viscosity measurement is essential for the quality assurance of liquid products, as well as for monitoring the viscosity of clinical fluids as a potential hemodynamic biomarker. They demonstrated multiplexed viscosity measurements of Newtonian fluids of varying viscosities and viscosity measurements of non-Newtonian fluid at different shear rate conditions. Samper et al. have developed and manufactured 3D-printed microfluidic device which can be easily integrated with the electrochemical biosensor for the detection of biomarkers such as glucose, lactate, and glutamate (Samper et al., 2019). The time resolution of the device is characterized by recording short lactate concentration pulses.

TABLE 1 | Comparative analysis of various 3D printing methods with a special focus on materials used, their benefits, and drawbacks.

Technique	Principle	Material	Advantage	Disadvantage
SLA	UV initiated polymerization cross section by cross section	Resin (epoxy based with proprietary or acrylate)	Large part can be easily manufactured, uncured material can be used, high accuracy, good for complex built, and good scalability	Slow building process, expensive, reduction in the durability of the product due to the involvement of moisture, heat, and chemicals
DLP	Photocuring by a digital projector screen to project layers by squared voxels.	Photo-resin and photopolymer	Excellent accuracy of laying, high resolution, and uncured photopolymer can be reused	Insecurity of the consumable material and difficult to print large structure
SLS	Laser induced sintering of powder particles	PVC, metallic powder, and polyamide	High strength and high resolution	Only metal parts can print, finishing or postprocessing required due to its grainy roughness, and difficulty in material change over
PolyJet process	Deposition of the droplets of the photocurable liquid material and cured	Polymer	Multiple jetting heads are available to build materials, different levels of flexibility, allows using different colored photopolymers, high accuracy, and smooth surface	Vulnerable to heat and humidity, lose strength over time, relatively higher cost than others, and sharp edges are often slightly rounded.
LOM	Paper cutting	Sheet metals, paper, cellulose, and plastic	Large parts can easily manufacture and low cost	Time-consuming and specific material types can be used
DLW	Laser-based	Fused silica, glass, etc.	Colorful printing	Post–surface treatment is required and low strength
Inkjet printing	Extrusion of ink and powder liquid binding	Hydrogel or photo-resin	High accuracy and very high surface finishes	Slow build process, low mechanical properties, to remove the moisture post processing is required, the grainy or rough appearance
FDM	Extrusion-based	Nylon, polylactic acid, wax blend, acrylonitrile butadiene, and styrene	Consume less time, high quality, and high speed	Weak mechanical properties
Bioprinting	Laser/UV	PCL, PLLA, and PEG	Cheap and high speed	Lack of accuracy in positioning of droplets

TABLE 2 | Summary of 3D printing technique used in biomedical application.

3D printing technique	Materials used	Applications	References
Stereolithography	Clear resin, pyrolytic graphite sheets, acrylate based resin, clear methacrylate-based resin, acrylate- and epoxy-based mixture, and PDMS	Detection of *Salmonella* bacteria, detection of electrochemiluminescence, sensing of metabolites detection of cancer biomarker proteins, diagnosis of malaria detection of genotoxic potential, diagnosis the malaria, detection of ATP, detection of prostate-specific antigen, monitoring the blood viscosity, and detection of *Salmonella typhimurium* DNA by LAMP	Lee et al. (2014); Bishop et al. (2015); Ragones et al. (2015); Tang et al. (2017); Dirkzwager et al. (2016); Kadimisetty et al. (2017); Sibbitt and He, (2017); Santangelo et al. (2017); Fraser et al. (2018); Kadimisetty et al. (2018a); Kadimisetty et al. (2018b); Oh and Choi (2018); Ruiz et al. (2020)
DLP	Photo-curable resin acrylate-based	Detection *Escherichia coli*	Park et al. (2017)
Extrusion-based technique	Polylactide and acrylonitrile butadiene styrene	Influenza virus, detection of lactate detection of cancer biomarkers, detection of glucose and lactate, detection of insulin, detection of MRSA, andsmartphone-based toxicity biosensor	Krejcova et al. (2014); Roda et al. (2014); Kadimisetty et al. (2016); Su et al. (2016); Yao et al. (2018); Chudobova et al. (2014); Cevenini et al. (2016); Zargaryan et al. (2020)
Inkjet 3D printing	Casting wax material	Cancer detection	Chen et al. (2019)
PolyJet process	Acrylate-based polymer	Oxygen recognition in the streamlining of red blood cells, nitric oxide detection and neurotransmitter detection, and detection of ATP	Erkal et al. (2014); Chen et al. (2014)
Ultra 3SP technique	Acrylonitrile butadiene styrene (ABS) white	Detection the level of glucose and lactate, glutamate, glucose, and lactate	Gowers et al. (2015); Samper et al. (2019)
Wax printing technique	Cellulose paper and filter paper	Carcinoma antigen 125, cell viability, and chemosensitivity	Wang et al. (2013); Fu et al. (2020)
MultiJet	Visijet M3 crystal polymer82 and Visijets 100 hydroxylated wax83	Treatment of an AMR infection	Sweet et al. (2020)
Bioprinting	Photocurable resin, hydrogels, and viscous materials	Making of vascular channel	Lee et al. (2010); Wu et al. (2011)

The device is employed to record simultaneous glutamate, glucose, and lactate concentration changes simulating the physiological response to spreading depolarization events in the cerebrospinal fluid dialysate. The system is also used in the ICU to monitor a patient's brain injury remotely, demonstrating its potential for clinical surveillance. Chen et al. designed a 3D-

printed microfluidic device to separate circulating tumor cells from human blood samples (Chen et al., 2019). The inner structure of microfluidic channels is functionalized with anti-EpCAM antibodies to have a clear capture of successful human cell lines of EpCAM (such as colon cancer SW480, prostate cancer PC3, and breast cancer MCF-7). Sweet et al. developed a 3D μ-concentration gradient generator (μ-CGG) prototype with the help of additive manufacturing to employing a unique 3D microchannel network (Sweet et al., 2020). 3D μ-CGG is used to identify the optimal drug compositions through antimicrobial susceptibility testing for the treatment of antimicrobial-resistant (AMR) infections. The AMR infection occurs when bacteria, viruses, fungi, and parasites adapt over time and no longer react to antibiotics that make infections more difficult to treat and increase the risk of disease spread, serious illness, and death. The MultiJet 3D printing technique and materials Visijet M3 crystal polymer82 and Visijets 100 hydroxylated wax83 are used to fabricate the 3D μ-CGG device.

Zargaryan et al. developed hybrid microfluidic devices that incorporate both 3D-printed and paper-based elements. This method operates by 3D printing directly onto a standard laboratory filter paper using widely available commercial fused deposition modeling printers (Zargaryan et al., 2020). They designed finger-actuated reservoirs and reversible mechanical valves that can be intuitively controlled by untrained users to demonstrate the capabilities of this technology. The intuitive design of device operation can be particularly useful for self-governing point-of-care research that reduces the burden on laboratory or healthcare systems during periods of need, such as the COVID-19 pandemic or other global health crises. Ruiz et al. defined a two-stage 3D printing process for the development of hybrid microfluidic devices integrating both hard and soft materials by using low-cost 3D consumer printers (Ruiz et al., 2020). Printed hard components are first created by a stereolithography (SLA) printer moved to a second FDM printer where a soft printed part is connected to the FDM printing. Three different types of hybrid microfluidics devices are microfluidic quick connect component, finger-actuated pump, and microfluidic reactor chip with screw-seal sample inlet ports, which are used to host isothermal amplification and detection of *Salmonella typhimurium* DNA by loop-mediated isothermal amplification (LAMP). Fu et al. presented a novel paper-like microfluidics 3D cell culture system to research cell viability and chemosensitivity in 3D environments using colorimetric measurement techniques (Fu et al., 2020). The cellulose filter paper was selected as a cell culture substrate with its advantages of biocompatibility,

inexpensive, enough source, and easy operation. The paper-based cell culture microfluidic device is fabricated by the wax printing 3D technique; it consisted of two layers: the upper layer was used for cell culture, while the lower layer was used for medium supply. According to the study of cell viability and chemosensitivity, the result indicates that the 3D culture microenvironment was effectively supplied by a paper unit. Based on this study, the anticancer drug successfully presented a specific cytotoxic effect on MCF-7 and HepG2 cultured using this wick-like paper-based system. **Table 2** summarizes details about various 3D printing technique used in different biomedical application.

CONCLUSION

The key advantages of 3D printing are freedom of design, mass customization, and the ability to print complex structures with minimal waste. In this review, we have discussed various 3D printing techniques for designing versatile microfluidic systems for different biomedical applications. Here, we explore a broad variety of 3D printing technologies available and highlight those that have so far been applied to microfluidic devices. 3D printing is an emerging technique with a variety of diagnostic devices for the detection of various clinically important analytes including glucose, lactate, glutamate, and biomarkers related to malaria, cancer, etc. With the surveyed and compiled literature, we strongly believe that the 3D printing technology if integrated with different modern techniques including microfluidics may lead to many benefits and possibilities in the medical therapies and industries.

AUTHOR CONTRIBUTIONS

PP, RS, CD, and ND prepared the manuscript. RK, PS and AS provided their valuable inputs to further improve the manuscript.

FUNDING

REFERENCES

Ahangar, P., Cooke, M. E., Weber, M. H., and Rosenzweig, D. H. (2019). Current biomedical applications of 3d printing and additive manufacturing. *Appl. Sci.* 9 (8), 1713. doi:10.3390/app9081713

Amin, A., Knowlton, S., Hart, A., Yenilmez, B., Ghaderinezhad, F., Katebifar, S., et al. (2016). 3D-printed microfluidic devices. *Biofabrication.* 8, 022001. doi:10.1088/1758-5090/8/2/022001

Bishop, G. W., Satterwhite-Warden, J. E., Bist, I., Chen, E., and Rusling, J. F. (2015). Electrochemiluminescence at bare and dna-coated graphite electrodes in 3d-printed fluidic devices. *ACS Sens.* 1 (2), 197202. doi:10.1021/acssensors.5b00156

Bragheri, F., Martinez Vazquez, R., and Osellame, R. (2016). Three-dimensional microfabrication using two-photon polymerization. *Microfluidics*, 310–334. doi:10.1016/b978-0-323-35321-2.00016-9

Cevenini, L., Calabretta, M. M., Tarantino, G., Michelini, E., and Roda, A. (2016). Smartphone-interfaced 3D printed toxicity biosensor integrating bioluminescent "sentinel cells". *Sens. Act. B: Chem.* 225, 249–257. doi:10.1016/j.snb.2015.11.017

Chen, C., Wang, Y., Lockwood, S. Y., and Spence, D. M. (2014). 3D-printed fluidic devices enable quantitative evaluation of blood components in modified storage solutions for use in transfusion medicine. *Analyst.* 139 (13), 3219–3226. doi:10.1039/c3an02357e

Chen, J., Liu, C. Y., Wang, X., Sweet, E., Liu, N., Gong, X., et al. (2019). 3D printed microfluidic devices for circulating tumor cells (CTCs) isolation. *Biosens. Bioelectron.* 2019, 111900. doi:10.1016/j.bios.2019.111900

Chudobova, D., Cihalova, K., Skalickova, S., Zitka, J., Rodrigo, M. A. M., Milosavljevic, V., et al. (2014). 3D-printed chip for detection of methicillin-resistant *Staphylococcus aureus* labeled with gold nanoparticles. *Electrophoresis.* 36 (3), 457466. doi:10.1002/elps.201400321

Dirkzwager, R. M., Liang, S., and Tanner, J. A. (2016). Development of aptamer-based point-of-care diagnostic devices for malaria using three-dimensional printing rapid prototyping. *ACS Sens.* 1 (4), 420–426. doi:10.1021/acssensors.5b00175

Erkal, J. L., Selimovic, A., Gross, B. C., Lockwood, S. Y., Walton, E. L., McNamara, S., et al. (2014). 3D printed microfluidic devices with integrated versatile and reusable electrodes. *Lab Chip.* 14, 2023–2032. doi:10.1039/c4lc00171k

Fraser, L. A., Kinghorn, A. B., Dirkzwager, R. M., Liang, S., Cheung, Y. W., Lim, B., et al. (2018). A portable microfluidic aptamer-tethered enzyme capture (APTEC) biosensor for malaria diagnosis. *Biosens. Bioelectron.* 100, 591–596. doi:10.1016/j.bios.2017.10.001

Fu, S., Zuo, P., and Ye, B. (2020). A novel wick-like paper-based microfluidic device for 3D cell culture and anti-cancer drugs screening. *Biotechnol. J.* 16, 2000126. doi:10.1002/biot.202000126

Gowers, S. A. N., Curto, V. F., Seneci, C. A., Wang, C., Anastasova, S., Vadgama, P., et al. (2015). 3D printed microfluidic device with integrated biosensors for online analysis of subcutaneous human microdialysate. *Anal. Chem.* 87, 7763–7770. doi:10.1021/acs.analchem.5b01353

Hagedorn, Y. (2017). Laser additive manufacturing of ceramic components. *Laser Addit. Manuf.* 2017, 163–180. doi:10.1016/b978-0-08-100433-3.00006-3

Han, T., Kundu, S., Nag, A., and Xu, Y. (2019). 3D printed sensors for biomedical applications: a review. *Sensors.* 19 (7), 1706. doi:10.3390/s19071706

Hanada, Y., Sugioka, K., Shihira-Ishikawa, I., Kawano, H., Miyawaki, A., and Midorikawa, K. (2011). 3D microfluidic chips with integrated functional microelements fabricated by a femtosecond laser for studying the gliding mechanism of cyanobacteria. *Lab Chip.* 11 (12), 2109. doi:10.1039/c1lc20101h

Hwang, H. H., Zhu, W., Victorine, G., Lawrence, N., and Chen, S. (2017). 3D-Printing of functional biomedical microdevices via light- and extrusion-based approaches. *Small Methods.* 2 (2), 1700277. doi:10.1002/smtd.201700277

Iordache, F. (2019). Bioprinted scaffolds. *Mater. Biomed. Eng.* 2019, 35–60. doi:10.1016/b978-0-12-816901-8.00002x

Kadimisetty, K., Malla, S., and Rusling, J. F. (2017). Automated 3-D printed arrays to evaluate genotoxic chemistry: E-cigarettes and water samples. *ACS Sens.* 2 (5), 670–678. doi:10.1021/acssensors.7b00118

Kadimisetty, K., Mosa, I. M., Malla, S., Wardena, J. E. S., Kuhns, T., Faria, R. C., et al. (2016). 3D-Printed supercapacitor-powered electrochemiluminescent protein immunoarray. *Biosens. Bioelectron.* 15, 188–193. doi:10.1016/j.bios.2015.09.017

Kadimisetty, K., Song, J., Doto, A. M., Hwang, Y., Peng, J., Mauk, M. G., et al. (2018a). Fully 3D printed integrated reactor array for point-of-care molecular diagnostics. *Biosens. Bioelectron.* 109, 156–163. doi:10.1016/j.bios.2018.03.009

Kadimisetty, K., Spak, A. P., Bhalerao, K. S., Sharafeldin, M., Mosa, I. M., Lee, N. H., et al. (2018b). Automated 4-sample protein immunoassays using 3D-printed microfluidics. *Anal. Methods.* 10 (32), 4000–4006. doi:10.1039/c8ay01271g

Knowlton, S., Hsiang Yu, C., Ersoy, F., Emadi, S., Khademhosseini, A., and Tasoglu, S. (2016). 3D-printed microfluidic chips with patterned, cell-laden hydrogel constructs. *Biofabrication.* 8, 025019. doi:10.1088/1758-5090/8/2/025019

Ko, D.-H., Gyak, K.-W., and Kim, D. -P. (2017). Emerging microreaction systems based on 3D printing techniques and separation technologies. *J. Flow Chem.* 7 (3–4), 72–81. doi:10.1556/1846.2017.00013

Krejcova, L., Nejdl, L., Rodrigo, M., Rodrigo, M. A., Zurek, M., Matousek, M., et al. (2014). 3D printed chip for electrochemical detection of influenza virus labeled with CdS quantum dots. *Biosens. Bioelectron.* 54, 421–427. doi:10.1016/j.bios.2013.10.031

Lee, W., Kwon, D., Chung, B., Jung, G. Y., Au, A., Folch, A., et al. (2014). Ultrarapid detection of pathogenic bacteria using a 3D immunomagnetic flow assay. *Anal. Chem.* 86 (13), 6683–6688. doi:10.1021/ac501436d

Lee, W., Lee, V., Polio, S., Keegan, P., Lee, J.-H., Fischer, K., et al. (2010). On-demand three-dimensional freeform fabrication of multi-layered hydrogel scaffold with fluidic channels. *Biotechnol. Bioeng.* 105, 1178. doi:10.10.1002/bit.22613

Matter-Parrat, V., and Liverneaux, P. (2019). Impression 3D en chirurgie de la main. *Hand Surg. Rehabilitat.* doi:10.1016/j.hansur.2019.09.006

Melchels, F. P. W., Feijen, J., and Grijpma, D. W. (2010). A review on stereolithography and its applications in biomedical engineering. *Biomaterials.* 31 (24), 6121–6130. doi:10.1016/j.biomaterials.2010.04.050

Mohamed, O. A., Masood, S. H., and Bhowmik, J. L. (2015). Optimization of fused deposition modelling process parameters: a review of current research and future prospects. *Adv. Manufacturing.* 3 (1), 42–53. doi:10.1007/s40436-014-0097-7

Molitch-Hou, M. (2018). Overview of additive manufacturing process. *Add. Manuf.* 2018, 1–38. doi:10.1016/b978-0-12-812155-9.000013

Mukherjee, P., Rani, A., and Saravanan, P. (2019). Polymeric materials for 3D bioprinting. *3D Print. Tech. Nanomedicine.* 2019, 63–81. doi:10.1016/b978-0-12-815890-6.00004-9

Munir, K. S., Li, Y., and Wen, C. (2017). Metallic scaffolds manufactured by selective laser melting for biomedical applications. *Metall. Foam Bone* 1–23. doi:10.1016/b978-0-08-101289-5.00001-9

Muzaffar, A., Ahamed, M. B., Deshmukh, K., Kovářík, T., Křenek, T., and Pasha, S. K. K. (2020). 3D and 4D printing of pH-responsive and functional polymers and their composites. *3D and 4D Print. Polymer Nanocomp. Mat.* 2020, 85–117. doi:10.1016/b978-0-12-816805-9.00004-1

Oh, S., and Choi, S. (2018). 3D-Printed capillary circuits for calibration-free viscosity measurement of Newtonian and Non-Newtonian fluids. *Micromachines* 9 (7), 314. doi:10.3390/mi9070314

Papaioannou, T. G., Manolesou, D., Dimakakos, E., Tsoucalas, G., Vavuranakis, M., and Tousoulis, D. (2019). 3D bioprinting methods and techniques: applications on artificial blood vessel fabrication. *Acta Cardiol. Sin.* 35 (3), 284. doi:10.6515/ACS.201905_3510.6515/ACS.201905_35(3).20181115A

Park, C., Lee, J., Kim, Y., Kim, J., Lee, J., and Park, S. (2017). 3D-printed microfluidic magnetic preconcentrator for the detection of bacterial pathogen using an ATP luminometer and antibody-conjugated magnetic nanoparticles. *J. Microbiol. Meth.* 132, 128–133. doi:10.1016/j.mimet.2016.12.001

Ragones, H., Schreiber, D., Inberg, A., Berkh, O., Kosa, G., Freeman, A., et al. (2015). Disposable electrochemical sensor prepared using 3D printing for cell and tissue diagnostics. *Sensors Actuators B: Chem.* 216, 434–442. doi:10.1016/j.snb.2105.04.065

Roda, A., Guardigi, M., Calabria, D., Calabretta, M. M., Cevenini, L., and Michelini, E. (2014). A 3D-printed device for a smartphone-based chemiluminescence biosensor for lactate in oral fluid and sweat. *Analyst.* 139 (24), 6494–6501. doi:10.1039/c4an01612b

Ruiz, C., Kadimisetty, K., Yin, K., Mauk, M. G., Zhao, H., and Liu, C. (2020). Fabrication of hard-soft microfluidic devices using hybrid 3D printing. *Micromachines.* 11 (6), 567. doi:10.3390/mi11060567

Salonitis, K. (2014). "Stereolithography," in *Comprehensive materials processing*. Amsterdam, Netherlands: Elsevier, 19–67. doi:10.1016/b978-0-08-096532-1.01001-3

Samper, I. C., Gowers, S. A. N., Rogers, M. L., Murray, D. R. K., Jewell, S. L., Pahl, C., et al. (2019). 3D printed microfluidic device or online detection of neurochemical changes with high temporal resolution in human brain microdialysate. *R. Soc. Chem. Lab Chip.* 19, 2038–2048. doi:10.1039/c9lc00044e

Santangelo, M. F., Libertino, S., Turner, A. P. F., Filippini, D., and Mark, W. C. (2017). Integrating printed microfluidics with silicon photomultipliers for miniaturised and highly sensitive ATP bioluminescence detection. *Biosens. Bioelectron.* 99, 464–470. doi:10.1016/j.bos.2017.07.05510.1016/j.bios.2017.07.055

Schönberger, M., and Hoffstetter, M. (2016). Generative manufacturing technologies—the future? *Emerging Trends Med. Plast. Eng. Manufacturing.* 2016, 107–174. doi:10.1016/b978-0-323-37023-3.00004-x

Sibbitt, J. P., and He, M. (2017). 3D printing of microfluidics for point of care diagnosis. *Bio Sustain. Manufacturing.* 2017, 2778. doi:10.1115/msec2017-2778

Singh, R., Singh, S., and Hashmi, M. S. J. (2016). "Implant materials and their processing techanologies," in Reference module in materials science and materials engineering. doi:10.1016/b978-0-12-8.04156-4

Su, C. K., Yen, S. C., Li, T. W., and Sun, Y. C. (2016). Enzyme-immobilized 3D-printed reactors for online monitoring of rat brain extracellular glucose and lactate. *Anal. Chem.* 88 (12), 6265–6273. doi:10.1021/acs.analchem.6b00272

Sweet, E., Yang, B., Chen, J., Vickerman, R., Lin, Y., Long, A., et al. (2020). 3D microfluidic gradient generator for combination antimicrobial susceptibility testing. *Microsys. Nanoeng.* 6, 92. doi:10.1038/s41378-020-00200-7

Symes, M. D., Kitson, P. J., Yan, J., Richmond, C. J., Cooper, G. J. T., Bowman, R. W., et al. (2012). Integrated 3D-printed reactionware for chemical synthesis and analysis. *Nat. Chem.* 4, 349. doi:10.1038/NCHEM.1313

Tang, C. K., Vaze, A., and Rusling, J. F. (2017). Automated 3D-printed unibody immunoarray for chemiluminescence detection of cancer biomarker proteins. *Lab Chip.* 17 (3), 484–489. doi:10.1039/c6lc01238h

Tappa, K., and Jammalamadaka, U. (2018). Novel biomaterials used in medical 3d printing techniques. *J. Funct. Biomater.* 9 (1), 17. doi:10.3390/jfb9010017

Tarn, M., and Nicole, P. (2013). Microfluidics. *Mol. Sci. Chem. Eng.* 2013, 1–7. doi:10.1016/b978-0-12-409547-2.05351-8

Wang, S., Ge, L., Yan, M., Yu, J., Song, X., Ge, S., et al. (2013). 3D microfluidic origami electrochemiluminescence immunodevice for sensitive point-of-care testing of carcinoma antigen 125. *Sensors Actuators B: Chem.* 176, 1–8. doi:10.1016/j.snb.2012.08.035

Weisgrab, G., Ovsianikov, A., and Costa, P. F. (2019). Functional 3D printing for microfluidic chips. *Adv. Mater. Technol.* 4, 1900275. doi:10.1002/admt.201900275

Wu, W., Deconinck, A., and Lewis, J. A. (2011). Omnidirectional printing of 3D microvascular networks. *Adv. Mater. Weinheim.* 23 (24), H178–H183. doi:10.1002/adma.201004625

Yao, P., Xu, T., and Tung, S. (2018). Pneumatic microfluidic device by 3D printing technology for insulin determination. *IEEE 12th Int. Conf. Nano/Molecular Med. Eng. (Nanomed).* 2018, 8641565. doi:10.1109/nanomed.2018.8641565

Yeong, W. Y., Sudarmadji, N., Yu, H. Y., Chua, C. K., Leong, K. F., Venkatraman, S. S., et al. (2010). Porous polycaprolactone scaffold for cardiac tissue engineering fabricated by selective laser sintering. *Acta Biomater.* 6 (6), 2028–2034. doi:10.1016/j.actbio.2009.12.033

Zargaryan, A., Farhoudi, N., Haworth, G., Ashby, J. F., and Au, S. H. (2020). Hybrid 3D printed-paper microfluidics. *Nat. Res.* 10, 18379. doi:10.1038/s41598-020-75489-5

Zhang, Y. (2019). Three-dimensional-printing for microfluidics or the other way around? *Int. J. Bioprint.* 5 (2), 192. doi:10.18063/ijb.v5i2.192

Check for updates

Importance of Standards in Biomedical Device and Its Role in Strengthening the Healthcare Sector

Gajjala Sumana*, Rajesh and D. K. Aswal

Council of Scientific and Industrial Research-National Physical Laboratory, New Delhi, India

Biomedical Metrology group of CSIR-NPL (Council of Scientific and Industrial Research—National Physical Laboratory), India is contributing significantly for establishing National Biomedical equipment standardswhich are traceable to primary standards to cater the quality control regulation in Health sector. This initiative has great impact on the health policy and Nation's economy as well. The laboratory has recently established biomedical equipment standard facility and disseminated the services to Industries, stake holders, hospitals and accredited laboratories. Although, the laboratory is successfully providing biomedical equipment calibration services for last 2 years, the sensitization of the information on the recently established metrological capabilities is required, which has great implications in implementation of India's New medical Device rule 2017 effectively. The present paper describes the summary on the significant achievements and role of National Physical Laboratory in supporting the Indian medical device regulations.

Keywords: biomedical, metrology, quality, infrastructure, calibration, growth

INTRODUCTION

Ministry of Health and Family welfare of Government of India has published "New Medical Device and *in vitro* diagnostic regulations in 2017" and as per the new regulations, ministry's undertaken organization, central drugs standard control organization has issued medical device rule 2017 and are being implemented in India with effect from January 1, 2018[1] Medical device regulations accentuate the major requirement of quality control and periodic calibration checks of medical equipment to minimize the medical device errors. In the medical equipment market, the quality control is very important for the correct diagnosis and correct treatment of the patients. Precise and accurate measurements are vital for taking appropriate medical decisions. Whereas, un-calibrated medical devices lead to critical errors in equipment leading to wrong diagnosis, medical device failures causing causality and deaths. Therefore, regular calibration of the biomedical equipment to assure the accurate and precise measurements which are traceable to national standards is very crucial in implementing National Quality health infrastructure in Health sector. In this context, CSIR-NPL, Indian National Metrological Institute is serving the country by providing calibration facilities traceable to National standards to support the quality regulation of Medical equipment.

IMPLICATIONS OF BIOMEDICAL METROLOGY IN HEALTHCARE SECTOR

Recently in September 2019, World Health Organization has estimated that nearly 134 million

---

[1] https://cdsco.gov.in/opencms/opencms/en/Medical-Device-Diagnostics/Medical-Device-Diagnostics/.
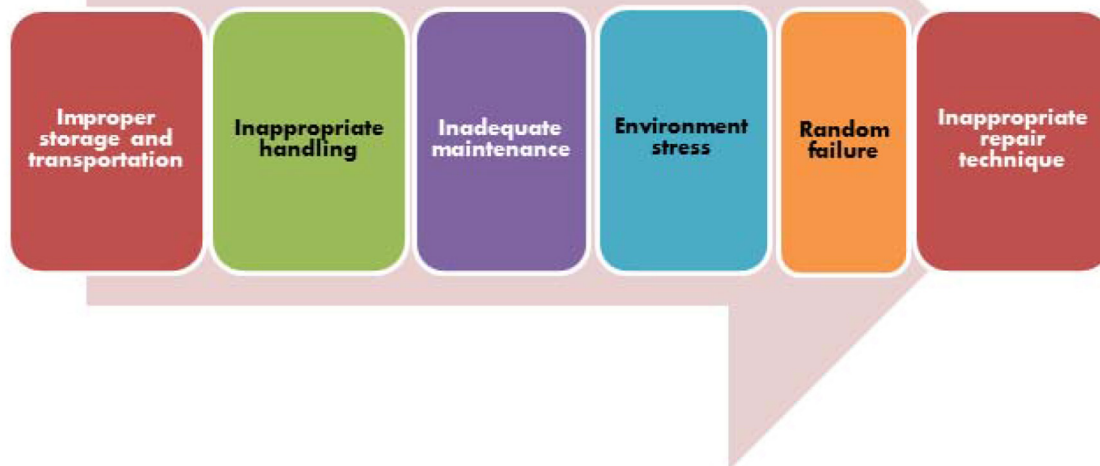
FIGURE 1 | Common causes for biomedical equipment error.

medical errors occur in hospitals in low- and middle-income countries including the biomedical equipment errors[2] The common biomedical equipment errors are depicted in **Figure 1**. As per the Harvard University report 2013, Medical errors are the third leading cause of death in the United States with causalities as high as 0.4 million (Jha et al., 2013). According to WHO estimation ∼80% failures of medical equipment can be prevented by their proper maintenance, calibration and periodic inspections. Estimates indicate that among various reasons for the medical equipment errors, inadequate maintenance alone accounts for about 60% and 20% are accounted to inappropriate handling, environmental stress and wear-out etc. WHO (2011) as depicted in (**Figure 2**).

Besides healthcare, the quality control in medical devices and its implementation have great implications in the National economy as well. "Make in India" sector survey on Medical Devices estimated that the Indian medical device market has great potential and its market value is estimated to increase steeply to USD 50 billion by 2025. Currently, the market value of Biomedical and Healthcare industry is around USD 5.2 billion, which is one of the largest economic sectors and is contributing greatly in National economy. Presently, India is the fourth largest medical device manufacturing country in Asia with an average turnover of Rs 450–500 million[3] Implementing corrective measures such as regulating the medical quality

infrastructure, regular accreditation of biomedical equipment, development of standards, adopting the standard procedural protocols in healthcare institutions are a few steps that have great impact in the industrial development of Biomedical devices. In this context, CSIR-National Physical Laboratory is playing a pivotal role in healthcare sector by developing equipment standards and providing calibration as per the internationally accepted technical standards for boosting up the domestic biomedical industries and calibration laboratories.

REGULATORY RECOMMENDATIONS

Medical device regulations are regulated by the National authority and it varies from country to country. In India, the medical device regulations are regulated by Central Drugs Standard Control Organization. According to Indian regulatory Authority, the medical equipment has to satisfy adequate safety, performance and quality norms as per ISO-17025 guidelines. Medical devices have been classified into four classes as per the risk based qualification viz. class A (low risk), class B (low moderate risk), class C (moderate risk), and class D (high risk).

As per the Indian regulatory authorities, the biomedical electrical equipment should conform to technical standards as per the guidelines of Electro-technical Commission (IEC-60601) (Costa Monteiro and Leon, 2015), International Organization for Standardization (ISO-17025)[4] and Bureau of Indian standards (BIS) published Indian standards and procedures. Therefore, as per the BIS documentation and IEC standards and country's legal

FIGURE 2 | Biomedical equipment errors.
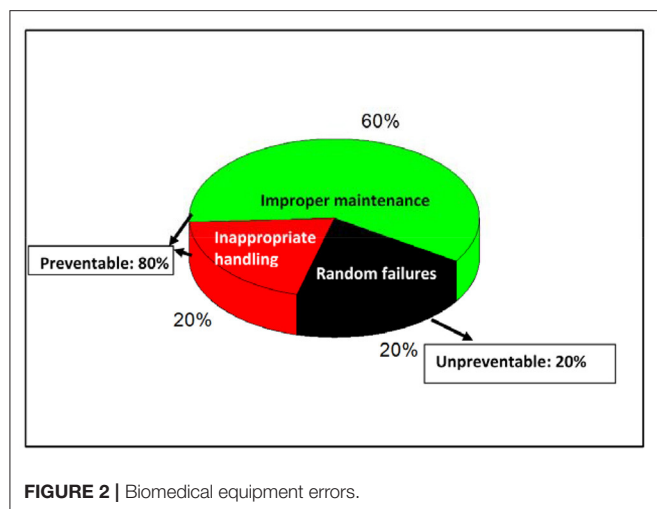
metrology requirements, CSIR-National physical laboratory is working toward the creation and maintenance of the biomedical equipment standards.

BIOMEDICAL METROLOGY PROGRAM AT CSIR-NATIONAL PHYSICAL LABORATORY

CSIR-National Physical Laboratory, Indian National Metrological Institute, has taken initiative to create and maintain national standards in biomedical instrumentation with traceability to National Standards. In September 2018, CSIR-NPL has established apex level biomedical equipment standard for Defibrillator and Defibrillator analyzer where the measurements are traceable to National standards (Rajesh et al., 2019). CSIR-NPL is providing apex level calibration facilities for clinical thermometers, blood pressure monitors and magnetic resonance etc. Efforts are being made to develop and disseminate

the standards for biomedical equipment such as Electrical safety analyzer, Infusion and Syringe pumps, dialysis equipment and Incubators etc. The development of Biomedical equipment standards for calibration of Medical devices and dissemination of these standards to industries, secondary laboratories and hospitals will have a huge impact on National healthcare sector in reducing the health complications due to medical device errors.

Keeping the above importance of the issue in view, CSIR-National Physical Laboratory through biomedical metrology program is working on the following objectives:

- Establishing the National standards of Biomedical equipment comparable to International standards through continuous Research and Development.
- Dissemination of Apex level calibration standards as per National and International standards to hospitals, clinical labs, biomedical industries and institutes and other stakeholders.
- To support the regulatory bodies in the context of newly enacted "Medical Device Rule 2017" effective from 1st Jan 2018 and ISO 17025:2017.
- Training on Testing and Calibration of Biomedical Instruments.

CONCLUSIONS

CSIR-National Physical Laboratory of India is playing a critical role in implementing the quality control of biomedical equipment by providing calibration traceable to primary standards. The importance of biomedical metrology and its implications in National Healthcare and country economy are highlighted in the present manuscript.

AUTHOR CONTRIBUTIONS

All Authors have contributed for the onset of the biomedical metrology activities at NPL.

REFERENCES

Costa Monteiro, E., and Leon, L. F. (2015). Metrological reliability of medical devices. *J. Phys. Conf. Ser.* 588. doi: 10.1088/1742-6596/588/1/012032

Jha, A. K., Larizgoitia, I., Audera-Lopez, C., Prasopa-Plaizier, M., Waters, H., and Bates, D. W. (2013). The global burden of unsafe medical care: analytic modelling of observational studies. *BMJ Qual. Saf.* 22, 809–815. doi: 10.1136/bmjqs-2012-001748

Rajesh, V. K. T., Sumana, G., Agarwal, V.V., Ojha, V. N., and Aswal, D. K. (2019). CSIR-NPL establishes an apex-level calibration facility for defibrillator analyzer and defibrillator machine. *Current Sci.* 117:25. doi: 10.18520/cs/v117/i2/179-180

WHO (2011). WHO Medical equipment maintenance programme overview. WHO Medical device technical series Available online at: https://apps.who.

int/iris/bitstream/handle/10665/44587/9789241501538_eng.pdf/jsessionid=156EC3788A40D9EB8B7E9CD5EAA741BB?sequence=1

Nanostructured β-tricalcium Phosphate (Ca3(PO4)2 Based Electrochemical Sensor for Detection of Methyl Parathion and Mercury (II) Ions

Narayanan Sudhan[1] and Chinnathambi Sekar[2]*

[1]*Department of Chemistry, Thiagarajar College, Madurai, India, [2]Department of Bioelectronics and Biosensors, Alagappa University, Karaikudi, India*

In this work, we have fabricated a new electrochemical sensor based on β-tricalcium phosphate (Ca3(PO4)2) nanoparticles (NPs) modified glassy carbon electrode (GCE) for the selective nonenzymatic determination of methyl parathion and mercury (II) ions independently. β-tricalcium phosphate (β-TCP) NPs were prepared by chemical precipitation method and structural and morphological properties were investigated by XRD, FTIR, and SEM. The electrochemical behavior of MP and mercury (Hg^{2+}) ions were investigated by cyclic voltammetry (CV) and square wave voltammetry (SWV) techniques using β-TCP/GCE. The modified electrode exhibited excellent electrocatalytic activity towards both the MP and Hg over a wide linear range from 0.15 to 141 µM and 1–381 µM with the lowest detection limits of 88 and 136.4 nM respectively. The sensor has high selectivity towards MP and Hg in the presence of major interfering compounds such as 3-nitrophenol, 4-nitrophenol, 4-aminophenol, catechol, hydroquinone and heavy metals such as lead, cadmium and arsenic. Applicability of the fabricated sensor for detection of MP and Hg (II) ions has been tested in tap water by standard addition method.

Keywords: ß-Tricalcium phosphate, electrochemical sensor, methyl parathion (MP), mercury ion, environmental applications and catalysis

INTRODUCTION

Organophosphorus pesticides (OPs) are extensively used as insecticides in the field of agriculture to protect crops, seeds and to get high yield with high quality (Mulchandani et al., 2001; Obare et al., 2010). However, these pesticides are neurotoxic which can cause several diseases in both humans and animal (Silva et al., 2004; Chuan et al., 2015). Methyl parathion (MP) is a type of nitro aromatic organophosphorus pesticide which is widely used to prevent agricultural losses by controlling pests and insects. It is used prevalently due to its cost effectiveness and high insecticidal activity (Niazi and Yazdanipour, 2007; Sanghavi et al., 2012). MP's ability to bio-accumulate and its low solubility means that it can easily be adsorbed on the surface of water and soil which could result in various problems to our eco-system. Moreover, high dosages of MP lead to inhibition of acetyl cholinesterase activity in the brain and leads to disturbances in normal neuron transmission (Yang et al., 2008; Thota and Ganesh, 2016). More than 100 thousand people die every year due to MP pesticide driven contamination of food and drinking water. Therefore, with the spotlight on public health, there

is a need to develop reliable, highly sensitive and easily operable methods for the monitoring of MP concentration in the environment and food items. Various methods such as spectroscopic, chromatographic techniques like high performance liquid chromatography (Cappiello et al., 2002; Hyötyläinen et al., 2004; Berijani et al., 2006; Moinfar and Hosseini, 2009; Hassan et al., 2010) and electrochemical methods (Shulga and Kirchhoff, 2007; Liang et al., 2012) have been used for determination of MP. Among them, electrochemical techniques were most suitable for monitoring the MP concentration, because of its high sensitivity, selectivity and low-cost (Liu and Lin, 2006; Du et al., 2011). Though there are electrochemical sensors for MP determination, these methods depend heavily on enzymes (Mulchandani et al., 1999; Liu and Lin, 2006; Gong et al., 2009; Du et al., 2011; Hossain et al., 2011; Li et al., 2011; Du et al., 2012; Ge et al., 2013). These enzyme based electrochemical sensors are usually less favored for practical usage because they suffer from many disadvantages such as high cost, instability, de-naturation, difficulty in getting pure form of enzymes, subsequent storage problems and short life time. In order to overcome these problems, novel enzyme free sensor devices for methyl parathion detection such as MWCNTs–PAAM) based composite (Zeng et al., 2012), carboxylic acid functionalized single walled carbon nanotubes-cyclodextrin (f-SWCNTs-CD) (Yao et al., 2014), mono-6-thio-cyclodextrin–gold nanoparticles–single walled carbon nanotubes SHCD/AuNPs/SWCNTs (Fu et al., 2015), gadolinium hexacyano ferrate–graphene nanosheets (GdHCF/GNs) (Li et al., 2014) zirconia nanoparticles (ZrO2NPs) (Parham and Rahbar, 2010) have been developed.

Heavy metal ions such as cadmium, lead, arsenic, mercury are major contributors to environmental pollution, albeit in very low concentrations, because of their undesirable involvement in many natural and industrial applications. Mercury and its compounds are highly toxic and when they accumulate in human organs such as liver, heart muscle, and brain. They can easily interact with protein and enzymes which, in turn, results in the inactivation of some important cell functions in our body leading to various diseases like kidney dysfunction, central nervous system disorders, even death at high exposure (Harris et al., 2003; Triunfante et al., 2009; Bodo et al., 2010; Johri et al., 2010). As a result, attention has been directed to the determination of mercury ions in foodstuff and pharmaceutical products and the environment. Traditional analytical tools for the determination of mercury ions include atomic absorption spectroscopy (AAS) (Kenawy et al., 2000; Pohl, 2009) and inductively coupled plasma mass spectrometry (ICP-MS) (Caroli et al., 1999; Silva et al., 2009). Compared to the above-mentioned techniques, electrochemical methods offer several advantages in terms of cost, simplicity and quickness. Moreover, in electrochemical techniques, different voltammetric methods can be employed for mercury detection (Aragay and Merkoc, 2012). Several reports are available for electrochemical determination of mercury ion; PdO/NP-CPE (El Aroui et al., 2014), EDTA/CPE (Moutcine and Chtaini, 2018), EDTA-PANI/SWCNTs/SS (Deshmuk et al., 2018), Chloroplatinum (II) complex-MWCNTs paste electrode (Mdisa et al., 2017) and Av- HA/GCE (Kanchana et al., 2015).

Calcium phosphate (Ca/P) bioceramics are well known bioactive compound and are used in surgical fields for orthopedic and dental implants, because of their excellent osteoconductivity. Hydroxyapatite (Ca10(PO4)6(OH), octacalcium phosphate (Ca8H2(PO4)6·5(H2O)), tricalcium phosphate (Ca3(PO4)2), calcium hydrogen phosphate dihydrate (CaHPO4.2H2O), dicalcium phosphate anhydrous (CaHPO4), tetracalcium phosphate (Ca4(PO4)2O) and amorphous calcium phosphate (Ryu et al., 2002) are different crystalline calcium phosphates that have been applied in many biological mineralization processes. Among them, tricalcium phosphate has been given great attention and it is widely used as an ideal temporary scaffold for bone implant and dental repair material, because of its close chemical resemblance to biological apatite present in human hard tissues. Tricalcium phosphate can be divided into three forms based on its thermal stability namely α, ß- and α′-phases. Of these, a-TCP is hydrolysable while ß-TCP is a stable material with superior properties such as non-toxicity, antigenicity, non-carcinogenicity, high biodegradability and thermal stability (Tadayyon et al., 2003). Though with relatively poor performance in terms of the lowest detection limit and linear range, the a-TCP modified carbon paste electrode (TCP/CPE) was used for the determination of Pb2+ by electrochemical method (Chourak et al., 2016).

The present work reports the fabrication of an enzyme free electrochemical sensor for methyl parathion determination and mercury ion detection using ß-tricalcium phosphate modified GCE. The fabricated electrode was employed for determination of MP and mercury (II) ions in tap-water samples.

MATERIALS AND METHODS

Reagents

Methyl Parathion was purchased from Sigma Aldrich, Mercuric Chloride, Calcium Nitrate tetra hydrate and di-ammonium hydrogen phosphate were purchased from Merck Private Limited, Mumbai. All other chemicals were of analytical reagent grade and used without any further purification. 0.1 M of Phosphate buffer solution was prepared from Na2HPO4 and NaH2PO4 (Merck, Mumbai) and the pH was adjusted to seven and five for MP and Hg respectively by adding 0.1 M HCl. De-ionized water was used throughout the experiments.

Apparatus

Electrochemical measurements were carried out on CHI 609D workstation. A three-electrode cell system was used with a modified glassy carbon electrode as the working electrode. An Ag/AgCl was used as the reference electrode and a platinum wire electrode as the counter electrode. All experiments were carried out at room temperature. Cyclic voltammograms (CVs) were acquired at a scan rate of $50 \, mVs^{-1}$ in 0.1 M phosphate buffer containing various concentrations of methyl parathion and HgCl2 individually. The structure and morphology of the ß-TCP were characterized by powder X-ray powder diffraction (XRD) using a XPERT-PRO diffractometer with Cu Kα radiation (1.5406Å) at 40 kV and Field emission scanning electron

microscopy (FE-SEM) using FEG Quanta. Fourier transform infrared (FTIR) observations were recorded from 400 to 4,000 cm^{-1} at room temperature with a Schimadzu-IR-Affinity by KBr pellet technique.

Synthesis of ß-Tricalcium phosphate

β-Tricalcium phosphate was prepared by a simple chemical precipitation method. Initially, calcium nitrate tetrahydrate [Ca(NO3)2·4H2O] powder and di-ammonium hydrogen phosphate [(NH4)2HPO4] solution were mixed with constant stirring to get homogenous solution. The solution turned white color turbid immediately which was made transparent by adding phosphate ion solution into calcium. Subsequently, ammonium solution (NH4OH) was added drop wise in the above mixture to maintain the pH 8.0. Stirring was continued for 2°h, and the precipitate was allowed to settle overnight, then filtered, dried and finally calcinated at 700°C in ambient atmosphere.

Electrode Preparation

Glassy carbon electrodes (3 mm dia) were polished with 0.05 mm alumina powder on polishing cloth, rinsed thoroughly with deionized water between each polishing step, sonicated and dried at room temperature. These electrodes were modified by drop casting method. Here, tricalcium phosphate nanoparticles were dispersed into deionized water (5°mg/ml−1) by ultrasonicating for about 30 min to get a stable and uniform suspension. Typically, 10 µL of this ß -TCP suspension was drop casted onto the GCE and the water was allowed to evaporate at room temperature in air.

RESULT AND DISCUSSION

Characterization of Synthesized Powder

Powder XRD pattern of the pristine ß-Tricalcium phosphate sample is shown in (**Figure 1A**). The XRD pattern corresponds well with that of the standard ß-TCP crystallites (ICDD PDF Card No-09–0,169) indicating that the product obtained is mainly composed of the ß-TCP form of calcium phosphate with rhombohedral structure. No characteristics peaks

of impurities such as calcium hydroxide and calcium phosphates were observed. Crystallite size was calculated by the Debye-Scherer formula ($D = K\lambda/\beta1/2cos\theta$) where λ is the wavelength, $\beta1/2$ is the full width at half maximum (FWHM), θ is the diffraction angle, K is the shape factor constant. The average crystallite size of ß -TCP was calculated as 28 nm after several measurements.

(**Figure 1B**) shows the FT-IR spectra of pure ß-TCP samples. The IR characteristic peaks of phosphate groups appeared between 900 and 1,160 cm^{-1}. In particular, the peak around at 924 cm^{-1} confirms the formation of high crystalline ß-tricalcium phosphate phase. A small peak at 728 cm^{-1} is attributed to the presence of PO^{4-} group, which is characteristic of calcium pyrophosphate phase. The peaks between 900 and 1,200 cm^{-1} represent the stretching vibration of phosphate ions. The presence of two characteristic bands at around 568 and 604 cm^{-1} is due to the asymmetric stretching vibration of PO^{3-} (**Supplementary Figure S1A,B**) shows FE-SEM micrographs of the ß-TCP at two different magnifications confirm the formation of homogenously distributed elongated rod-shaped nanoparticles.

Electrochemical Investigation of Methyl Parathion

Cyclic voltammetry was used to investigate the electrochemical behavior of MP at the ß-TCP modified GCE in PBS (pH 7.0) at a scan rate 50 mV/s (**Supplementary Figure S2A**). shows the CVs of 50 µM MP at bare GCE (curve a) and a ß-TCP/GCE (curve b) respectively. Noticeably, a small defined oxidation wave and large reduction peak appeared for both bare and modified GCEs. The large cathodic peak shows the reduction of nitrogroup in MP to 2-phenylhydroxylamine. During the reverse scan, a small anodic peak indicates the conversion of hydroxylamine to nitrobenzene. When compared with bare GCE, the ß- TCP/GCE exhibited significantly enhanced redox reaction which could partly be attributed to the efficient adsorption property of tricalcium phosphate nanoparticles. No obvious peak was observed on the ß-TCP/GCE in the absence of MP. A sharp reduction peak appeared after incubation of 50 µM of MP in electrolyte
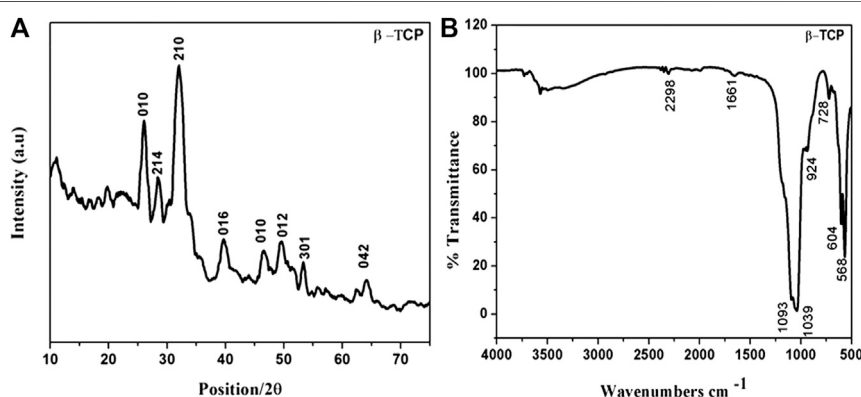

FIGURE 1 | (A) shows the powder XRD pattern and **(B)** FT-IR spectra of ß -TCP NPs.

solution in (**Supplementary Figure S2B**). These results suggest that the ß-TCP catalyzes the reaction and enhance the reduction of MP through electron transfer at the electrode-electrolyte interface.

(**Supplementary Figure S2C**) shows the effect of scanning rate on cyclic voltammograms of 50 µM MP at the ß-TCP/GCE in PBS at pH 7.0. The reduction peaks increase linearly with the increase of scan rates from 10 to 100 mVs^{-1} and exhibit a linear relation to the square root of the scan rate, which implies that the redox reaction of MP at the ß-TCP/GCE is a surface adsorption-controlled process. The above results also demonstrate that the proposed sensor facilitates electron transfer towards MP sensing. The methyl parathion has different electrochemical behaviors in different electrolytes. The effects of electrolytes, such as HCl, phosphate buffer, acetate buffer, and KNO3, on reduction peak currents of MP were studied and the results show that the MP has the best electrochemical responses in 0.1 M PBS with the appearance of well defined cathodic peaks with the lowest background current.

(**Supplementary Figure S2D**) shows the cyclic voltammograms of 50 µM of MP at ß-TCP/GCE in 0.1 M PBS at different pH values. The pH was varied from four to nine by the addition of HCl or NaOH in PBS electrolyte. The best peak current with lowest background current appeared for pH 7.0. At lower low pH values, the peak current is reduced possibly due to the immobilization of MP on the electrode surface and/or dissolution of ß-TCP in acidic medium. When the pH is higher than 7.0, peak current decreased and the shape of the peak is changed due to the lack of protons H^{+}. Hence, we have chosen pH value as 7.0 for all subsequent measurements.

Determination of Methyl Parathion by SWV

Electrochemical determination of MP at ß-TCP/GCE was realized by square wave voltammetric technique in 0.1 M PBS (pH 7.0) (**Figure 2A**). shows the voltammograms recorded during addition of aliquot from the stock of solution methyl parathion. It was noted that the cathodic peak current increases linearly with the increasing concentration of MP from 0.15 to 141 µM. A linear relationship

between the cathodic peak current ipa (µA) and concentrations C (µM) of MP has been deduced as Ipa (µA) = −4.6229CMP (µM)− 5.09 (R2 = 0.99518) (**Figure 2B**). The lowest limit of detection (LOD) was estimated as 88 nM and the results are compared with the literature values (**Supplementary Table S1**). This significant LOD over a wide linear range could be attributed to the intrinsic porous nature, efficient adsorptivity and improved electrocatalytic ability of the ß-TCP nanoparticles.

Selectivity, Reproducibility and Stability Studies for Methyl Parathion Sensor

A significant benefit of ß-TCP NPs is its good selectivity towards MP sensing by avoiding and discriminating the interference of several isostructural compounds. Here we have evaluated the spirited test for selectivity by square wave voltammetry technique (**Supplementary Figure S3**). shows an interference study of MP sensor in the presence of 100 fold excess of co-existing phenolic compounds such as four-aminophenol, nitrophenol isomers, hydroquinone, catechol, and some other compounds like nitrite, SO42−, Mg2+, K+, and Na+. The presence of these competing molecules and ions did not have an obvious influence on the current response of MP on the ß-TCP/GCE. The results demonstrate that the ß-TCP sensor can be used directly for detecting MP even in complex solutions. To characterize the reproducibility of the ß-TCP/GCE, 15 consecutive measurements were made for 50 µM MP at the same electrode. The results showed a relative standard deviation (RSD) of 2.97%, revealing that the ß-TCP modified GCE had good reproducibility. The stability of the ß-TCP/GCE sensing device was also examined by measuring CV peak current of 50 µM MP after storing the electrode for 10 days in a refrigerator. The ß-TCP/GCE retained 91% of the original values, demonstrating that the sensing device had better long-term stability.

Real Sample Analysis

The analytical application of the fabricated sensor was tested in tap water and vegetable samples by the standard addition method. Methyl parathion stock solution was added into tap
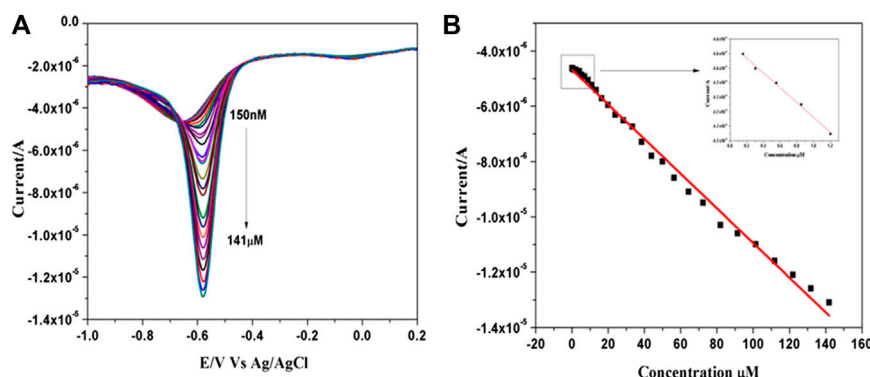

FIGURE 2 | (A) SWVs recorded for various concentration of MP ranging from 0.15 to 141 µM in 0.1 M PBS (pH 7.0) at ß-TCP/GCE. **(B)** Corresponding linear calibration plot.

water in 0.1 M PBS (pH 7.0) and the measurements were done at ß-TCP/GCE without any prior treatment and the results are presented in **Supplementary Table S2**. It can be noticed that fabricated sensor exhibits a good recovery in the range of 96–98% for MP determination in tap water. Similarly, square wave voltammograms were recorded for Momordica Charantia extract (colloquially known as bitter gourd) in the presence of various concentration of MP in 0.1 M PBS and the results are shown in **Supplementary Table S2**. Here also, the ß-TCP/GCE revealed highest percentage of recovery (90–100%) indicating its suitability for real sample analysis.

Electrochemical Detection of Mercury (Hg^{2+}) at β -TCP/GCE

(**Figure 3A**) shows the cyclic voltammetric behavior of mercury (Hg^{2+}) obtained in 0.1 M PBS (pH 5.0) containing 0.1 mM HgCl2 solution at bare GCE and β-TCP modified GCE at the scan rate of 50 mVs^{-1}. A sharp anodic oxidation peak is observed at 0.197 V corresponding to oxidation of metallic mercury (Hg0→Hg2++ 2e–) in both bare and ß-TCP modified GCE. The peak current (ipa) values of bare GCE and ß-TCP/GCE were found to be 23.3 and 35.2 µA respectively. There is a reasonable increment in the oxidation peak current of TCP/GCE when compared to that of bare GCE which reveals that the ß-TCP has good catalytic activity. The porous nature of TCP leads to the high adsorption of mercury ion on the surface of the electrode which promotes high electron transfer at the electrode-electrolyte interface without requiring any pre-concentration time as reported in literature (Kanchana et al., 2015). Mercury (Hg^{2+}) ions are known to have different electrochemical behaviors in different electrolytes. The effects of electrolytes, such as HCl, phosphate buffer, acetate buffer, and KNO3, on oxidation peak currents of Hg2+ were studied and the results show that the Hg^{2+} ions have the best electrochemical responses in 0.1 M PBS. When the measurements were performed in this electrolyte, well defined peaks with the lowest background current were obtained.

The effect of pH on the oxidation of mercury at the ß-TCP/GCE in 0.1 M PBS containing 1 mM HgCl2 solution was investigated by SWV studies (**Figure 3B**). The anodic peak current is strongly dependent on the pH of the solution with the maximum current observed at pH 5.0. At higher pH values (>5.0), the peak current decreased rapidly and the peak shape was also destroyed which could be attributed to the high participation of OH$^-$ resulting in the hydrolysis of Hg^{2+} to form mercury hydroxide. Similarly, SWV measurements at lower pH values (<5.0) yield lower oxidation current due to the dissolution of ß-TCP in high acidic medium. Based on these observations, pH 5.0 was chosen as the optimum value for the supporting electrolyte.

Square wave voltammetry (SWV) was used to examine the sensitivity of the fabricated electrode towards the detection of Hg^{2+} ions (**Figure 4A**). shows the SWV response of the ß- TCP/ GCE to the successive addition of mercury in 0.1 M PBS at pH 5.0. The electrode exhibited a rapid and sensitive response to the change of mercury concentration and an obvious increase in anodic peak current upon successive addition of mercury. Further, the current increased linearly with increasing Hg^{2+} concentration over the range of 1–380 µM and a linear relationship between the anodic peak current ipa (µA) and concentrations C (µM) of Hg2+ have been deduced as follows; Ipa (µA) = 0.576 CHg2+ (µM)+7.638 (R2 = 0.99784) (**Figure 4B**). The lowest detection limit was found to be 136 nM and is comparable with the results obtained from many sensors (**Supplementary Table S3**) as reported in the literature. The present experiments demonstrated that it is possible to determine Hg^{2+} using ß-TCP modified GCE without surface fouling of the electrode for repeated measurements. These results confirmed that ß-TCP modified electrode provides a good electro catalytic activity towards the detection of heavy metal mercury.

Tap water samples were selected for real sample analysis using the standard addition method. The developed sensor (TCP/GCE) was applied to test mercury ion in tap water samples. Standard stocks mercuric chloride solution was added into tap water and
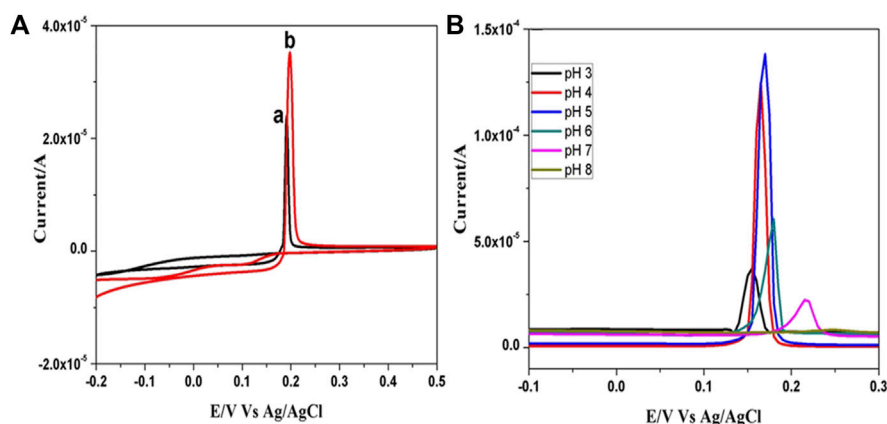
FIGURE 3 | (A) CVs of 0.1 mM Hg^{2+} in 0.1 M PBS (pH 5.0) at a) bare GCE,b) ß-TCP modified GCE at scan rate 50 mVs^{-1}; **(B)** SWV studies of 1mM Hg^{2+} in 0.1 M PBS at different pH from three to eight at ß-TCP/GCE at scan rate 50 mVs^{-1}.
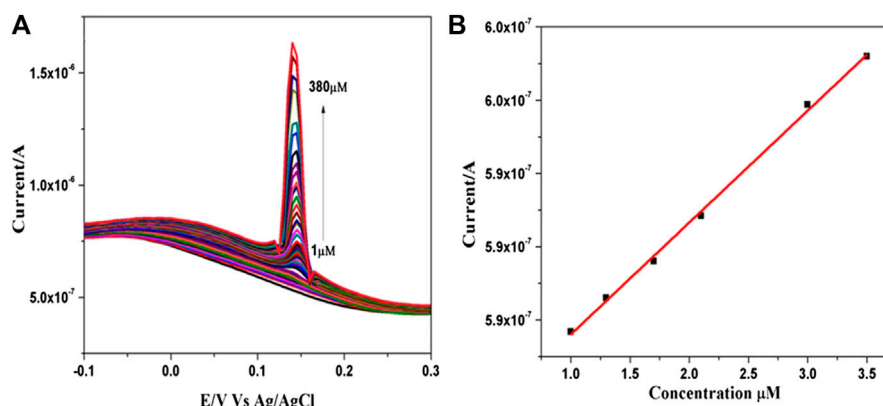
FIGURE 4 | (A) SWVs recorded for various concentration of HgCl2 ranging from 1 to 380 µM in 0.1 M PBS (pH 5.0) at ß-TCP modified GCE. **(B)** Corresponding linear calibration plot.

analyzes were done without any prior treatment. The results are presented in (**Supplementary Table S4**). It is obvious from the table that a good recovery could be obtained. Thus, the proposed sensor can be used to determine mercury ions in environmentally polluted water samples.

CONCLUSION

A novel and simple strategy for the sensitive detection of methyl parathion and heavy metal mercury individually using the ß-TCP/GCE is presented in this paper for the first time. The results confirm that in the case of unmodified bare GCE, the voltammograms of both MP and mercury (II) ion exhibit just a small peak current, whereas the peak current is significantly enhanced on ß-TCP/GCE. Well-defined reduction peak for MP and enhanced oxidation peak current for mercury (II) ion have been obtained owing to the excellent catalytic activity of ß-TCP NPs. In addition, the ß -TCP/GCE electrode exhibited good reproducibility, long-term stability, and high sensitivity without using any specific electron transfer mediator or any other surfactant. The modified electrode shows the extraordinary selectivity for determination of methyl parathion and mercury without interference of high concentration of co-existing molecules. Furthermore, the practical application of the modified electrode was demonstrated in tap water samples by using SWV method with satisfactory results.

REFERENCES

Aragay, G., and Merkoçi, A. (2012). Nanomaterials application in electrochemical detection of heavy metals. *Electrochim. Acta* 84, 49–61. doi:10.1016/j.electacta. 2012.04.044

Berijani, S., Assadi, Y., Anbia, M., Milani Hosseini, M. R., and Aghaee, E. (2006). Dispersive liquid-liquid microextraction combined with gas chromatography-flame photometric detection. *J. Chromatogr. A* 1123, 1–9. doi:10.1016/j.chroma. 2006.05.010

DATA AVAILABILITY STATEMENT

The raw data supporting the conclusions of this article will be made available by the authors, without undue reservation.

AUTHOR CONTRIBUTIONS

NS carried out the nanoparticles synthesis, experiments, analysed the XRD, FTIR, SEM, electrochemical behavior and wrote the paper; CS supervised the whole work and revised the paper.

ACKNOWLEDGMENTS

SUPPLEMENTARY MATERIAL

The Supplementary Material for this article can be found online at: https://www.frontiersin.org/articles/10.3389/fnano.2021.632652/ full#supplementary-material.

Bodo, M., Balloni, S., Lumare, E., Bacci, M., Calvitti, M., Dell'Omo, M., et al. (2010). Effects of sub-toxic Cadmium concentrations on bone gene expression program: results of an *in vitro* study. *Toxicol. In Vitro.* 24, 1670–1680. doi:10.1016/j.tiv.2010.05.020

Cappiello, A., Famiglini, G., Palma, P., and Mangani, F. (2002). Trace level determination of organophosphorus pesticides in water with the new direct-electron ionization LC/MS interface. *Anal. Chem.* 74, 3547–3554. doi:10.1021/ ac015685f

Caroli, S., Forte, G., Iamiceli, A. L., and Galoppi, B. (1999). Determination of essential and potentially toxic trace elements in honey by inductively coupled

plasma-based techniques. *Talanta* 50, 327–336. doi:10.1016/S0039-9140(99)00025-9

Chourak, R., Elouahli, A., Hatim, Z., Chtaini, A., and Kheribech, A. (2016). "Electro analytical determination of lead using tricalcium phosphate apatite modified carbon paste electrode," in *Research and reviews in electrochemistry 06 304155314 © 2016* (Trade Science Inc).

Chuan, Y., Hong, S., Hua-Feng, F., and Zhi-Cheng, T. (2015). Sensitive simultaneous determination of nitrophenol isomers at poly(p-aminobenzene sulfonic acid) film modified graphite electrode. *Electrochim. Acta.* 156, 163–170. doi:10.1016/j.elecom.2006.11.021

Deshmuk, M. A., Celiesiute, R., Ramanaviciene, A., Shirsat, M. D., and Ramanavicius, A. (2018). EDTA_PANI/SWCNTs nanocomposite modified electrode for electrochemical determination of copper (II), lead (II) and mercury (II) ions. *Electrochim. Acta.* 259, 930–938. doi:10.1016/j.electacta.2017.10.131

Du, D., Liu, J., Zhang, X., Cui, X., and Lin, Y. (2011). One-step electrochemical deposition of a graphene-ZrO2 nanocomposite: preparation, characterization and application for detection of organophosphorus agents. *J. Mater. Chem.* 21, 8032–8037. doi:10.1039/C1JM10696A

Du, D., Wang, J., Wang, L., Lu, D., and Lin, Y. (2012). Integrated lateral flow test strip with electrochemical sensor for quantification of phosphorylated cholinesterase: biomarker of exposure to organophosphorus agents. *Anal. Chem.* 84, 1380–1385. doi:10.1021/ac202391w

El Aroui, F., Lahrich, S., Farahi, A., Achak, M., El Gaini, L., Manoun, B., et al. (2014). Electrochemical determination of mercury(II) in ambient water at palladium oxide/graphite composite electrodes. *J. Taiwan Inst. Chem. Eng.* 45, 2725–2732. doi:10.1016/j.jtice.2014.05.003

Fu, X-C., Zhang, J., Tao, Y-Y., Wu, J., Xie, C-G., and Kong, L-T. (2015). Three-dimensional mono-6-thio-β-cyclodextrin covalently functionalized gold nanoparticle/single-wall carbon nanotube hybrids for highly sensitive and selective electrochemical determination of methyl parathion. *Electrochimica Acta* 153, 12–18. doi:10.1016/j.electacta.2014.11.144

Ge, X., Zhang, W., Lin, Y., and Du, D. (2013). Magnetic Fe3O4@TiO2 nanoparticles-based test strip immunosensing device for rapid detection of phosphorylated butyrylcholinesterase. *Biosens. Bioelectron.* 50, 486–491. doi:10.1016/j.bios.2013.07.017

Gong, J., Wang, L., and Zhang, L. (2009). Electrochemical biosensing of methyl parathion pesticide based on acetylcholinesterase immobilized onto Au-polypyrrole interlaced network-like nanocomposite. *Biosens. Bioelectron.* 24, 2285–2288. doi:10.1016/j.bios.2008.11.012

Harris, H. H., Pickering, I. J., and George, G. N. (2003). The chemical form of mercury in fish. *Science* 301, 1203. doi:10.1126/science.1085941

Hassan, J., Farahani, A., Shamsipur, M., and Damerchili, F. (2010). Rapid and simple low density miniaturized homogeneous liquid-liquid extraction and gas chromatography/mass spectrometric determination of pesticide residues in sediment. *J. Hazard. Mater.* 18, 869–871. doi:10.1016/j.jhazmat.2010.08.008

Hossain, M. M., Faisal, S. N., Kim, C. S., Cha, H. J., Nam, S. C., and Lee, H. J. (2011). Amperometric proton selective strip-sensors with a microelliptic liquid/gel interface for organophosphate neurotoxins. *Electrochemistry Commun.* 13, 611–614. doi:10.1016/j.elecom.2011.03.024

Hyötyläinen, T., Lüthje, K., Rautiainen-Rämä, M., and Riekkola, M-L. (2004). Determination of pesticides in red wines with on-line coupled microporous membrane liquid-liquid extraction-gas chromatography. *J. Chromatogr. A.* 1056, 267–271. doi:10.1016/j.chroma.2004.06.112

Johri, N., Jacquillet, G., and Unwin, R. (2010). Heavy metal poisoning: the effects of cadmium on the kidney. *Biometals* 23, 783–792. doi:10.1007/s10534-010-9328-y

Kanchana, P., Sudhan, N., Anandhakumar, S., Mathiyarasu, J., Manisankar, P., and Sekar, C. (2015). Electrochemical detection of mercury using biosynthesized hydroxyapatite nanoparticles modified glassy carbon electrodes without preconcentration. *RSC Adv.* 5, 68587–68594. doi:10.1039/C5RA11424A

Kenawy, I. M. M., Hafez, M. A. H., Akl, M. A., and Lashein, R. R. (2011). Determination by AAS of some trace heavy metal Ions in some natural and biological samples after their preconcentration using newly chemically modified chloromethylated polystyrene-PAN ion-exchanger. *Anal. Sci.* 16, 493–500. doi:10.2116/analsci.16.493

Li, H., Li, J., Yang, Z., Xu, Q., and Hu, X. (2011). A novel photoelectrochemical sensor for the organophosphorus pesticide dichlofenthion based on nanometer-sized titania coupled with a screen-printed electrode. *Anal. Chem.* 83, 5290–5295. doi:10.1021/ac200706k

Li, Y., Xu, M., Li, P., Dong, J., and Ai, S. (2014). Nonenzymatic sensing of methyl parathion based on graphene/gadolinium Prussian Blue analogue nanocomposite modified glassy carbon electrode. *Anal. Methods* 6, 2157–2162. doi:10.1039/C3AY41820K

Liang, H., Miao, X., and Gong, J. (2012). One-step fabrication of layered double hydroxides/graphene hybrid as solid-phase extraction for stripping voltammetric detection of methyl parathion. *Electrochemistry Commun.* 20, 149–152. doi:10.1016/j.elecom.2012.04.010

Liu, G., and Lin, Y. (2006). biosensor based on self-assembling acetylcholinesterase on carbon nanotubes for flow injection/amperometric detection of organophosphate pesticides and nerve agents. *Anal. Chem.* 78, 835–843. doi:10.1021/ac051559q

MdIsa, I., Saidin, M. I., Ahmad, M., Hashim, N., Bakar, S. A., Ali, N. M., et al. (2017). Chloroplatinum(II) complex-modified MWCNTs paste electrode for electrochemical determination of mercury in skin lightening cosmetics *Electrochim. Acta.* 253, 463–471. doi:10.1016/j.electacta.2017.09.092

Moinfar, S., and Hosseini, M-R. M. (2009). Development of dispersive liquid-liquid microextraction method for the analysis of organophosphorus pesticides in tea. *J. Hazard. Mater.* 169, 907–911. doi:10.1016/j.jhazmat.2009.04.030

Moutcine, A., and Chtaini, A. (2018). Electrochemical determination of trace mercury in water sample using EDTA-CPE modified electrode. *Sensing Bio-sensing Res.* 17, 30–35. doi:10.1016/j.sbsr.2018.01.002

Mulchandani, A., Mulchandani, P., Chen, W., Wang, J., and Chen, L. (1999). Amperometric thick-film strip electrodes for monitoring organophosphate nerve agents based on immobilized organophosphorus hydrolase. *Anal. Chem.* 71, 2246–2249. doi:10.1021/ac9813179

Mulchandani, A., Chen, W., Mulchandani, P., Wang, J., and Rogers, K. R. (2001). Biosensors for direct determination of organophosphate pesticides. *Biosens. Bioelectron.* 16, 225–230. doi:10.1016/s0956-5663(01)00126-9

Niazi, A., and Yazdanipour, A. (2007). Spectrophotometric simultaneous determination of nitrophenol isomers by orthogonal signal correction and partial least squares. *J. Hazard. Mater.* 146, 421–427. doi:10.1016/j.jhazmat.2007.03.063

Obare, S. O., De, C., Guo, W., Haywood, T. L., Samuels, T. A., Adams, C. P., et al. (2010). Fluorescent chemosensors for toxic organophosphorus pesticides: a review. *Sensors* 10 (7), 7018–7043. doi:10.3390/s100707018

Parham, H., and Rahbar, N. (2010). Square wave voltammetric determination of methyl parathion using ZrO2-nanoparticles modified carbon paste electrode. *J. Hazard. Mater.* 177, 1077–1084. doi:10.1016/j.jhazmat.2010.01.031

Pohl, P. (2009). Determination of metal content in honey by atomic absorption and emission spectrometries. *TrAC Trends Anal. Chem.* 28, 117–128. doi:10.1016/j.trac.2008.09.015

Ryu, H. S., Youn, H. J., Hong, K. S., Chang, B. S., Lee, C. K., and Chung, S. S. (2002). An improvement in sintering property of β-tricalcium phosphate by addition of calcium pyrophosphate. *Biomaterials* 23, 909–914. doi:10.1016/S0142-9612(01)00201-0

Sanghavi, B. J., Hirsch, G., Karna, S. P., and Srivastava, A. K. (2012). Potentiometric stripping analysis of methyl and ethyl parathion employing carbon nanoparticles and halloysite nanoclay modified carbon paste electrode. *Anal. Chim. Acta.* 735, 37–45. doi:10.1016/j.aca.2012.05.029

Shulga, O., and Kirchhoff, J. R. (2007). An acetylcholinesterase enzyme electrode stabilized by an electrodeposited gold nanoparticle layer. *Electrochem. commun.* 9, 935–940. doi:10.1016/j.elecom.2006.11.021

Silva, D., Cortez, C. M., Cunha-Bastos, J., and Louro, S. R. W. (2004). Methyl parathion interaction with human and bovine serum albumin. *Toxicol. Lett.* 147, 53–61. doi:10.1016/j.toxlet.2003.10.014

Silva, E. L., Roldan, P. D. S., and Giné, M. F. (2009). Simultaneous preconcentration of copper, zinc, cadmium, and nickel in water samples by cloud point extraction using 4-(2-pyridylazo)-resorcinol and their determination by inductively coupled plasma optic emission spectrometry. *J. Hazard. Mater.* 171, 1133–1138. doi:10.1016/j.jhazmat.2009.06.127

Tadayyon, A., Arifuzzaman, S. M., and Rohani, S. (2003). Reactive crystallization of brushite under steady state and transient conditions: modeling and experiment. *Ind. Eng. Chem. Res.* 42, 6774–6785. doi:10.1021/ie030354+

Thota, R., and Ganesh, V. (2016). Selective and sensitive electrochemical detection of methyl parathion using chemically modified overhead projector sheets as flexible electrodes. *Sensors and Actuators B.* 227, 169–177. doi:10.1016/j.snb.2015.12.008

Triunfante, P., Soares, M. E., Santos, A., Tavares, S., Carmo, H., and Bastos, M. D. L. (2009). Mercury fatal intoxication: two case reports. *Forensic Sci. Int.* 184, e1-e6. doi:10.1016/j.forsciint.2008.10.023

Yang, J., Yang, C., Jiang, H., and Qiao, C. (2008). Overexpression of methyl parathion hydrolase and its application in detoxification of organophosphates. *Biodegradation* 19, 831–839. doi:10.1007/s10532-008-9186-2

Yao, Y., Zhang, L., Xu, J., Wang, X., Duan, X., and Wen, Y. (2014). Rapid and sensitive stripping voltammetric analysis of methyl parathion in vegetable samples at carboxylic acid-functionalized SWCNTs-β-cyclodextrin modified electrode. *J. Electroanalytical Chem.* 713, 1–8. doi:10.1016/j.jelechem.2013.11.024

Zeng, Y., Yu, D., Yu, Y., Zhou, T., and Shi, G. (2012). Differential pulse voltammetric determination of methyl parathion based on multiwalled carbon nanotubes-poly(acrylamide) nanocomposite film modified electrode. *J. Hazard. Mater.* 30, 217–218. doi:10.1016/j.jhazmat.2012.03.033

In vitro Toxico-genomics of Etoposide Loaded Gelatin Nanoparticles and Its *in-vivo* Therapeutic Potential: Pharmacokinetics, Biodistribution and Tumor Regression in Ehrlich Ascites Carcinoma (EAC) Mice Model

Imran Moin, Largee Biswas, Md Zafaryab, Namrata Kumari, Ankita Leekha, Disha Mittal and Anita Kamra Verma *

Kirori Mal College, University of Delhi, New Delhi, India

Globally, breast cancer is the foremost cause of mortality among women detected with cancer, with 21% diagnosed in India alone. Etoposide loaded gelatin nanoparticles (EGNP) were prepared and its physical characterization (size:150nm±0.241; zeta potential −29.32 mV) was done along with *in-vitro* studies to assess biotoxicity, intracellular ROS, cell cycle arrest and death caused by EGNPs. We report the molecular pathways induced by EGNP *in-vitro*, pharmacokinetics, biodistribution and tumor regression *in-vivo* in Balb/c mice. Gene expression profiling of Bax, Bcl$_2$, p53, Caspase-3, RIPK1, RIPK3 and *ß*-actin as internal control were done by RT-PCR wherein Etoposide and EGNP treated MCF-7 cells showed higher expressions of apoptotic genes-Bax, p53, caspase-3, lower expression of anti-apoptotic gene-Bcl$_2$ when compared to control. Enhanced expression of necroptosis-RIPK1 were observed, while RIPK3 was insignificant. Since, RIPK1 regulates necroptosis and apoptosis, expression of apoptotic markers confirmed apoptotic molecular mechanisms. Negligible hemolysis of Gelatin nanoparticles (GNP), and EGNP at selected dosages confirmed biocompatibility. *In vivo* pharmacokinetics and biodistribution were done by ^{99}Tc-labelled nanoparticles indicating increased circulation of EGNPs, allowing accumulation at the tumor site by Enhanced permeability and retention (EPR) phenomena. Tumor regression indicates the efficacy of EGNP by reducing the tumor burden when compared to void GNP and Etop *per se*, resulting in increased life span. High biocompatibility and bio-efficacy of EGNPs prove their therapeutic potential in cancer treatment.

Keywords: EGNPs, biodistribution, pharmacokinetics, necroptosis, apoptosis, toxicogenomics, tumor regression

INTRODUCTION

Cancer is a global life-threatening problem, only second to cardiovascular disease. Past few decades have witnessed an exponential rise in incidence of cancer, by about 33%. Breast Cancer is the most frequently occurring cancer worldwide affecting ~2.5 million females every year and the total cancer cases in India are predicted to be ~170,000 as per WHO report which is higher by ~14% amongst all

cancers in India (Jain et al., 2020). Breast cancer incidence in both sexes and in age-specific manner has increased by 14% uptil 2018. Globally, there is a 43% increase in cancer incidence as a result of aging (contributing 13%) and burst in population growth (15%) (Fitzmaurice et al., 2017).

Successful cancer therapeutics include alkylating agent, antimetabolites drugs, and naturally occurring alkaloids such as Vinblastine, Vincristine, Etoposide, Irinotecan, Teniposide, Topotecan, Paclitaxel, Docetaxel etc (Shu-Ting et al., 2016). Etoposide (Etop) being a podophyllotoxin derivative and an inhibitor of deoxyribonucleic acid (DNA) topoisomerase II is preferred as it primarily effects the G2 phase in cell cycle (Siddiqui et al., 2015). Etop administration is challenging due to its lipophilic nature and short half-life in serum. It further prevents cancer cell growth and DNA replication by inducing apoptosis in cancer cell. Physiologically, apoptosis is the main mechanism for eliminating unwanted cells (Montecucco et al., 2015). Apoptosis resistance is a hallmark of innumerable cancer cells that limits the success of conventional chemotherapy. Reports further suggest that the response of tumor cells to various chemotherapeutic drug was not confined only to apoptosis but also includes other modes of cell death (Brown and Attardi, 2005) like caspase-independent apoptosis, necroptosis, paraptosis, pyroptosis, and slow cell death, whose morphologic and biochemical characteristics vary from current definitions of the major cell death pathways (Ricci and Zong, 2006). Therefore, targeting non-apoptotic pathway may emerge as an alternative strategy to combat the menace of cancer. The programmed necrosis emerged as a potential backup mechanism to apoptosis that was assessed here. Unlike apoptosis, necroptosis is a caspase-independent death program that may be mediated by receptor interacting protein kinase-3 (RIPK3) (Moriwaki and Chan, 2013). When caspase inhibition occurs, the cellular inhibitor of apoptosis proteins (cIAPs) get depleted, tumor necrosis factor (TNF) receptor-1 then stimulates a cascade that terminates by binding RIPK3 with its upstream molecule-RIPK1 via the RIP homotypic interaction motif (RHIM). Phosphorylation of RIPK1 and RIPK3 stabilizes the complex triggering formation of necrosome. Mixed lineage kinase domain-like (MLKL) a substrate of RIPK3 is recruited by stimulated, RIPK3 (Sun et al., 2012), and gets phosphorylated to form oligomers that gets transported to the intracellular membranes as well as the plasma membrane, which finally ruptures the membrane (Cai et al., 2014; Chen et al., 2014; Dondelinger et al., 2014; Wang et al., 2014).

Toxicogenomics has been considered as a promising tool for measurement of the gene expression pattern elicited by toxicant exposure (Nuwaysir et al., 1999). Toxicity can be reliably indicated by toxicogenomics (Pognan, 2007; Afshari et al., 2011); gene expression profiles at an early stage accurately projected the potential for non-genotoxic carcinogenicity, carcinogenicity and hepato-carcinogenicity (Nie et al., 2006; Ellinger-Ziegelbauer et al., 2008).

Exceptional progress in nanotechnological development towards administering lipophilic drugs offer immense promise to enhance circulation time of drug combined with drug stability to achieve targeted delivery of therapeutic molecule (Elzoghby et al., 2012; Singh et al., 2013). A vital parameter for innovatively engineering a nanoparticle for application both in vitro and in vivo is its biocompatibility in the biological system (Hubbell and Chilkoti, 2012) that can be achieved by modulating various factors like fabrication procedures, careful selection of cross-linkers and surfactants; nevertheless, its the biopolymers that have the most critical role as they contribute the framework in which the drug molecules have to be entrapped, and finally, it is the surface of the polymer that will intermingle with the biological fluids (Vonarbourg et al., 2006; De Jong and Borm, 2008; Jabr-Milane et al., 2008). Therefore, use of natural polymers like chitosan, alginate, and gelatin has aroused excessive attention in nanotechnology as these biopolymers display all the earlier-mentioned characteristics, and additionally, they are water soluble and biodegradable (Tabata, 2009; Cesàro et al., 2012; Singh et al., 2014). Gelatin is a naturally occurring versatile FDA (United States) approved polymer having exceptional properties like biocompatibility, biodegradability with ease of chemical modification attained by the fractional hydrolysis of collagen (Kaul and Amiji, 2004; Magadala and Amiji, 2008; Elzoghby, 2013). Being a polyampholyte, gelatin exhibits both cationic and anionic groups, along with the hydrophobic group in an estimated ratio of 1:1:1, making this polypeptide unique. Gelatin based nanoparticles have been synthesized using various techniques like desolation that uses acetone/alcohol as a desolvating agent for gelatin in aqueous solution for dehydrating the polymer chain resulting in a conformational change (Fuchs et al., 2012). Irrespective of the protocol for fabrication, GNPs have been expansively used for drug/gene delivery carrying cargo that is either hydrophilic or hydrophobic anticancer drugs, vaccine and proteins (Saxena et al., 2005; Zwiorek et al., 2005). Herein, we report the varied adverse effects of Etop that can be reduced by encapsulating it in GNPs (EGNPs). The synthesized GNPs were characterized for its size, zeta potential, surface morphology and encapsulation. We report the bio-efficacy, ROS generation and cell cycle analysis induced by EGNPs in MCF-7 breast cancer cell line and HEK-293 cells and compared these results with etoposide per se. Furthermore, these nanoparticles were evaluated for its ability to regulate different cell death pathways. EGNPs might emerge as a promising drug delivery system for improved therapeutic index of lipophilic Etop as assessed by pharmacokinetics, biodistribution and tumor regression in-vivo in Balb/c mice.

Chemicals Used for Experiments

Gelatin (Bovine, Type B, 175 Bloom) Etoposide, MTT [(4,5-dimethylthiazol-2-yl)-2,5-diphenyltetrazolium bromide], Nec-1 [Necrostatin-1], zVAD, were all procured from Sigma Chemical Co., (St. Louis, MO, United States). Acetone, Chloroform, Isopropanol, Ethanol, Glutaraldehyde (25% v/v), L-cysteine and Dimethyl sulphoxide (DMSO) were obtained from SRL Pvt Ltd. India. Dulbecco's modified Eagle's medium (DMEM), Antibiotic cocktail containing streptomycin and penicillin, Trypsin were procured from HiMedia Pvt Ltd. Fetal bovine serum (FBS) was purchased from GIBCO. Trizol was obtained from Invitrogen. Primers (Forward and reverse) for RIPK-1, RIPK-3, MLKL, Bax, Bcl2, Caspase 9, p53 were procured from Thermo scientific.

METHODS

Synthesis of Gelatin Nanoparticles

Gelatin-5% (type-B; 75 bloom) dissolved in warm(~50°C) distilled water (25ml) was UV-degraded at room temperature (RT) for 12h. The UV-degraded gelatin solution was then titrated with an equal volume of acetone and the precipitate was dissolved in an equal volume of warm deionized water (~50°C), further pH was adjusted to 2.5. A second step desolvation was carried out and 7% glutaraldehyde was added dropwise. The clear supernatant was discarded after centrifugation at 20,000g for 19min. After washing the pellet, it was suspended in acetone and left overnight under constant stirring. After 24h slightly turbid solution containing nanoparticles was harvested (Saxena et al., 2005; Moin et al., 2018).

Dynamic Laser Scattering and Nanoparticle Tracking Analysis

Dynamic Light Scattering (DLS) and zeta potential measurements were calculated on Malvern Zetasizer Nano ZS equipped with a solid state HeNe laser (= 633nm). All the samples were measured three times at 25°C. The intensity-weighted mean diameter was used as the hydrodynamic size. The particle size distribution was evaluated using polydispersity index (PdI) (Verma et al., 2011).

Nano Sight NS 300 (Nano Sight, Malvern, United Kingdom) was used for the NTA measurement, equipped with a Viton fluoro-elastomer O-ring and a sample chamber with 640nm laser. The chambers were injected with a requisite amount of samples using sterile syringe. The samples were measured with gain adjustments and manual shutter for 40s and data was captured by NTA 2.0 Build 127. The NTA software analyze the size of all the particles to calculate the arithmetic values which corresponds to the SD values and mean size obtained by the software.

Entrapment Efficiency (%)

Etop was entrapped by our earlier published procedure. Etop was solubilized in DMSO under vigorous stirring and bath sonication was added to 5mg/ml of GNPs. The free Etop was entrapped in GNPs. The solution was filtered through a filter [100KDa cut off] to separate free Etop from EGNP. The absorbance of free Etop was read in a spectrophotometer (Cary 60 UV-Vis, Agilent Technologies) (Verma et al., 2005). The EE% was calculated as:

$$EE\% = \frac{[Drug]total - [Drug]free}{[Drug]total} \qquad (1)$$

Where, free Drug and total Drug are the sum of total Drug added along with free Drug, respectively.

Bio-Toxicity Assay

Cytotoxicity of EGNP, void gelatin nanoparticles (GNP) and Etop *per se* was estimated by established/published protocol

(Leekha et al., 2016). Briefly, the requisite cells were seeded in ninty six well microplates. Cells were subjected to varied concentrations of GNP, EGNP and Etop *per se*, and incubated for 24 and 48h at 37°C. After incubation, MTT was added in each well. After 4 h, media was discarded carefully. Added DMSO to solubilize the formazan crystals formed after the reaction, and using a UV-spectrometer absorbance was observed at 570nm.

The % Cytotoxicity was calculated by

$$\%Cytotoxicity = \frac{[Absorbance\,(control) - Absorbance\,(test)]}{Absorbance\,(control)} \times 100 \qquad (2)$$

Where, Absorbance (control) is the absorbance of control sample and Absorbance (test) is absorbance of test sample.

Quantitation of Intracellular ROS Generation

For investigation of ROS generation, 1×10^6 cells were seeded in petri-plates and kept overnight in RPMI-1640 supplemented with 10% FBS were incubated with Etop, GNP and EGNP. Cells were harvested after treatment, and incubated with 25μM of DCF-DA at 37 °C for 40 min, and the plates were subsequently wrapped in aluminium foil to restrain entering of light. Fluorescence intensity was measured in arbitrary units by means of spectrofluorimeter (Agilent Technologies, United States) having an excitation at 485nm, and an emission at 529nm, respectively, having the slit-width adjusted to 5.0 (Leekha et al., 2016)

Cell Cycle Assessment

MCF-7 cells and HEK-293 cells were cultured in 6-well plates till they reach the logarithmic growth phase, after 24h they were treated with various concentrations of Etop, EGNP and GNPs. Post 18h of treatment, cells were trypsinized and centrifuged for 10min at 1,100rpm in a cooled centrifuge. The harvested cells were washed three times with PBS, and fixed with 70% ethanol for 4h at 4°C. After fixing, the cells were washed again with PBS and then cells were incubated with Propidium Iodide (20μg/ml) and DNase-free RNase. Samples were analyzed at the BD Aria11: Becton and Dickinson, San Jose, CA Flow Cytometer. The percentages of cells in the G1, S, and G2 phases of the cell cycle were calculated using FlowJO software.

Expression of Apoptotic Proteins

Cells (1×10^6) were plated and allowed to adhere overnight. After 24h of the treatment with selected concentration of the Etop, EGNP, Nec1+Etop, Nec1+EGNP, zVAD + Etop and zVAD + EGNP; PBS was used to wash the cells and total RNA were extracted from treated and untreated MCF-7 cells using Trizol reagent (Invitrogen, CA, United States) as per the manufacture's instruction. The concentration and quality of RNA were quantified using a nanophotometer (Thermo Fisher, United States). cDNA was synthesized through the commercially available kit easy i-script cDNA synthesis

(Bio-Rad, USA). Real time PCR (SYBR green) was done on Quant Studio 5 Applied Biosystem PCR, through defined annealing temperature for specific genes to check the expressions of apoptotic and necroptotic genes. The sequences of primer used for Bax, Bcl2, p53, Caspase-3, RIPK1, RIPK3, MLKL and Actin were designed as described in Supplementary Table S3.

Ex vivo Hemolysis

To measure the hemolytic activity, mice whole blood was used and evaluated as per established protocol (Verma et al., 2005). The heparinized blood was washed twice with PBS (pH 7.4). RBC were suspended in PBS at 1:1 ratio. The RBC were incubated with PBS, GNP, Etop *per se*, and EGNP up to 4h at 37°C. The absorbance of lysed RBC was measured using UV-visible spectrophotometer (Bio-Tek, United States) at 540nm, after incubation of 2 and 4h, and percent hemolysis was evaluated using the following formula

$$\%\text{Hemolysis} = \frac{\text{Abs of positive control} - \text{Abs of sample X 100}}{\text{Abs of positive control}}$$

(3)

Radiolabeling of Gelatin Nanoparticles

The radiolabeling of Etop *per se* and EGNP was done with $^{99m}\text{TcO4}^-$ by direct labelling method. Shortly, 100μl of $^{99m}\text{TcO4}^-$ normal saline was added to Etop and EGNP. Then, the pH was adjusted to 6.5 and incubated for 15min at 37°C. The radiolabeled formulation was purified from free $^{99m}\text{TcO4}-$, by passing through a column [Sephadex G-20] radiocolloids and then eluted with normal saline. The purity of the labelled formulation was verified by Instant thin-layer chromatography (ITLC) by means of silica gel-coated fiber sheets (Gelman Science Inc., Ann Arbor, MI, United States) and the mobile phase was acetone. The Rf value of free $^{99m}\text{TcO4}^-$ was found to be in the range of 0.9–1.0, a well-type γ ray spectrometer (Type CRS 23C, Electronic Corporation of India Ltd. Hyderabad, India) was used for counting the radioactivity.

Biodistribution

Inbred, 4–6weeks old female Balb/c mice weighing around 20–25g were selected and studies were performed as per our standardized previously published protocol (Verma and Sachin, 2008). The animals were anaesthetized followed by injection of ^{99m}Tc-labeled EGNP and Etop (1mg/kg body weight) were administrated through the tail vein. As per decided time point, the study groups of four mice Etop *per se*, and EGNP ^{99m}Tc- were used. Post the required time period the animals were sacrificed by cervical dislocation and various tissues (liver, kidney, spleen, heart, lung, intestine, stomach, brain, and blood) were harvested. Using shielded well-type γ-ray spectrometer (Type CRS 23C, Electronic Corporation of India Ltd., Hyderabad, India), the radioactivity was measured.

Gamma Scintigraphic Imaging

100μCi of the 99mTc- dosage formulation of GNP, Etop *per se*, and EGNP was injected in rabbit through the external ear vein.

Single Photon Emission Computerized Tomography (SPECT, LC 75-005, Diacam, Siemens, United States) was conducted after 4 and 24h of administration of formulation.

Tumor Regression

Female Balb/c mice were purchased from Small Animal Facility (SAF), AIIMS Delhi and were maintained at relative humidity of 55 ± 5%, temperature 25 ± 2°C, and normal chow diet (Golden feed). All the experiments performed were approved by Institutional Animal Ethics Committee (IAEC), K.M. College, University of Delhi (Reg No. 1666/GO/Re/S/12/CPCSEA and Protocol no. DU/KR/IAEC/2018/03). Subcutaneous Ehrlich Ascites Carcinoma (EAC) mice model was used to assess tumor regression. EAC cells were maintained in the peritoneum of female Balb/c mice (20–25g) by serial intraperitoneal passage at regular intervals of 7–10days (Verma et al., 2018). To assess tumor inhibition ~1.5×10^6 cells in 100μl of sterile PBS were injected subcutaneously on the dorsal lower back. Mice were monitored regularly and tumor size was measured every alternate day till it reached a measurable size.

Tumor bearing female Balb/c mice were randomly divided into groups, having five animals per group. Group I was considered the Control (tumor bearing, untreated) receiving Saline, Group II Etop receiving 1mg/kg; Group III GNP receiving 1mg/kg; Group IV EGNP receiving 1mg/kg daily intravenously (i.v) for 14days (7days after the tumor inoculum). All the mice were observed for tumor regression and survival. The tumor volume was measured on alternate days using a vernier calliper.

$$\text{Tumour Volume} = \frac{\left[\text{Length x (Breath)}^2\right]\text{cm}^3}{2}$$

(4)

After 21days, the mice were euthanised and tumors were harvested and weighed. To minimize personal bias, all measurements were done by same examiner.

Statistical Analysis

The results were articulated as the Mean standard deviation. Evaluation amongst groups were evaluated by One-way ANOVA and the respective means were separated by Tukey's test using the Prism (5.0) software (Prism software Inc. CA, United States). The levels of significance were accepted at ≤0.05 level.

RESULTS AND DISCUSSION

Currently, there is an increased demand for biopolymeric nanoparticles as a means for enhanced delivery of lipophilic chemotherapeutic moieties. For the preparation of homogenous nanoparticles under controlled parameters two-step desolvation method was used to synthesize GNPs; any perturbation of pH i.e a slight increase or decrease alters the net negative or positive charges, principally due to the ionization of -COOH and -NH$_2$ groups, respectively. As a cross linker, glutaraldehyde was used to saturate the functional amino groups

FIGURE 1 | Physical Characterization of GNP **(A)** NTA video frame (A) **(B)** size of the GNP **(C)** Zeta potential of GNP = −29.5mV **(D)** UV Spectra of Etop and EGNP before filtering and after filtering at 257nm. Calculated Entrapment Efficiency = 29%.
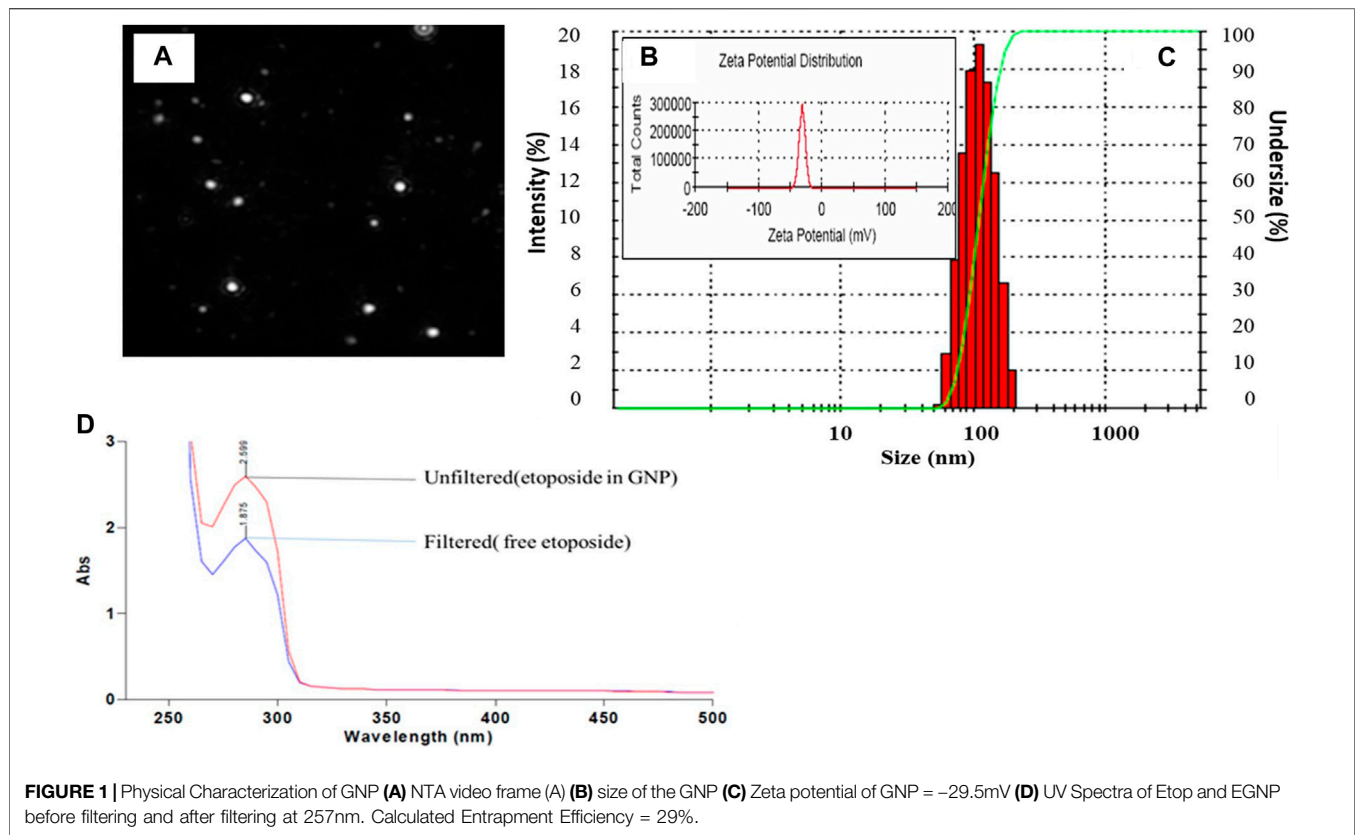
that were accessible for the interaction of the covalent amino-reactive ligands. Size of GNPs was dependent on the number of cross-links, but the cross-linker was used as minimal as possible in order to prevent toxicity from free aldehyde groups. Additionally, L-cysteine was used to quench the aldehyde groups that might possibly produce the free sulfhydryl groups on the surface of GNPs (Coester et al., 2000). **Figure 1** depicts the characterization of GNP where, Fig (A) shows video frame of the morphology of the nanoparticles followed by size by DLS ie. 150nm ±0.241 (1B). The zeta potential (ZP) of GNP was -29.32mV as represented in **Figure 1C**. Nanoparticles having ZP of > +25mV or < −25mV usually have high degree of stability. Lower dispersions ZP values will often lead to aggregation, coagulation, or flocculation due to Van der Waal's interparticle attraction (Shnoudeh et al., 2019), **Figure 1D** indicates the UV spectra of both Etop *per se* and EGNP. Figure S1 represents the UV spectra of Gelatin polymer and GNPs. The entrapment efficiency of Etop in EGNPs was ~29% (**Figure 1D**).

The GNPs were stable for 90h at different pH and temperature (Saxena et al., 2005) The nanoparticle sizing is critical, as the biodistribution and pharmacokinetics of the gelatin nanoparticles is largely going to be governed by this factor, with surface charge. The synthesis of Gelatin nanoparticles involves using a desolvation agent to remove low molecular weight fractions, allows the remaining high molecular weight precipitate to form ~100–300nm particles after chemical crosslinking. Experimental modifications to pH, crosslinker concentration and desolvation

agent are routinely employed to obtain desirable nanoparticle sizes (typically less than 200nm), charges (higher charges indicate greater nanoparticle stability) and chemical bonding (Elzoghby, 2013; Hudson and Margaritis, 2014).

The IC 50 was calculated to assess the biotoxicity Etop, GNP and EGNP on MCF-7 and HEK-293 cells by cell viability assay using MTT that reduces the yellow coloured tetrazolium salt to purple coloured formazan crystals. The metabolic activities are proportional to the developed colour owing to the NAD(P)H-dependent cellular oxidoreductase enzymes in living cells (Mosmann, 1983; Berridge et al., 2005). This accurate quantitation regarding proliferation rate or viability of cells is regularly used to assess a linear relationship among the metabolically active cells with respect to the color intensity. **Table S4** represents the IC50 of Etop *per se* was 142.67μg/ml in MCF–7 cells, post 24 h, while in HEK-293 it was 1,337.49μg/ml. GNP had negligible cytotoxicity on both the cell lines. IC50 of EGNP was observed to be lowest i. e 74.14μg/ml indicating maximum anti-cancer efficacy (**Figure 2**).

For further evaluation of mechanistic pathways 100μg/ml dose of Etop *per se* and equivalent Etop in EGNP was carefully chosen. In our earlier published studies GNPs and EGNPs were seen to localize in cells leading to buildup of oxidative stress and DNA damage (Moin et al., 2018). The mechanical pathways of nanoparticles to induce cellular damage and cell death induction are not yet fully understood. The pathways induced by EGNP in cellular damage and cell death are not completely known but most frequently p53 appears to play a

FIGURE 2 | Dose dependent cytotoxicity on MCF-7 and HEK-293 of Etop, GNP and EGNP for 24h **(A)** Etoposide **(B)** GNP **(C)** EGNP. Data were expressed in mean ± S.E.M (N = 3).
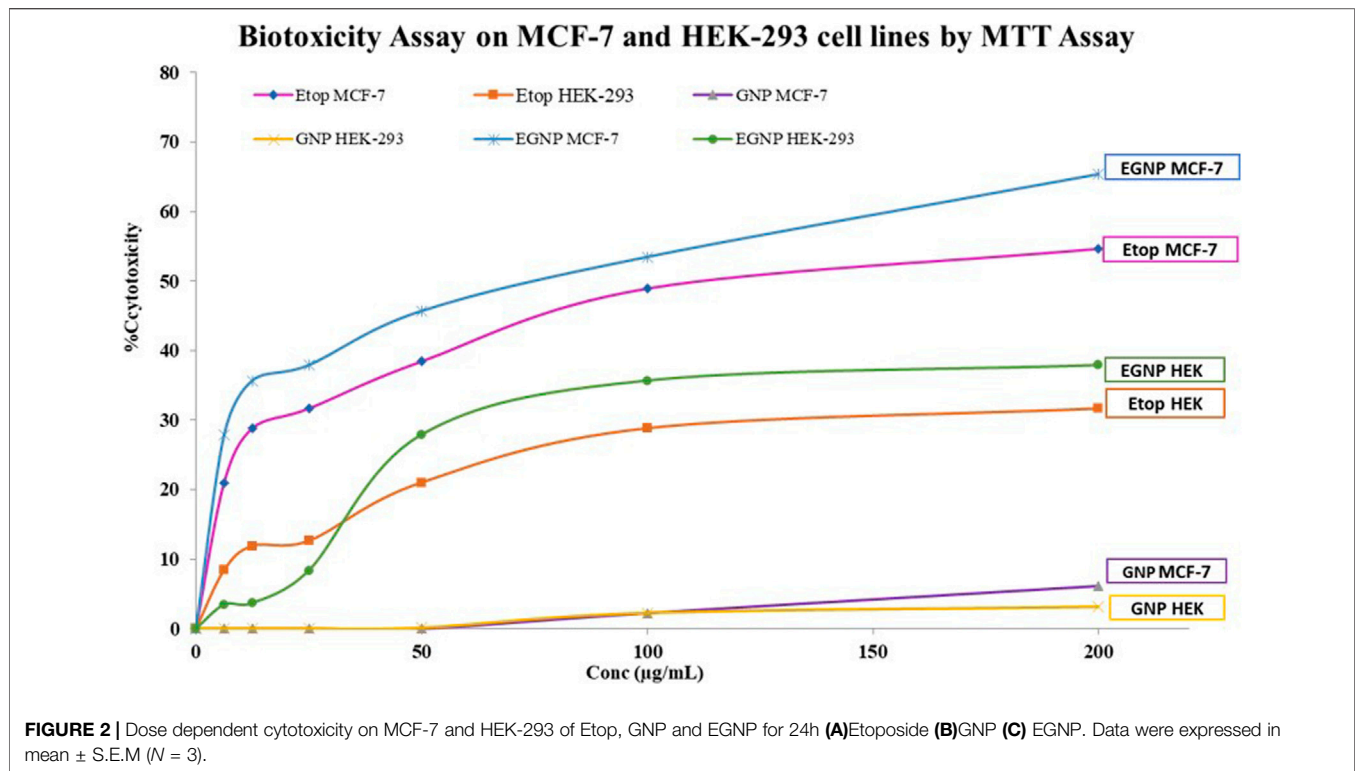
major role in ROS induced DNA damage and apoptotic cellular responses (Shafagh et al., 2015). Increased intensity of DCFDA indicated enhanced ROS generation in MCF-7 when compared to HEK-293 cells (**Supplementary Figure S2**).

EGNPs triggered enhanced release of intracellular Ca^{2+} in MCF-7 making them susceptible to Etop at a lower concentration. The twin-functional role of Etop makes it a pro-oxidant owing to its affinity to intracellular thiols in the cells. This redox perturbation possibly contributes to its carcinogenic potential and genotoxicity resulting in antitumor efficacy. In recent years, the paradigm of cell death regulation infers not only apoptosis but other form of programmed or regulated necrosis i.e. necroptosis. Moin et al., 2018, discussed the mechanism of Etop and EGNP in MCF-7 cells hypothesizing the occurrence of necroptosis. We have previously reported the influence of redox paradox of Etop on intracellular biochemical pathways that influenced cell death whereby cells were progressing both towards necroptosis and apoptosis. (Moin et al., 2018).

Herein, we assessed the levels of the major proteins responsible for the formation of Necroptosome i.e. RIPK1, RIPK3 and MLKL in the presence of both an apoptotic inhibitor zVAD and a necroptotic inhibitor Nec-1. The role of RIPK1 and RIPK3 have been expansively explored in infectious diseases. We evaluated the expression of RIPK1, RIPK3 and MLKL along with the expression of apoptotic biomarkers in MCF-7 cell line by Real-time PCR (qPCR). High expression of RIPK1 in EGNP + zVAD confirmed necroptosis, as zVAD is known to block the caspase activity (**Figure 3**). Expression of RIPK3 in Etop

and EGNP were visible, but the expression of EGNP + zVAD was low and upregulation of RIPK3 expression in EGNP + Nec-1 was significant. Although, this indicated the presence of RIPK3, but interestingly there was no evidence of necroptosis. Negligible expression of MLKL led to the understanding that lack of formation of a necroptosome was inhibiting necroptosis as it is essential for triggering necroptosis. EGNP induced high expression of RIPK1 too, so we could hypothesize that high expression of RIPK1 may push the cell towards apoptosis. Also, earlier reports suggest that RIPK1 can regulate not only necroptosis but also apoptotic cell death (Vandenabeele et al., 2013). We further confirmed the expression of apoptotic markers like p53, Bax, Caspase 9 and anti-apoptotic genes Bcl2 (**Figure 4**). Our findings suggested that Etop and EGNP treated MCF-7 cells showed enhanced expression of apoptotic gene Bax, and lower expression of anti-apoptotic gene i.e. Bcl2, when compared to their individual treatment and control. The mRNA for pro-apoptotic protein Bax was significantly elevated in cells treated with Etop and EGNP whereas the anti-apoptotic Bcl-2 signal was significantly decreased. The Bax/Bcl-2 ratio indicates enhanced apoptotic process (**Figure 5**). Etop induces apoptosis either *via* caspase dependent pathways or caspase independent pathways (Degterev et al., 2005). Literature suggests that necroptosis is normally driven by expression of RIPK3, that may be activated following phosphorylation of the serine/threonine kinase RIPK1 (Cho, 2018). RIPK3 possibly stimulates a switch in the cell's metabolism, that causes an increase in production of mitochondrial ROS that culminates in cell death (Zhang et al., 2009; Vanlangenakker et al., 2011). Further, necroptosis may emerge as an alternative form of cell death that can substitute
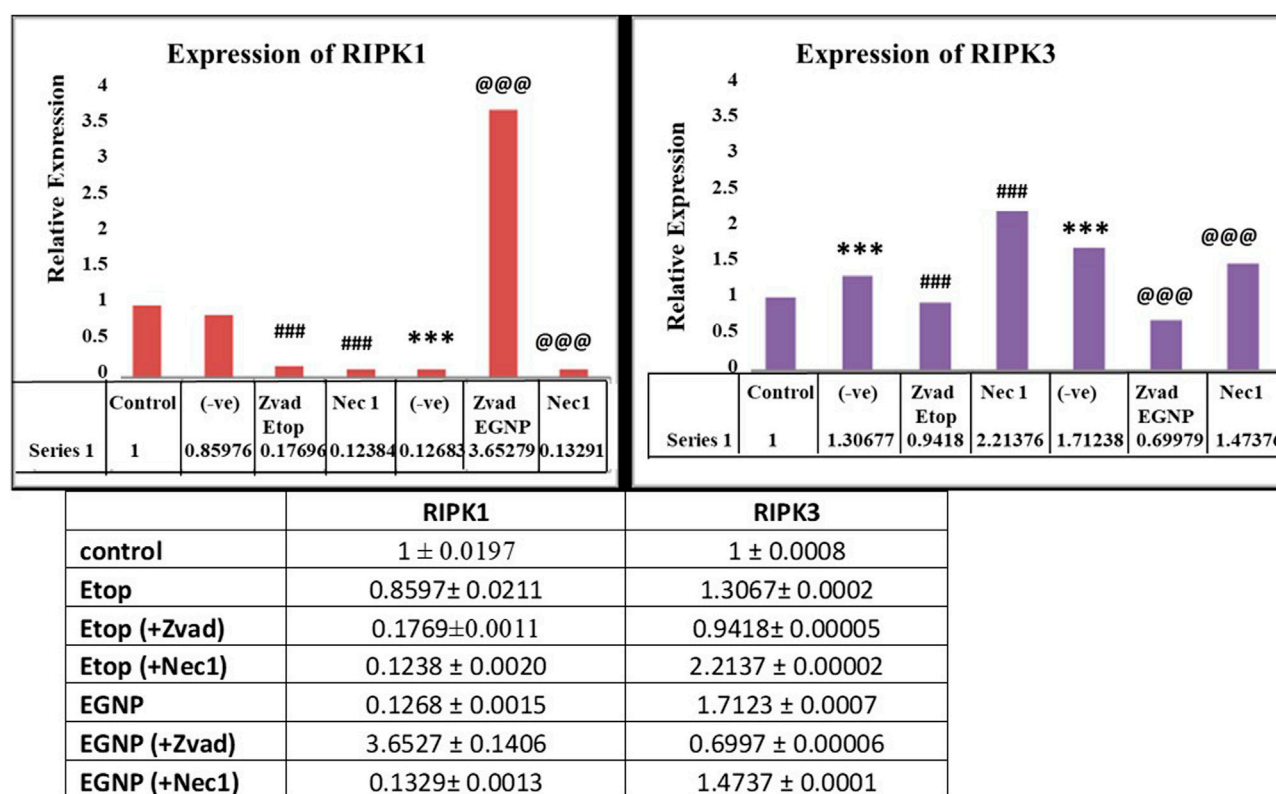
FIGURE 3 | Gene expression of RIPK1 and RIPK3 with. Etop, EGNP, zVAD+Etop, zVAD+EGNP, Nec-1+Etop and Nec-1+EGNP treated groups. Expression of GAPDH taken as internal control. Data were expressed in mean ± S.E.M (N = 3). *denotes significant difference between Control vs treated groups. # denotes significant difference between Etop vs Nec1/Zvad. @ denotes significant difference between Etop vs Nec1/Zvad. *$p < 0.05$.

	RIPK1	RIPK3
control	1 ± 0.0197	1 ± 0.0008
Etop	0.8597± 0.0211	1.3067± 0.0002
Etop (+Zvad)	0.1769±0.0011	0.9418± 0.00005
Etop (+Nec1)	0.1238 ± 0.0020	2.2137 ± 0.00002
EGNP	0.1268 ± 0.0015	1.7123 ± 0.0007
EGNP (+Zvad)	3.6527 ± 0.1406	0.6997 ± 0.00006
EGNP (+Nec1)	0.1329± 0.0013	1.4737 ± 0.0001

apoptosis, when caspase activation is blocked. Undoubtedly, necroptosis embodies a significant pathway for increasing sensitivity of tumor cells to anticancer therapies. Moreover, its potentiation may represent a crucial and an important treatment window to eliminate tumor cells, particularly those resistant to apoptosis (Giampietri et al., 2014). Even though, the conventional form of cell death is frequently concealed by other forms of cell death, it recommences as a back-up mechanism, when the other pathways are blocked.

Cell cycle arrest after treatment with Etop, GNP and EGNP along with control group on MCF-7 and HEK-293 cells was performed and the percentages of cells in G1, S, and G2/M were calculated using FlowJo software. We observed that MCF-7 cells treated with Etop, GNP and ENGP showed the significant cell cycle perturbation, G1/G0 arrest as compared to the untreated control. However, in case of HEK-293 cells treated with Etop, GNP and ENGP showed non-significant cell cycle perturbation. (**Supplementary Figure S3**, Supplementary data). **Figure 6** shows the hypothesized mechanism of the action of Etoposide/Etoposide formulation.

In order to conduct any *in vivo* study, it was essential to evaluate the biocompatibility of the nanoparticles with red blood cells (RBC) (Dobrovolskaia et al., 2008). Biocompatibility was evaluated by hemolysis assay induced by Etop *per se*, GNP, EGNP incubated with fresh mice blood

for 2 and 4h. Around 4% hemolysis (**Supplementary Figure S4**, Supplementary data) was detected in all experimental groups proving their biocompatibility ($p < 0.001$) with red blood cells compared to that of positive control (Triton X) at both the time intervals.

In spite of the anti-neoplastic efficacy of Etop, the adverse effects and pharmacokinetic hindrances such as fever, nausea, bone marrow suppression and hair loss are often limiting its use (Urban et al., 2019). Another significant pharmacokinetic drawback of Etop is its hydrophobicity (Soni and Yadav, 2014) and inconsistent bioavailability ranging from 25–74%, which is considerably high intra- and inter-patient variation, and a half-life of 4–11h (Duong et al., 2019). This short half-life often reduces the duration of exposure of Etop to cancer cells, thereby, minimizing its efficacy. Clinical results have revealed that exposure time coupled with slow release of Etop are decisive factors for maximizing its impact, since its target, i.e., topoisomerase II, will only be expressed in cells that are in mitosis phase (Snehalatha et al., 2008). To overcome the pharmacokinetic deterrents of Etop, FDA approved gelatin has been used as an excipient.

Influence of stannous chloride on labelling efficiency of Etop, GNPs and EGNPs was assessed. Etop, GNPs were labelled with ^{99m}Tc with high labelling efficiency by direct method. Amount of stannous chloride($SnCl_2$) required to reduce [99m]Tec is necessary
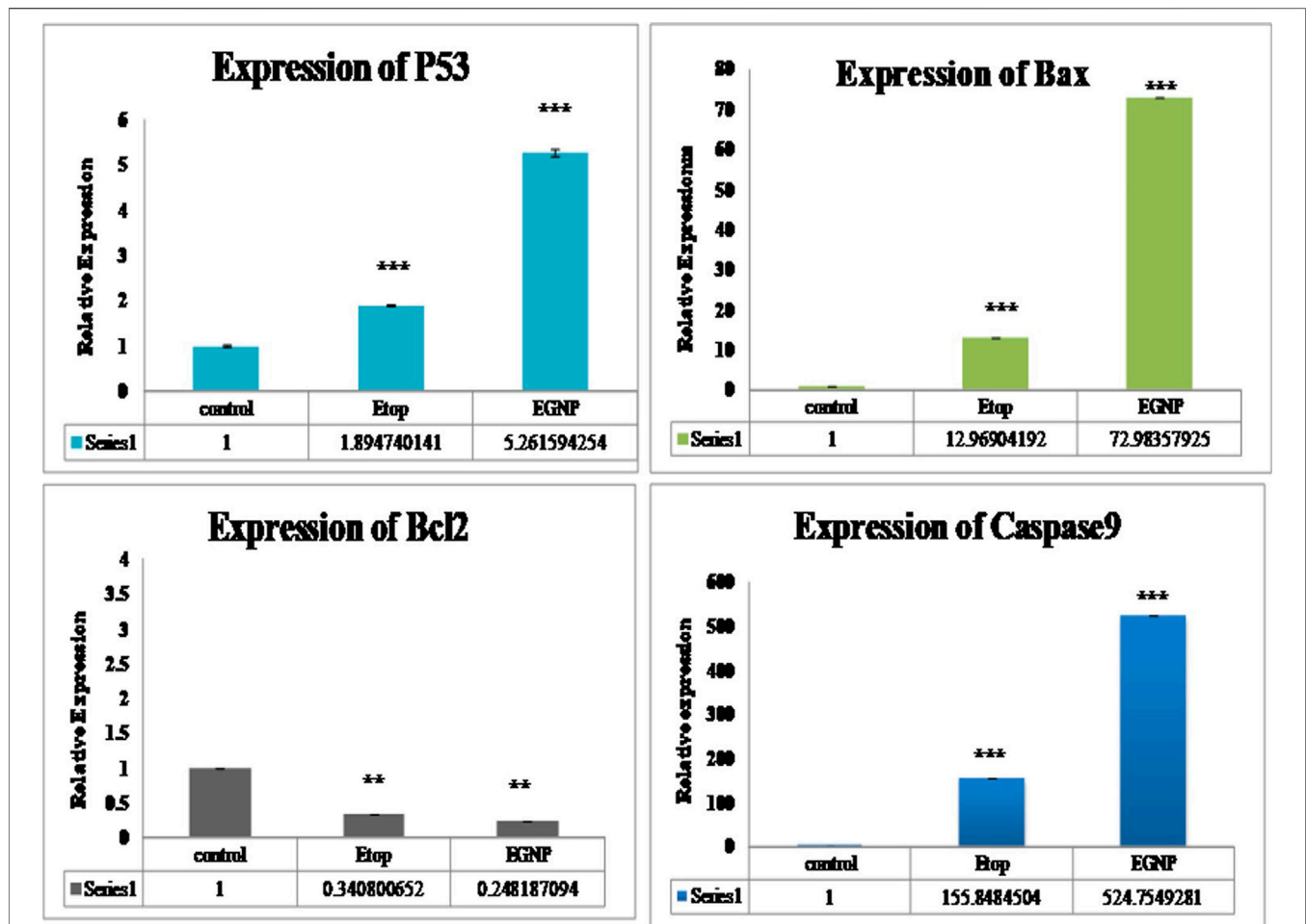
FIGURE 4 | Gene expression of p53, Bcl2, Bax, Caspase 9 with Etop, EGNP, treated groups. Expression of Beta-Actin taken as internal control. Data were expressed in mean ± S.E.M (N = 3). *denotes significant difference between Control vs treated groups. *$p < 0.05$.

in the labelling process as an enhanced amount results in the formation of radio colloids, that are unwanted. Also, reduced amounts of $SnCl_2$ results in meagre labelling efficiency. The influence of $SnCl_2$ on the labelling efficiency is shown in Supplementary Table S2 (Supplementary Data).

Herein, the optimal amount of $SnCl_2$ required for high labelling efficiency, with a low amount of free and R/H ^{99m}Tc, was observed to be 100μg for all preparations. Incubation time in which maximum percentage of labelling occurs was further optimized as 15min post-addition of ^{99m}Tc -pertechnetate to the formulation. To optimize the above parameters at each time point, quality control checks were done by TLC using ITLC strips.

In vitro Stability

Radiolabelled preparations were assessed for their stability in the presence of Phosphate buffered saline (PBS) and sera. *In vivo* physiological micro-environment like pH and temperature was simulated for evaluating the stability of the labelled Etop, GNPs and EGNPs. Stability data in PBS and sera at different time points
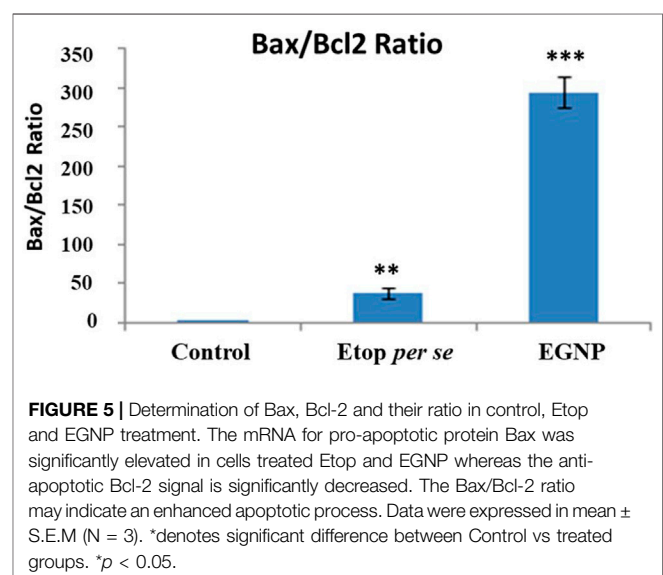
FIGURE 5 | Determination of Bax, Bcl-2 and their ratio in control, Etop and EGNP treatment. The mRNA for pro-apoptotic protein Bax was significantly elevated in cells treated Etop and EGNP whereas the anti-apoptotic Bcl-2 signal is significantly decreased. The Bax/Bcl-2 ratio may indicate an enhanced apoptotic process. Data were expressed in mean ± S.E.M (N = 3). *denotes significant difference between Control vs treated groups. *$p < 0.05$.

FIGURE 6 | Hypothesized mechanism of action of etoposide/etoposide formulation and toxicological approach to study the nanoparticles toxicity. EGNPs enter the cells *via* endocytosis to form the endosomal complex. Due to the differences in pH, etoposide is released from EGNPs to inhibit topoisomerase II activity. Free etoposide can also activate RIPK1 which further phosphorylates the RIPK3. This then recruits MLKL to form the necrosome that triggers necropoptosis. Over expression of RIPK1 can also stimulate mitochondrial based apoptosis. Our results show enhanced expression of RIPK1 and RIPK3 and decreased expression of MLKL but exhibits necroptosis that is probably because of enhanced RIPK3.

are represented in **Supplementary Table S3**. All preparations were stable in upto 24h at different time points and in their respective media, ^{99m}Tc- labelled preparations have shown a percentage of radiolabelling of more than 90%. The stability of the labelled complexes in different conditions clearly indicates the utility of the label as a marker for biodistribution studies.

With this assurance, biodistribution and pharmacokinetic studies were conducted in Balb/c mice and rabbit, respectively. Biodistribution of ^{99m}TcGNP and ^{99m}TcEGNP in Balb/c mice indicated maximum accumulation in kidney in terms of % uptake/gm in kidney (13.10 %uptake/gm), liver and blood after 1 h, that subsequently decreased upto 24h (**Figures 7A,B**). The activity in lung, liver and spleen after first hour of administration was found to be almost same at all time points. ^{111}In and ^{64}Cu Radiolabelling of nanoparticles enables the visualization of the interactions between the nanoparticles and the kidneys by PET and SPECT, requiring only attomolar doses of injected particles (10–18mol l−1). For example, labelling silica nanoparticles with ^{124}I allows imaging of their *in vivo* transport through the kidneys in patients with cancer (Bujie et al., 2018); The retention in the non-target tissues was comparable for all the probes, with low uptake in most of the assessed organs and higher levels of activity in the kidneys.

(Starmans et al., 2013). Half-life ($t_{1/2}$) in context of GNPs and EGNPs is a useful evaluation to observe the pharmacokinetics and is referred to as the time taken for nanoparticles concentration in the blood to reduce to half its initial value. The elimination rate constant and half life time values indicated prolonged circulation of ^{99m}TcEGNP in the blood owing to a lower elimination rate when compared to ^{99m}TcGNP and ^{99m}TcEtop (**Figure 7C**). This result when coupled with pharmacokinetics of ^{99m}TcEGNP illustrated the reduced activity of ^{99m}TcEGNP at 4h. Both liver and kidney showed enhanced accumulation of ^{99m}TcEGNP. **Figure 5B** as indicated by the gamma scintigraphy images in rabbit exhibiting accumulation of ^{99m}TcGNP and ^{99m}TcEGNP in various organs performed post 2 and 24h administration (**Figure 5D**. The hot spots in rabbit represents the accumulation of ^{99m}TcGNP and ^{99m}TcEGNP that was coupled with the result of bio-distribution. Plasma molecules and particles may perfuse deeper and more evenly into the tumor tissue. Therefore, while designing nanoparticles it is essential to control the size to overcome the criteria described earlier. Consequently, an optimal size of nanoparticles that can deliver adequate cargo of drugs to be dispersed homogeneously in solid tumors is desired to induce maximum therapeutic efficacy that is reported between 10 and 200nm in diameter (Allen and Cullis, 2004).
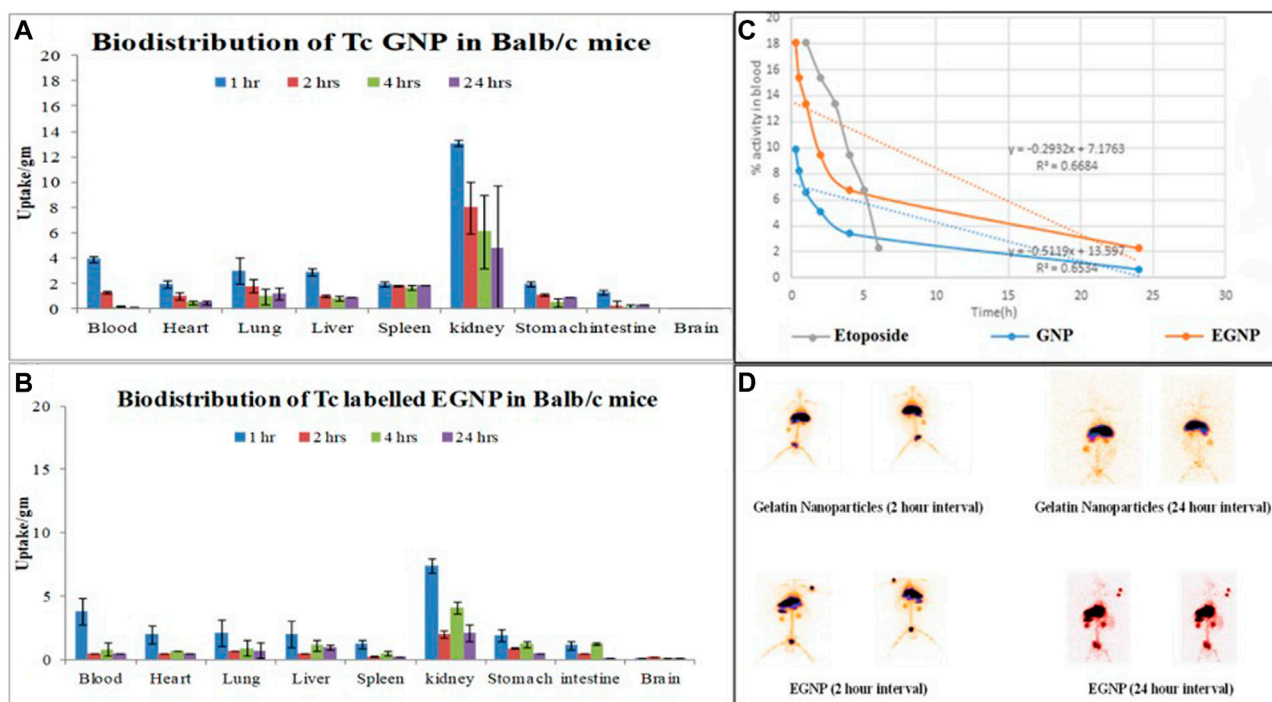
FIGURE 7 | Graph illustrate the *in vivo* bio-distribution of [99m]TcGNP in **(A,B)** [99m]TcEGNP various organs of Balb/c mice **(C)** blood pharmacokinetics of intra-venously injected ^{99m}Tc-Etop, [99m]TcGNP and [99m]TcEGNP in rabbit **(D)** *In vivo* gamma scintigraphic imaging representing the accumulation of [99m]TcGNP and [99m]TcEGNP post 2 h and 24 h of injection through the ear vein of rabbit.
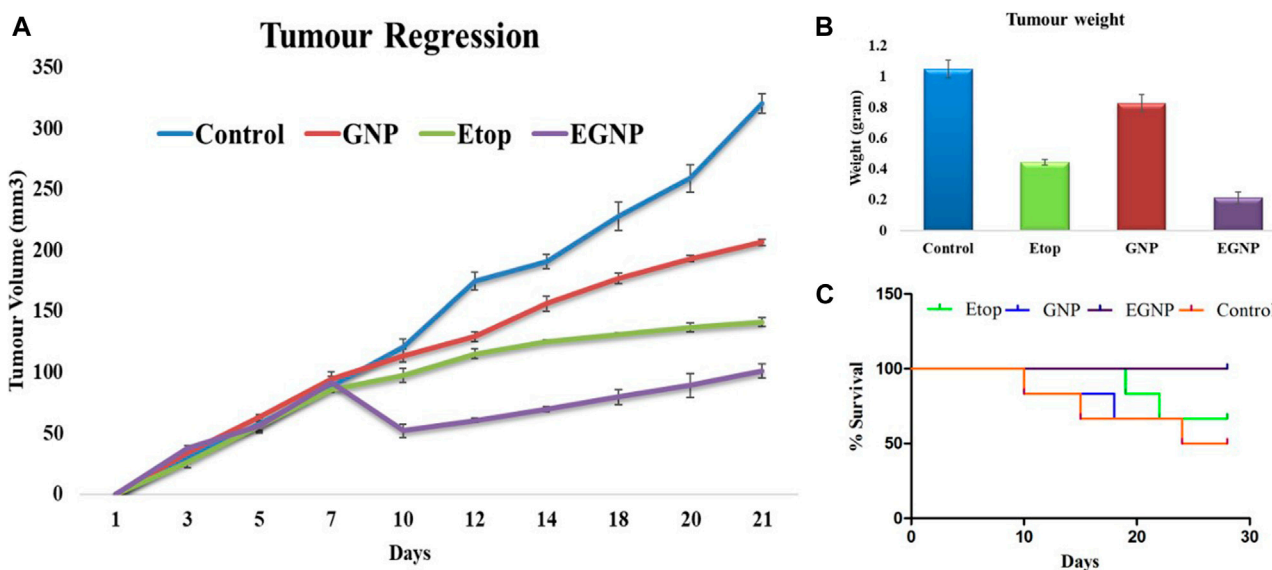
FIGURE 8 | *In vivo* studies in Balb/c mice after administering Etop, GNP and EGNP. **(A)** Tumour regression study for a period of 21 days. showed EGNP has better anti-tumour efficacy as compared to Etop *per se*. **(B)** Tumours were weighed after 21 days. EGNP treatment has been able to reduce the weight and size of tumours effectively in comparison to Etop *per se* and control. **(C)** Percent Survival.

EAC is a homogenous tumor showing efficient capacity for ease of transplant, quick proliferation, assured malignancy, originally hyper-diploid, and described due to the absence of tumor-specific transplantation antigen (Othman et al., 2018).

Tumor regression efficacy of synthesized EGNP were evaluated. Our subcutaneous EAC solid tumor model does not exceed 20mm at the largest diameter, which is considered acceptable in standard procedures using mouse models. After 21days, results of tumor regression analysis indicated that our EGNP formulation causes significant reduction in tumor size when compared to Etop *per se*. Tumor progression was evident in Control and GNP treated mice (**Figure 8**).

Anti-tumor efficacy of EGNP may be contributed to the Enhanced permeability and retention effect (EPR). EPR effect is possible in solid tumors as the drug delivery system can be passively accumulated based on its size and enhanced circulation time in the blood thereby reducing the tumor burden (Allen and Cullis, 2004; Maeda, 2013).

The promising results in the terms of percentage survival (100%) and decreased tumor volume in case of EGNP are accredited to increase in accumulation at the tumor site that causes sustained release of etoposide drug from our smart, pH responsive gelatin nanoparticles resulting in long-time circulation in the body. The steady release of Etop from GNPs could be attributed to lysosomal degradation and acidic tumor environment. Hence, the results proved the therapeutic efficacy of the GNPs as a biocompatible drug delivery carrier for Etop delivery for cancer therapy.

CONCLUSION

The sustained expansion of nanotechnology entails an inclusive understanding of the probable mechanisms of their toxicity for appropriate safety evaluation and identification of expressed biomarkers. Their impact on biological pathways have begun to emerge as the complex death paradigms that are needed to be explained by activation of different death pathways in a context-dependent manner. We report preparation of GNPs in the size range of ~150nm with PDI of 0.257; Physical characterization specified a spherical morphology and a size that was in unison with the NTA data. Etop, a highly hydrophobic, low molecular weight drug was entrapped in GNPs. The therapeutic efficacy is only possible by its hydrolysis inside the target cells where Etop *per se* is released. Increased biotoxicity was observed by EGNPs at a much lower concentration of Etop in MCF-7 cells when compared to HEK-293 cells. Crucially, EGNPs were efficient as it enabled reduction in the concentration of etoposide without negotiating the efficacy of cell mortality. Results of the long term biotoxicity study concluded that the EGNPs formulations were efficient in reducing the viability of MCF-7 cells over a period of three days, whereas pure Etop exerted its maximum efficiency within 24h. Moreover, specific apoptosis inhibitors, such as zVAD, can further shed light on the presence of apoptosis. With respect to caspase inhibition, the serine proteases RIPK1 and RIPK3 could possibly switch apoptosis to necroptosis, a pro-inflammatory and regulated form of cell death, characterized by loss of plasma membrane permeability and release of intracellular contents, such as LDH. Therefore, explicating the nanoparticles induced activation of molecular mechanistic cell death signaling pathways would be crucial for development of novel strategies to abate nanotoxicity. Gene expression profiling is further expected to recognize the various mechanisms that trigger the potential toxicity of drug molecules. Overall, to improve the efficacy of classical cancer drugs, treatment-driven gene expression vagaries can be exploited and their pre-treatment prediction could be of enormous clinical value to evolve a guided cancer therapy regimen.

DATA AVAILABILITY STATEMENT

The raw data supporting the conclusions of this article will be made available by the authors, without undue reservation.

ETHICS STATEMENT

This article does not contain any studies with human participants or animals performed by any of the authors. However, the animal study was reviewed and approved by Institutional Animal Ethics Committee, K.M. College, University of Delhi.

AUTHOR CONTRIBUTIONS

AV has made significant contributions to the conception and design of this work, as well as the drafting, data interpretation, and revision of this manuscript. IM has contributed significantly to the experimental work, data acquisition and analysis of data. LB, ZY, NK, AL, DM, contributed towards paper in data acquisition, formatting, revision and final approval of this manuscript.

FUNDING

ACKNOWLEDGMENTS

SUPPLEMENTARY MATERIAL

The Supplementary Material for this article can be found online at: https://www.frontiersin.org/articles/10.3389/fnano.2021.624083/full#supplementary-material.

REFERENCES

Afshari, C. A., Hamadeh, H. K., and Bushel, P. R. (2011). The evolution of bioinformatics in toxicology: advancing toxicogenomics. *Toxicol. Sci.* 120 (Suppl_1), S225–S237. doi:10.1093/toxsci/kfq373

Allen, T. M., and Cullis, P. R. (2004). Drug delivery systems: entering the mainstream. *Science* 303 (5665), 1818–1822. doi:10.1126/science.1095833

Berridge, M. V., Herst, P. M., and Tan, A. S. (2005). Tetrazolium dyes as tools in cell biology: new insights into their cellular reduction. *Biotechnol. Annu. Rev.* 11, 127–152. doi:10.1016/S1387-2656(05)11004-7

Brown, J. M., and Attardi, L. D. (2005). The role of apoptosis in cancer development and treatment response. *Nat. Rev. Cancer.* 5, 231–237. doi:10.1038/nrc1560

Bujie, D., Mengxiao, Y., and Zheng, J. (2018). Transport and interactions of nanoparticles in the kidneys. *Nat. Rev. Mater.* 3, 358–374. doi:10.1038/s41578-018-0038-3

Cai, Z., Jitkaew, S., Zhao, J., Chiang, H. C., Choksi, S., Liu, J., et al. (2014). Plasma membrane translocation of trimerized MLKL protein is required for TNF-induced necroptosis. *Nat. Cell Biol.* 16, 55–65. doi:10.1038/ncb2883

Cesàro, A., Bellich, B., and Borgogna, M. (2012). Biophysical functionality in polysaccharides: from Lego-blocks to nano-particles. *Eur. Biophys. J.* 41 (4), 379–395. doi:10.1007/s00249-011-0753-9

Chen, X., Li, W., Ren, J., Huang, D., He, W. T., Song, Y., et al. (2014). Translocation of mixed lineage kinase domain-like protein to plasma membrane leads to necrotic cell death. *Cell Res.* 24, 105–121. doi:10.1038/cr.2013.171

Cho, Y. S. (2018). The role of necroptosis in the treatment of diseases. *BMB Rep.* 51 (5), 219–224. (2018). doi:10.5483/bmbrep.2018.51.5.074

Coester, C., Kreuter, J., von Briesen, H., and Langer, K. (2000). Preparation of avidin-labelled gelatin nanoparticles as carriers for biotinylated peptide nucleic acid (PNA). *Int. J. Pharm.* 196 (2), 147–149. doi:10.1016/s0378-5173(99)00409-3

De Jong, W. H., and Borm, P. J. (2008). Drug delivery and nanoparticles: applications and hazards. *Int. J. Nanomedicine.* 3 (2), 133–149. doi:10.2147/ijn.s596

Degterev, A., Huang, Z., Boyce, M., Li, Y., Jagtap, P., Mizushima, N., et al. (2005). Chemical inhibitor of nonapoptotic cell death with therapeutic potential for ischemic brain injury. *Nat. Chem. Biol.* 1 (2), 112–119. doi:10.1038/nchembio711

Dobrovolskaia, M. A., Clogston, J. D., Neun, B. W., Hall, J. B., Patri, A. K., and McNeil, S. E. (2008). Method for analysis of nanoparticle hemolytic properties *in vitro. Nano Lett.* 8 (8), 2180–2187. doi:10.1021/nl0805615

Dondelinger, Y., Declercq, W., Montessuit, S., Roelandt, R., Goncalves, A., Bruggeman, I., et al. (2014). MLKL compromises plasma membrane integrity by binding to phosphatidylinositol phosphates. *Cell Rep.* 7, 971–981. doi:10.1016/j.celrep.2014.04.026

Duong, J., Veal, G., Nath, C., Shaw, P., Errington, J., Ladenstein, R., et al. (2019). Population pharmacokinetics of carboplatin, etoposide and melphalan in children: a re-evaluation of paediatric dosing formulas for carboplatin in patients with normal or mild impairment of renal function, *Br. J. Clin. Pharmacol.* 85, 136–146. doi:10.1111/bcp.13774

Ellinger-Ziegelbauer, H., Gmuender, H., Bandenburg, A., and Ahr, H. J. (2008). Prediction of a carcinogenic potential of rat hepatocarcinogens using toxicogenomics analysis of short-term *in vivo* studies. *Mutat. Res.* 637 (1–2), 23–39. doi:10.1016/j.mrfmmm.2007.06.010

Elzoghby, A. O., Samy, W. M., and Elgindy, N. A. (2012). Protein-based nanocarriers as promising drug and gene delivery systems. *J. Control. Release.* 161 (1), 38–49. doi:10.1016/j.jconrel.2012.04.036

Elzoghby, A. O. (2013). Gelatin-based nanoparticles as drug and gene delivery systems: reviewing three decades of research. *J. Control. Release.* 172 (3), 1075–1091. doi:10.1016/j.jconrel.2013.09.019

Fitzmaurice, C., Fitzmaurice, C., Allen, C., Barber, R. M., Barregard, L., Bhutta, Z. A., et al. (2017). Global, regional, and national cancer incidence, mortality, years of life lost, years lived with disability, and disability-adjusted life-years for 32 cancer groups, 1990 to 2015: a systematic analysis for the global burden of disease study. *JAMA Oncol.* 3 (4), 524–548. doi:10.1001/jamaoncol.2016.5688

Fuchs, S., Klier, J., May, A., Winter, G., Coester, C., and Gehlen, H. (2012). Towards an inhalative invivo application of immunomodulating gelatin nanoparticles in horse-related preformulation studies. *J. Microencapsul.* 29 (7), 615–625. doi:10.3109/02652048.2012.668962

Giampietri, C., Starace, D., Petrungaro, S., Filippini, A., and Ziparo, E. (2014). Necroptosis: molecular signalling and translational implications. *Int. J. Cell Biol.* 2014, 490275. doi:10.1155/2014/490275

Henwood, J. M., and Brogden, R. N. (1990). Etoposide. A review of its pharmacodynamic and pharmacokinetic properties, and therapeutic potential in combination chemotherapy of cancer. *Drugs* 39 (3), 438–490. doi:10.2165/00003495-199039030-00008

Hubbell, J. A., and Chilkoti, A. (2012). Chemistry. Nanomaterials for drug delivery. *Science* 337, 303–305. doi:10.1126/science.1219657

Hudson, D., and Margaritis, A. (2014). Biopolymer nanoparticle production for controlled release of biopharmaceuticals. *Crit. Rev. Biotechnol.* 34 (2), 161–179. doi:10.3109/07388551.2012.743503

Jabr-Milane, L., van Vlerken, L., Devalapally, H., Shenoy, D., Komareddy, S., Bhavsar, M., et al. (2008). Multi-functional nanocarriers for targeted delivery of drugs and genes. *J. Control. Release.* 130 (2), 121–128. doi:10.1016/j.jconrel.2008.04.016

Jain, V., Kumar, H., Anod, H. V., Chand, P., Gupta, N. V., Dey, S., et al. (2020). A review of nanotechnology-based approaches for breast cancer and triple-negative breast cancer. *J. Control. Release.* 326, 628–647. doi:10.1016/j.jconrel.2020.07.003

Kaul, G., and Amiji, M. (2004). Biodistribution and targeting potential of poly(ethylene glycol)-modified gelatin nanoparticles in subcutaneous murine tumor model. *J. Drug Target.* 12 (9–10), 585–591. doi:10.1080/10611860400013451

Leekha, A., Gurjar, B. S., Tyagi, A., Rizvi, M. A., and Verma, A. K. (2016). Vitamin C in synergism with cisplatin induces cell death in cervical cancer cells through altered redox cycling and p53 upregulation. *J. Cancer Res. Clin. Oncol.* 142 (12), 2503–2514. doi:10.1007/s00432-016-2235-z

Maeda, H. (2013). The link between infection and cancer: tumor vasculature, free radicals, and drug delivery to tumors via the EPR effect. *Cancer Sci.* 104 (7), 779–789. doi:10.1111/cas.1215

Magadala, P., and Amiji, M. (2008). Epidermal growth factor receptor-targeted gelatin-based engineered nanocarriers for DNA delivery and transfection in human pancreatic cancer cells. *AAPS J.* 10 (4), 565–576. doi:10.1208/s12248-008-9065-0

Moin, I., Biswas, L., Mittal, D., Leekha, A., Kumari, N., and Verma, A. K. (2018). Crosstalk of ER stress, mitochondrial membrane potential and ROS determines cell death mechanisms induced by etoposide loaded gelatin nanoparticles in MCF-7 breast cancer cells. *J. Nanomed Nanotechnol.* 9 (513), 2. doi:10.4172/2157-7439.1000513

Montecucco, A., Zanetta, F., and Biamonti, G. (2015). Molecular mechanisms of etoposide. *EXCLI J.* 14, 95–108. doi:10.17179/excli2015-561

Moriwaki, K., and Chan, F. K. (2013). RIP3: a molecular switch for necrosis and inflammation. *Genes Dev.* 27, 1640–1649. doi:10.1101/gad.223321.113

Mosmann, T. (1983). Rapid colorimetric assay for cellular growth and survival: application to proliferation and cytotoxicity assays. *J. Immunol. Methods* 65, 55–63. doi:10.1016/0022-1759(83)90303-4

Nie, A. Y., McMillian, M., Parker, J., Leone, A., Bryant, S., Yieh, L., et al. (2006). Predictive toxicogenomics approaches reveal underlying molecular mechanisms of nongenotoxic carcinogenicity. *Mol. Carcinog.* 45 (12), 914–933. doi:10.1002/mc.20205

Nuwaysir, E. F., Bittner, M., Trent, J., Barrett, J. C., and Afshari, C. A. (1999). Microarrays and toxicology: the advent of toxicogenomics. *Mol. Carcinog.* 24 (3), 153–159. doi:10.1002/(sici)1098-2744(199903)24:3<153::aid-mc1>3.0.co;2-p

Othman, A. I., El-Sherbiny, I. M., ElMissiry, M. A., Ali, D. A., and AbdElhakim, E. (2018). Polyphenon-E encapsulated into chitosan nanoparticles inhibited proliferation and growth of Ehrlich solid tumor in mice. *Egypt. J. Basic Appl. Sci.* 5 (1), 110–120. doi:10.1016/j.ejbas.2017.10.008

Plowman, J., Dykes, D. J., Hollingshead, M., Simpson-Herren, L., and Alley, M. C. (1997). "Human tumor xenograft models," in *Anticancer drug development guide: preclinical screening, clinical trials, and approval*. Editor B Teicher (Totowa, NJ: Humana Press), 101–125.

Pognan, F. (2007). Toxicogenomics applied to predictive and exploratory toxicology for the safety assessment of new chemical entities: a long road

with deep potholes, *Prog. Drug Res.* 64, 219–238. doi:10.1007/978-3-7643-7567-6_9

Ricci, M. S., and Zong, W. X. (2006). Chemotherapeutic approaches for targeting cell death pathways. *Oncologist.* 11 (4), 342–357. doi:10.1634/theoncologist.11-4-342

Saxena, A., Sachin, K., Bohidar, H., and Verma, A. K. (2005). Effect of molecular weight heterogeneity on drug encapsulation efficiency of gelatin nano-particles. *Colloids Surf. B Biointerfaces.* 45, 42–48. doi:10.1016/j.colsurfb.2005.07.005

Shafagh, M., Rahmani, F., and Delirezh, N. (2015). CuO nanoparticles induce cytotoxicity and apoptosis in human K562 cancer cell line via mitochondrial pathway, through reactive oxygen species and p53. *Iran J. Basic Med. Sci.* 18 (10), 993–1000.

Shnoudeh, A. J., Hamad, I., Abdo, R. W., Qadumii, L., Jaber, A. Y., Surchi, H. S., et al. (2019). Synthesis, characterization, and applications of metal nanoparticles. *Adv. Pharm. Product. Develop. Res.* 30, 527–612. doi:10.1016/b978-0-12-814427-5.00015-9

Shu-Ting, P., Zhi- Ling, L., Zhi-Xu, H., Jia-Xuan, Q., and Shu-Feng, Z. (2016). Molecular mechanisms for tumour resistance to chemotherapy. *Clin. Exp. Pharmacol. Physiol.* 43, 723–737. doi:10.1111/1440-1681.12581

Siddiqui, M. F., Muqaddas, M., and Sarwar, S. (2015). Biochemical mechanisms of etoposide; upshot of cell death. *Int. J. Pharm. Sci. Res.* 6 (12), 4920–4939. doi:10.13040/IJPSR.0975-8232.6(12).4920-39

Singh, D., Singh, D., Choi, S. M., and Han, S. S. (2013). Enhanced proliferation and growth of human lung epithelial cells on gelatin microparticle loaded with Ephedra extracts. *J. Nanomater.* 2013, 909120. doi:10.1155/2013/909120

Singh, D., Han, S. S., and Shin, E. J. (2014). Polysaccharides as nanocarriers for therapeutic applications. *J. Biomed. Nanotechnol.* 10 (9), 2149–2172. doi:10.1166/jbn.2014.1958

Snehalatha, M., Venugopal, K., Saha, N., Babbar, M.K., and Sharma, R.K. (2008). Etoposide loaded PLGA and PCL nanoparticles II: biodistribution and pharmacokinetics after radiolabeling with Tc-99m. *Drug Deliv.* 15, 277–287.

Soni, G., and Yadav, K. S. (2014). High encapsulation efficiency of poloxamer-based injectable thermoresponsive hydrogels of etoposide. *Pharm. Dev. Technol.* 19, 651–661. doi:10.3109/10837450.2013.819014

Starmans, L. W., van Duijnhoven, S. M., Rossin, R., Berben, M., Aime, S., Daemen, M. J., et al. (2013). Evaluation of 111In-labeled EPep and FibPep as tracers for fibrin SPECT imaging. *Mol. Pharm.* 10 (11), 4309–4321. doi:10.1021/mp400406x

Sun, L., Wang, H., Wang, Z., He, S., Chen, S., Liao, D., et al. (2009). Mixed lineage kinase domain-like protein mediates necrosis signaling downstream of RIP3 kinase. *Cell.* 148, 213–227. doi:10.1016/j.cell.2011.11.031

Tabata, Y. (2009). Biomaterial technology for tissue engineering applications. *J. R. Soc. Interf.* 6 (3), S311–S324. doi:10.1098/rsif.2008.0448.focus

Urban, T. A., Lucena, M., Gaffney, K., Dean, R. M., Gerds, A. T., Hamilton, B. K., et al. (2019). Comparison of the tolerability of busulfan, cyclophosphamide, etoposide (BuCyVP) versus carmustine, etoposide, cytarabine, melphalan (BEAM) for autologous hematopoietic cell transplant (AHCT) in Hodgkin lymphoma, *Biol. Blood Marrow Transplant.* 25, S277–S278. doi:10.1016/j.bbmt.2018.12.344

Vandenabeele, P., Grootjans, S., Callewaert, N., and Takahashi, N. (2013). Necrostatin-1 blocks both RIPK1 and IDO: consequences for the study of cell death in experimental disease models. *Cell Death Differ.* 20 (2), 185–187. doi:10.1038/cdd.2012.151

Vanlangenakker, N., Vanden Berghe, T., Bogaert, P., Laukens, B., Zobel, K., Deshayes, K., et al. (2011). cIAP1 and TAK1 protect cells from TNF-induced necrosis by preventing RIP1/RIP3-dependent reactive oxygen species production. *Cell Death Differ.* 18 (4), 656–665. doi:10.1038/cdd.2010.138

Verma, A. K., Pandey, R. P., Chanchal, A., and Sharma, P. (2011). Immuno-potentiating role of 687 encapsulated proteins of infectious diseases in biopolymeric nanoparticles as a potential delivery system. *J. Biomed. Nanotechnol.* 7 (1), 63–64.

Verma, A. K., and Sachin, K. (2008). Novel hydrophilic drug polymer nano-conjugates of Cisplatin showing long blood retention profile: its release kinetics, cellular uptake and bio-distribution. *Curr. Drug Deliv.* 5, 120–126. (2008). doi:10.2174/156720108783954806

Verma, A. K., Sachin, K., Saxena, A., and Bohidar, H. B. (2005). Release kinetics from bio-polymeric nanoparticles encapsulating protein synthesis inhibitor-cycloheximide, for possible therapeutic applications. *Curr. Pharmaceut. Biotechnol.* 6 (2), 121–130.

Vonarbourg, A., Passirani, C., Saulnier, P., and Benoit, J. P. (2006). Parameters influencing the stealthiness of colloidal drug delivery systems. *Biomaterials.* 27 (24), 4356–4373. doi:10.1016/j.biomaterials.2006.03.039

Wang, H., Sun, L., Su, L., Rizo, J., Liu, L., Wang, L. F., et al. (2014). Mixed lineage kinase domain-like protein MLKL causes necrotic membrane disruption upon phosphorylation by RIP3. *Mol. Cell.* 54, 133–146. doi:10.1016/j.molcel.2014.03.003

Zhang, D. W., Shao, J., Lin, J., Zhang, N., Lu, B. J., Lin, S. C., et al. (2009). RIP3, an energy metabolism regulator that switches TNF-induced cell death from apoptosis to necrosis. *Science* 325 (5938), 332–336. doi:10.1126/science.1172308

Zwiorek, K., Kloeckner, J., Wagner, E., and Coester, C. (2005). Gelatin nanoparticles as a new and simple gene delivery system. *J. Pharm. Pharm. Sci.* 7 (4), 22–28.

Synergism of Zinc Oxide Quantum Dots with Antifungal Drugs: Potential Approach for Combination Therapy against Drug Resistant *Candida albicans*

Preeti Chand[1], Sangeeta Kumari[2], Neelima Mondal[2], Surinder P. Singh[3]* and Tulika Prasad[1]*

[1]Special Centre for Nano Sciences and AIRF, Jawaharlal Nehru University, New Delhi, India, [2]School of Life Sciences, Jawaharlal Nehru University, New Delhi, India, [3]CSIR-National Physical Laboratory, Dr. K. S. Krishnan Marg, New Delhi, India

Candidiasis caused by *Candida albicans* is one of the most common microbial infections. Azoles, polyenes, allylamines, and echinocandins are classes of antifungals used for treating *Candida* infections. Standard drug doses often become ineffective due to the emergence of multidrug resistance (MDR). This leads to the use of higher drug doses for prolonged duration, resulting in severe toxicity (nephrotoxicity and liver damage) in humans. However, combination therapy using very low concentrations of two or more antifungal agents together, can lower such toxicity and limit evolution of drug resistance. Herein, 4–6 nm zinc oxide quantum dots (ZnO QDs) were synthesized and their *in vitro* antifungal activities were assessed against drug-susceptible (G1, F1, and GU4) and resistant (G5, F5, and GU5) isolates of *C. albicans*. In broth microdilution assay, ZnO QDs exhibited dose dependent growth inhibition between 0 – 200 µg/ml and almost 90% growth was inhibited in all *Candida* strains at 200 µg/ml of ZnO QDs. Synergy between ZnO QDs and antifungal drugs at sub-inhibitory concentrations of each was assessed by checkerboard analysis and expressed in terms of the fractional inhibitory concentration (FIC) index. ZnO QDs were used with two different classes of antifungals (azoles and polyenes) against *Candida* isolates: combination 1 (with fluconazole); combination 2 (with ketoconazole); combination 3 (with amphotericin B), and combination 4 (with nystatin). Results demonstrated that the potency of combinations of ZnO QDs with antifungal drugs even at very low concentrations of each was higher than their individual activities against the fungal isolates. The FIC index was found to be less than 0.5 for all combinations in the checkerboard assay, which confirmed synergism between sub-inhibitory concentrations of ZnO QDs (25 µg/ml) and individual antifungal drugs. Synergism was further confirmed by spot assay where cell viabilities of *Candida* strains were significantly reduced in all combinations, which was clearly evident from the disappearance of fungal cells on agar plates containing antifungal combinations. For safer clinical use, the *in vitro* cytotoxic activity of ZnO QDs was assessed against HeLa cell line and it was found that ZnO QDs were non-toxic at 25 µg/ml. Results suggested that the combination of ZnO QDs with drugs potentiate antimicrobial activity through multitargeted action. ZnO QDs

could therefore offer a versatile alternative in combination therapy against MDR fungal pathogens, wherein lowering drug concentrations could reduce toxicity and their multitargeted action could limit evolution of fungal drug resistance.

INTRODUCTION

Recurrence of local and systemic fungal infections have posed a life-threatening public health problem globally for immunocompromised individuals, and treatment for fungal infections is estimated to cost around more than $7.2 billion (Benedict et al., 2019). *Candida* species are the most notorious, opportunistic fungal pathogens, known to cause oral and systemic candidiasis (Lamoth et al., 2018). Individuals with cancer treatment, organ transplantation surgeries, congenital immunodeficiency syndromes, acquired immunodeficiency syndrome (AIDS), and indwelling medical devices are frequently infected by *Candida*, resulting in morbidity and mortality due to invasive candidiasis (Prasad et al., 2011; Pal et al., 2017; Tso et al., 2018; Xiao et al., 2019). Antifungal drugs such as triazoles (fluconazole, itraconazole, and voriconazole) constitute the first line of standard treatment for candidiasis but due to their fungistatic action, fungal strains acquire resistance in due course toward the standard doses of these drugs (Watt et al., 2013). The next class of antifungal drugs comprises of polyenes (amphotericin B and nystatin) and next-generation echinocandins (caspofungin and micafungin). Although polyenes are effective fungicidal compounds, amphotericin B has toxic side effects such as renal impairment (Spampinato and Leonardi, 2013). Echinocandins are safer than amphotericin B and disrupt fungal cell wall integrity by inhibiting synthesis of β (1,3)-D-glucan (a fungal cell wall component). But echinocandins have a few drawbacks such as poor oral availability, high cost, and administration by intravenous injection only; which limit their use as standard treatment for invasive candidiasis (Spampinato and Leonardi, 2013).

Consequently, due to the limited antifungal arsenal, researchers have sought to improve treatment via different approaches. The approach of combination therapy consisting of two or more drugs in synergism has been considered as an alternative for treatment (Ahmed et al., 2014; Campitelli et al., 2017) to achieve broad spectrum antimicrobial activity and simultaneously reduce the risk of acquiring resistance during therapy. Combination therapy in place of monotherapy was therefore, introduced as a novel, safe, effective therapy, especially to target drug resistant strains and improve survival rate in high-risk life-threatening infections (Tamma et al., 2012). The objective behind this use of combination therapy was to lower the toxicity by reducing the standard administrative doses of drugs and improve the clinical efficacy of existing drugs (Campitelli et al., 2017). It is speculated that combination therapy affects multiple cellular/molecular targets in microbial pathogens, which prevents acquisition of MDR (Worthington and Melander, 2013; Campitelli et al., 2017). In combination therapy, the effect of interactions between two drugs is classified into three types: synergism, indifferent, and antagonism. The combination is called synergistic when the effect of combined drugs is greater than a single drug, indicating two different cellular targets for their action (Campitelli et al., 2017). While if the treatment shows no distinct difference, the combination is considered indifferent and if the effect is smaller than a single drug, then it is called antagonistic (Campitelli et al., 2017). Notably, the antagonistic effect might be due to the competition of both drugs for the same target, which might also be the reason for the antagonistic behavior of the amphotericin B and fluconazole combination against *Cryptococcus gattii*, where both compete for the same target, viz., ergosterol (Santos et al., 2012).

Use of two different classes of drugs targeting multiple components of fungal cells might be an effective strategy for treatment of fungal infections and in that context nanoparticles (NPs) might be an ideal choice for combination therapy because of their nano size, ease of surface modification, excellent antimicrobial activity, and cost-effective synthesis (Radhakrishnan et al., 2018a; Radhakrishnan et al., 2018b). Smaller, spherical NPs (within 50 nm) were highly permeable even in drug-resistant microbes which showed altered cell membrane/cell wall and overexpression of drug efflux pumps (Baptista et al., 2018). Moreover, the unique surface chemistry of NPs allows their conjugation with biomolecules for targeted drug delivery by facilitating controlled and sustained drug release (Wang et al., 2017). But toxicity due to NPs have been reported, which restricts the use of NPs as preferred antimicrobial agents for treatment. However, among various NPs, the ZnO NP, a semiconductor metal oxide, is extensively used in the medicinal industry and believed to be a biosafe, biocompatible, and non-toxic nanomaterial (Ali et al., 2018). Biocompatibility studies revealed no significant toxicity of ZnO NPs either in cell lines or during topical application for skin infection (Pati et al., 2014; Barman, 2015; Yusof et al., 2019). In addition to having excellent antimicrobial activity and preventing microbial biofilm deposition on implants, ZnO NPs also promoted proliferation of normal cells and angiogenesis (Memarzadeh et al., 2015; Oleshko et al., 2020). Hence, ZnO NPs were used for incorporation in implant and scaffold development (Pati et al., 2014; Barman, 2015; Yusof et al., 2019). Moreover, ZnO NPs displayed the potential for use as a supplement of Zn (essential micronutrient) in diet for regulation of innate and adaptive immune responses, enhancement of growth and development, prevention of local and systemic candidiasis, etc. (Swain et al., 2016; Yusof et al., 2019).

ZnO NPs mediate broad spectrum antimicrobial activity through targeting multiple cellular and molecular mechanisms,

which might prevent further acquisition of fungal drug resistance (Sirelkhatim et al., 2015). Therefore, it is likely that ZnO NPs in combination with other antifungal drugs might lead to a reduction in standard doses of antifungals, cost of treatment, and drug toxicity (Benedict et al., 2019). Furthermore, the size-dependent microbial toxicity of ZnO NPs was widely documented, wherein reduction in size increased antimicrobial activity (Preeti et al., 2020a; Jin et al., 2009; Joshi et al., 2009; Palanikumar et al., 2014; Sirelkhatim et al., 2015; da silva et al., 2019.

Spherical nanoparticles (commonly within 10 nm) with size comparable to or less than the Bohr radius of the material, where quantum confinement effects are prominent, are known as "quantum dots" (QDs) (Poulopoulos et al., 2012; Samanta et al., 2018). The quantum confinement in QDs create surface defects and produce active sites, which react with oxygen and hydroxyl ions to form highly reactive hydroxyl and superoxide radicals (Mudunkotuwa et al., 2012; Siddiqi et al., 2018). The smaller size in case of ZnO QDs facilitate higher dissolution of Zn^{2+} ions in solution, which could be responsible for the augmentation of reactive oxygen species (ROS) and thus resulting in peroxidation of biomolecules and cell death in microbial pathogens (Joshi et al., 2009; Asok et al., 2015). A recent study reported broad spectrum microbicidal activity of ZnO QDs (5–6 nm) against MDR pathogens (*E. coli* and *C. albicans*), implying that antimicrobial activity of nano ZnO can be tuned by controlling the size (Preeti et al., 2020b). Antimicrobial activity of ZnO QDs has been reported singly against various microbial pathogens. However, in this study, we have demonstrated the use of ZnO QDs in combination with antifungal drugs of different classes against drug-susceptible and drug-resistant *Candida albicans* strains, in order to develop a biosafe, nano-based versatile alternative of combination therapy against MDR fungal pathogens, wherein drug concentrations can be lowered to reduce toxicity with the simultaneous advantage of multitargeted action to limit evolution of fungal drug resistance.

MATERIALS AND METHODS

Materials

Yeast extract, peptone, dextrose, and agar for fungal cell culture were purchased from Fisher Scientific (India) and Hi-Media (India). Absolute ethanol was obtained from Alfa Aesar (MA, United States) and hexane from Merck (NJ, United States). Zinc acetate dihydrate, lithium hydroxide monohydrate, standard antifungal drugs (fluconazole, ketoconazole, amphotericin B, and nystatin), dimethyl sulfoxide (DMSO) solvent, and cell culture media DMEM (Dulbecco's Modified Eagle's medium) were procured from Sigma Aldrich (United States). Penicillin-streptomycin antibiotic mix and fetal bovine serum (FBS) were obtained from Fisher Scientific (India) and trypan blue was obtained from Hi-Media (India).

Fungal Strains

Three isogenic matched pairs of *Candida albicans* (*C. albicans*) strains (G1 and G5, F1 and F5, and GU4 and GU5) were used in this study. These strains were provided as a kind gift by Joachim Morschhäuser, University of Würzburg, Germany. The strain

description is given in **Table 1**. These strains were originally isolated after regular intervals from three AIDS patients suffering from oropharyngeal candidiasis (OPC). During the course of azole therapy administered to these OPC patients, drug-susceptible G1, F1, and GU4 evolved after several months to highly drug-resistant G5, F5, and GU5, respectively due to acquisition of MDR (Franz et al., 1998; Franz et al., 1999).

Growth Media and Culture Conditions

The three isogenic matched pairs of *C. albicans* strains (G1 and G5, F1 and F5, and GU4 and GU5) were grown on (1% (w/v) yeast extract, 2% (w/v) peptone, and 2% (w/v) dextrose) (YEPD) media at 30°C for 14–16 h under continuous shaking at 140–150 rpm. Exponentially grown log phase microbial cells were used for all experiments. The cells were stored at 4°C on YEPD plates containing 2.5% agar.

Antifungal Compounds

Two different classes of standard antifungal drugs: azoles (fluconazole and ketoconazole) and polyenes (amphotericin B and nystatin) and ZnO QDs were used as test compounds. The stock solutions (2 mg/ml) of fluconazole were prepared in deionized (milli Q) water, while ketoconazole, amphotericin B, and nystatin were dissolved in DMSO. The stock solution (4 mg/ml) of ZnO QDs was prepared in deionized water (milli Q) and sonicated for 1 h before use.

Mammalian Cell Culture

Human cervical cancer cell line, HeLa was obtained from the American Type Culture Collection (Manassas, VA) and grown in DMEM media supplemented with 10% heat-inactivated FBS and 1% penicillin-streptomycin. Further, the cell line was incubated and maintained at 37°C under a humidified condition with 5% CO_2 (Gurung et al., 2019).

Synthesis and Characterization of Zinc Oxide Quantum Dots

ZnO QDs were synthesized using zinc acetate dihydrate as the precursor, as described earlier (Meulenkamp, 1999) with slight modifications. Briefly, the ethanolic solution of zinc acetate dihydrate (0.1 M) was prepared by refluxing the solution for 30 min. After that, the ethanolic solution of lithium hydroxide monohydrate (0.14 M) was added drop-wise on zinc acetate dihydrate solution kept under vigorous stirring for 1 h. Subsequently, ZnO QDs were precipitated by adding *n*-hexane and collected by centrifugation. After drying at 60°C under vacuum, ZnO QDs were obtained as white powder and their structural, optical, and functional properties were characterized using the following techniques.

The optical property of ZnO QDs was characterized using a UV-Vis spectrophotometer (Perkin Elmer, UV-Vis Spectrophotometer Lambda 35, Singapore). For structural characterization, X-ray diffraction (XRD) pattern was recorded in the scan range of 20°–80° diffraction angle and a step size of 0.016° using an X-ray powder diffractometer with Cu Kα radiation (λ = 1.5418Å) (PANalytical X'Pert PRO

C. albicans strains	Description and molecular changes	References
G1	• Drug-susceptible	Franz et al. (1998)
G5	• Drug-resistant • Enhanced *MDR1* mRNA levels • Mutation in *ERG11* gene • Change from *ERG11* heterozygosity to homozygosity	Franz et al. (1998)
F1	• Drug-susceptible	Franz et al. (1998)
F5	• Drug-resistant • Enhanced *MDR1* and *ERG11* mRNA levels	Franz et al. (1998)
GU4	• Drug-susceptible	Franz et al. (1999)
GU5	• Drug-resistant • Enhanced *CDR1/2* mRNA levels	Franz et al. (1999)

diffractometer, Almelo Netherlands). The shape and size of ZnO QDs were analyzed by a transmission electron microscope (TEM) (JEM 2100F; JEOL, Tokyo, Japan) using Image Tool software (multipoint image database software for grain and particle analysis; Dietermann and Heuser Solution GmbH, Greifenstein, Germany). High resolution TEM (HRTEM) analysis was done to visualize planar lattice spacing (d spacing) and electron diffraction pattern. The elemental composition of ZnO QDs was determined by EDX-mapping and spectra was obtained from TEM equipped with an energy-dispersive X-ray (EDX) spectrometer (EDS; Bruker Nano GmbH, Berlin, Germany).

Assessment of *In Vitro* Antifungal Activity of Zinc Oxide Quantum Dots

In vitro antifungal activity of ZnO QDs against isogenic matched pairs of *C. albicans* strains (F1 and F5, G1 and G5, and GU4 and GU5) was assessed by the broth microdilution method, as described by the standard protocol of the Clinical and Laboratory Standards Institute (CLSI) (Clinical and Laboratory Standards Institute, 2008; Prasad et al., 2005; Preeti et al., 2020a; Radhakrishnan et al., 2018a; Radhakrishnan et al., 2018b). The broth microdilution assay was performed in 96-well microtiter plates in triplicate. *Candida* strains were grown overnight, then resuspended in 0.9% saline in order to achieve an optical density (OD) of 0.1 at 600 nm, which corresponded to $0.5–1 \times 10^6$ CFU/ml. These cells were further diluted 100-fold in YEPD media to attain a final concentration of 10^4 CFU/ml. ZnO QDs ranging in concentration between 0–200 µg/ml were added to the YEPD media in plates containing cells of respective strains and incubated at 30°C for 48 h. Respective growth controls for the fungal strains were maintained without ZnO QDs. Minimum inhibitory concentration (MIC) was determined by measuring the OD at 600 nm at the lowest concentration of ZnO QDs that completely inhibited the growth of the fungal cells, and the percentage of growth inhibition was calculated from the differences in OD between the cells grown in the presence and absence of ZnO QDs.

Determination of Synergy Between Antifungal Agents by the Fractional Inhibitory Concentration Index in a Checkerboard Assay

The synergy between ZnO QDs and antifungal drugs was determined by calculating the fractional inhibitory concentration (FIC) index in a checkerboard assay. The individual potency of four different combinations comprising of ZnO QDs and antifungal drugs (fluconazole, ketoconazole, amphotericin B, and nystatin), where each was used at very low concentrations, was assessed by comparing with their individual activities against isogenic matched pairs of *C. albicans* strains (G1 and G5, F1 and F5, and GU4 and GU5).

FIC index was determined by a two-dimensional broth microdilution checkerboard assay, as described in the Clinical Microbiology Procedures Handbook (Moody, 2004). The assay was performed in 96-microtiter plates, where YEPD media was added aseptically in all wells and the concentration range was between 0.178–200 µg/ml for ZnO QDs, 0.125–64 µg/ml for fluconazole, and 0.015–8 µg/ml each for ketoconazole, amphotericin B, and nystatin. In each plate, the antifungal drug was serially diluted along the abscissa, while ZnO QDs were serially diluted along the ordinate. Subsequently, inoculum of 10^4 CFU/ml of each *Candida* strain was prepared separately in YEPD media. Then, 100 µl of the respective cell suspension was added into each well of the 96-well plates containing test compounds and incubated for 48 h at 30°C. The MICs of each antifungal drug alone, ZnO QDs alone, and their combinations were determined both visually and by measuring the ODs of cells at 600 nm using a microtiter plate reader. The inhibition in growth of fungal cells was calculated with respect to the growth control (absence of both drugs and ZnO QDs).

The ΣFIC index was calculated as follows:

$$\sum FIC\ Index\ =\ FIC_A\ +\ FIC_B$$

TABLE 2 | MIC values of antifungal drugs against *C. albicans* strains.

C. albicans strains	Fluconazole alone	Ketoconazole alone	Amphotericin B alone	Nystatin alone
	MIC (µg/ml)	MIC (µg/ml)	MIC (µg/ml)	MIC (µg/ml)
G1	8	1	2	4
G5	≥50	2	2	4
F1	16	4	2	4
F5	≥50	4	2	4
GU4	16	0.5	4	2
GU5	≥100	2	4	4

Here

$$FIC_A = \frac{MIC \ of \ agent \ A \ in \ combination}{MIC \ of \ agent \ A \ alone}$$

$$FIC_B = \frac{MIC \ of \ agent \ B \ in \ combination}{MIC \ of \ agent \ B \ alone}$$

Where

A is the individual antifungal drug (fluconazole, ketoconazole, amphotericin B, and nystatin) and B is ZnO QDs.

Interpretation of interactions in combinations of A (antifungal drug) and B (ZnO QDs) is as follows:

When the FIC index is ≤0.5, the combination is synergistic, at >0.5 to <4.0, the combination is indifferent, and at ≥4.0, the combination is antagonistic.

Spot Assay

A spot assay was performed to confirm the synergism between ZnO QDs and the four different antifungal drugs (fluconazole, ketoconazole, amphotericin B, and nystatin) against isogenic matched pairs (G1 and G5, F1 and F5, and GU4 and GU5) of *C. albicans* (Mukhopadhyay et al., 2004; Prasad et al., 2005; Preeti et al., 2020b; Radhakrishnan et al., 2018a; Radhakrishnan et al., 2018b). In the spot assay, separate YEPD plates were prepared by adding ZnO QDs alone, antifungal drugs alone, and four combinations containing both ZnO QDs and individual drugs (fluconazole, ketoconazole, amphotericin B and nystatin). Overnight grown log phase cells of each strain were separately resuspended in 0.9% saline and OD of each cell suspension at 600 nm was adjusted to 0.1. Subsequently, CFU/ml was calculated and 5-fold serial dilutions containing 1×10^6 cells/ml cells were prepared. A total of 5 µl of each serially diluted cell suspension was spotted onto each YEPD plate containing ZnO QDs alone, antifungal drugs alone, and four combinations containing both ZnO QDs and individual drugs. The plates were incubated for 48 h at 30°C. A separate growth control plate was also maintained without ZnO QDs and drugs. The images were then recorded and growth differences were evaluated by comparison with the growth control.

In Vitro Cytotoxic Activity of Zinc Oxide Quantum Dots

The *in vitro* cytotoxic activity of ZnO QDs was evaluated on HeLa cell line using a trypan blue exclusion assay (Gurung et al., 2019). Approximately 4×10^4 cells were plated in a culture dish containing DMEM media and allowed to adhere for 12 h, then

ZnO QDs (0 and 25 µg/ml) were added and incubated for 48 h in a humidified incubator (5% CO_2) at 37°C. After that, cells were trypsinized, harvested, and resuspended in equal volumes of phosphate buffer saline (PBS) and 0.4% trypan blue for cell counting. Thereafter, viable (unstained) and non-viable (blue-stained) cells were counted using a hemocytometer to find out the total numbers of living and dead cells after treatment with ZnO QDs.

Statistical Analysis

All experiments were performed at least three times and results are represented as the mean ± standard deviation (SD). A one-way ANOVA test was performed using GraphPad Prism version 8 (GraphPad Software, San Diego, CA) for validating the reproducibility and significance of results. The difference between the means was considered statistically significant at $^*p \leq 0.05$.

RESULTS AND DISCUSSION

Physicochemical Characterization of Zinc Oxide Quantum Dots

Figure 1A shows the typical absorption peak of ZnO QDs at 365 nm (corresponding to band gap of 3.4 eV), indicating the formation of ZnO QDs. **Figure 1B** represents the X-ray diffraction (XRD) peaks at 31.89°, 35.45°, 36.46°, 47.82°, 56.77°, 62.90°, and 68.40°. XRD confirmed a single phase hexagonal wurtzite structure, which was in agreement with JCPDS (Joint Committee on Powder Diffraction Standards), file no. 36–1,451. Furthermore, the TEM image (**Figure 2A**) revealed the average size of ZnO QDs to be ~ 4–6 nm (**Figure 2B**), while HRTEM confirmed the d spacing as 0.201 nm between the atomic planes of ZnO QDs (**Figure 2C**), which was in accordance with XRD data. The corresponding selected area electron diffraction (SAED) pattern confirmed the crystalline nature of ZnO QDs and the obtained rings matched with the diffraction planes of the XRD spectra (**Figure 2D**). TEM-EDX mapping revealed the presence of only zinc and oxygen elements in ZnO QDs (**Figure 2E**), while EDX spectra displayed typical sharp peaks of zinc around 1 and 8.6 keV and a single peak of oxygen at 0.5 keV, indicating no trace of impurity in the sample (**Figure 2F**).

Antimicrobial Potential of Zinc Oxide Quantum Dots

Severe fungal infections occur as a consequence of several health problems in immunocompromised cases due to acquired
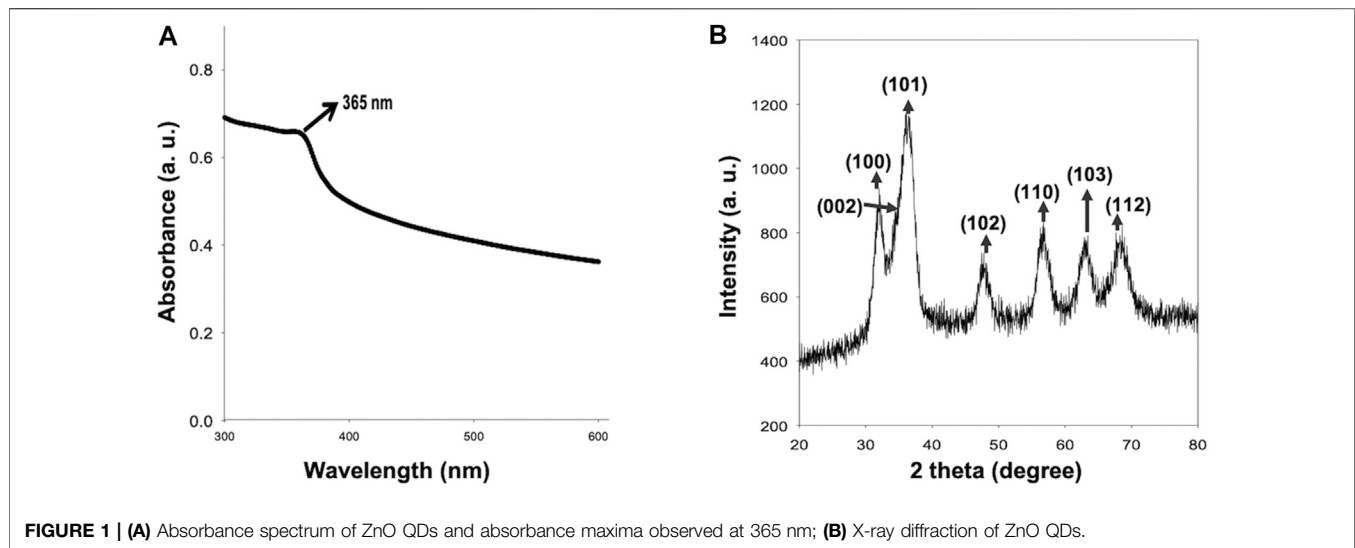
FIGURE 1 | (A) Absorbance spectrum of ZnO QDs and absorbance maxima observed at 365 nm; **(B)** X-ray diffraction of ZnO QDs.

immunodeficiency syndrome (AIDS), organ transplantation, chemotherapy, cancer, asthma, corticosteroid therapies, etc. Rampant use of antifungals in immunocompromised individuals have led to increasing incidence of fungal drug resistance. The pathogenesis and severity of fungal infection depend on various immunological and non-immunological factors. *C. albicans* is the most common, opportunistic fungal pathogen and forms a part of human microbiota, however, its pathogenesis depends on the immunity of the individual. Since the last few decades, several MDR strains of *Candida* spp. causing severe invasive candidiasis have emerged (Franz et al., 1998; Franz et al., 1999; Colombo et al., 2017). A study of *Candida* species in patients with AIDS showed 33% of late-stage patients with drug-resistant strains of *Candida* albicans in their oral cavities (White et al., 1998). Oropharyngeal candidiasis (OPC) is one of the most prevalent fungal infections occurring in HIV patients (occurrence range between 0.9 and 83%). Drug resistance in *C. albicans* is mainly responsible for failure of antifungal therapy when administered in standard doses (Patil et al., 2018). Interestingly, Franz et al. studied the mechanisms for acquired drug resistance in isogenic matched pairs of *C. albicans* strains (isolated from three AIDS patients, who were suffering from OPC and received azole standard therapy) and found that during the course of treatment, the drug-susceptible strains (G1, F1, and GU4) acquired drug resistance and evolved into drug-resistant G5, F5, and GU5. The proposed primary mechanisms for resistance toward azoles and polyenes include ergosterol gene mutation, alterations in membrane permeability, and efflux pump overexpression, which result in altered drug target (ergosterol), reduced drug uptake, and increased efflux of drugs from the cells (Franz et al., 1998; Franz et al., 1999; Srivastava et al., 2018).
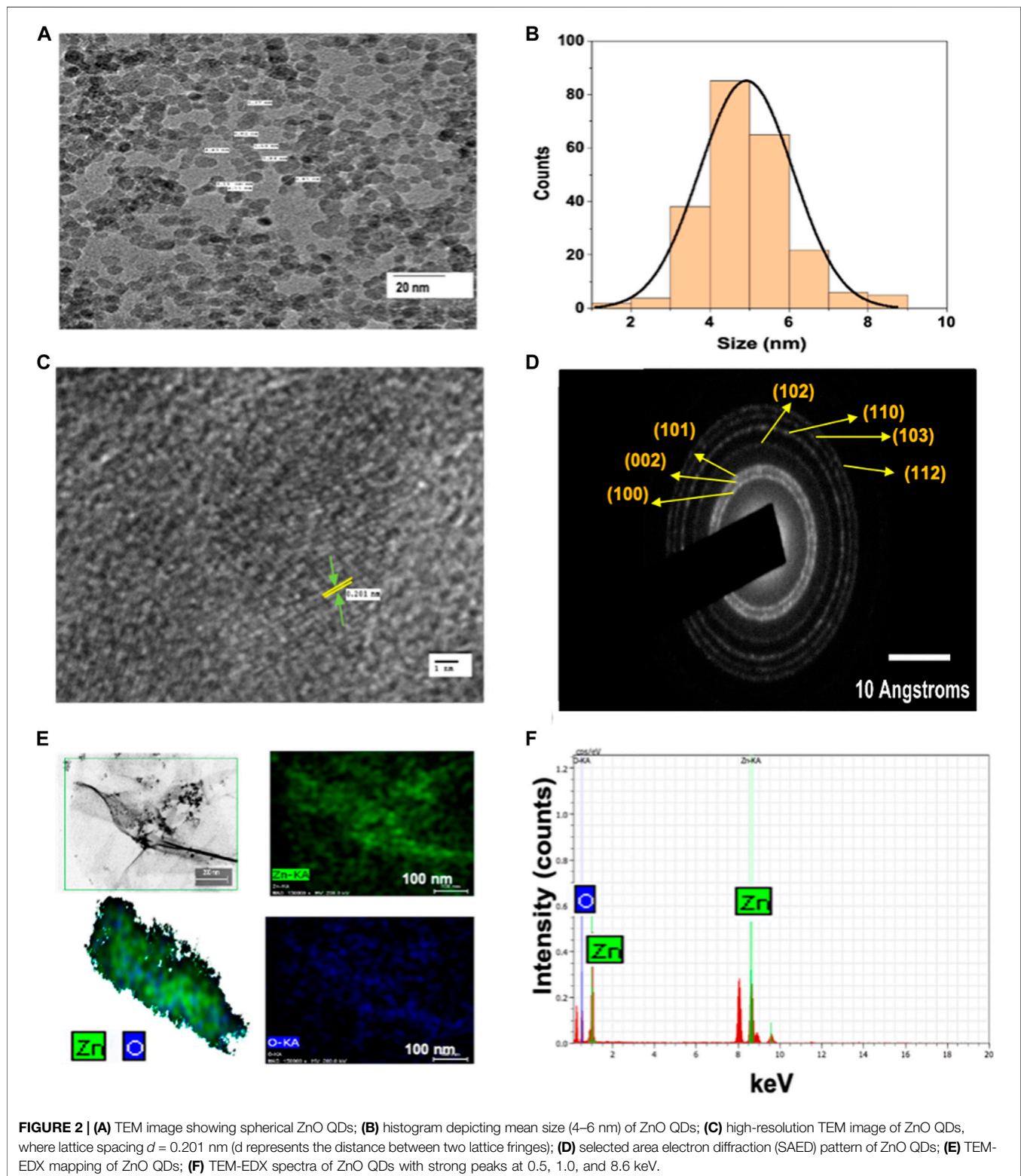
In order to improve the treatment outcome of microbial infections, nano-based drug compositions might be ideal candidates to address the challenges of microbial drug resistance by favoring multitargeted action, broad spectrum activity, and lower host toxicity (Radhakrishnan et al., 2018a; Radhakrishnan et al., 2018b). In addition to standard susceptibility testing and appropriate drug dosing, one of the ways to prevent drug resistance is the use of combination antifungal therapy. Therefore, in order to develop a nano-based therapeutic agent, we first investigated the antimicrobial activity of ZnO QDs against three isogenic matched pairs of *C. albicans* strains (drug-susceptible G1, F1, GU4 and drug-resistant G5, F5, and GU5) using a broth microdilution assay. Subsequently, synergy of ZnO QDs in different combinations with four antifungal drugs was assessed against the *C. albicans* strains using a checkerboard assay. Individual potency of these four different combinations of ZnO QDs and antifungal drugs (fluconazole, ketoconazole, amphotericin B, and nystatin), which were used at very low concentrations of each, was assessed by comparing their individual activities against the isogenic matched pairs of *C. albicans* strains.

Broth Microdilution Assay

The broth microdilution assay was performed in the presence of different concentrations of ZnO QDs between 0–200 µg/ml. Results demonstrated that ZnO QDs exhibited dose-dependent growth inhibition of all *C. albicans* strains (G1 and G5, F1 and F5, and GU4 and GU5) (**Figure 3A**). The maximum growth of cells was observed in control (without ZnO QDs), and growth of cells gradually decreased with increasing concentration of ZnO QDs (25–200 µg/ml) (**Figure 3A**). Further, the percentage of growth inhibition was calculated from the differences in OD at 600 nm between the fungal strains grown in the absence and presence of different concentrations of ZnO QDs. Interestingly, our results revealed almost 90, 90, 87, 85, 75, and 90% growth inhibition, respectively for the strains G1, G5, F1, F5, GU4, and GU5 at 200 µg/ml, however, 25–100 µg/ml of ZnO QDs showed growth inhibition between 30 and 50% for the strains (**Figure 3B**).

Respective growth controls for the fungal strains were maintained without ZnO QDs.

FIGURE 2 | (A) TEM image showing spherical ZnO QDs; **(B)** histogram depicting mean size (4–6 nm) of ZnO QDs; **(C)** high-resolution TEM image of ZnO QDs, where lattice spacing d = 0.201 nm (d represents the distance between two lattice fringes); **(D)** selected area electron diffraction (SAED) pattern of ZnO QDs; **(E)** TEM-EDX mapping of ZnO QDs; **(F)** TEM-EDX spectra of ZnO QDs with strong peaks at 0.5, 1.0, and 8.6 keV.

Fractional Inhibitory Concentration Index

The effect of interaction of drugs in combination is assessed by FIC index in the checkerboard assay (Doern, 2014). In this study, synergy between ZnO QDs and different antifungal drugs against *C. albicans* strains (G1 and G5, F1 and F5, and GU4 and GU5) was assessed by checkerboard assay and expressed in terms of FIC index. Firstly, MIC was determined for each drug (fluconazole, ketoconazole, amphotericin B, and nystatin)
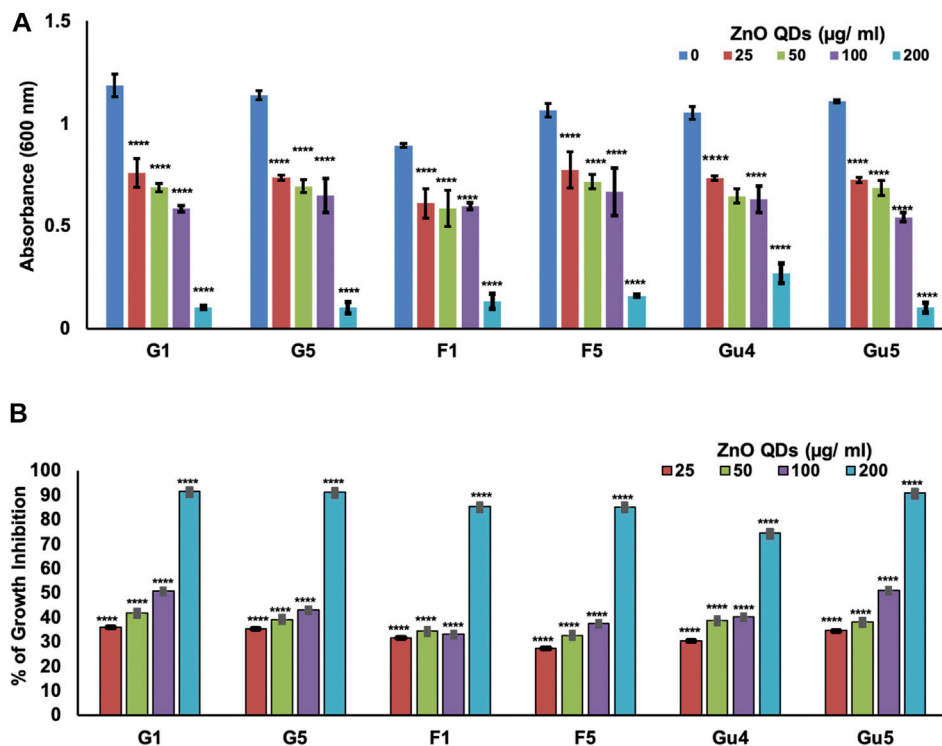
FIGURE 3 | Determination of dose-dependent antimicrobial activity of ZnO QDs against *C. albicans* strains (isogenic matched pairs G1 and G5, F1 and F5, and GU4 and GU5): **(A)** Determination of growth by measurement of OD_{600nm} using the broth microdilution method for *C. albicans* cells grown at 30°C in the presence of 0, 25, 50, 100, and 200 µg/ml of ZnO QDs, respectively. The values given are mean ± SD of three independent sets of experiments. **** represents *p* < 0.0001, calculated with respect to growth control (absence of ZnO QDs); **(B)** Percentage of growth inhibition of *C. albicans* strains (isogenic matched pairs) in the presence of ZnO QDs (0, 25, 50, 100, and 200 µg/ml). The values given are mean ± SD of three independent sets of experiments. **** represents *p* < 0.0001, calculated with respect to growth control (absence of ZnO QDs).

TABLE 3 | FIC index for different combinations of ZnO QDs and antifungal drugs tested against *C. albicans* strains.

	FIC index and interpretation for effect of QDs and drug combinations			
C. albicans strains	ZnO QDs + fluconazole	ZnO QDs + ketoconazole	ZnO QDs + amphotericin B	ZnO QDs + nystatin
G1	0.37 **Synergistic**	0.13 **Synergistic**	0.32 **Synergistic**	0.25 **Synergistic**
G5	0.165 **Synergistic**	0.14 **Synergistic**	0.32 **Synergistic**	0.18 **Synergistic**
F1	0.25 **Synergistic**	0.12 **Synergistic**	0.32 **Synergistic**	0.12 **Synergistic**
F5	0.165 **Synergistic**	0.12 **Synergistic**	0.32 **Synergistic**	0.12 **Synergistic**
GU4	0.25 **Synergistic**	0.15 **Synergistic**	0.17 **Synergistic**	0.37 **Synergistic**
GU5	0.156 **Synergistic**	0.13 **Synergistic**	0.22 **Synergistic**	0.25 **Synergistic**

against *C. albicans* strains (G1 and G5, F1 and F5, and GU4 and GU5). **Table 2** lists the MIC for each drug against respective *Candida* strains. Subsequently, based on MIC obtained for ZnO

QDs and each antifungal drug, singly and in combination, the FIC index for each combination was calculated as given in the Material and Methods section. Results demonstrated that the
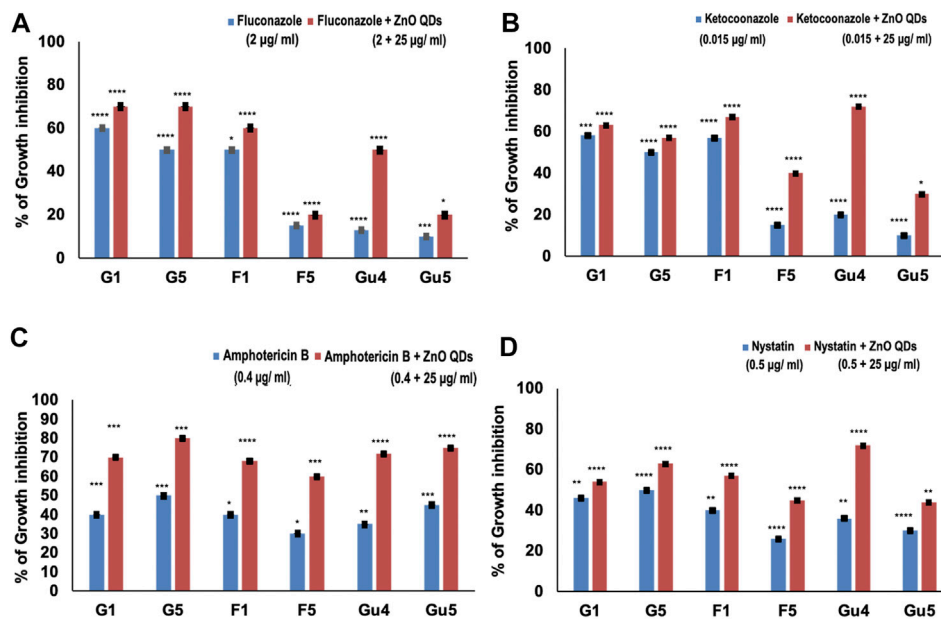
FIGURE 4 | Percentage of growth inhibition in C. albicans strains (isogenic matched pairs G1 and G5, F1 and F5, and GU4 and GU5) in the presence of both drugs and ZnO QDs as compared to growth control (absence of drugs and ZnO QDs): **(A)** Fluconazole + ZnO QDs; **(B)** Ketoconazole + ZnO QDs; **(C)** Amphotericin B + ZnO QDs; **(D)** Nystatin + ZnO QDs. The values are mean ± SD of three independent sets of experiments. **** represents $p < 0.0001$, *** represents $p < 0.0002$, ** represents $p < 0.0046$, * represents $p < 0.0408$, calculated with respect to growth control.

potency of combinations of ZnO QDs and antifungal drugs even at very low concentrations of each was higher than their individual activities against the fungal isolates. FIC index obtained in the checkerboard assay was less than 0.5 for all combinations tested (ZnO QDs + fluconazole; ZnO QDs + ketoconazole; ZnO QDs + amphotericin B and ZnO QDs + nystatin), which confirmed synergism between sub-inhibitory concentrations of both ZnO QDs (25 μg/ml) and individual antifungal drugs (**Table 3**). ZnO QDs and fluconazole exhibited synergism in combination, at a concentration of fluconazole which was 2 to 8-fold lower than the respective MIC values for fluconazole alone against the fungal strains tested (**Figure 4A**). Similarly, ZnO QDs displayed good synergistic activity in combination with very low concentrations of 0.015 μg/ml of ketoconazole, 0.4 μg/ml of amphotericin B, and 0.5 μg/ml of nystatin, and the concentration of each antifungal drug used in combination was much lower than the respective individual MIC values obtained for each drug against *Candida* strains (**Figures 4B–D**). Moreover, an increase in growth inhibition by 10–20% was observed in all strains for the four combinations of ZnO QDs and antifungal drugs, as compared to the strains grown in the presence of either individual drugs or only ZnO QDs (**Figure 4**).
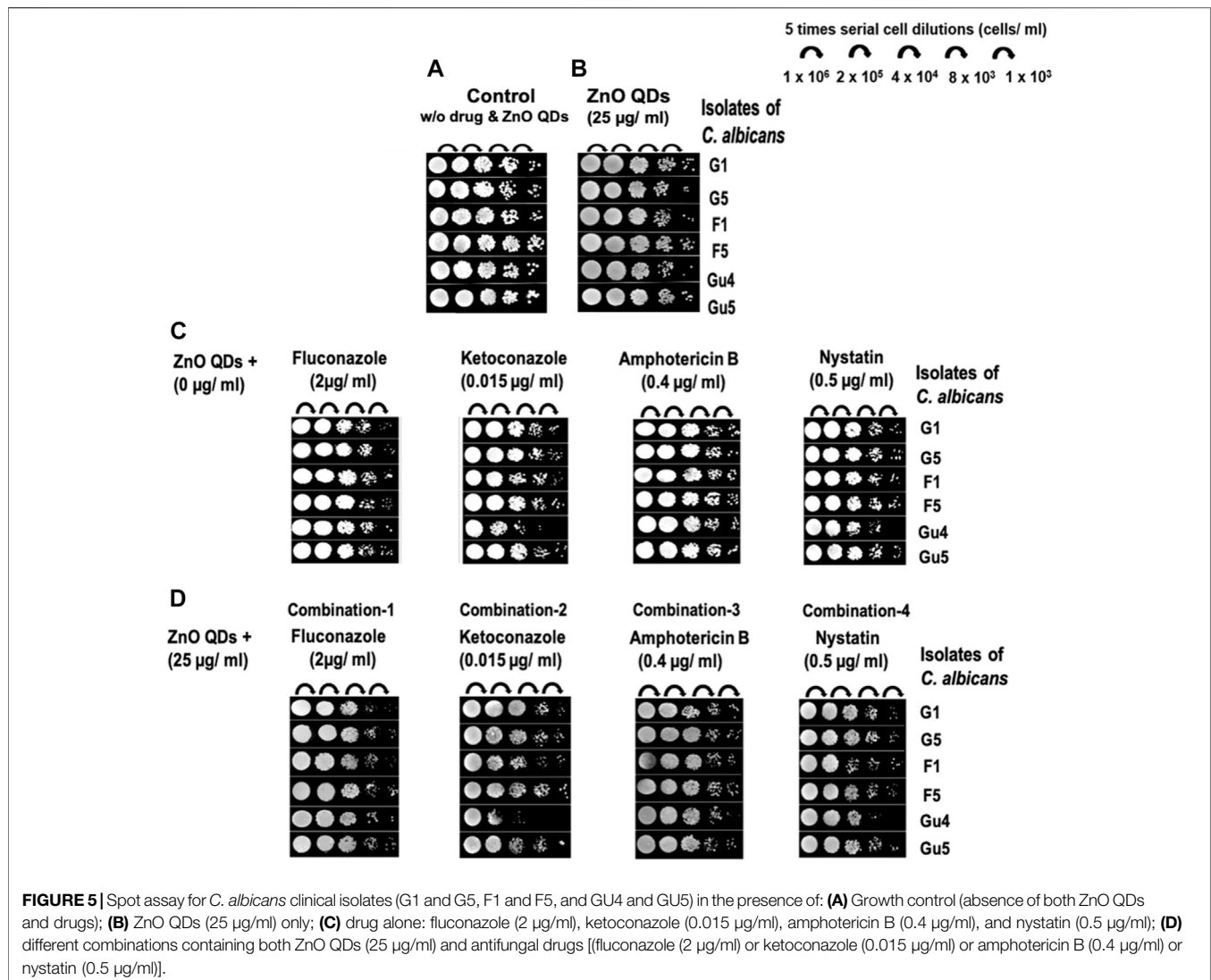
Synergism observed in combinations indicates that ZnO QDs and individual drugs (fluconazole, ketoconazole, amphotericin B, and nystatin) probably share a non-competitive cellular target, which potentiates the antifungal activity against both drug-susceptible (G1, G5, and F1) and resistant (G5, F5, and GU5) strains, even at concentrations much lower than their respective

individual MICs. However, the FIC index for the checkerboard assay has certain limitations since it only tests antimicrobials for a fixed incubation time rather than a continuous time frame and is also not capable of testing more than two antimicrobials at a time (combinations of three and four antimicrobials cannot be tested), which can slow down the assessment of potential synergistic combinations appropriately (Rybak and McGrath, 1996; Doern, 2014). Therefore, spot assay was further performed in this study to validate the results.

Spot Assay
The spot assay (**Figure 5**) further confirmed the synergism exhibited between ZnO QDs and antifungal drugs in combinations (**Table 4**). As compared to growth control (without ZnO QDs or drugs) in **Figure 5A**, a slight growth inhibition and reduction in fungal colonies was observed for all strains in the presence of sub-inhibitory concentration of ZnO QDs (**Figure 5B**) and individual antifungals drugs (**Figure 5C**). However, this reduction in cell viabilities was further increased for all *C. albicans* strains in the presence of different combinations of ZnO QDs and antifungal drugs, which was clearly evident from the disappearance of fungal cells on agar plates (**Figure 5D**).

The FIC index (**Table 3**) and spot assay (**Figure 5**) results indicate that ZnO QDs might be a potential adjuvant for antifungal combination therapy. The standard antifungal classes of drugs, i.e., azoles and polyenes act by inhibiting ergosterol biosynthesis and targeting the ergosterol moiety, respectively in the fungal membrane, whereas multiple

FIGURE 5 | Spot assay for *C. albicans* clinical isolates (G1 and G5, F1 and F5, and GU4 and GU5) in the presence of: **(A)** Growth control (absence of both ZnO QDs and drugs); **(B)** ZnO QDs (25 µg/ml) only; **(C)** drug alone: fluconazole (2 µg/ml), ketoconazole (0.015 µg/ml), amphotericin B (0.4 µg/ml), and nystatin (0.5 µg/ml); **(D)** different combinations containing both ZnO QDs (25 µg/ml) and antifungal drugs [(fluconazole (2 µg/ml) or ketoconazole (0.015 µg/ml) or amphotericin B (0.4 µg/ml) or nystatin (0.5 µg/ml)].

mechanisms of action are proposed for ZnO QDs such as high penetrability, greater retention, generation of oxidative stress, etc. When combined together, ZnO QDs and antifungal drugs might have exerted a concerted impact and were able to counter MDR in drug-resistant *Candida* strains (G5, F5, and GU5) (Asok et al., 2015; Sirelkhatim et al., 2015; da Silva et al., 2019; Gold et al., 2018; Tiwari et al., 2018).

This study demonstrates the promising potential of ZnO QDs for both single and combination antifungal therapy against MDR fungal pathogens. Since, ZnO QDs in combination with respective antifungal drugs exhibit synergism and can potentiate antifungal activity even at very low concentrations, use of ZnO QDs in combination therapy can reduce the toxicity of antifungal compounds. Additionally, simultaneous multitargeted action in combination therapy can prevent the development of fungal drug resistance.

However, for safer clinical use of ZnO QDs, we further investigated the *in vitro* cytotoxic activity of ZnO QDs against the HeLa cell line.

In Vitro Cytotoxic Activity

The *in vitro* cytotoxic activity of ZnO QDs (0, 5, and 25 µg/ml) was assessed by trypan blue assay in HeLa cell line and expressed as the percentage of viable cells after treatment with ZnO QDs, as compared to control cells without any treatment. Almost 93 and 86% cell viability was observed in the presence of 5 and 25 µg/ml of ZnO QDs, respectively, indicating that there was negligible toxicity to mammalian cells at 25 µg/ml of ZnO QDs (**Figure 6**) and hence, ZnO QDs at this concentration exhibited synergism with antifungal drugs and therefore, may be suitable for combination therapy.

CONCLUSION

Monotherapy against microbial infections often allow for the emergence of MDR in microbes with time and makes the standard drug doses ineffective leading to failure in treatment.
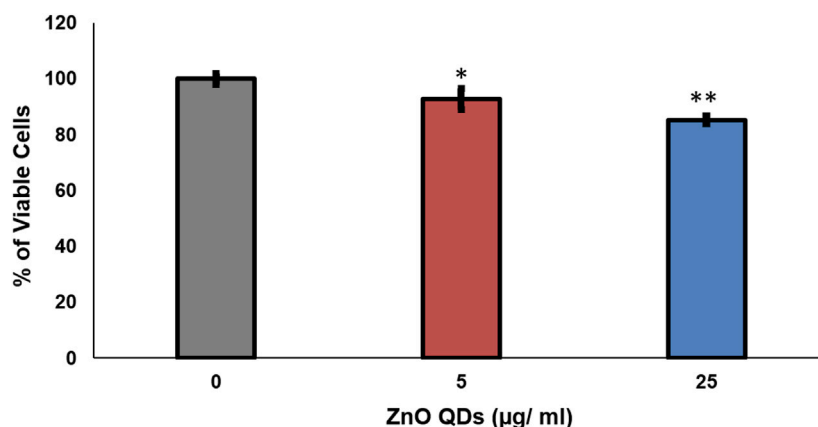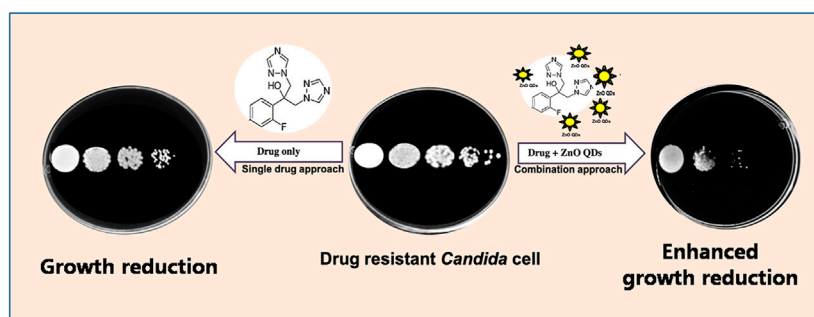
FIGURE 6 | *In vitro* cytotoxic activity of ZnO QDs against HeLa cell line. The values are mean ± SD of three independent sets of experiments. ** represents $p < 0.001$, * represents $p < 0.01$, calculated with respect to growth control.

SCHEME 1 | Graphical illustration of this study.

TABLE 4 | Concentrations of ZnO QDs and antifungal drugs used in different combinations for spot assays.

Combination	ZnO QDs + drug	ZnO QDs (concentration in µg/ml)	Drug used (concentration in µg/ml)
1	ZnO QDs + fluconazole	25	Fluconazole (2)
2	ZnO QDs + ketoconazole	25	Ketoconazole (0.015)
3	ZnO QDs + amphotericin B	25	Amphotericin B (0.4)
4	ZnO QDs + nystatin	25	Nystatin (0.5)

The bold represents a particular drug combination and the respective detail is provided in the next column only as ZnO QDs +Fluconazole , ZnO QDs +Ketoconazole, ZnO QDs +Amphotericin B And ZnO QDs +Nystatin. No further explanation is required.

Additionally, the high rates of morbidity and mortality caused by fungal infections are associated with availability of the limited antifungal arsenal and high toxicity of the compounds. Because of many similarities between fungal and human cells, identifying novel drug targets remains challenging. Owing to the limited availability of antifungal compounds, researchers have sought to improve treatment via different approaches. Therefore, to overcome these problems, combination therapy is considered for treatment (Ahmed et al., 2014; Campitelli et al., 2017). The combination therapy approach, however, is likely to offer a broader antimicrobial spectrum, lower toxicity of the antimicrobial compounds due to synergism at much lower concentrations in combination, and reduce the risk of acquiring resistance during therapy. Herein, we report synergism between sub-inhibitory concentrations of both ZnO QDs and individual antifungal drugs against all drug-susceptible and drug-resistant isolates of *C. albicans* tested. ZnO QDs thus appear to be a potential adjuvant in combination antifungal therapy against MDR fungal pathogens (**Scheme 1**), wherein drug toxicity can be reduced and their simultaneous multitargeted synergistic action can limit development of fungal drug resistance.

DATA AVAILABILITY STATEMENT

The raw data supporting the conclusions of this article will be made available by the authors, without undue reservation.

ETHICAL STATEMENT

The *Candida albicans* clinical isolates were kind gifts from Joachim Morschhauser, University of Wurzburg, Germany. These isolates have been extensively studied and their molecular characterization has been reported by various researchers all over the world, which is also mentioned in the materials and methods section of this study. The present study only involved *C. albicans* strains and did not require any samples from patients or involvement of any animal or human subject in the study. Therefore, no ethical approval was required.

AUTHOR CONTRIBUTIONS

PC, SPS, and TP contributed to the concept and design of the study. PC conducted all experiments. PC and SK performed cytotoxicity assay on HeLa cells. PC and TP participated in the acquisition of data and statistical analysis. PC, NM, SPS, and TP participated in interpretation of data and drafting of the manuscript. SPS and TP contributed to editing the manuscript and revised it critically for significant intellectual content. All authors read and approved the final manuscript.

FUNDING

ACKNOWLEDGMENTS

SUPPLEMENTARY MATERIAL

The Supplementary Material for this article can be found online at: https://www.frontiersin.org/articles/10.3389/fnano.2021.624564/full#supplementary-material

REFERENCES

Ahmed, A., Azim, A., Gurjar, M., and Baronia, A. K. (2014). Current Concepts in Combination Antibiotic Therapy for Critically Ill Patients. *Indian J. Crit. Care Med.* 18, 310–314. doi:10.4103/0972-5229.132495

Ali, A., Phull, A.-R., and Zia, M. (2018). Elemental Zinc to Zinc Nanoparticles: Is ZnO NPs Crucial for Life? Synthesis, Toxicological, and Environmental Concerns. *Nanotechnol. Rev.* 7, 413–441. doi:10.1515/ntrev-2018-0067

Asok, A., Ghosh, S., More, P. A., Chopade, B. A., Gandhi, M. N., and Kulkarni, A. R. (2015). Surface Defect Rich ZnO Quantum Dots as Antioxidants Inhibiting α-amylase and α-glucosidase: a Potential Anti-diabetic Nanomedicine. *J. Mater. Chem. B* 3, 4597–4606. doi:10.1039/c5tb00407a

Baptista, P. V., McCusker, M. P., Carvalho, A., Ferreira, D. A., Mohan, N. M., Martins, M., et al. (2018). Nano-Strategies to Fight Multidrug Resistant Bacteria-"A Battle of the Titans". *Front. Microbiol.* 9, 1441. doi:10.3389/fmicb.2018.01441

Barman, A. (2015). "Review on Biocompatibility of ZnO Nano Particles," in *Advancements of Medical Electronics. Lecture Notes in Bioengineering*. Editors S. Gupta, S. Bag, K. Ganguly, I. Sarkar, and P. Biswas (New Delhi: Springer), 343–352. doi:10.1007/978-81-322-2256-9_32

Benedict, K., Jackson, B. R., Chiller, T., and Beer, K. D. (2019). Estimation of Direct Healthcare Costs of Fungal Diseases in the United States. *Clin. Infect. Dis.* 68 (11), 1791–1797. doi:10.1093/cid/ciy776

Campitelli, M., Zeineddine, N., Samaha, G., and Maslak, S. (2017). Combination Antifungal Therapy: a Review of Current Data. *J. Clin. Med. Res.* 9, 451–456. doi:10.14740/jocmr2992w

Clinical and Laboratory Standards Institute (2008). *Reference Method for Broth Dilution Antifungal Susceptibility Testing of Filamentous Fungi; Approved Standard-Second Edition*. CLSI Document M38-A2. Wayne: Clinical and Laboratory Standards Institute. Available at: https://clsi.org/media/1455/m38a2_sample.pdf

Colombo, A. L., de Almeida Júnior, J. N., Slavin, M. A., Chen, S. C., and Sorrell, T. C. (2017). *Candida* and Invasive Mould Diseases in Non-Neutropenic Critically Ill Patients and Patients with Haematological Cancer. *Lancet Infect. Dis.* 17, e344–e356. doi:10.1016/S1473-3099(17)30304-3

da Silva, B. L., Caetano, B. L., Chiari-Andréo, B. G., Pietro, R. C. L. R., and Chiavacci, L. A. (2019). Increased Antibacterial Activity of ZnO Nanoparticles: Influence of Size and Surface Modification. *Colloids Surf.B Biointerfaces* 177, 440–447. doi:10.1016/j.colsurfb.2019.02.013

Doern, C. D. (2014). When Does 2 Plus 2 Equal 5? A Review of Antimicrobial Synergy Testing. *J. Clin. Microbiol.* 52, 4124–4128. doi:10.1128/JCM.01121-14

Franz, R., Kelly, S. L., Lamb, D. C., Kelly, D. E., Ruhnke, M., and Morschhäuser, J. (1998). Multiple Molecular Mechanisms Contribute to a Stepwise Development of Fluconazole Resistance in Clinical *C. albicans* Strains. *Antimicrob. Agents Chemother.* 42, 3065–3072. doi:10.1128/AAC.42.12.3065

Franz, R., Ruhnke, M., and Morschhauser, J. (1999). Molecular Aspects of Fluconazole Resistance Development in *Candida albicans*. *Mycoses* 42, 453–458. doi:10.1046/j.1439-0507.1999.00498.x

Gold, K., Slay, B., Knackstedt, M., and Gaharwar, A. K. (2018). Antimicrobial Activity of Metal and Metal-Oxide Based Nanoparticles. *Adv. Therap.* 1, 1700033. doi:10.1002/adtp.201700033

Gurung, S. K., Dana, S., Mandal, K., Mukhopadhyay, P., and Mondal, N. (2019). Downregulation of C-Myc and p21 Expression and Induction of S Phase Arrest by Naphthalene Diimide Derivative in Gastric Adenocarcinoma Cells. *Chemico-Biol. Inter.* 304, 106–123. doi:10.1016/j.cbi.2019.02.010

Husen, A., Mahmud, S., Seeni, A., Kaus, N. H. M., Ann, L. C., Bakhori, S. K. M., et al. (2015). Review on Zinc Oxide Nanoparticles: Antibacterial Activity and Toxicity Mechanism. *Nano-Micro Lett.* 7(3), 219–242. doi:10.1007/s40820-015-0040-x

Jin, T., Sun, D., Su, J. Y., Zhang, H., and Sue, H.-J. (2009). Antimicrobial efficacy of Zinc Oxide quantum dots against *Listeria monocytogenes*, *Salmonella enteritidis*, and *Escherichia coli* O157: H7. *J. Food Sci.* 74 (1), M46–M52. doi:10.1111/j.1750-3841.2008.01013.x

Joshi, P., Chakraborti, S., Chakrabarti, P., Haranath, D., Shanker, V., Ansari, Z. A., et al. (2009). Role of Surface Adsorbed Anionic Species in Antibacterial Activity of ZnO Quantum Dots against *Escherichia coli*. *J. Nanosci. Nanotech.* 9 (11), 6427–6433. doi:10.1166/jnn.2009.1584

Lamoth, F., Lockhart, S. R., Berkow, E. L., and Calandra, T. (2018). Changes in the Epidemiological Landscape of Invasive Candidiasis. *J. Antimicrob. Chemother.* 73, i4–i13. doi:10.1093/jac/dkx444

Memarzadeh, K., Sharili, A. S., Huang, J., Rawlinson, S. C. F., and Allaker, R. P. (2015). Nanoparticulate Zinc Oxide as a Coating Material for Orthopedic and Dental Implants. *J. Biomed. Mater. Res.* 103, 981–989. doi:10.1002/jbm.a.35241

Meulenkamp, E. A. (1999). Electron Transport in Nanoparticulate ZnO Films. *J. Phys. Chem. B* 103 (37), 7831–7838. doi:10.1021/jp9914673

Moody, J. A. (2004). *Synergism Testing: Broth Microdilution Checkboard and Broth Macrodilution Methods* in *Clinical Microbiology Procedures Handbook*. Editor H. D. Isenberg (Washington, DC: ASM Press), 1–28. doi:10.1128/9781555818814.ch5.16

Mudunkotuwa, I. A., Rupasinghe, T., Wu, C.-M., and Grassian, V. H. (2012). Dissolution of ZnO Nanoparticles at Circumneutral pH: A Study of Size Effects in the Presence and Absence of Citric Acid. *Langmuir* 28 (1), 396–403. doi:10.1021/la203542x

Mukhopadhyay, K., Prasad, T., Saini, P., Pucadyil, T. J., Chattopadhyay, A., and Prasad, R. (2004). Membrane Sphingolipid-Ergosterol Interactions Are Important Determinants of Multidrug Resistance in *Candida albicans*. *Antimicrob. Agents Chemother.* 48, 1778–1787. doi:10.1128/aac.48.5.1778-1787.2004

Oleshko, O., Husak, Y., Korniienko, V., Pshenychnyi, R., Varava, Y., Kalinkevich, O., et al. (2020). Biocompatibility and antibacterial properties of ZnO-incorporated anodic oxide coatings on TiZrNb Alloy. *Nanomaterials* 10, 2401. doi:10.3390/nano10122401

Pal, M. (2017). Morbidity and Mortality Due to Fungal Infections. *J. Appl. Microbiol. Biochem.* 1, 1–3. doi:10.21767/2576-1412.100002

Palanikumar, L., Ramasamy, S. N., and Balachandran, C. (2014). Size-dependent Antimicrobial Response of Zinc Oxide Nanoparticles. *IET Nanobiotechnol.* 8 (2), 111–117. doi:10.1049/iet-nbt.2012.0008

Pati, R., Mehta, R. K., Mohanty, S., Padhi, A., Sengupta, M., Vaseeharan, B., et al. (2014). Topical Application of Zinc Oxide Nanoparticles Reduces Bacterial Skin Infection in Mice and Exhibits Antibacterial Activity by Inducing Oxidative Stress Response and Cell Membrane Disintegration in Macrophages. *Nanomedicine: Nanotechnology, Biol. Med.* 10, 1195–1208. doi:10.1016/j.nano.2014.02.012

Patil, S., Majumdar, B., Sarode, S. C., Sarode, G. S., and Awan, K. H. (2018). Oropharyngeal Candidosis in HIV-Infected Patients-An Update. *Front. Microbiol.* 9, 980. doi:10.3389/fmicb.2018.00980

Poulopoulos, P., Lewitz, B., Straub, A., Pappas, S. D., Droulias, S. A., Baskoutas, S., et al. (2012). Band-gap Tuning at the Strong Quantum Confinement Regime in Magnetic Semiconductor EuS Thin Films. *Appl. Phys. Lett.* 100 (21), 211910. doi:10.1063/1.4720167

Prasad, T., Saini, P., Gaur, N. A., Vishwakarma, R. A., Khan, L. A., Haq, Q. M. R., et al. (2005). Functional Analysis of *CaIPT1*, a Sphingolipid Biosynthetic Gene Involved in Multidrug Resistance and Morphogenesis of *Candida albicans*. *Antimicrob. Agents Chemother.* 49, 3442–3452. doi:10.1128/AAC.49.8.3442-3452.2005

Prasad, T., Sethumadhavan, S., and Fatima, Z. (2011). "Altered Ergosterol Biosynthetic Pathway–An Alternate Multidrug Resistance Mechanism Independent of Drug Efflux Pump in Human Pathogenic Fungi *C. albicans*," in *Science against Microbial Pathogens: Communicating Current Research and Technological Advances, Microbiology Series*. Editor A. Méndez-Vilas Badajoz (Spain: Formatex Research Center), 757–768.

Preeti, Prasad, T., Magoo, D., Meena, K., Ghorai, S. M., and Kaur, H. (2020a). Elucidation of the Antimicrobial Capabilities of Spirooxindole Fused Heterocycles Synthesized via Catalyst Free Method. *Indian J. Nat. Sci.* 10, 27323–27330.

Preeti, Radhakrishnan, V. S., Radhakrishnan, S., Mukherjee, S., Singh, S. P., and Prasad, T. (2020b). ZnO Quantum Dots: Broad Spectrum Microbicidal Agent against Multidrug Resistant Pathogens *E. coli* and *C. albicans*. *Front. Nanotechnol.* 2, 576342. doi:10.3389/fnano.2020.576342

Radhakrishnan, V. S., Dwivedi, S. P., Siddiqui, M. H., and Prasad, T. (2018a). *In Vitro* studies on Oxidative Stress-Independent, Ag Nanoparticles-Induced Cell Toxicity of *C. albicans*, an Opportunistic Pathogen. *Int. J. Nanomedicine* 13, 91–96. doi:10.2147/IJN.S125010

Radhakrishnan, V. S., Reddy Mudiam, M. K., Kumar, M., Dwivedi, S. P., Singh, S. P., and Prasad, T. (2018b). Silver Nanoparticles Induced Alterations in Multiple Cellular Targets, Which Are Critical for Drug Susceptibilities and Pathogenicity in Fungal Pathogen (*Candida albicans*). *Int. J. Nanomed.* 13, 2647–2663. doi:10.2147/IJN.S150648

Rybak, M. J., and McGrath, B. J. (1996). Combination Antimicrobial Therapy for Bacterial Infections. *Drugs* 52, 390–405. doi:10.2165/00003495-199652030-00005

Samanta, P. K. (2018). Strong and Weak Quantum Confinement and Size Dependent Optoelectronic Properties of Zinc Oxide. *Ann. Univ. Craiova Phys.* 28, 17–23.

Santos, J. R. A., Gouveia, L. F., Taylor, E. L. S., Resende-Stoianoff, M. A., Pianetti, G. A., César, I. C., et al. (2012). Dynamic Interaction between Fluconazole and Amphotericin B against *Cryptococcus Gattii*. *Antimicrob. Agents Chemother.* 56, 2553–2558. doi:10.1128/AAC.06098-11

Siddiqi, K. S., ur Rahman, A., Tajuddin and Husen, A. (2018). Properties of Zinc Oxide Nanoparticles and Their Activity against Microbes. *Nanoscale Res. Lett.* 13, 141. doi:10.1186/s11671-018-2532-3

Sirelkhatim, A., Mahmud, S., Seeni, A., Kaus, N., Ann, L. C., Bakhori, S., et al. (2015). Review on Zinc Oxide Nanoparticles: Antibacterial Activity and Toxicity Mechanism. *Nanomicro Lett.* 7 (3), 219–242. doi:10.1007/s40820-015-0040-x

Spampinato, C., and Leonardi, D. (2013). *Candida* Infections, Causes, Targets, and Resistance Mechanisms: Traditional and Alternative Antifungal Agents. *BioMed. Res. Int.* 2013, 204237. doi:10.1155/2013/204237

Srivastava, V., Singla, R. K., and Dubey, A. K. (2018). Emerging Virulence, Drug Resistance and Future Anti-fungal Drugs for *Candida* Pathogens. *Curr. Top Med. Chem.* 18 (9), 759–778. doi:10.2174/1568026618666180528121707

Swain, P. S., Rao, S. B., Rajendran, D., Dominic, G., and Selvaraju, S. (2016). Nano Zinc, An Alternative to Conventional Zinc as Animal Feed Supplement: A Review. *Anim. Nutr.* 2 (3), 134–141. doi:10.1016/j.aninu.2016.06.003

Tamma, P. D., Cosgrove, S. E., and Maragakis, L. L. (2012). Combination Therapy for Treatment of Infections with Gram-Negative Bacteria. *Clin. Microbiol. Rev.* 25(3), 450–470. doi:10.1128/CMR.05041-11

Tiwari, V., Mishra, N., Gadani, K., Solanki, P. S., Shah, N. A., and Tiwari, M. (2018). Mechanism of Anti-bacterial Activity of Zinc Oxide Nanoparticle against Carbapenem-Resistant *Acinetobacter Baumannii*. *Front. Microbiol.* 9, 1218. doi:10.3389/fmicb.2018.01218

Tso, G. H. W., Reales-Calderon, J. A., and Pavelka, N. (2018). The Elusive Anti-*Candida* Vaccine: Lessons from the Past and Opportunities for the Future. *Front. Immunol.* 9, 897. doi:10.3389/fimmu.2018.00897

Wang, L., Hu, C., and Shao, L. (2017). The Antimicrobial Activity of Nanoparticles: Present Situation and Prospects for the Future. *Int. J. Nanomedicine* 12, 1227–1249. doi:10.2147/IJN.S121956

Watt, K., Manzoni, P., Cohen-Wolkowiez, M., Rizzollo, S., Boano, E., Jacqz-Aigrain, E., et al. (2013). Triazole Use in the Nursery: Fluconazole, Voriconazole, Posaconazole, and Ravuconazole. *Curr. Drug Metab.* 14 (2), 193–202. doi:10.2174/138920013804870583

White, T. C., Marr, K. A., and Bowden, R. A. (1998). Clinical, Cellular, and Molecular Factors that Contribute to Antifungal Drug Resistance. *Clin. Microbiol. Rev.* 11 (2), 382–402. doi:10.1128/cmr.11.2.382

Worthington, R. J., and Melander, C. (2013). Combination Approaches to Combat Multidrug-Resistant Bacteria. *Trends Biotechnology* 31 (3), 177–184. doi:10.1016/j.tibtech.2012.12.006

Xiao, Z., Wang, Q., Zhu, F., and An, Y. (2019). Epidemiology, Species Distribution, Antifungal Susceptibility and Mortality Risk Factors of Candidemia Among Critically Ill Patients: a Retrospective Study from 2011 to 2017 in a Teaching Hospital in China. *Antimicrob. Resist. Infect. Control.* 8, 89. doi:10.1186/s13756-019-0534-2

Yusof, H. M., Mohamad, R., and Zaidan, U. H. (2019). Microbial Synthesis of Zinc Oxide Nanoparticles and Their Potential Application as an Antimicrobial Agent and a Feed Supplement in Animal Industry: a Review. *J. Anim. Sci. Biotechnol.* 10, 57. doi:10.1186/s40104-019-0368-z

Advantages of publishing in Frontiers

OPEN ACCESS
Articles are free to read
for greatest visibility
and readership

FAST PUBLICATION
Around 90 days
from submission
to decision

HIGH QUALITY PEER-REVIEW
Rigorous, collaborative,
and constructive
peer-review

TRANSPARENT PEER-REVIEW
Editors and reviewers
acknowledged by name
on published articles

Frontiers
Avenue du Tribunal-Fédéral 34
1005 Lausanne | Switzerland

Visit us: www.frontiersin.org
Contact us: frontiersin.org/about/contact

REPRODUCIBILITY OF RESEARCH
Support open data
and methods to enhance
research reproducibility

DIGITAL PUBLISHING
Articles designed
for optimal readership
across devices

FOLLOW US
@frontiersin

IMPACT METRICS
Advanced article metrics
track visibility across
digital media

EXTENSIVE PROMOTION
Marketing
and promotion
of impactful research

LOOP RESEARCH NETWORK
Our network
increases your
article's readership